Impact of Aggregate Gradation and Filler Type on Marshall Properties of Asphalt Concrete

Saad Issa Sarsam
Professor
College of engineering- University of Baghdad
E-mail: saadisasarsam@coeng.uobaghdad.edu.iq

Kadhum Hulial Sultan
MSc. student
College of engineering- University of Baghdad
E-mail: hulail_kadhum@yahoo.com

ABSTRACT

As asphalt concrete wearing course (ACWC) is the top layer in the pavement structure, the material should be able to sustain stresses caused by direct traffic loading. The objective of this study is to evaluate the influence of aggregate gradation and mineral filler type on Marshall Properties. A detailed laboratory study is carried out by preparing asphalt mixtures specimens using locally available materials including asphalt binder (40-50) penetration grade, two types of aggregate gradation representing SCRB and ROAD NOTE 31 specifications and two types of mineral filler including limestone dust and coal fly ash. Four types of mixtures were prepared and tested. The first type included SCRB specification and limestone dust, the second type included SCRB specification and coal fly ash, the third types included ROAD NOTE 31 specification and limestone dust and the fourth type included ROAD NOTE 31 specification and coal fly ash. The optimum asphalt content of each type of mixtures was determined using Marshall Method of mix design. 60 specimen were prepared and tested with dimension of 10.16 cm in diameter and 6.35 cm in height. Results of this study indicated that aggregate gradation and filler type have a significant effect on optimum asphalt content and Marshall Properties. From the experimental data, it was observed that the value of Marshall Stability is comparatively higher when using fly ash as filler as compared to limestone dust.

Keywords: asphalt concrete mixture, aggregate gradation, mineral filler, Marshall Properties.

تأثير اختلاف تدرج الركام ونوع المادة المالئة على خصائص مارشال للخرسانة الاسفلتية

سعد عيسى سرسم
استاذ
جامعة بغداد-كلية الهندسة – قسم الهندسة المدنية

كاظم هليل سلطان
طالب ماجستير
جامعة بغداد-كلية الهندسة – قسم الهندسة المدنية

الخلاصة

ان طبقة الخرسانة الاسفلتية هي الطبقة العليا في تشكيل الرصفة وهذا يتطلب ان تكون المواد المستخدمة قادرة على مقاومة الاجهادات الناتجة عن حركة المرور العالية المباشرة. الهدف الرئيسي من البحث هو تحديد تاثير اختلاف التدرج ونوع المادة المالئة على خصائص مارشال للخرسانة الاسفلتية. الدراسة المختبرية المفصلة نفذت بتحضير نماذج من الخرسانة الاسفلتية عن طريق استخدام مواد متوفرة محلياً والتي تتظمن اسفلت سمنت ذو الاختراق (40-50) ونوعين من تدرج الركام الذين يمثلان المواصفة العراقية للطرق والجسور والمواصفة البريطانية وكذلك تم استخدام نوعين من المادة المالئة والذين يمثلان غبار الحجر الجيري ورماد الفحم المتطاير. تم تحضير اربعة انواع من الخلطات, كانت الخلطة الاولى مكونة من تدرج مواصفة الطرق والجسور وغبار الحجر الجيري والثانية مكونة من تدرج مواصفة الطرق والجسور ورماد الفحم المتطاير

والثالثة مكونة من تدرج المواصفة البريطانية وغبار الحجر الجيري والرابعة مكونة من تدرج المواصفة البريطانية ورماد الفحم المتطاير. تم ايجاد نسبة الاسفلت المثلى لكل نوع من الخلطات باستخدام طريقة تصميم مارشال. تم تحضير وفحص 60 نموذج بقطر 10,16 سم وارتفاع 6,35 سم . اظهرت نتائج هذه الدراسة الى ان تدرج الركام ونوع المادة المالئة لهما تاثير كبير على خصائص مارشال ونسبة الاسفلت المثالية. لوحظ ايضاً ان قيمة ثبات مارشال اعلى نسبياً عند استخدام رماد الفحم المتطاير كمادة مالئة بدلاً عن غبار الحجر الجيري.

الكلمات الرئيسيه: خلطة الخرسانة الاسفلتية, تدرج الركام, المادة المعدنية المالئة, خصائص مارشال.

1. INTRODUCTION

In order to provide comfortable ride and withstand the effects arising from traffic loading and climate, pavement materials should be designed to achieve a certain level of performance and the performance should be maintained during the service life, **Zhi Suo and Wing, 2008**. Fillers as one of the components in an asphalt mixture, play a major role in determining the properties and the behavior of the mixture, especially the binding and aggregate interlocking effects, **Sarsam, 1984**. Mineral fillers serve a dual purpose when added to asphalt mixes, the portion of the mineral filler that is finer than the thickness of the asphalt film blends with asphalt cement binder to form a mortar or mastic that contributes to improved stiffening of the mix. Particles larger than the thickness of the asphalt film behave as mineral aggregate and hence contribute to the contact points between individual aggregate particles, **Puzinauskas, 1969**. In general, filler have various purposes among which, they fill voids and hence reduce optimum asphalt content and increase stability, meet specifications for aggregate gradation, and improve bond between asphalt cement and aggregate, **Bouchard, 1992**. Gradation is defined as the distribution of particle sizes expressed as a percent of the total weight. If the specific gravities of the aggregates used are similar, the gradation in volume will be similar to the gradation in weight.

2. RESEARCH OBJECTIVE

The objective of this research is to investigating the influence of using two types of aggregate gradation and two types of mineral filler on optimum asphalt content and Marshall Properties.

3. BACKGROND

Ali et al. 1996 investigated the effects of fly ash on the material and mechanical properties of asphalt mixtures; results from this study indicated that fly ash can be used as a mineral filler to improve resilient modulus characteristics and stripping resistance. **Sarsam, 2015**, studied the effect of adding nano material such as fly ash and silica fumes on the properties of asphalt cement, it was concluded that such nano materials have positive effect on asphalt cement rheological properties. **Sarsam, 2013** concluded that nano materials such as coal fly ash and lime have improved the physical properties of asphalt cement. **Kallas and Puzinauskas, 1967** believed that filler performed a dual role in asphalt-aggregate mixtures. A portion of the filler with particles larger than the asphalt film will contribute in producing the contact points between aggregate particles, while the remaining filler is in colloidal suspension in the asphalt binder, resulting in a binder with a stiffer consistency. They also found that the stabilities of asphalt mixtures increased up to a certain filler concentration, then decrease with additional filler. A study was made by **Matthews and Monismith, 1992** on effects of gradation on the asphalt content where both wearing and binder mixes were considered. Further, they have carried out regression analysis on test data to investigate the relationship between asphalt content and gradation. Their study shows that no correlation exists between asphalt content and the percent passing the 4.75mm (No. 4) and 2.36mm (No. 8) sieves for the wearing mix. On the other hand, for binder mixes there exists a relationship between changes in gradation and measured asphalt content that shows as the mix becomes finer for the given sieve size, the asphalt content increases. **Roberts et al., 1996** suggested that gradation is perhaps the most important property which affects almost all the important properties of a bituminous mixture, including stiffness, stability, durability, permeability, workability, fatigue resistance, frictional resistance, and resistance to moisture damage. **Sarsam, 1987** studied the effect of various gradations on Marshall properties of asphalt concrete, it was concluded that gap gradation exhibit more stability and low flow values when compared to dense graded mixes.

4. MATERIAL CHARACERISTIC

4.1 Asphalt Cement

Asphalt cement of (40-50) penetration grade from Nasiriya refinery was used in this work. The physical properties of original asphalt cement are presented in **Table 1.**

4.2 Aggregate

Coarse and fine aggregates were obtained from AL-Ukhaydir- Karbala quarry; their physical properties are listed in **Table 2**.

4.3 Mineral Filler

Two types of mineral filler were used in this work; limestone dust produced in the lime factory in Karbala governorate and coal fly ash obtained from local market. **Table 3** shows major physical properties.

4.4 Selection of Design Aggregate Gradation

The selected gradation in this work followed the **SCRB, 2003** specification, with 12.5 (mm) nominal maximum size and **ROAD NOTE 31, 1993** specification with 12.5 (mm) nominal maximum size. **Fig.1, Fig. 2, Table 4** and **Table 5** show selected aggregate gradation. The implementation of both aggregate gradations in this research work could aid in understanding the effect of environmental condition on physical properties of asphalt concrete since the SCRB specification is recommended for hot climate, while ROAD NOTE 31 is recommended for cold climate condition.

4.5 Preparation of Marshall Specimen

Four groups of Marshall Specimens were prepared and used in this work to obtain optimum asphalt binder content; five percentages of asphalt cement (3.5, 4, 4.5, 5 and 5.5) % and 15 specimen were used for each type of mixture. These four groups of mixture were tested for determination of optimum asphalt requirements as follows:

a.) Determine the optimum asphalt binder content for SCRB grading specification and using limestone dust as a mineral filler, Mixture Type I.
b.) Determine the optimum asphalt binder content for SCRB grading specification and using coal fly ash as a mineral filler, Mixture Type II.

c.) Determine the optimum asphalt binder content for ROAD NOTE 31 grading specification and using limestone dust as a mineral filler, Mixture Type III.

d.) Determine the optimum asphalt binder content for ROAD NOTE 31 grading specification and using coal fly ash as a mineral filler, Mixture Type IV.

60 specimens were used in this work to determine optimum asphalt binder content, The specimens were prepared in accordance with (ASTM D1559), Marshall mold, spatula, and compaction hammer were heated on a hot plate to a temperature between (140-150 ºC). The aggregate was first sieved, washed, and dried to a constant weight at 110 ºC. Coarse and fine aggregates were combined with mineral filler to meet the specified gradation in section (4.4). Aggregates and filler were heated to (160 ºC), asphalt was heated up to (150) ºC prior to mixing, and it was added to the hot aggregate and mixed for two minutes on hot plate until all aggregate particles were coated with asphalt cement. The compaction temperature was (140) ºC, which gives a viscosity (280 $\pm$ 30) cSt. The (75) blows of compaction hammer are applied with a free fall of 4.536 kg (10 lb) sliding weight and a free fall of (457.2) mm. After compaction, the base plate is removed and the same blows are applied to the bottom of the specimen that has been turned around. The specimen in mold was left to cool at room temperature for 24 hours, then it was extracted from the mold using mechanical jack. **Fig. 3** shows preparation of Marshall Specimens.

4.6 Testing of Marshall Specimens

4.6.1 Determination of maximum theoretical specific gravity

The purpose of conducting this test is to determine the maximum theoretical specific gravity of loose HMA specimens. The maximum theoretical specific gravity was determined according to (ASTM D2041-03). 1500 gm was needed in this test for each type of mixture with maximum nominal aggregate size of (12.5 mm). This test was conduct for each percent of asphalt content (3.5, 4, 4.5, 5 and 5.5)%. **Fig. 4** presents the apparatus used to obtain maximum specific gravity.

4.6.2 Determination of flow and stability of specimens

Procedure of preparing and testing specimens was according to (ASTM D1559) .This method covers the measure of the resistance to plastic flow of cylindrical specimens (2.5 in. height × 4.0 in. diameter) of asphalt paving mix after conditioning in water bath at 60 °C for 30 minute. A load was applied with a constant rate of (50.8) mm/min until the maximum load was reached. The maximum load resistance and the corresponding strain values were recorded as Marshall stability and flow respectively. Three specimens for each type of mixture were prepared and tested and average results are reported. **Fig. 5** shows Marshall apparatus of this test.

5. DISCUSSION OF TEST RESULTS

5.1 Optimum Asphalt Content (OAC)

The optimum asphalt content was 4.9 %, 4.7 %, 4.7 % and 4.5 % for mixtures type I, type II, type III and type IV respectively. The Marshall Properties which are considered to select the optimum asphalt content; stability, bulk density, and air voids, while other properties; flow, VMA, and VFA are considered to confirm the required limits by SCRB specification.

5.2 Marshall Stability

Stability is an important property of the asphalt mixture in the wearing course design. Marshall Stability gives the indication about the resistance of asphalt mixture to permanent deformation, a high value of Marshall stability indicates increased Marshall Stiffness. The high stiffness of asphalt mixture means good resistance to traffic loadings but it also indicates lower flexibility which is required for long term performance, high stiffness values are not recommended due to thermal cracking which expected to occur in future. **Fig. 6** shows the effect of aggregate gradation and filler type on Marshall stability. It is noted that the Marshall stability was increased by 13.39% when using fly ash as a mineral filler instead of limestone dust with SCRB gradation and it was increased by 32.63 % when using fly ash as a mineral filler when compared to mix with limestone dust with ROAD NOTE 31 gradation. such results comply with the findings of **Pradan and Roy, 2008**. Also, It is noted that the Marshall stability was decreased by 15.17 % when using ROAD NOTE 31 gradation as compared with SCRB gradation with using limestone dust as a mineral filler, while it was decreased by 0.78 % when using ROAD NOTE 31 gradation instead of SCRB gradation with using coal fly ash as a mineral filler. The data are listed from **Table 6** to **Table 9**.

5.3 Marshall Flow

Generally, high flow values indicate a plastic mix that is more prone to permanent deformation problem due to traffic loads, whereas low flow values may indicate a mix with higher than normal voids and insufficient asphalt for durability and could result premature cracking due to mixture brittleness during the life of the pavement. **Fig.7** shows the effect of aggregate gradation and filler type on Marshall flow. It can be observed that the Marshall flow was increased by 24.13 % when using fly ash as a mineral filler instead of limestone dust with **SCRB, 2003** gradation. such results comply with the findings of **Rahman and Sobhan, 2013**. and **Kar et al., 2014**. Also it is also noted that the Marshall flow was decreases by 6.06 % when using fly ash as a mineral filler instead of limestone dust with ROAD NOTE 31 gradation. such results comply with the findings of **Pradan and Roy, 2008**. Also, it is noted that the Marshall flow was decreases by 13.79 % when using SCRB gradation Instead of ROAD NOTE 31 gradation with using limestone dust as a mineral filler, while Marshall flow was increases by 13.88 % when using SCRB grading Instead of ROAD NOTE 31 gradation when using fly ash as a mineral filler. The data are listed from **Table 6** to **Table 9**.

5.4 Bulk Density

In the Marshall Mix design procedure, the density varies with asphalt content in such a way that it increases with increasing asphalt content in the mixture. The density reaches a peak and then begins to decrease because additional asphalt cement produces thicker films around the individual aggregates, and tend to push the aggregate particles further apart subsequently resulting lower density. The effect of aggregate gradation and filler type on bulk density is illustrated in **Fig.8**. This figure indicates that the bulk density increases when using fly ash as a mineral filler for both SCRB gradation and ROAD NOTE 31 gradation. It is also found that the bulk density was decreased when using SCRB gradation as compared to ROAD NOTE 31 gradation when using limestone dust as a mineral filler, and it is noted that the bulk density was decreased when using SCRB grading as compared to ROAD NOTE 31 gradation when using fly ash as a mineral filler. The data are listed from **Table 6** to **Table 9**.

5.5 Voids in Total Mixture (VTM %)

Air void in the mixture is an important parameter because it permits the properties and performance of the mixture to be predicted for the service life of the pavement, and percentage of air voids is related to durability of asphalt mixture. Air void proportion around 4% is enough to prevent bleeding or flushing that would reduce the skid resistance of the pavement and increase fatigue resistance susceptibility. **Fig. 9** shows the effect of aggregate gradation and filler type on voids in total mix (VTM) percent's. It is clear from the figure that the air void was decreased when using fly ash as a mineral filler as compared to limestone dust with SCRB gradation. such results comply with the findings of **Kar et al., 2014**, while when using fly ash as a mineral filler with ROAD NOTE 31 gradation, air void is increases. such results comply with the findings of **Rahman and Sobhan, 2013**. It is also found that the air void is decreases when using ROAD NOTE 31 gradation with using limestone dust as a mineral filler, and it is noted that the air void is increases when using ROAD NOTE 31 gradation with fly ash as a mineral filler. The data are listed from **Table 6** to **Table 9**.

5.6 Voids Filled with Asphalt (VFA%)

Voids filled with asphalt (VFA) are the void spaces that exist between the aggregate particles in the compacted paving asphalt mixture that are filled with binder. The purpose for the VFA is to avoid less durable asphalt mixtures resulting from thin films of binder on the aggregate particles in light traffic situations. **Fig. 10** shows the effect of aggregate gradation and filler type on void filled with asphalt. It indicates that void filled with asphalt was increased when using fly ash as a mineral filler with SCRB gradation. Such results comply with the findings of **Rahman and Sobhan, 2013**, while when using fly ash as a mineral filler with ROAD NOTE 31 gradation, void filled with asphalt was decreased. It is also noted that void filled with asphalt was decreased when using ROAD NOTE 31gradation with using both limestone dust and coal fly ash as a mineral filler. The data are listed from **Table 6** to **Table 9**.

5.7 Voids in Mineral Aggregate (VMA%)

The voids in the mineral aggregate is the total available volume of voids between the aggregate particles in the compacted paving mixture that includes the air voids and the voids filled with effective asphalt content expressed as a percent of the total volume. It is significantly important for the performance characteristics of a mixture for any given mixture, the VMA must be sufficiently high enough to ensure that there is space for the required asphalt cement, for its durability purpose, and air space. If the VMA is too small, there will be no space for the asphalt cement required to coat around the aggregates and this subsequently results in durability problems. On the other hand, if VMA is too large, the mixture may suffer stability problems. **Fig.11** shows the effect of aggregate gradation and filler type on void in mineral aggregate (VMA). It is clear from the figure that voids in mineral aggregate were decreased when using fly ash as mineral filler with both SCRB and ROAD NOTE 31 gradation. It is noted that the void in mineral aggregate was decreased when using ROAD NOTE 31 gradation instead of SCRB gradation when using both limestone dust and coal fly ash as a mineral filler. Such results comply with the findings of Kar **et al., 2014.** The data are listed from **Table 6** to **Table 9.**

6. CONCLUSION

1. Optimum asphalt content requirement was lower when coal fly ash was implemented as a mineral filler at both types of aggregate gradation SCRB and ROAD NOTE 31 specifications.
2. Optimum asphalt content requirement for grading of ROAD NOTE 31 specification was lower than SCRB specification at both types of mineral filler limestone dust and coal fly ash.
3. Marshall stability was increased by 13.39% and 32.63% when using fly ash as a mineral filler instead of limestone dust with both types of aggregate gradation (SCRB and ROAD NOTE 31) gradation. On the other hand, Marshall stability was decreased by 15.17 % and 0.78% when using ROAD NOTE 31 gradation as compared with SCRB gradation for both types of mineral filler limestone dust coal fly ash.
4. Marshall flow was increased by 24.13 % when using fly ash as a mineral filler instead of limestone dust with SCRB gradation, while it was decreased by 6.06 % when using fly ash as a mineral filler instead of limestone dust with ROAD NOTE 31 gradation.
5. Marshall flow was decreased by 13.79 % when using SCRB gradation instead of ROAD NOTE 31 gradation with using limestone dust as a mineral filler, while it was increased by 13.88 % when using SCRB grading instead of ROAD NOTE 31 gradation when using fly ash as a mineral filler.
6. Bulk density increases when using fly ash as a mineral filler for both SCRB gradation and ROAD NOTE 31 gradation.
7. Bulk density was decreased when using SCRB gradation as compared to ROAD NOTE 31 gradation for both limestone dust and coal fly ash.

REFFRENCES

- Ali N, Chan JS, Simms S, Bushman R, Bergan AT, 1996, *Mechanistic evaluation of fly ash asphalt concrete mixtures.* Journal of Materials in Civil Engineering, ASCE 8(1):19-25.
- Bouchard, G. P., 1992, *Effect of Aggregates and Mineral Fillers On asphalt Mixtures Performance,* ASTM, STP 1147, Richard C. Meininger, Ed., American Society for Testing and Material, Philadelphia.
- BS. 1993 *A guide to the structural design of bitumen surfaced roads in tropical and sup tropical countries, ROAD NOTE 31,* Transport research laboratory, Crowthorne, Berkisher, United kingdom.
- Kar D., Panda M. and Giri J. P., 2014, *Influence of Fly Ash as a Filler in Bituminous Mixes*, Department of Civil Engineering, NIT Rourkela, Odisha, India.
- Kallas BF, Puzinauskas VP, 1967, *A study of mineral fillers in asphalt paving mixtures*. Proceedings of the Association of Asphalt Paving Technologists 36:493-528.
- Matthews, J. M. and Monismith, C. L., 1992, *The Effect of Aggregate Gradation on the Creep response of Asphalt Mixtures and Pavement Rutting Estimates*, *Effect of Aggregates and Mineral Fillers On asphalt Mixtures Performance*, ASTM STP 1147, Richard C. Meininger, Ed., American Society for Testing and Material, Philadelphia.
- Pradan and Roy, 2008, *Effect of Fillers on bituminous paving Mixes*, Bachelor of Technology in Civil Engineering, National Institute of Technology.
- Puzinauskas, V.P., 1969. *Filler in Asphalt Mixtures*. The Asphalt Institute Research Report 69-2, Lexington, Kentucky.
- Rahman M.N. and M.A. Sobhan, 2013, *Use of Non-Conventional Fillers on Asphalt-Concrete Mixture*, Department of Civil Engineering, Rajshahi University of Engineering and Technology, Rajshahi-6204, Bangladesh.
- Roberts, F. L., Kandhal, P. S., Brown, E. R., Lee, D., and Kennedy, T., 1996, *Hot Mix Asphalt Materials, Mixtures Design, and Construction*, NAPA Education Foundation, Lanham, Maryland. First Edition, pp. 241-250.
- Sarsam S. 1987, *Effect of various gradations on the properties of Asphaltic Concrete using two design methods,* Indian Highways IRC Vol. 15 No.10.India.
- Sarsam S. 1984, *A study of mineral filler in dense graded Asphalt Concrete*, Indian Highways IRC Vol. 12 No.12. India.

- Sarsam S., 2013, *Improving Asphalt Cement Properties by Digestion with Nano materials*, Research and Application of Material Journal, RAM, Vol.1, No.6, (P 61-64). Sciknow Publications Ltd. USA.
- Sarsam S. 2015, *Impact of Nano Materials on Rheological and Physical Properties of Asphalt Cement*, International Journal of Advanced Materials Research, Public science framework, American institute of science, Vol. 1, No. 1, pp. 8-14, USA.
- State Commission of Roads and Bridges SCRB, 2003. *Standard Specification for Roads & Bridges*, Ministry of Housing & Construction, Iraq.
- Zhi Suo, Wing Gun Wong, 2008, *Analysis of fatigue crack growth behavior in asphalt concrete material in wearing course*, Construction and Building Materials, Available online 20 February.

Table 1. Physical properties of asphalt cement.

Property	Unit	Test Result	SCRB (2003) Specifications
Penetration, (25˚C, 100 gm, 5 sec) ASTM D 5	0.1 mm	42	40 – 50
Softening point (Ring & Ball) ASTM D 36	℃	49	----
Ductility (25 ˚ C, 5 cm/min) ASTM D 113	cm	140	>100
Specific gravity 25˚C ASTM D70	----	1.04	----
Flash point (cleave land open cup) ASTM D 92	℃	256	>232
After Thin - Film Oven Test ASTM D 1754			
Retained Penetration of Residue (25 ˚C , 100 gm , 5 sec)	%	67	>55%
Ductility (25 ˚ C , 5 cm/min)	cm	83	>25
Loss on Weight % (163 ˚ C , 50 gm , 5 hr)	%	0.35	----

Table 2. Physical properties of aggregate.

Property	Coarse aggregate		Fine aggregate	
	Test Result	ASTM Designation No.	Test Result	ASTM Designation No.
Bulk Specific Gravity	2. 542	ASTM C 127	2.558	ASTM C 128
Apparent Specific Gravity	2.554		2.563	
Water Absorption %	1.076 %		1.83 %	
Wear % (Los Angeles Abrasion)	17.92 %	ASTM C 131	----	----

Table 3. Physical properties of limestone dust and coal fly ash.

Property	Physical Properties	
	Limestone Dust	Coal Fly Ash
% Passing Sieve No. 200	98%	94%
Specific Gravity	2.617	2.6455
Specific surface area m 2/kg	389	338

Table 4. Specification limits and selected gradation of HMA mixtures for wearing course according to SCRB (2003).

Sieve Opening (mm)	Sieve Size	% passing by weight of total aggregate	
		Selected gradation	SCRB (2003) specifications Limits (Type IIIA)
19	3/4"	100	100
12.5	1/2"	95	90 – 100
9.5	3/8"	83	76 – 90
4.75	No.4	59	44 – 74
2.36	No.8	43	28 – 58
0.3	No.50	13	5 – 21
0.075	No.200	7	4 – 10

Table 5. Specification limits and selected gradation of HMA mixtures for wearing course according to ROAD NOTE 31 (1993).

Sieve Opening (mm)	Sieve Size	% passing by weight of total aggregate	
		Selected gradation	Road Note 31 (1993) specifications Limits
19	3/4"	100	100
12.5	1/2"	90	80 – 100
4.75	No.4	63	54 – 72
2.36	No.8	50	42 – 58
1.18	No.16	41	34 – 48
0.6	No.30	32	26 – 38
0.3	No.50	23	18 – 28
0.15	No.100	16	12 – 20
0.075	No.200	9	6 – 12

Table 6. Effect of asphalt content on marshall and density- air voids properties for mixture Type I.

Asphalt Content %	Bulk density (gm/cm3)	Marshall Stability (KN)	Marshall Flow (mm)	VTM (%)	VFA (%)	VMA (%)
3.5	2.2074	9.48	2.400	9.2165	44.6185	16.6448
4	2.2367	10.50	2.580	7.3753	53.8309	15.9760
4.5	2.2698	11.43	2.700	5.3579	64.6941	15.1767
5	2.2834	11.20	2.980	4.1393	72.6122	15.1152
5.5	2.2759	9.96	3.600	3.8040	75.9795	15.8393

Table 7. Effect of asphalt content on Marshall and density- air voids properties for mixture Type II.

Asphalt Content %	Bulk density (gm/cm3)	Marshall Stability (KN)	Marshall Flow (mm)	VTM (%)	VFA (%)	VMA (%)
3.5	2.2228	9.0580	2.6300	8.6432	46.3833	16.1223
4	2.2589	9.9670	2.9600	6.5141	57.1404	15.2018
4.5	2.3010	10.4730	3.5300	4.1170	70.7385	14.0712
5	2.2953	11.8380	3.7300	3.7004	74.8818	14.7329
5.5	2.2899	8.1130	3.8400	3.2736	78.7153	15.3812

Table 8. Effect of asphalt content on Marshall and density- air voids properties for mixture Type III.

Asphalt Content %	Bulk density (gm/cm3)	Marshall Stability (KN)	Marshall Flow (mm)	VTM (%)	VFA (%)	VMA (%)
3.5	2.1788	12.232	2.460	10.4627	41.1723	17.7827
4	2.2083	12.977	2.720	8.6271	49.5521	17.1013
4.5	2.3002	13.605	3.100	4.1543	70.5442	14.1011
5	2.2882	9.295	3.590	4.0023	73.3116	14.9966
5.5	2.2845	8.573	3.800	3.5017	77.5239	15.5807

Table 9. Effect of asphalt content on Marshall and density- air voids properties for mixture Type IV.

Asphalt Content %	Bulk density (gm/cm3)	Marshall Stability (KN)	Marshall Flow (mm)	VTM (%)	VFA (%)	VMA (%)
3.5	2.2254	8.004	2.430	8.6115	46.5038	16.0997
4	2.2891	8.148	2.980	5.3425	62.2256	14.1453
4.5	2.3012	9.617	3.180	4.1845	70.4026	14.1410
5	2.2955	8.399	3.410	3.7687	74.5379	14.8021
5.5	2.2886	8.105	3.810	3.4019	78.0547	15.5052

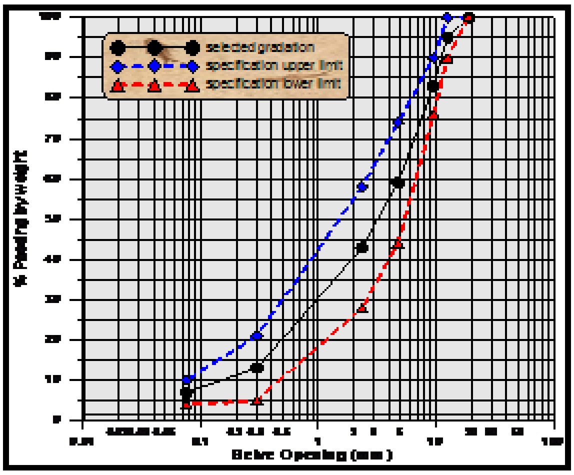

Figure 1. Specification limits and selected gradation according to SCRB (2003).

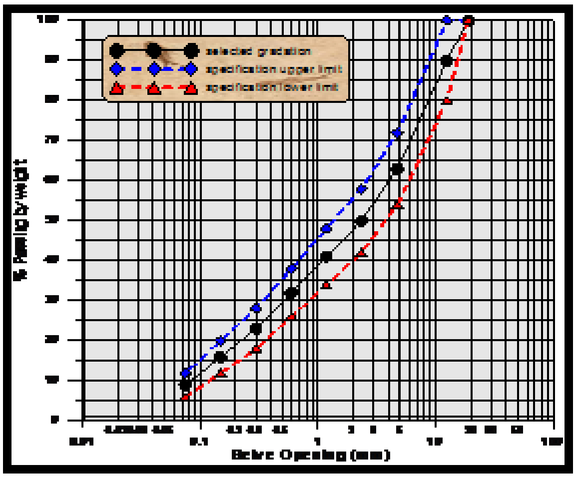

Figure 2. Specification limits and selected gradation according to ROAD NOTE 31 (1993).

Figure 3. Part of prepared of marshall specimens.

Figure 4. Maximum theoretical specific gravity apparatus.

Figure 5. Marshall test device.

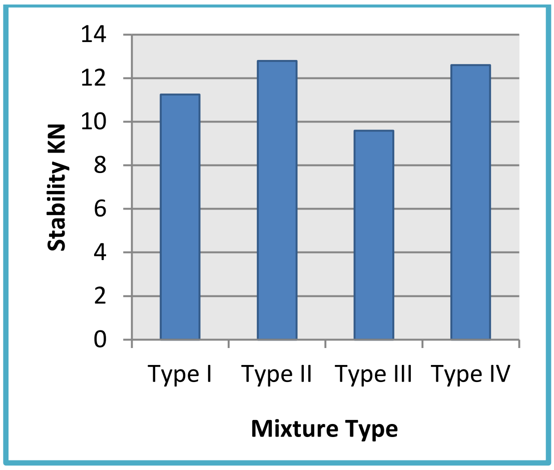

Figure 6. Effect of aggregate gradation and filler type on Marshall stability.

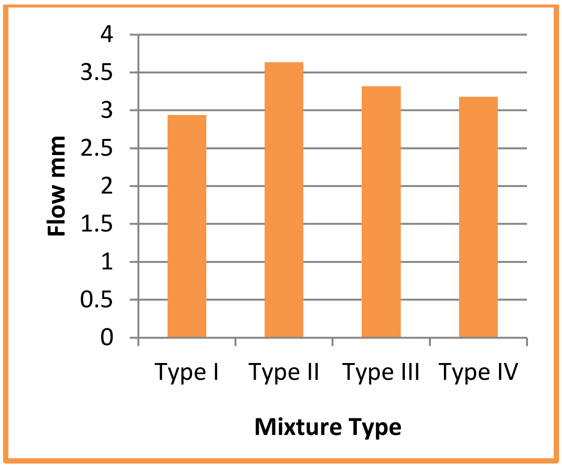

Figure 7. Effect of aggregate gradation and filler type on Marshall flow.

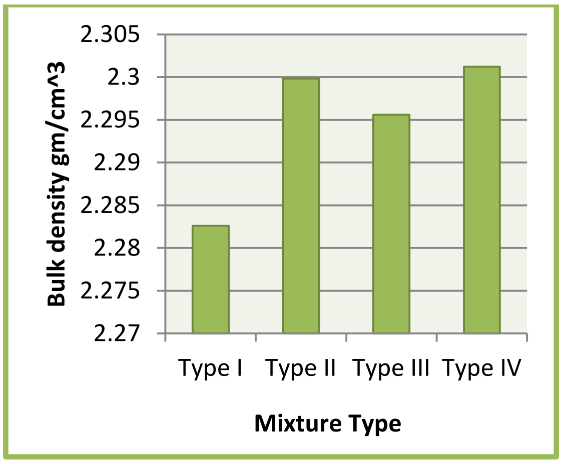

Figure 8. Effect of aggregate gradation and filler type on bulk density.

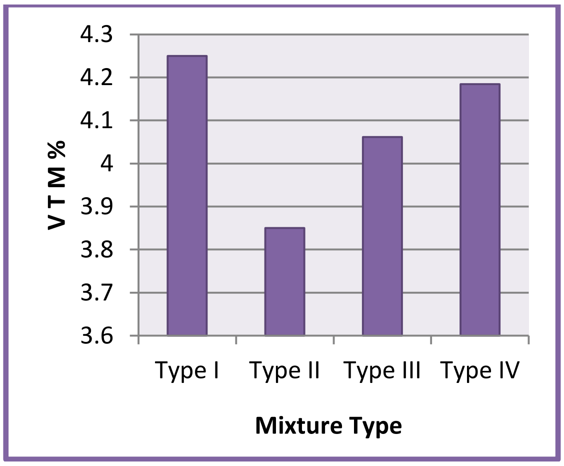

Figure 9. Effect of aggregate gradation and filler type on VTM.

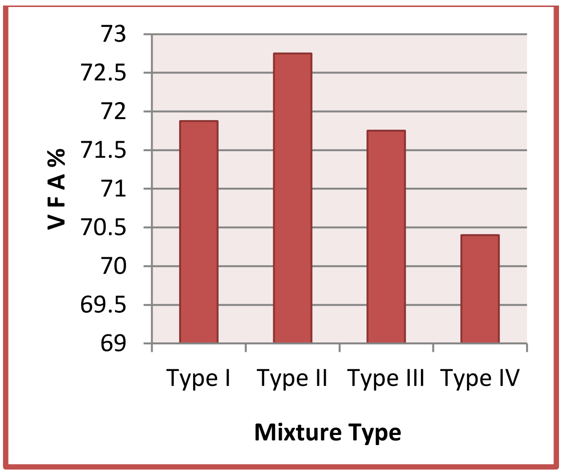

Figure 10. Effect of aggregate gradation and filler type on VFA.

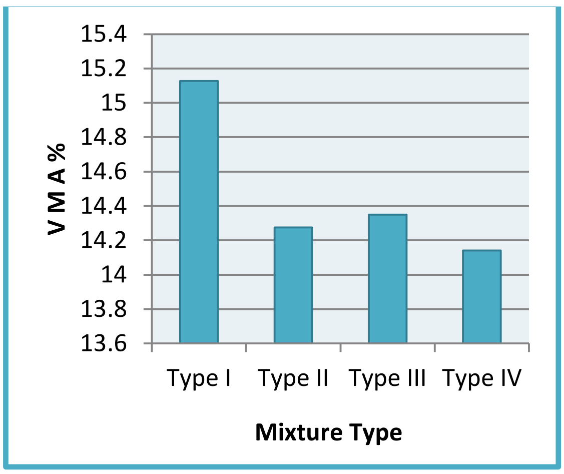

Figure 11. Effect of aggregate gradation and filler type on VMA.

Indoor Positioning and Monitoring System Using Smartphone and WLAN (IPMS)

Alaa Hamza Omran
M.Sc. Student
College of Engineering - University of Baghdad
Email: engineeralaa90@gmail.com

Hamid Mohammed Ali
Assist Professor
College of Engineering - University of Baghdad
Email: habdul_hussain@yahoo.com

ABSTRACT

Buildings such as malls, offices, airports and hospitals nowadays have become very complicated which increases the need for a solution that helps people to find their locations in these buildings. GPS or cell signals are commonly used for positioning in an outdoor environment and are not accurate in indoor environment. Smartphones are becoming a common presence in our daily life, also the existing infrastructure, the Wi-Fi access points, which is commonly available in most buildings, has motivated this work to build hybrid mechanism that combines the APs fingerprint together with smartphone barometer sensor readings, to accurately determine the user position inside building floor relative to well-known landmarks in the floor. Also the proposed system offers a monitoring activity which lets the administrator to watch and locate certain user inside the building.The system is tested in a big building indoor environment and achieved positioning accuracies of approximately 2.1 meters.

Key words: Indoor Positioning System, Indoor Localization System, Indoor Monitoring System, Smart Phones, fingerprinting, Barometer sensor, WLAN, IPMS.

نظام مراقبه وتحديد موقع الشخص داخل البنايه باستخدام الهاتف الذكي وشبكه لاسلكيه محليه

حامد محمد علي
استاذ مساعد
كليه الهندسه – جامعه بغداد

الاء حمزه عمران
طالبه ماجستير
كليه الهندسه – جامعه بغداد

الخلاصة

اصبحت المباني مثل مراكز التسوق والمكاتب والمطارات والمستشفيات في الوقت الحاضر معقده للغايه ممايزيد الحاجه الى وجود حل يساعد الناس في ايجاد موقعهم في هذه المباني. ويعد نظام تحديد المواقع العالمي واشاره ابراج الاتصالات احدى الطرق الشائعه في تحديد مواقع الاشخاص خارج تلك المباني ولكنها ليست دقيقه في تحديد مواقع الاشخاص داخل المباني. ان وجود الهواتف الذكيه في حياتنا اليوميه بصوره شائعه وكذلك توفر البنيه التحتيه القائمه على وجود نقاط الوصول قد حفز على بناء نظام هجين يجمع بصمه نقاط الوصول مع قراءات جهاز الاستشعارفي الهاتف الذكي لتحديد موقع الشخص بدقه على الطابق نسبه الى علامه معروفه في هذا الطابق. ايضا النظام المقترح يوفر خاصيه المراقبه التي تسمح للمشرف بمشاهده وايجاد موقع شخص معين داخل البنايه. وقد تم اختبار النظام في بنايه كبيره حيث بلغت نسبه الدقه في تحديد موقع الشخص مايقارب 2,1 متر.

1. INTRODUCTION

Indoor positioning system recently has become an important topic in the research area due to the growing demand for location aware systems that filter information based on the location of the current smartphone. Many approaches, mechanisms, have been suggested and built for efficient and accurate indoor positioning system. However, each of which comes with its merits and demerits. GPS is the most widely used satellite based positioning system, which offers maximum coverage. GPS cannot be deployed inside buildings, because it requires line-of-sight transmission between receivers and satellites which is not possible in indoor environment due to the obstacles inside the buildings, **Hightower,** and **Borriello**, **2001. Balas, 2011.** presents a crowdsourcing-based localization system for estimating the positions of the devices through using smartphone sensor and Wi-Fi readings. However, the accuracy of this approach is approximately 7m which decreases the performance of the system, furthermore, as mentioned in **Balas, 2011.** the number of training data points has to be high in order to have a small error and people might not provide this data whenever they are asked to by the phone. Most probably, the users will provide data while in their offices or in the common areas and not while they are walking down the hallways. **Li, 2012.** presents an indoor positioning system using smartphone sensors; this system interacts with a user to get the initial location through user input, and provides the current position estimate on an indoor map. However, smartphone sensor suffers from noises which makes reliable step detection hard task, the random bouncing of mobile phones, caused by putting phone in a pocket, switching from left to right hand, operating on touch screen, or taking a phone call, can generate false positives in the detection; The step length of a person's walking can vary quite a lot over time, due to speed, terrain, and other environmental constraints. Furthermore, it is well understood that people with different physical profiles such as height, weight, sex, or walking style have different step length. In order to eliminate the challenges as mentioned above, additional overhead and complexity are presented in the implementation algorithm. **Kothari, et al., 2012.** present an indoor positioning system based on Wi-Fi Access Points incorporated with smartphone sensor. However, it needs a pioneer robot equipped with a SICK LM200 laser rangefinder for collecting signals from the APs during the process of APs detection which means an additional hardware is needed results in increasing the complexity of implementation as well as increasing the cost. **Aboodi, and Wan, 2012.** present an indoor positioning system based on RSS fingerprint in conjunction with trilateration technique. However, using trilateration technique imposes a constraint on the floor's infrastructure because each floor should contain at least three APs. Also, it uses LSE (Least Square Estimation), Min-Max and Kalman filter algorithms which increases the complexity of the implementation as well as increasing in the response time.

The rest of the paper is organized as follows. Section 2 describes in details the proposed system mechanism. Section 3 describes the performance evaluation of the proposed system and provides a comparison of indoor positioning techniques based on their accuracies. Finally, section 4 concludes the paper.

2. PROPOSED SYSTEM

This section logically illustrates the mechanism of the proposed system structure together with each module that constructs the overall system architecture. The proposed system consists of two phases; the training phase which is used to collect the strongest signal strength, of each AP, in each floor in the building to be sent and stored in the database server. The localization phase is used to retrieve the strongest signal strength from the database server then in conjunction with current smartphone readings of AP signal strength and smartphone barometer are used to determine user position.

2.1 Training Phase

Fig. 1 shows the main components used in the training phase. The main function of the training phase is to collect and record RSS of every AP, Pressure and height for each floor inside the site. In this work the system is planned to work on a site which consists of a number of buildings each building consists of a number of floors. Also each floor, which has its own pressure and height, is equipped with one or more APs. Hence, each AP is identified by: site name, building name, floor number, AP name, received signal strength (RSS), and AP MAC address. Before the training phase starts, the system administrator smartphone is loaded with a utility that is responsible for collecting the above mentioned information and then sent to be stored in the database server. Later In the localization phase, these information in conjunction with information collected in real time, are used to determine the local position of user. The steps that are involved in the training phase are listed below:

1) The training phase utility is loaded in the system administrator smart phone and it is used only during the training phase by the system administrator.
2) The site name is entered manually by the system administrator smartphone and sent to be stored in the database server.
3) For each building, the system administrator walk through, the name of the building is entered manually and sent to be stored in the database server.
4) For each floor, of each building, the floor number is entered manually and sent to be stored in the database server.
5) Now for each floor while the administrator is walking through, the utility of the administrator smartphone detects each AP and continuously read signal strength of each AP, as each AP is recognized by its MAC address. When reaching to the end of the certain floor, the number of recorded RSS for each AP is minimized at the Smartphone to the one of the strongest RSS recorded for each AP; then, the strongest RSS of each AP is sent to be stored in database server. Also, a well-known landmark such as common room in the floor, associated with each AP, is also sent to be recorded in the database server. Note, the landmark should not be far away from the AP more than one meter.
6) In addition, the utility of the administrator smartphone also detects the pressure, which is used to calculate the height value, for each floor and send the height to be stored at the database server. Note that, each floor has its own pressure and height values that are different from other floors. The purpose of storing the height value, for each floor, will be explained and analysed in the localization phase, section (2.2).

Fig. 2 shows the flowchart of the training phase for a building. **Fig. 3** shows the Database entries.

2.2 Localization Phase

Fig. 4 shows the main components used in the localization phase. This phase constitutes the main objective of this paper which is responsible for providing "**Locate Me"** service, this phase determines and notifies the user (through her/his smartphone) about her/his position relative to well-known landmark inside the building. Also, it provides **"Monitoring"** service which lets the administrator to locate certain users inside the building. Before discussing and analyzing the technique and the approach used in this phase, it is found necessary to list the steps that would clear the operation of different interoperated components:

A. Locate Me Service

1) While the user is walking inside the building, the **"Locate Me"** utility, embedded in the smartphone, detects and reads the Wi-Fi RSS of the APs, pressure (for height calculations) for the current floor and then compare them with retrieved RSS and height (which are stored in the server during training phase), remember that each AP, in the building, is recognized by site name, building name, floor number, AP's name, RSS and its MAC address. Then a mechanism called "Fingerprint Mechanism", explained later in section (2.3) is used to determine the closest AP (the one with strongest RSS) to the user and then it converts the strongest RSS to a distance that represents how far the user is from the AP (landmark). Note that, the purpose of extracting the height and pressure of each floor (using the smartphone Barometer sensor) is: it happens that the detected closest AP to the user is in another floor, actually not in the floor where the user exists. Hence the use of the pressure and height, which are unique for each floor, will determine in which floor the user exists.

2) A "Filter Scheme" mechanism, shown in **Fig. 4**, is used to purify and removing the noise that is associated with APs RSS and then determine the accurate and final position of the user to be displayed on the user smartphone. The "Filter Scheme" mechanism is explained in details later in section (2.5).

B. Monitoring Service

The monitoring service provides the administrator the capability of watching the users inside the building. This service mainly depends on the "**Locate Me**" service. Thus whenever the " **Locate Me**" service is activated then all the information regarding users position are periodically send and stored in the database server to be accessed by the administrator for the purpose of monitoring. This service is explained in section (2.4).

2.3 Fingerprint Mechanism

Finger print mechanism, is the process of storing information at the training phase to be retrieved at any time during the localization phase. It is important to know there are two types of indoor localization, vertical and horizontal indoor localizations, it is necessary to distinguish between them as follows:

1) Vertical localization which is the process of estimating user's location according to which floor number the user exists.

2) Horizontal localization which is the process of estimating user's location on the specific floor relative to well-known landmark at this floor.

2.3.1 Vertical Localization

A problem that exists with the Wi-Fi mechanism is the number of APs for a fingerprint can be changed because of the nature of radio waves. Especially inside buildings, external factors like moving object, open or closed doors, change the signal strengths of the APs. An AP that was measured during the training phase might not be received during the localization phase and vice versa. Therefore, to account for these changes in the environment, the proposed system depends mainly on the Barometer sensor of the smartphone in the vertical localization.

The proposed system uses Wi-Fi signal strength and the smartphone Barometer sensor to estimate vertical user's location, which floor number the user may exist. Barometer sensor is used to measure height (altitude) and pressure, note that pressure and height have different values in each floor in a specific building.

In the localization phase, the Wi-Fi signals of the APs are detected by the user's smartphone. Then the MAC addresses of the APs, from which the signals are received by the smartphone, are compared with MAC addresses of the retrieved AP signals (stored in the database server during the training phase). Furthermore, the Barometer sensor reading, associated with each detected AP, is retrieved from the database server to be compared with current Barometer sensor reading to determine which APs are in the floor where the user exists.

It is important to note, the Barometer sensor reading is changing with time, suppose the Barometer sensor has a height value equal to 150.5 m at 10 O'clock morning. This value will be altered according to the change in the parameters: pressure, temperature and humidity. Thus, the Barometer sensor will have different reading after an hour, changing in height may be increased or decreased according to the parameters mentioned above. This problem results in producing error when the localization phase occurs at time different from the time of the training phase.

The proposed system fixes this problem through storing the Barometer sensor reading at each floor in the database server, during training phase, arranged from the first floor to the last floor of a specific building. Now, during the localization phase, which must start at the first floor, the reading of the Barometer sensor at the first floor is subtracted from the value of the Barometer sensor of the first floor stored during training phase, the result represents the difference between the two values. This difference represents a new value called "Reference Point", the new value added to the all Barometer sensor readings, of each floor, that are detected and stored at the database server during the training phase. For example, suppose a building consists of three floors:

Let $Height_{training1}$ = 150.5 at first floor, $Height_{training2}$ = 153 at second floor and $Height_{training3}$= 157 at the third floor, if Barometer sensor reading has values equal to $Height_{localization1}$=164 at first floor, $Height_{localization2}$=167 at second floor and $Height_{localization3}$ = 170 at third floor. Then during the localization phase, the following equations are applied:

$Reference\ Point = Height_{localization1}$ - $Height_{training1}$ (1)

=164-150.5=13.5

$Height_{localization\ new1} = Height_{localization1}$ - *Reference Point* (2)

=164-13.5= 150.5 which is exactly 150.5, the training phase value of the first floor.

$Height_{localization\ new2} = Height_{localization2}$-*Reference Point* (3)

= 167-13.5=153.5 which is approximate to 153, the training phase value of the second floor.

$Height_{localization\ new3} = Height_{localization3}$-*Reference Point* (4)

= 170-13.5=156.5 which is approximate to 157, the training phase value of the third floor.

The above new Height Barometer localization values are stored in a temporary list, inside the smartphone, and updated continuously while the user is moving inside the building. Actually, the list is updated every 5 seconds, according to the above mentioned procedure, to eliminate the problem of Barometer sensor readings variations in different times of the day. Actually, In other words every 5 seconds a new Reference Point is calculated and the above mentioned equations are applied again.

2.3.2 Horizontal Localization

It is time now to determine the horizontal localization, suppose the following scenario:

After performing the training phase for the first floor, suppose there are four APs called A, B, C, D and each one has its own RSS value; these values are listed in **Table 1**.
During the localization phase, the detected APs and their own RSS are listed in **Table 2** which illustrates that the user is closest to AP B which has strongest RSS. Now, to find the closest AP to the user, the Euclidean distance rule shown in Eq. (5) is applied.

$$D=\sqrt{(RSS_{tr} - RSS_{lo})^2} \tag{5}$$

Where D represents Euclidean distance; RSS_{tr} represents received signal strength at training phase; RSS_{lo} represents received signal strength at localization phase.

Note that, the standard form of the Euclidean equation as used in previous works, **Navarro, et al., 2011.** and **Grossmann, et al., 2008.** includes summation symbol inside the square root see Eq. (6):

$$D=\sqrt{\sum_{i=1}^{N}(RSS_{tr} - RSS_{lo})^2} \tag{6}$$

Where D represents Euclidean distance; RSS_{tr} represents received signal strength at training phase; RSS_{lo} represents received signal strength at localization phase; N is the number of the APs. Actually, Eq. (6) is used in the environment where group of APs are collected together to represent certain well-known landmark at the floor. This approach is prone to error due to

the fact, suppose each floor has a number of APs which are collected in four groups. During positioning time the APs are detected in more than one group, as long as each group has a specific well-known landmark, then in order to estimate the closest well-known landmark, Eq. (6) is calculated for each group.
Therefore, the summation symbol is used in the process of calculation for each group; the group which has the smallest D has the closet position to the well-known landmark. However, whenever the number of matching APs is increased then D will be increased producing erroneous and inaccurate results.

In our proposal, the idea of APs groups is not adopted, during the localization phase all the APs of certain floor are detected and compared with corresponding retrieved APs. Therefore, the Euclidean equation is modified through eliminating the summation symbol from the equation. Hence the modified Euclidean equation is applied for the example of **Table 2** as follows:

D1= $\sqrt{(-50-(-60))^2} = 10$

D2= $\sqrt{(-55-(-50))^2} = 5$

D3= $\sqrt{(-50-(-70))^2} =20$

D4= $\sqrt{(-45-(-85))^2} =40$

It is clear that the smallest distance is D2 which means the user is closest to AP B. In order to calculate the distance in meter that how far the user is from AP B, Eq. (7) is used.

$$D_{meter} = 3 * 10^{(\frac{RSS}{110})} \quad (7)$$

$D_{meter} = 3 * 10^{(50/110)} = 8$m

Where D_{meter}, is the real distance that the user is far away from the well-known landmark. Note, referring to**, Park, 2007. Adchi,** and **LitePoint, 2014.** most of the APs have a maximum indoor range of 30m. Referring to **Galias, et al., 2013.** the minimum RSS level received by smartphone is -110db. Therefore, Eq. (7) has a maximum range of 30m. **Fig. 5** shows the flowchart of the localization phase, **"Locate Me"** service.

2.4 Monitoring Service

As mentioned in section (2.2), the localization phase offers **"Monitoring"** service for the administrator to locate users inside the building. Actually, as long as the user position is determined in **"Locate Me"** service, explained in section (2.3), then the "**Monitoring**" service is smoothly accomplished according to the following steps:

1) As soon as activating the system by the user, the IPMS starts the process of finding user position relative to the well-known land mark as explained in details in the "**Locate Me**" service. In other words, user smartphone starts the process of finding user position without user's knowledge.

2) This information is associated with the username which is inserted by the user during the process of system's activation.
3) This information is uploaded to the database server.
4) The administrator can access the database server at any time and retrieve user position.

Note, the procedure of finding user's position is repeated every 3 seconds which results in updating user's position every 3 to 5 seconds in the database server.

2.5 Filter Scheme

Filter is used to purify the result of finding the closest AP based on Euclidean distance algorithm. The idea is to make the algorithm so that the impact of large differences in RSS is reduced, thus filter out the large differences so that if the RSS difference is larger than a certain threshold, **So, et al., 2013.** the distance measure is no longer increased. Referring to Eq. (4):

$$Let\ (RSS_{tr} - RSS_{lo}) = C \tag{8}$$

$$D=\sqrt{C^2} \tag{9}$$

$$C= (RSS_{tr} - RSS_{lo}) \qquad if \qquad |RSS_{tr} - RSS_{lo}| < TH \tag{10}$$

$$C=TH \qquad if \qquad |RSS_{tr} - RSS_{lo}| \geq TH \tag{11}$$

Where TH is the threshold value.

Now, in order to compensate the effect of some cases such as user orientation, user height, how the user holds the smartphone, etc. RSS is shifted inside a certain range, **So, et al., 2013.**

$$D=\sqrt{(C+z)^2} \tag{12}$$

Where z is the shift value.

According to **So, et al., 2013,** TH between range 10 to 30db and z in range between 3 to 10.

3. PERFORMANCE EVALUATION

This section demonstrates and illustrates the practical performance results that are obtained from applying the proposed system in real environment; **Al Mansour Mall** building which consists of four floors. The reason of applying the proposed system, in the above mentioned site, is to have a test in vital place in real life which is crowded with people.

3.1 User Positioning System Testing

The training phase of **Al Mansour Mall** building is conducted for the entire building floors. While the localization (positioning) phase is conducted in third and fourth floors, where five locations were taken for the test in the third floor and ten locations are tested in the fourth floor. **Tables 3** and **Table 4** show the results obtained from the test. From the results, the proposed system achieved accuracy of approximately an average of 2.1m.
This section presents the results of testing the system from user point of view, in other words if the user is lost inside the building it is simple to find her/his location using the positioning system. Also suppose two friends lost each other inside crowded Mall; in this case each one

can find her/his location and send a text message to the other, using the positioning system, to meet each other again.

3.2 User Monitoring System Testing

This section presents the results from the administrator point of view; in this test the user has changed his location five times. **Table 5** illustrates the location results recorded by the administrator smartphone.

Accuracy (or location error) of a system is the important user requirement of positioning systems. Accuracy can be reported as an error distance between the estimated location and the actual mobile location. Sometimes, accuracy is also called the area of uncertainty; that is, the higher the accuracy is, the better the system is. Some compromise between "suitable" accuracy and other characteristics is needed. **Table 6** shows system accuracies.

Note, the third system, shown in **Table 6**, achieves quite good accuracy of 2m which is nearly equal to our proposal that achieves accuracy of an average of 2.1m. Actually, because this system depends solely on the smartphone sensors suffers many challenges, some of them mentioned in section 1and the others in **Li, et al., 2012.** which degrade system performance in the long run of use.
The fifth system, shown in **Table 6**, also achieves quite good accuracy of 2.6m. But this system depends solely on the Wi-Fi signals and because it uses complex mechanism, as mentioned in section 1, which consumes a lot of computation time that results in slow response time to the user.

4. CONCLUSION

A hybrid indoor positioning and monitoring system is built that integrates smartphone sensors and Wi-Fi fingerprinting. The main advantage of this research is the creation of a system that achieves the benefits of the flexibility, offering good coverage, user friendly, reducing the complexity of the implementation as much as possible, having a reasonable cost and finally producing high accuracy. The proposed IPMS is suitable for use at any time; using public database server which makes the proposed system services available 24 hours a day. The proposed IPMS depends on the APs of the building which are in turn produce building level coverage. The proposed IPMS enhances the mechanism of using the well-known fingerprint algorithm, K-nearest neighbor, for dealing with Wi-Fi signals during the training and localization phases respectively. Furthermore, it enhances the Barometer sensor readings which fix the problem of Barometer sensor readings variation with time. Finally, the proposed IPMS is highly reasonable which provides good accuracy and consistent position information. It was tested into two vital buildings; the results showed the average of accuracy of the proposed IPMS is approximately 2.1m.
Actually, to achieve the above mentioned accuracy, each landmark has to be attached or adjoined to corresponding AP. In case there is no familiar landmark attached to AP, then it is possible to attach a simple landmark that illustrates the location of the AP relative well-known landmark in the building floor.

REFERENCES

- Aboodi, A., and Wan, T., 2012, *Evaluation of Wi-Fi-based Indoor (WBI) Positioning Algorithm*, International Conference on Mobile, Ubiquitous, and Intelligent Computing, IEEE.

- Balas, C., 2011, *Indoor Localization of Mobile Device for a Wireless Monitoring System based on Crowdsourcing*, M.sc Thesis, University of Edinburgh, Edinburgh, United Kingdom.

- Calis, G., et al., 2013, *Analysis of the variability of RSSI values for active RFID-based indoor applications*, Turkish Journal of Engineering & Environmental Sciences, Vol. 37, pp. 186-210.

- Grossmann, U., et al., July 2008, *RSSI-Based WLAN Indoor Positioning Within a Digital Museum Guide*, International Journal of Computing, Volume 7, Issue 2.

- Hightower, J., and Borriello, G., 2001, *Location systems for ubiquitous computing, in Computer*, vol. 34, pp. 57-66.

- Kothari, N., et al., 2012, *Robust Indoor Localization on a Commercial Smartphone*, Computer Science, Elsevier, Vol. 10, pp. 1114-1120.

- Li, F. 2012, A Reliable and Accurate Indoor Localization Method Using Phone Inertial Sensors, ACM.

- LitePoint, *2013*, *IEEE 802.11ac: What Does it Mean for Test?*, A tendy Company.

- Navarro, E., Peuker, B., and Quan, M., 2011, *Wi-Fi Localization Using RSSI Fingerprinting*, Computer Engineering, Child Development, California Polytechnic State University, USA.

- Park, Y., Adchi, F., 2007, *Enhanced Radio Access Technologies for Next Generation Mobile Communication*, Spriger Sience and Business Media, ISBN 978-1-4020-5532-4.

- So, J., et al., May, 2013, *An Improved Location Estimation Method for Wi-Fi Fingerprint-based Indoor Localization*, International Journal of Software Engineering and Its Applications, Vol. 7, No. 3.

Table 1. First Floor APs at Database Server.

AP_Name	RSS (db)
A	-50
B	-55
C	-50
D	-45

Table 2 First Floor APs Detected during Localization Phase.

AP_Name	RSS (db)
A	-60
B	-50
C	-70
D	-85

Table 3 Third Floor Results.

AP_Name	Well-known landmark	Real Distance (m)	Estimation Distance (m)	Accuracy (m)
Barcelona Cafe	**Barcelona Cafe**	**6**	**8.1**	**2.1**
Barcelona Café 1	**Barcelona Café**	**9**	**11**	**2**
Clarks	**Clarks**	**5**	**7**	**2**
Party 21	**Party**	**7**	**8.9**	**1.9**
Cosmetic	**Cosmetic**	**4**	**5.7**	**1.7**

Table 4 Fourth Floor Results.

AP_Name	Well-known landmark	Real Distance (m)	Estimation Distance (m)	Accuracy (m)
Tche Tche inside	Tche Tche inside	5	7.3	2.3
Tche Tche outside	Tche Tche outside	7	9.9	2.9
Carnval	Carnval	9	10.9	1.9
Carnval Cinema	Carnval Cinema	6	7.5	1.5
Super Star Restaurant	Super Star Restaurant	4	5.5	1.5
Iraqi Cinema	Iraqi Cinema	3	4.9	1.9
Chicken Cottage	Chicken Cottage	7	9	2
Jungle Land	Jungle Land	8	10	2
Mangel Plus	Mangel Plus	6.5	8	1.5
Kanafanje1	Kanafanje café	11	13.6	2.6

Table 5 Monitoring System Accuracy.

Time PM	User's Estimation location	Real Distance (m)	Information at Admin Smartphone	Accuracy (m)
8:50	near to Chicken Cottage by 4 m	2.5	near to Chicken Cottage by 4 m	1.5
8:55	near to Jungle Land by 7 m	5	near to Jungle Land by 7 m	2
9:00	near to Mangel Plus by 9 m	7	near to Mangel Plus by 9 m	2
9:05	near to Super Star Restaurant by 5 m	3	near to Super Star Restaurant by 5 m	2
9:10	near to Carnval Cinema by 4 m	1.6	near to Carnval Cinema by 4 m	2.4

Table 6 System Accuracies.

System	Accuracy(m)
Global Positioning System (GPS), **Hightower,** and **Borriello, 2001**.	10
Indoor Localization of Mobile Device for a Wireless Monitoring System based on Crowdsourcing**, Balas, 2011**.	7
A Reliable and Accurate Indoor Localization Method Using Phone Inertial Sensors, **Li, 2012**.	2
Robust Indoor Localization on a Commercial Smartphone**, Kothari, et al., 2012.**	5
Evaluation of Wi-Fi-based Indoor (WBI) Positioning Algorithm**, Aboodi, and Wan, 2012.**	2.6
The Proposed System.	≈2.1

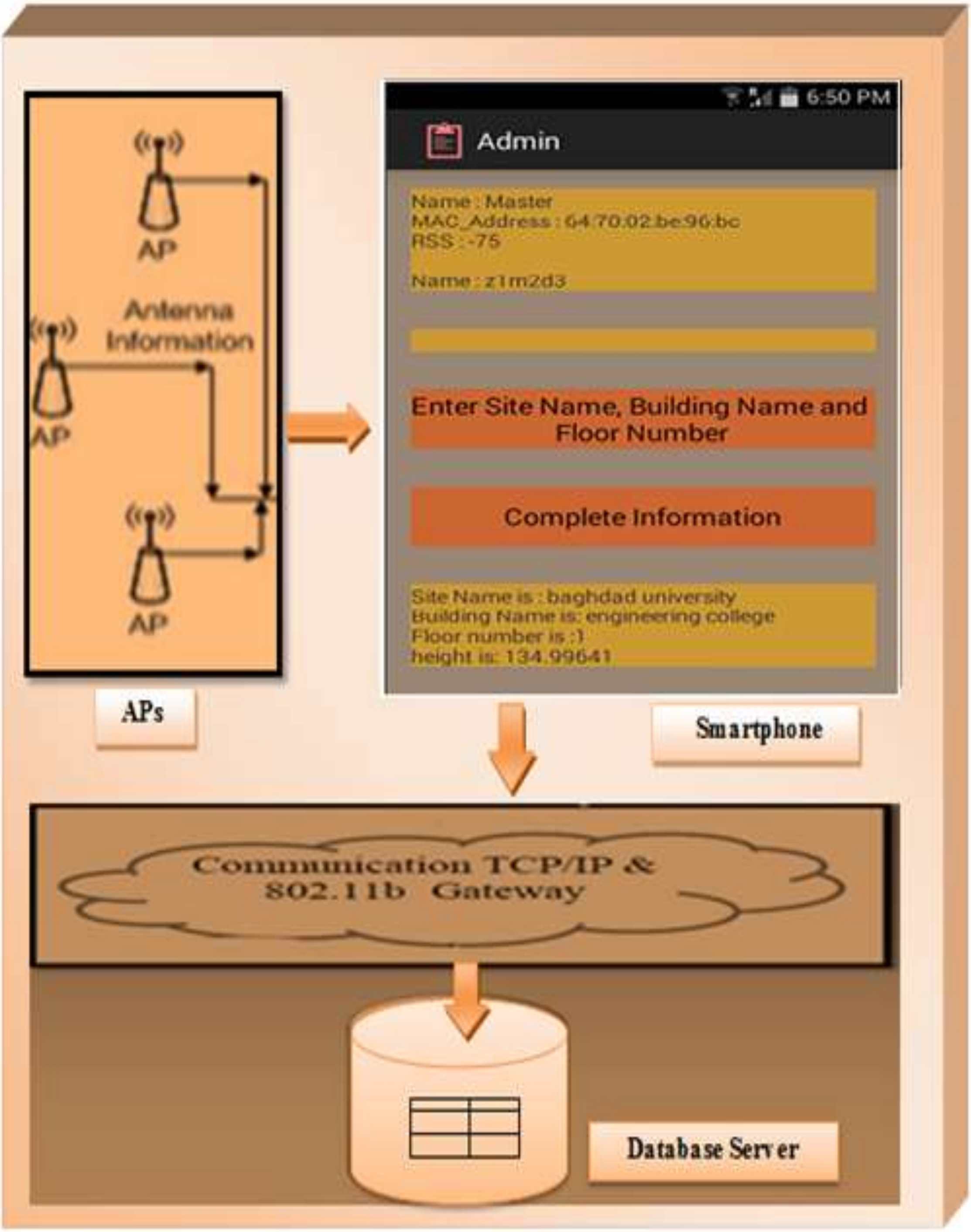

Figure 1 .Training Phase.

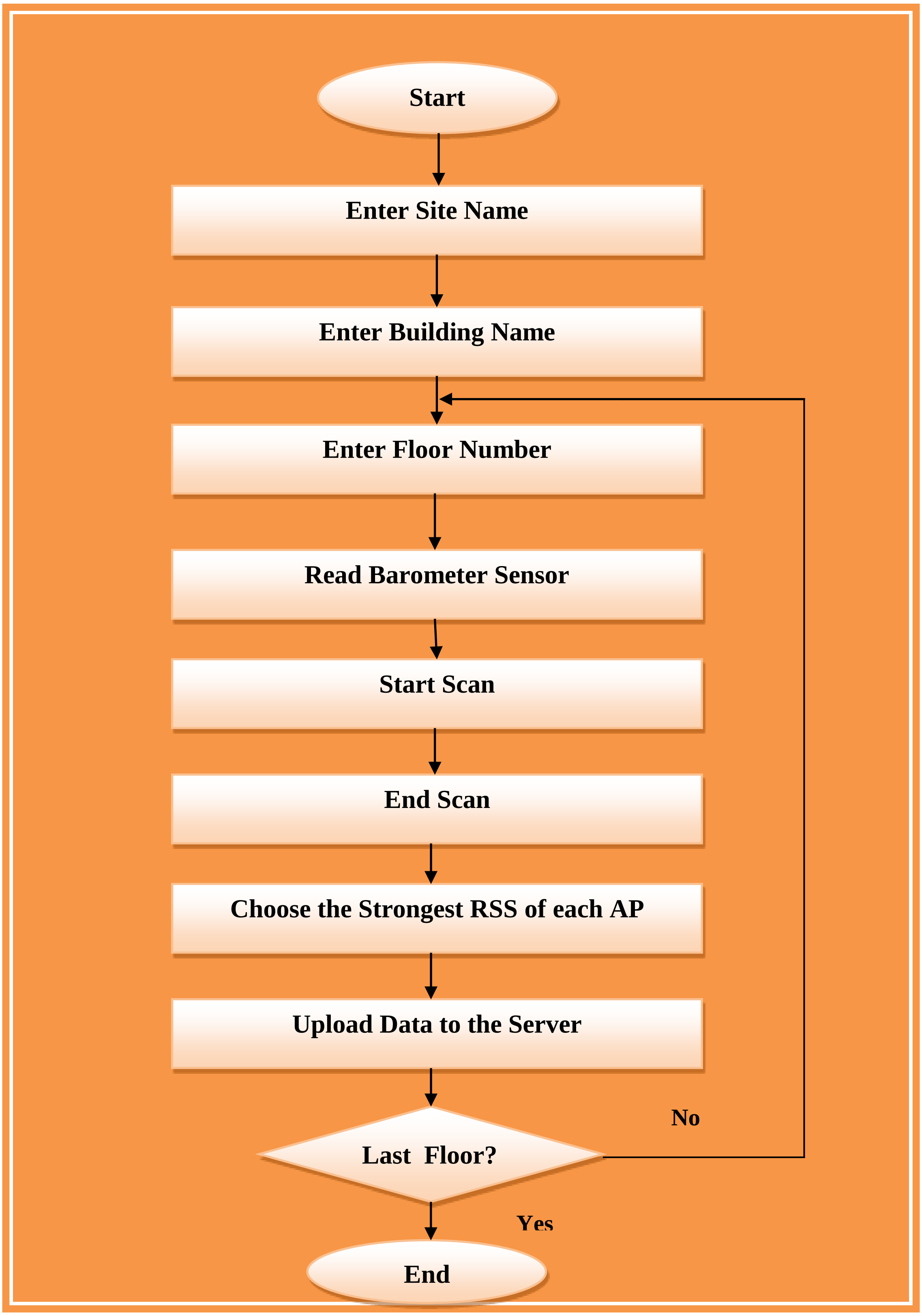

Figure 2. Flowchart of Training Phase.

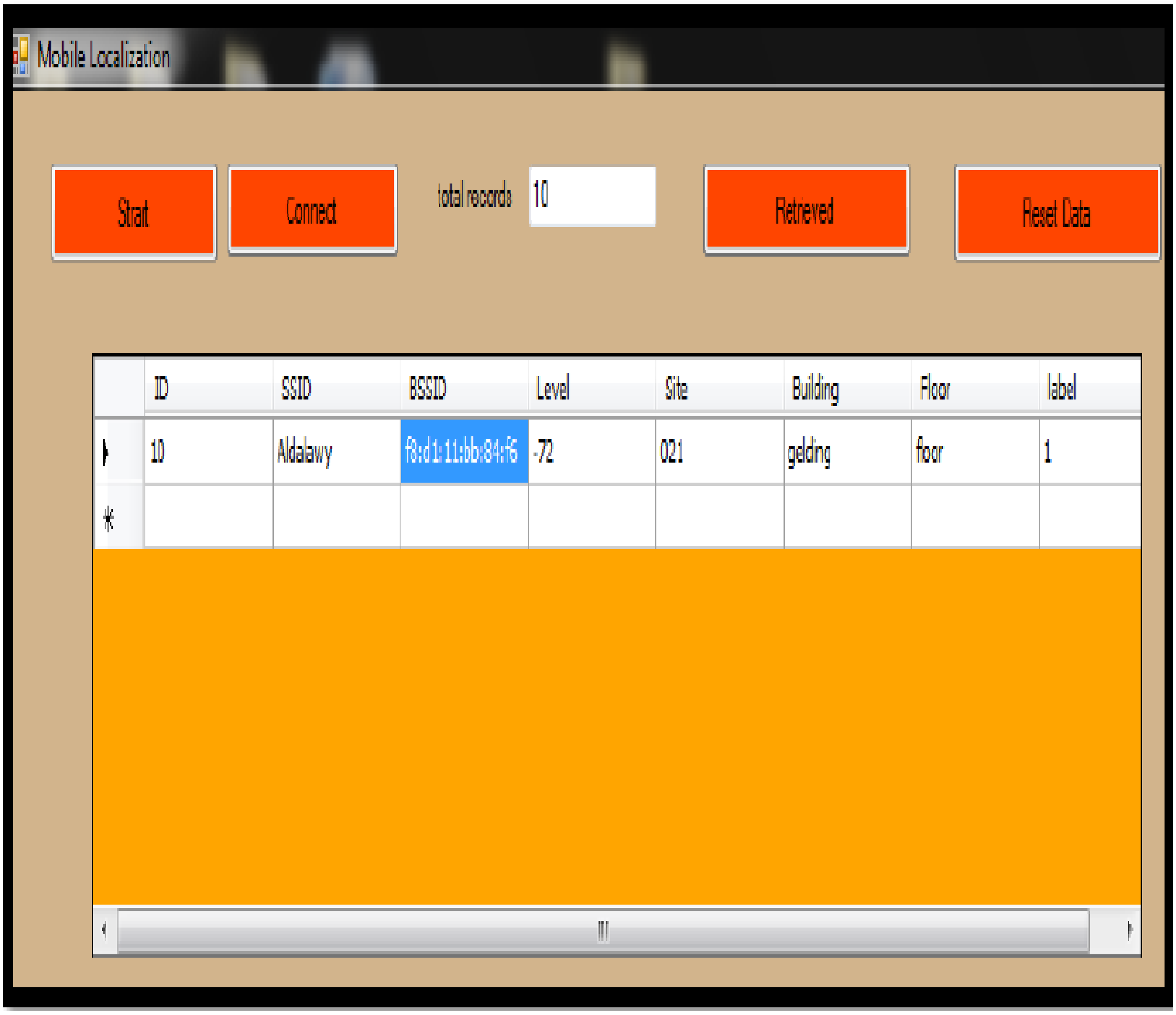

Figure 3. Database Entries.

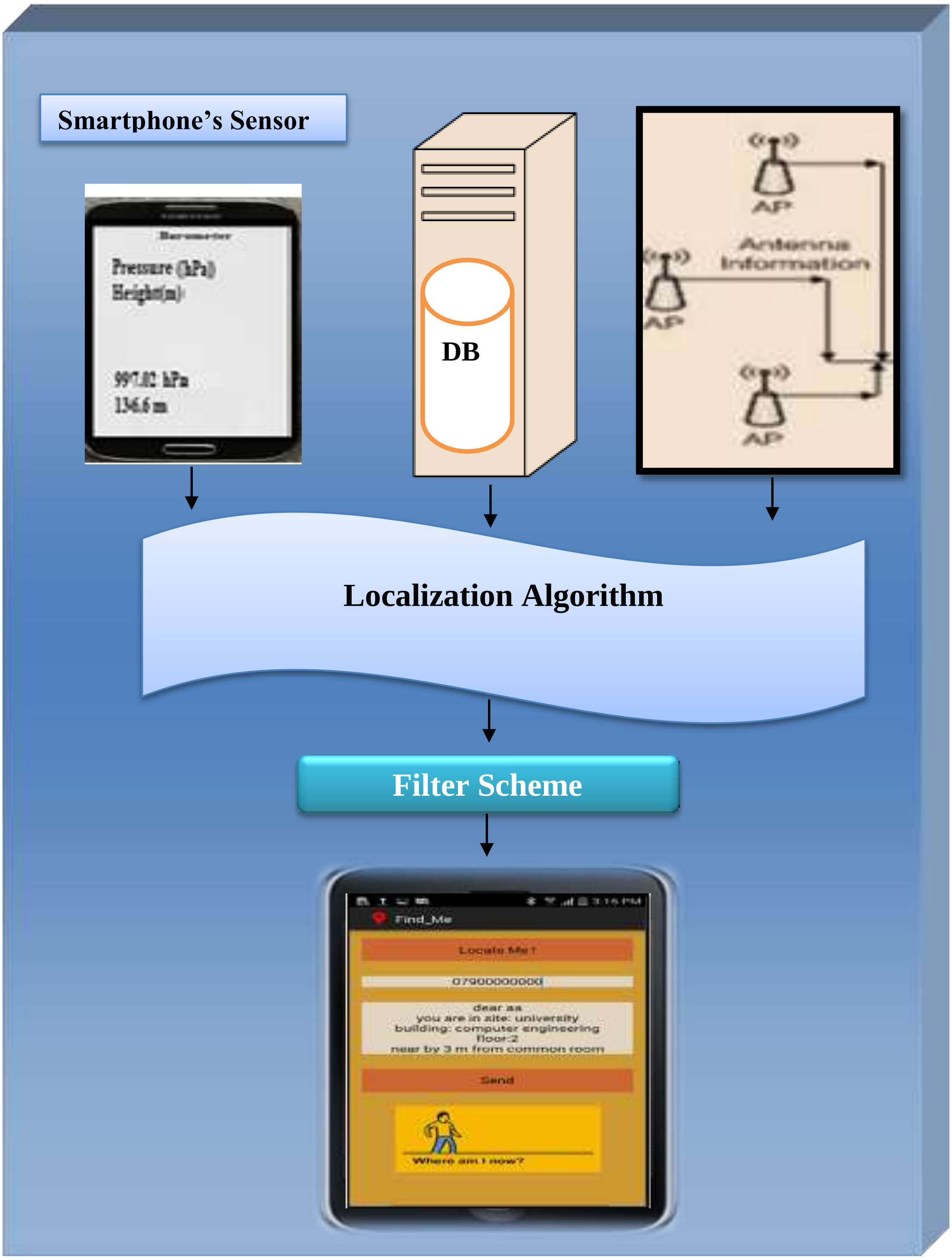

Figure 4. Localization Phase (Locate Me Service).

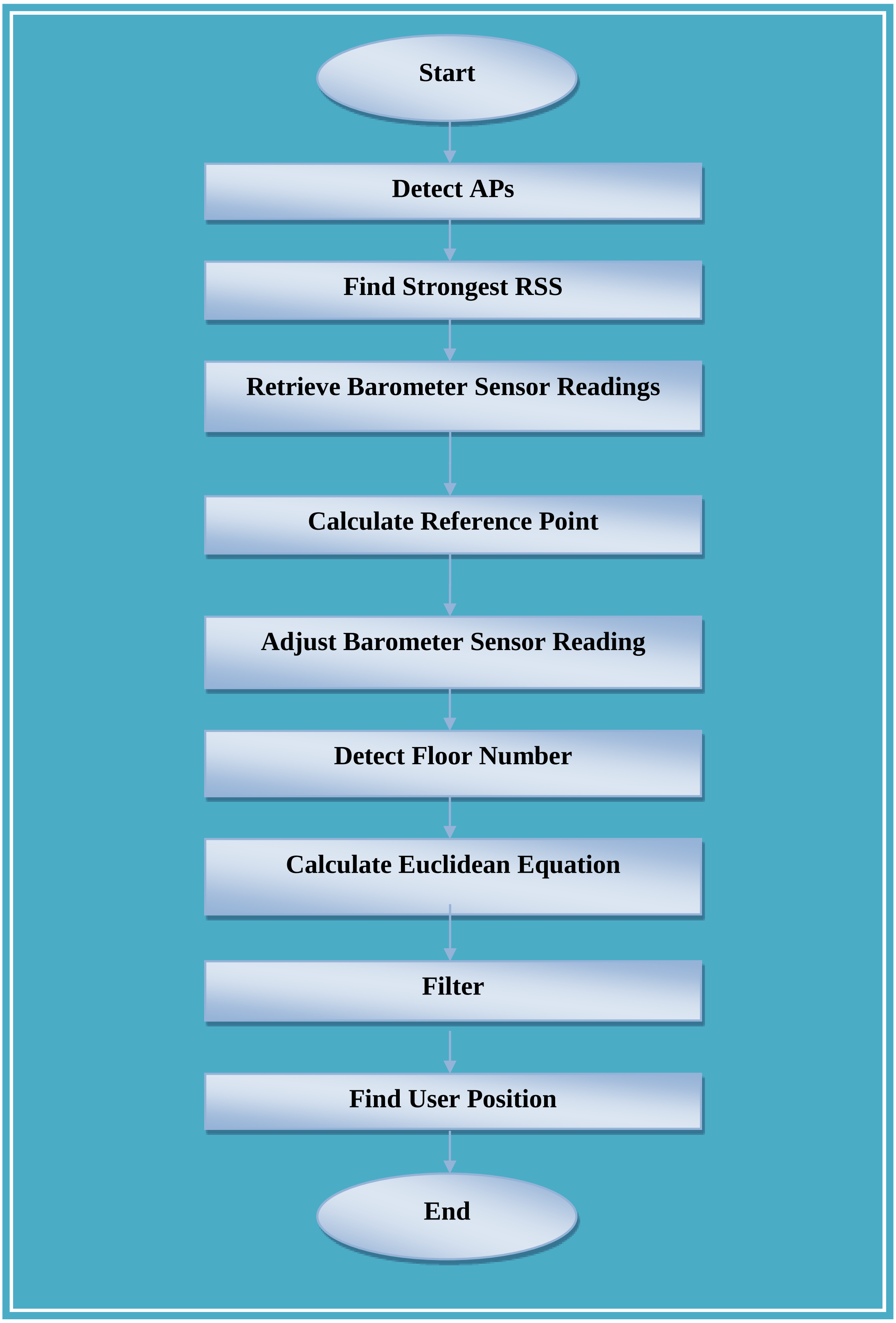

Figure 5. Flowchart of Localization Phase.

Study Effect of Central Rectangular Perforation on the Natural Convection Heat Transfer in an Inclined Heated Flat Plate

Lect. Kadhum Audaa Jehhef
Department of Equipment and Machine
Institute of Technology, Middle Technical University
Email: kadhum.audaa@yahoo.com

ABSTRACT

A numerical solutions is presented to investigate the effect of inclination angle (θ) , perforation ratio (m) and wall temperature of the plate (T_w) on the heat transfer in natural convection from isothermal square flat plate up surface heated (with and without concentrated hole). The flat plate with dimensions of (128 mm) length × (64 mm) width has been used five with square models of the flat plate that gave a rectangular perforation of (m=0.03, 0.06, 0.13, 0.25, 0.5). The values of angle of inclination were (0^o, 15^o 30^o 45^o 60^o) from horizontal position and the values of wall temperature (50^oC, 60 ^{o}C, 70 ^{o}C, 90 ^{o}C, 100^oC). To investigate the temperature, boundary layer thickness and heat flux distributions; the numerical computation is carried out using a very efficient integral method to solve the governing equation. The results show increase in the temperature gradient with increase in the angle of inclination and the high gradient and high heat transfer coefficients located in the external edges of the plate, for both cases: with and without holed plate. There are two separation regions of heat transfer in the external edge and the internal edges. The boundary layer thickness is small in the external edge and high in the center of the plate and it decreases as the inclination angle of plate increases. Theoretical results are compared with previous result and it is found that the Nusslet numbers in the present study are higher by **(**22 %) than that in the previous studies. And the results show good agreement in range of Raleigh number from 10^5 to 10^6.

Key words: natural convection, perforation plate, inclined flat plate.

دراسة تأثير تجويف مستطيل مركزي على انتقال الحرارة بالحمل الحراري الحر فوق صفيحة مائلة مسخنة

م.د. كاظم عودة جحف
قسم المكائن والمعدات
معهد تكنلوجيا- بغداد , الجامعة التقنية الوسطى

الخلاصة

قدمت دراسة عددية لاستقصاء تأثيرزاوية الميل (θ) ونسبة التجويف (m) ودرجة حرارة السطح (T_W) على انتقال الحرارة بالحمل الحر من صفيحة مستوية مربعة مسخنة من الوجه الاعلى (مع وبدون تجويف مركزي) والصفيحة بطول (128 ملم) وسمك (64 ملم) وتم استخدام خمس نماذج للصفيحة المربعة مع ثقب مستطيل ذات نسب تجويف مختلفة هي (m= 0.03, 0.06, 0.13, 0.25, 0.5) وبزوايا ميل مختلفة هي (0^o, 15^o, 30^o, 45^o, 60^o) من الوضع الافقي وقيم درجات حرارة متغيرة تتضمن (50^oC, 60 ^{o}C, 70 ^{o}C, 90 ^{o}C, 100^oC) ومن اجل دراسة توزيع كلا من درجة الحرارة وسمك الطبقة المتاخمة والفيض الحراري باستخدام التحليل العددي بطريقة التكامل لحل المعادلات الرياضية الحاكمة. اظهرت النتائج ان هناك زيادة في انحدار درجات الحرارة مع زيادة زاوية الميل للصفيحة. ويتمركز اعلى انحدار في درجات حرارة واعلى قيمة لمعامل انتقال الحرارة في الحافات الخارجية للصفيحة لكلتا الحالتين (مع وبدون تجويف).وهناك منطقتي انفصال لانتقال الحرارة تتمركز في الحافات الداخلية والخارجية للصفيحة المجوفة. ولوحظ ان سمك الطبقة المتاخمة الحرارية يكون قليل في الحافة الخارجية وعالي في مركز الصفيحة في حالة النموذج الخالي من تجويف. وتبدأ هذه الطبقة بالتناقص كلما ازدادت زاوية الميلان وتمت

مقارنة النتائج النظرية الحالية مع نتائج سابقة وجد ان اعداد نسلت في البحث الحالي اعلى بنسبة (22%) عما موجود في البحوث السابقة ووجد تقارب جيد بين النتائج في مدي رقم رالي من 10^5 الى 10^6.

الكلمات الرئيسيه: الحمل الحر, صفيحة مثقبة, صفيحة مستوية مائلة.

1. INTRODUCTION

Natural convection cooling of components in electronics which has been attached to printed circuit boards, which are placed vertically and horizontally in an enclosure, is currently of great interest to the microelectronics industry. Natural convection cooling is desirable because it doesn't require energy source, such as a forcing by fan and it is maintenance free and safe. Cavities with no obstructions were studied in the past few years such as **Zhong et. al., 1985** and **Saravanan and Kandaswamy, 2000.** The exact solutions available in the literature, especially that was related to the boundary layer thickness and temperature profiles and showed that there was a limited attention to study the effect of the perforation in the flat plate.

The heat transfer by natural convection applied to simple geometries such as flat plates, spheres, and cylinders, has been extensively studied for decades. **Ostrach, 1952,** was one who of those solves the boundary layer equations for natural convection from vertical flat plate using a numerical method. The set of three equations a continuity, momentum and energy were reduced to only two equations with their respective boundary conditions. He found that this type of flow was dependent on the Grashof number and Prandtl number.

The geometry of an inclined, semi infinite without holed flat plates had been considered by a number of researchers because of its engineering applications. Among whom are **Ganesan and Palani, 2003, Said et. al., 2005, Sparrow and Husar, 1969 and Patterson, et. al. 2007**. Most of these studies had been conducted by either numerical simulations or experimental observations. **Zekeriya and kurtul, 2006,** performed a numerical study of laminar natural convection in tilted rectangular enclosures that contain a vertically situated hot plate using the finite volume method with SIMPLE algorithm. The Raleigh number and the tilt angle of the enclosure were ranged from 10^5 to 10^7 and from 0^o to 90^o respectively. **Kobus and Wedekind 2000,** presented experimental heat transfer data and developed dimensionless correlation for natural convection from heated horizontal stationery isothermal circular disks over a wide range of Raleigh numbers. The air was used with variety of disks of different diameters and thickness-to-diameters aspect ratios. Another type of important convective heat transfer problem is the free and mixed convection boundary-layer flow near a flat plate which is inclined at a small arbitrary angle to the horizontal or vertical plate. **Jones, 1973** studied theoretically the free convection boundary-layer near a flat plate at small angles of inclinations to the horizontal by taking into account both the parallel and the normal to the plate temperature gradients which drive the fluid flow and both positive and negative inclination angles of the plate were considered. When the inclination angles of the plate was positive, both of the mechanisms which drive the flow produce favorable effective pressure gradients, so that the fluid continued to be accelerated along the plate to a final state, far from the leading edge, which was described by the classical free convection boundary-layer solution over a vertical flat plate. For negative inclination angles, although the pressure gradient associated with the processes remained favorable, separation of the boundary-layer from the plate eventually occured, since the buoyancy force opposes the motion. Important contributions to these convective flow configurations had also been made by several authors, notably by **Schneider, 1995, Umemura and Law, 1990 ,Weidman and Amberg, 1996** and **Waheed, 2001,** conducted a numerical study to solve the governing equation with the finite difference volume method for the disks and rings with outer diameter ($0.2 \leq r_1 \leq 0.9$) (where r_1 is the ratio of inner to outer diameter) heated from the upper surface with constant temperature in range of Grashof number ($10^3 \leq Gr_{Do} \leq 10^7$). He observed that the main process of heat transfer was conduction at Grashof number less than (10^3) and the convection at Grashof number less than (10^3). The maximum rate of heat transfer for the rings that had the same outer diameter for the disk was achieved at the inner diameter with outer diameter between (0.2-0.3).

Mohammed, 2002, studied experimentally the laminar heat transfer by natural convection from the disks. **Waheed, 2001,** used inclined upward and downward heated rings at constant temperature in the rang of Raleigh number ($1.7\times10^5 \leq Ra_{Do} \leq 3.1\times10^6$). The results showed that the average Nusselt number which depended wholly on the angle of inclination, and there was clear difference in the rates of heat transfer between the horizontal upward and downward surfaces where the effect of inner diameter was limited to the increase which leads to rates of heat transfer in the case of upward rings. Addition of the extended surface to the external edge leads to decrease in the rates of heat transfer for all inclination angles. **Abd, 2005,** presented a numerical study of three dimensional laminar natural convection heat transfer process from isothermal square plate and another plate with a circular perforation (ratio of perforation to the plate external length ranges from 0.6 to 0.8), and angle of inclination ranging from (0^o-180^o). The numerical study included solution of the momentum and energy equations by using the finite difference method for the range of Grashof number ($10^3 \leq Gr_{Do} \leq 5\times10^4$) with Prandtle number (Pr=0.72). The results showed that the maximum temperature gradient was achieved at external edge for the case of horizontal perforation square plate and heated from upward and at lower external edge for the case of inclination plate. The local Nusselt number for the perforation plate wholly depended on the inclination angles and the values of average Nusselt number with a higher level than the square plate and increase as the perforation ratio increase. While the values of average Nusselt number increases with increasing of the inclination angles for the upward heated square plate and reach the high limit at the vertical position, then decrease the inclination angles. **Kadhim, 2003,** studied three dimensional natural convection heat transfer from the rings and disks (inner to outer diameter equal to 0.2, 0.5 and 0.8) angles of inclination ranged from ($0^o \leq \theta \leq 180^o$) with Prandtle number (Pr=0.72). The results showed that the local Nusselt number wholly depends on the inclination angles. The variation in inner diameter caused a limited increase in the heat transfer rates in case of the heated upward rings and high effected in case of rings heated downward. The average Nusselt number increases with the increase in the angle of inclination and the ratio of inner to outer diameter for heated upward rings. Where the maximum value of average Nusselt number is in depended of the inclination angles, its change depends only on the inner to outer diameter ratio for these rings. The maim aim of this study is investigating the enhancement the shared influence of the plate perforation and angle inclination on the natural convection heat transfer process by using the numerical computation carried out using the integral method to solve the governing equation and compare the theoretical result with those of the previous studies.

2. PHYSICAL MODELS AND MATHEMATICAL FORMULATION

Consider the steady free convection flow of a viscous incompressible fluid over an inclined semi-infinite plate at an angle (θ), as shown in **Fig. 1**. The temperature of plate is assumed constant at (T_w) and the ambient fluid has the uniform temperature T_∞, where $T_w > T_\infty$. For this configuration, the assumption is that the Boussinesq approximation is valid **,Ioan 2001.**

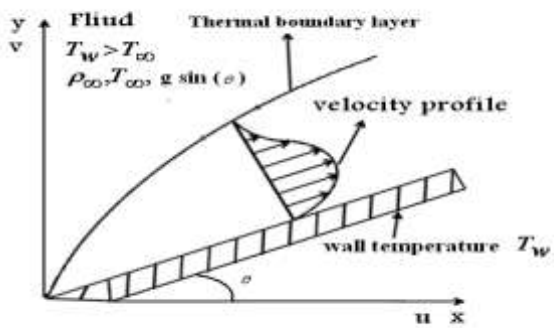

Figure 1. Physical models and coordinate systems of the heated inclined flat plate.

The body force by unit volume is –ρ g sin (θ), where g is the local acceleration of gravity. And the key assumptions are:

1) Constant properties (ρ, k, C_p), except for the variation in density that drives the flow
2) Pressure gradients perpendicular to the plate can be neglected.
3) Density variation can be approximated by a linear dependence on temperature. This is called the Boussinesq approximation.
4) Diffusive transport (of both momentum and energy) in the direction parallel to the plate can be neglected. There are also, of course, many other implied assumptions (steady-state situation, viscous dissipation is negligible in the energy equation, everything is constant in the z-direction (parallel to plate, perpendicular to gravity)).

First, will be look up the “general” governing equations in a reference text, to find the following equations. Any terms involving the z coordinate or the corresponding velocity component, can be neglected as well as the transient terms. This leaves: **Rolando, 2004,** the basic conservation Eqs. (1), (2) and (3) can be written as follows:

Continuity equation (overall mass balance)

$$u\frac{\partial(\rho u)}{\partial x}+v\frac{\partial(\rho u)}{\partial y}=0 \tag{1}$$

and momentum balance in x direction (parallel to plate and gravity) for a Newtonian fluid with constant ρ and μ.

$$\rho\left[\frac{\partial u}{\partial t}+u\frac{\partial u}{\partial x}+v\frac{\partial u}{\partial y}\right]=-\frac{\partial P}{\partial x}+\eta\left[\frac{\partial^2 u}{\partial x^2}+\frac{\partial^2 u}{\partial y^2}\right]-\rho g\sin(\theta) \tag{2}$$

For a horizontal flat plate, the energy balance for a Newtonian fluid with constant ρ and μ equation reduces to,

$$u\frac{\partial T}{\partial x}+v\frac{\partial T}{\partial y}=\alpha\frac{\partial^2 T}{\partial y^2} \tag{3}$$

where

$$\left[\frac{\partial u}{\partial t}\right]=0$$

$$\frac{\partial^2 u}{\partial x^2}<<\frac{\partial^2 u}{\partial y^2}$$

Then, Eq. (2) becomes:

$$\rho\left[u\frac{\partial u}{\partial x}+v\frac{\partial u}{\partial y}\right]=-\frac{\partial P}{\partial x}+\eta\left[\frac{\partial^2 u}{\partial y^2}\right]-\rho g\sin(\theta) \tag{4}$$

$$\frac{\partial P}{\partial x}=-\rho_\infty g\sin\theta \tag{5}$$

where ρ_∞ is the density outside the boundary layer. Replacing Eq. (5) in Eq. (4) yields

$$\rho\left[u\frac{\partial u}{\partial x}+v\frac{\partial u}{\partial y}\right]=g\sin(\theta)(\rho_\infty-\rho)+\eta\left[\frac{\partial^2 u}{\partial y^2}\right] \tag{6}$$

The first term on the right-hand side of Eq. (6) is the buoyancy force, where the density ρ is a variable. The density may be represented by a linear function of temperature for small temperature differences and the change in density is related to the thermal expansion, β, as: **Rolando, 2004,**

$$\beta=-\frac{1}{\rho}\left(\frac{\partial\rho}{\partial T}\right)_P \tag{7}$$

If β is approximated by:

$$\beta\cong-\frac{1}{\rho}\left(\frac{\rho_\infty-\rho}{T_\infty-T}\right) \tag{8}$$

then

$$\rho_\infty-\rho\cong\rho\beta(T-T_\infty) \tag{9}$$

and Eq. (2) becomes **,Rolando, 2004**:

$$u\frac{\partial u}{\partial x}+v\frac{\partial u}{\partial y}=g(\sin\theta)\beta(T-T_\infty)+\gamma\frac{\partial^2 u}{\partial y^2} \tag{10}$$

hence, the buoyancy force is related to the temperature difference.

Momentum integral method is approximate and much easier to apply to a wide range of problems than any exact method of solution. The idea behind this: is it is not really interest in the detailing of the velocity or temperature profiles beyond learning their slopes at the wall **(John, 2004)**. [These slopes give the shear stress at the wall is $\tau_w = \mu(\partial u/\partial y)_{y=0}$ and the heat flux at the wall is $q_w = k(\partial T/\partial y)_{y=0}$ **Schlichting, 1979**, where the boundary conditions are:

$T = T_w$ at $y = 0$
$T = T_\infty$ for $y \gg \infty$
$u = v = 0$ at $y = 0$
$u = v = 0$ for $y \gg \infty$

If the integral method is applied in Eqs. (10 and 3), these equations (momentum and energy equations) will be respectively,**John, 2004**:

$$\frac{d}{dx}\int_0^\delta u^2 dy \cong g\beta\int_0^\delta (T - T_\infty)dy - \nu\left.\frac{\partial u}{\partial y}\right|_{y=0} \quad (11)$$

$$\frac{d}{dx}\int_0^\delta u(T - T_\infty)dy \cong -\alpha\left.\frac{\partial T}{\partial y}\right|_{y=0} \quad (12)$$

The functional forms are assumed as follows **,John, 2004**

$$u = u_1\xi(1-\xi)^2 \quad (13)$$

and

$$\phi = \frac{T - T_\infty}{T_W - T_\infty} = (1-\xi)^2 \quad (14)$$

The first derivative of this equation with respect to (y) will be **,John, 2004**

$$\left.\frac{\partial T}{\partial y}\right|_{y=0} = -\frac{2}{\delta}(T_w - T_\infty) \quad (15)$$

where $\xi = \dfrac{y}{\delta}$

After the first derivative of Eq. (13) is used and equaled to zero in order to obtain the value of maximum velocity component termed u_1 substituting this equation with Eq. (15) into Eq. (11) gives the general solution of the laminar thermal boundary layer without pressure gradient

$$\frac{\delta}{x} = 3.93[0.952 + pr]^{\frac{1}{4}}(pr)^{-\frac{1}{2}}(Gr_x)^{-\frac{1}{4}} \quad (16)$$

the Gr_x is the local Grashof number

$$Gr_x = \frac{g\sin(\theta)\beta(T_W - T_\infty)x^3}{\nu^2}$$

where (θ) is the inclination angle of flat plate with horizontal position.

The solution of the boundary-layer equations for any convection heat transfer problem gives the velocity and temperature distributions. This is true for any type of solution (analytical or numerical) and for any type of convection (forced or natural). Once the solution is obtained, the heat-transfer coefficient is obtained by realizing that as we approach the solid surface, the velocity vector is tangent to the surface and the heat-flux vector is normal to the surface, thus the heat transfer is by conduction at the limit as the distance from the wall approaches zero. Therefore, for the problem described in the previous section, the heat flux is:

$$q = h(T_w - T_\infty) = k\frac{\partial T}{\partial y}\bigg|_{y=0} \tag{17}$$

Subtracting into Eq. (17), will give:

$$\frac{h}{k} = \frac{2}{\delta}$$

The value of δ from Eq. (16) is used to get the local heat transfer coefficient along the length of flat plate with respect to x component as follows:

$$h_x = 0.508(pr)^{\frac{1}{2}}[0.952 + pr]^{-\frac{1}{4}}k(Gr_x)^{\frac{1}{4}}x^{-\frac{1}{4}} \tag{18}$$

The Nusselt number is found from the following relation:

$$Nu_x = \frac{h_x x}{k} \tag{19}$$

The heat dissipation from the heated flat plate can be determined from the following relation:

$$Q = hA(T - T_W) \tag{20}$$

3. PROBLEM DEFINITION

In natural or free convective heat transfer, heat is transferred between a solid surface and a fluid moving over it, where the fluid motion is entirely caused by the buoyancy forces arising from density changes that result from the temperature variations in the fluid, this motion is called natural convection which can be either laminar or turbulent. However, because of the low velocities that usually exist in natural convection, laminar flow occurs more frequently than turbulent flow. In this paper, attention is therefore focused on two dimensional laminar natural convective flow. If the temperature differences are small enough, the fluid properties, except the fluid density, may be assumed to be constant (fluid density can not be assumed constant, because its variation induces the fluid motion).

In the present work a heated aluminum flat plate is used with dimensions of (128mm length × 64mm width) and additionally five models of central perforation are used heated from upward flat plate with dimension of rectangular perforates dimensions of (2mm×4mm), (4mm×8mm), (8mm×16mm), (16mm×32mm) and (32mm×64mm) are represented by the ratio of the flat plate length to the perforation length of (m=0.03, 0.06, 0.13, 0.25 and 0.5) respectively. The constant wall temperatures used in this search were (50^{o}C, 60 ^{o}C, 70 ^{o}C, 90 ^{o}C, 100 ^{o}C). **Fig. 2** illustrates the flat plate with and without central perforation and shows the perforation length.

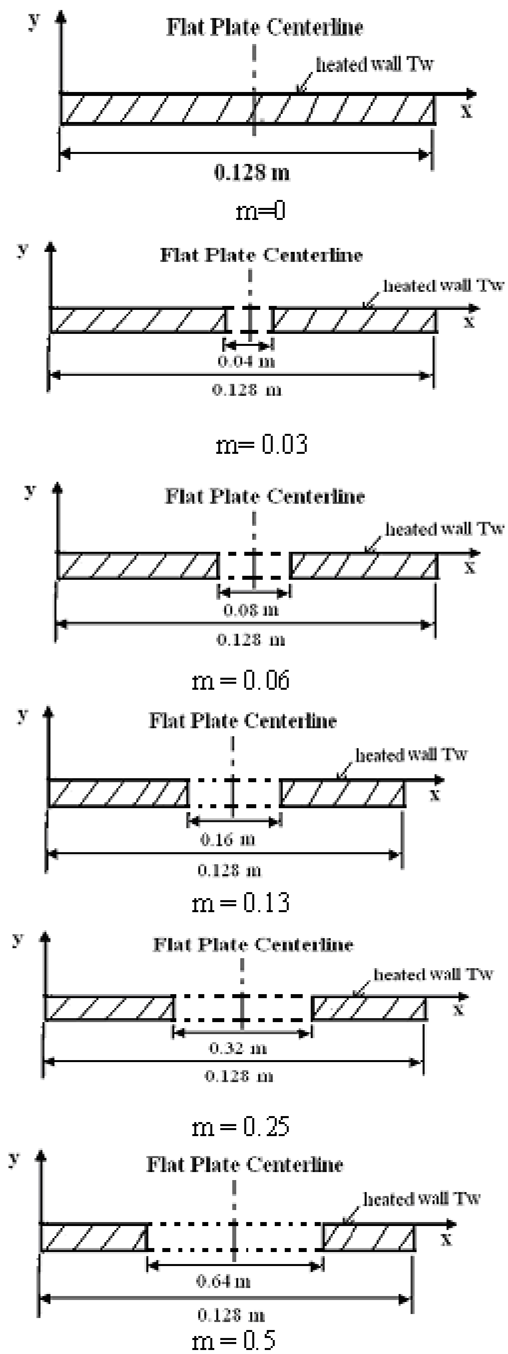

Figure 2. The studied models of flat plate have been heated from upward surface.

4. RESULTS AND DISCUSSION

The figures in this paper were generated by the (MATLAB 7) simulation program to study the effect of the five central rectangular perforations in the heated upward flat plate. **Figs. 3 and 4** show the relationship between the distribution of dimensionless wall temperatures gradient and the region above the flat plate represented by y-direction for the model of heated upward rectangle flat plate without perforation (m=0) for values along the x-direction ranging as follows (x/L_o =1, 0.75, 0.5, 0.25, 0.15, 0.06 and 0.03) at horizontal position ($\theta=0^o$). The results compared with the results of the model (m=0.13) for range of values along the x-direction (x/L_o =1, 0.75, 0.5, 0.25) at the same position ($\theta=0^o$). The numerical data shows that central perforation is used in the plate in order to avoid entering the slight declination region. The temperature gradients were located at positions (x/L_o = 0.03, 0.06 and 0.15) in the range of the central perforation. The figures show that high temperatures gradient along y-direction is achieved for the all models at the external edge while the low temperatures gradient exists at the internal edge of perforation models and increases with increasing the perforation ratio. And **Fig. 5** shows the development of the thermal boundary layer thickness (δ) along the x-direction of the heated flat plate for various value of the wall temperature (50^oC, 60 ^oC, 70 ^oC, 90 ^oC, 100^oC) for two selected models of (m=0 and 0.13) respectively at horizontal position ($\theta=0^o$). As is shown in these figures, the thermal boundary layer thickness (δ) is low at the external edge and increases gradually towards the flat plate center, because the fluid molecular density near the models edges is higher than that near the center with high velocity leading to generate the Plume (the thermal separation happens). As a result the thermal boundary layer thickness (δ) increases at the center more than at edges. The transmitted heat at the thermal separation region will be less than that at the external edge.

Fig. 6 shows the development of thermal boundary layer along x-axis for various values of wall temperature for the model of heated flat plate (m= 0.13). It is noticed that the thickness of thermal boundary layer increases gradually from the edge of flat plate towards the center and decreases as the wall temperature increases. in comparison with the model (m= 0.13) in **Fig.5** which shows in that the thickness of boundary layer is interrupted in the edge at (x=0.056 m) while in the centerline of flat plate at (x=0.064 m), the boundary layer thickness increases from the external edges towered the internal edge in which the thickness decreases with increase in the perforation ratio, compared with first model (m=0) show that the thickness of boundary layer decreases with increasing the perforation ratio because of the increase in the temperature gradient at the internal edges.

Figs. 7 and 8 present the effect of flat plate inclination angle on the thermal boundary layer thickness for two models of the heated plate (m= 0) and (m= 0.13). As shown in these figures, the thermal boundary layer decreases as the angle inclination deviates from horizontal towards inclined position because increasing the temperatures gradient, **Abd 2005**. Eventually; the effect of all models of upward heated flat plate on the dimensionless wall temperature gradients (φ) with y-direction are collected in **Fig. 9** that shows the increasing the dimension of the central perforation from (m=0 and 0.06) leads to increasing the dimensionless wall temperature gradients, then this increase goes down when the model (m=0.5) is used because the high area removed from the flat plat leading to decreasing the wall temperature distribution exposed to the ambient.

The local heat transfer coefficient h_{Lo} at horizontal position ($\theta=0^o$) of two models of heated plate (m= 0) and (m= 0.13) is shown in **Fig. 10** the maximum values are achieved in the external edge because of the movement of the thermal boundary layer, and the heat separation at this location of the flat plate. The local heat transfer coefficients decrease gradually from the edge of the flat plate towards the center and the minimum values are at centerline, where the local heat transfer coefficients increase as the wall temperatures increases. The effect of using perforation model of (m=0.13) shown in **Fig. 11**. There are two regions of the heat separation along the upper surface of heated flat plate: the first one exists in the external edge (x=0) of the plate because this edge is adjacent to the infinity medium and the second one at (x=0.056) near the perforation internal edge because this edge is adjacent to the finite medium. **Fig. 12** shows the effect of perforation ratio on the local Nusselt numbers for all models (m=0, 0.03, 0.06, 0.13, 0.25 and 0.5) with x-direction at horizontal position ($\theta=0^o$) the figure shows that the high value of local Nusselt numbers is located in the external edge of the heated flat plate and at perforation edge, The local Nusselt numbers increase as the perforation dimension increases and show that the model (m=0.5) shows high value of Nusselt numbers compared with other models.

Fig. 13 shows the relation between the logarithmic local Nusselt numbers with the algorithm of the local Raleigh numbers ($1.5\times10^5 \leq Ra_x \leq 6.3\times10^5$) at horizontal position ($\theta=0^o$), where the logarithm local Nusselt numbers increase as the perforation ratio increases, because by using the perforation technique, the extraction of the thermal separation region centric in the central of the plate. And when the inclination angles increase to ($\theta=30^o$) as in **Fig. 14** the relation between the logarithm of the local Nusslet numbers and the algorithm of the local Raleigh numbers ($1.01\times10^5 \leq Ra_x \leq 6.4\times10^5$) for the all models, show that the local Nusslet numbers increase as the perforation dimensions and the angle of inclination increase, and the high local Nusselt numbers of ($Nu = 0.761\ Ra^{0.201}$) of the model (m=0) and ($Nu = 0.985\ Ra^{0.211}$) of the model (m=0.13) where the perforation dimensions are (8mm×16mm) at inclination of angle of (30^o) and the increasing ratio between (m=0) and (m=0.13) is (23%) .

A comparison of average Nusselt numbers for the square plate in present study with those of the previous practical and numerical studies on the horizontal square heated plate for, **Abd 2005** illustrated in **Fig. 15** which shows the average Nusselt numbers for the present study at angle of inclination ($\theta = 0^o$) with no central perforation of model (m=0) increasing by (15 %). in the other hand, the results are compared with those of the previous studies which used horizontal heated disk for **Abd, 2005, Mohammed, 2002** and **Kadhim, 2003** as shown in **Fig. 16** which shows that the average Nusselt numbers agreement with the value studied by them. And at Raleigh number 1.47 $\times 10^5$ the model (m=0.5) shows that Nusselt numbers in the present study compared with those in the previous studies give an increase of about (20.3%), (22.6%) and (22.1 %) for the results of **Abd, 2005, Mohammed, 2002** and **Kadhim, 2003** respectively. This study show a good agreement in terms of the Nusselt numbers for the heated upward plate at angle of inclination (φ =30^o) with central perforation of model (m=0.25) compared with the square plate perforated with the circular perforation of **Abd, 2005** and rings of the,**Mohammed. 2002**.

6. CONCLUSIONS

A numerical investigation was carried out to study the natural convection heat transfer in the rectangular upward heated inclined perforated flat plate. In this paper, the influence of perforation ratio (m), Raleigh number (Ra), the angle of inclination (θ) and wall temperatures (T_w) were investigated. The numerical results show that: (1) the thermal boundary layer thickness increases as the wall temperature increases and as the angle of inclination decreases (2) The maximum values of local heat transfer coefficients are achieved at the leading edge of the flat plat for all models and at any angle of inclination. (3) The heat transfer process is enhanced with the perforation dimension increases. (4) The average Nusslet number for the present paper at angle of inclination (θ=0^o) with no central perforated perforation ratio (m=0) increases by (15 %). (5) The Nusselt number values agree with these values presented by previous studies, with increase by (22 %) at (Ra=1.47 $\times 10^5$) and (m=0.5).

REFERENCES

- Abd Y.H. 2005, *Numerical study for a three dimensional laminar natural convection heat transfer from an isothermal heated horizontal and inclined square plate and with a circule hole*" M. Sc. Thesis University of Technology.
- Ioan, L. M. 2001,*Convective Heat Transfer: Mathematical and Computational Modeling of Viscous Fluids and Porous Media*. Elsevier Science & Technology Books.
- Ganesan, P. & Palani, G. 2003, *Natural convection effects on impulsively started inclined plate with heat and mass transfer*, Heat and Mass Transfer, 39, 277–283.
- Jones, D. R. 1973. *Free convection from a semi-infinite flat plate inclined at a small angle to the horizontal*. Q. J. Mech. Appl. Math. 26, 77-98.
- John H. Lienhard 2004, *A Heat Transfer Textbook*" Mechanical Engineering. University of Houston.

- Kobus G.L and Wedekind R.O. 2000 , *An experimental investigation into Natural convection heat transfer from horizontal stationery isothermal circular disks* Department of Mechanical Engineering, Oakland University 5 May.
- Kadhim A.H., 2003, *Prediction of three dimensional natural convection from heated disks and rings at constant temperature*. J. Eng. and Technology. Vol.22, No.5, pp.229-248.
- Mohammed J.A., 2002,. *Measurement of three dimensional natural convection heat transfer from disks and rings facing upward and downward at constant temperature* M. Sc. Thesis University of Baghdad.
- Ostrach S., 1952. *An Analysis of Laminar Free-Convection Flow and Heat Transfer about a Flat Plate Parallel to the Direction of the Generating Body Force*. Report 1111-Supersedes NACA TN 2635.
- Patterson J.C, Lei C. and. Saha S.C. 2007. *On the Natural Convection Boundary Layer Adjacent to an Inclined Flat Plate Subject to Ramp Heating* School of Engineering James Cook University, Townsville, QLD 4811, Australia December.
- Umemura, A. and Law, C. K. 1990. *Natural Convection Boundary-Layer Flow Over a Heated Plate with Arbitrary Inclination*. J. Fluid Mech. 219, 571-584.
- Rolando A. Carrefio 2004, *Natural Convection Heat Transfer in Supercritical Fluid* Mechanical Engineering University of Puerto Rico.
- Saravanan S. and Kandaswamy P., 2000. *Natural Convection in low Prandtl number Fluids with a Vertical Magnetic Field*, ASME J. Heat Transfer, 122, pp. 602–606.
- Said, S. A. M., Habib, M. A., Badr, H. M. and Anwar, S. 2005. *Turbulent Natural Convection Between Inclined Isothermal Plates*, Computers & Fluid, 34, 1025–1039.
- Sparrow, E. M. and Husar, R. B., 1969. *Longitudinal Vortices in Natural Convection Flow on Inclined Plates* , J. Fluid. Mech.37, , 251–255.
- Schneider, W. 1995. *Laminar Mixed Convection Flows on Horizontal Surfaces*". In 3rd, Caribbean Congr. Fluid Dyn. Volume II, Simon Bolivar Univ., Caracas, pp. 1-7.
- Schlichting H., 1979. *Boundary Layer Theory*, seventh edition translated by Kestin J., McGraw-Hill Book Company , new york.
- Waheed A.M. 2001. *Numerical and Experimental Study Natural Convection Heat Transfer from Isothermal Horizontal Disks and Rings*. M. Sc. Thesis University of Technology
- Weidman, P. D. and Amberg, M. F. 1996. .*Similarity Solutions for Steady Laminar Convection Along Heated Plates with Variable Oblique Suction*. Newtonian and Daxcian fluid flow. Q. J. Mech. Appl. Math. 49,373-403.
- Zhong Z.Y., Yang K. T., Lloyd J. R., 1985. *Variable Property Effects in Laminer Natural Convection in a Square Enclosure*, ASME J. Heat Transfer, 17, pp. 133–138.
- Zekeriya and kurtul 2006 *Natural Convection in Tilted Rectangular Enclosures with a Vertically Situated Hot Inside*" Osmangazi University 7 July.

NOMENCLATURES

A	area of the heated plate, m^2
Nu	average Nusselt number, --
p	pressure, N/m2
g	acceleration due to gravity, m/s^2
t	dimensional time, s
Gr	Grashof number, ---
h	average heat transfer coefficient, $W/m^2.^oC$
h_x	local heat transfer coefficient, $W/m^2.^oC$
u, v	dimensional velocity components, m/s^2
x, y	dimensional coordinates, m
Nu_x	local Nusselt number, ---
Pr	Prandtl number, ---
m	perforation ratio, ---
k	thermal conductivity, $W/m.^oC$
T	predicted temperature
T_∞	ambient temperature
T_w	plate wall temperature
x	

Greek Symbols

α	thermal conductivity, m^2/s
β	volumetric coefficient of thermal expansion, 1/K
θ	angle of inclination, degree
ρ	density, kg/m^3
δ	boundary layer thickness, mm
ν	kinematic viscosity, m^2/s
μ	absolute viscosity, kg/m.s
φ	dimensionless temperature
ζ	dimensionless viscosity

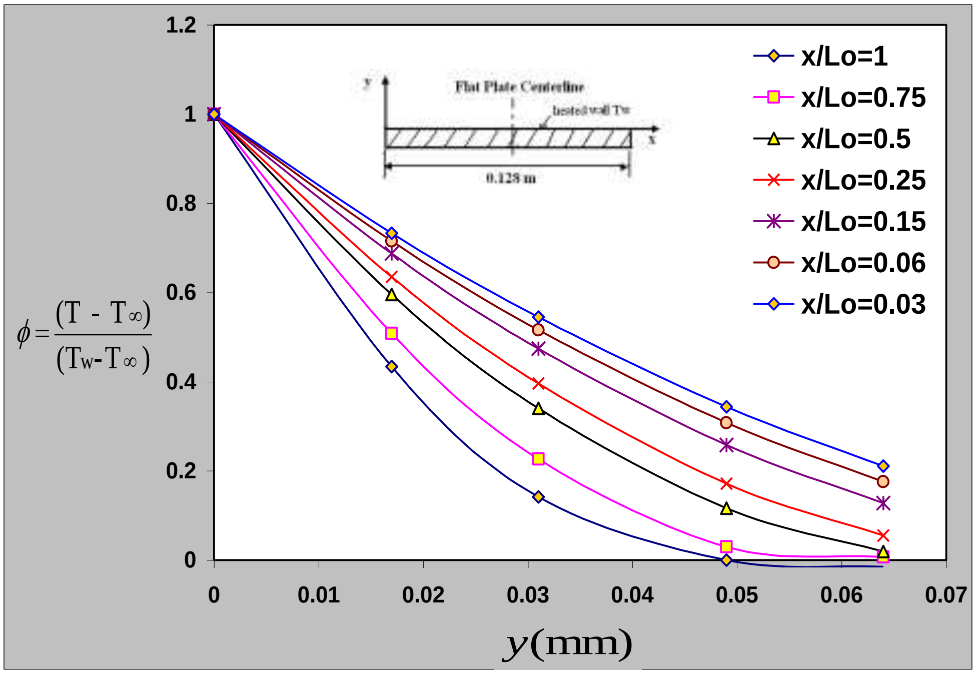

Figure 3. Dimensionless wall temperatures gradient vs. y-direction for the model of heated upward rectangle flat plate without perforation (m=0) for range values along the x-direction at horizontal position ($\theta=0^o$).

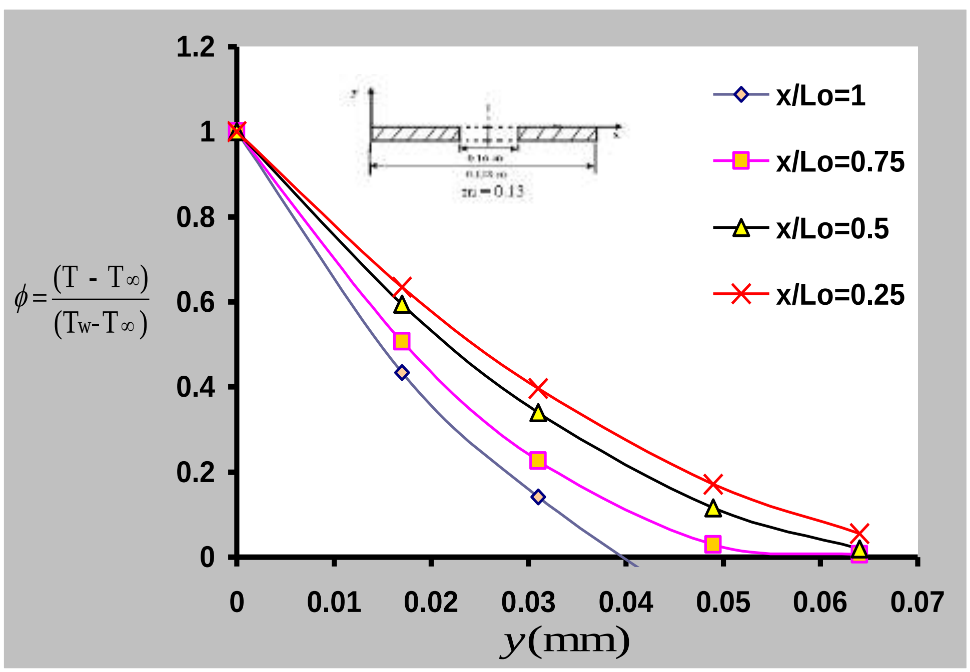

Figure 4. Dimensionless wall temperature gradients vs. y-direction for the model of heated upward rectangle flat plate with central perforation of dimension of (16mm×32mm) (m=0.13) for range values along the x-direction at horizontal position ($\theta=0^o$).

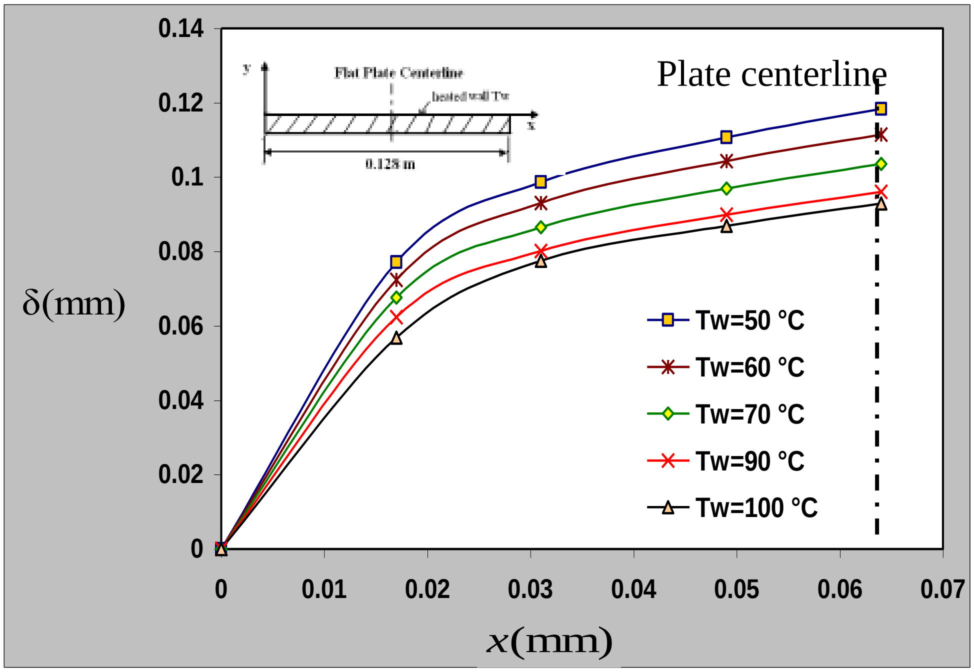

Figure 5. Thermal boundary layer thickness vs. x-direction for the model of heated upward rectangle flat plate without perforation (m=0) for a range of wall temperature.

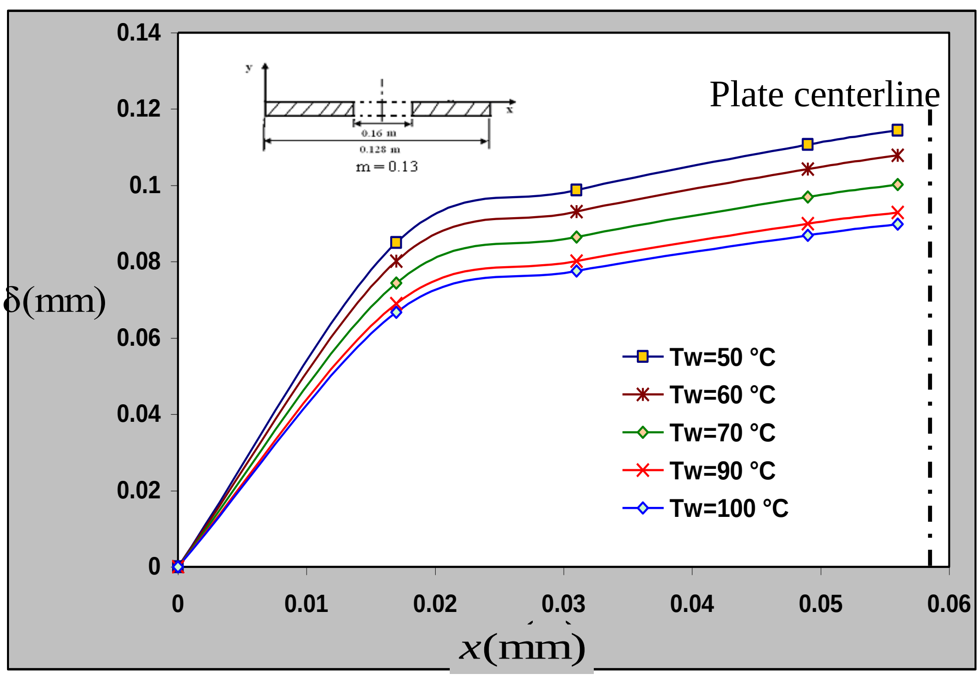

Figure 6. Thermal boundary layer thickness vs. x-direction for the model of heated upward rectangle flat plate with central perforation of dimensions (16mm×32mm) (m=0.13) for a range of wall temperature.

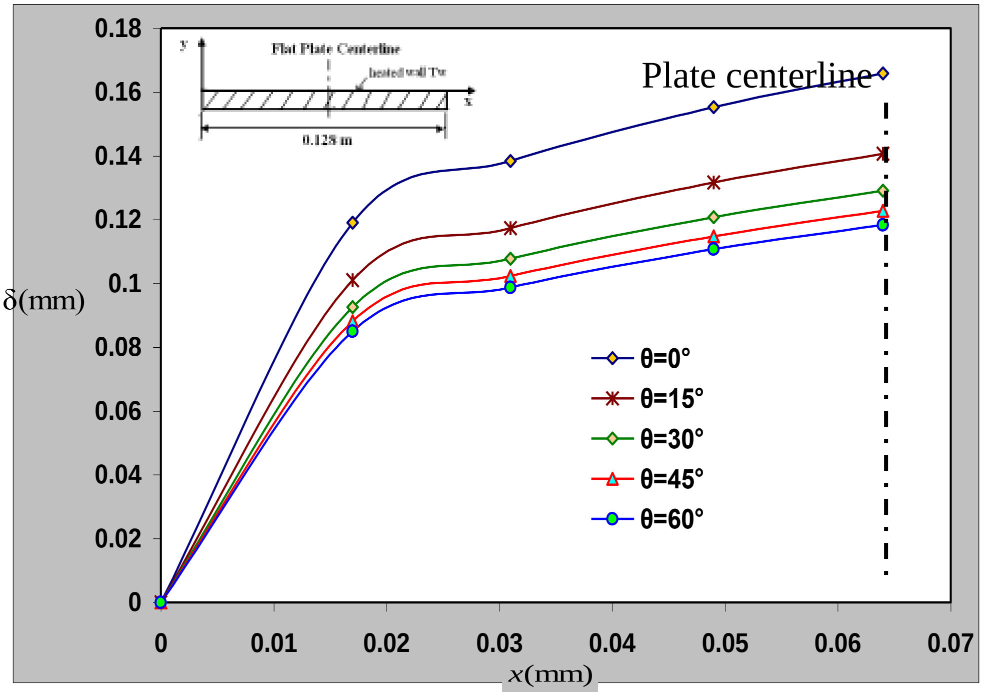

Figure 7. Thermal boundary layer thickness vs. x-direction for the model of heated upward rectangle flat plate without perforation (m=0) for a range of inclination angles.

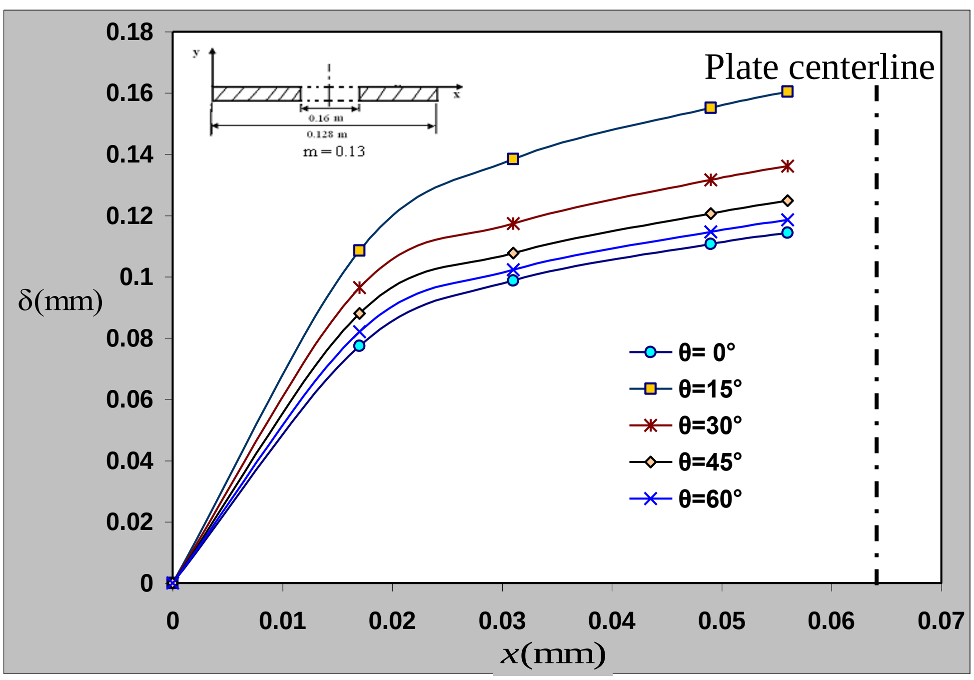

Figure 8. Thermal boundary layer thickness vs. x-direction for the model of heated upward rectangle flat plate with central perforation of dimensions (16mm×32mm) (m=0.13) for a range of inclination angles.

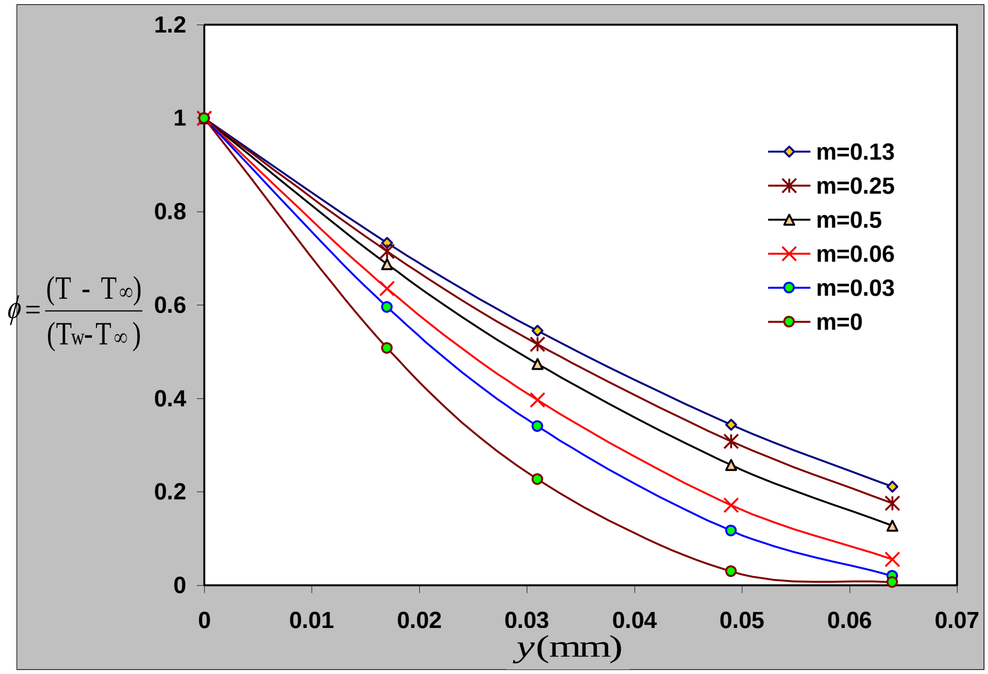

Figure 9. Dimensionless wall temperatures gradient vs. y-direction for the all studied models of heated upward rectangle flat plate.

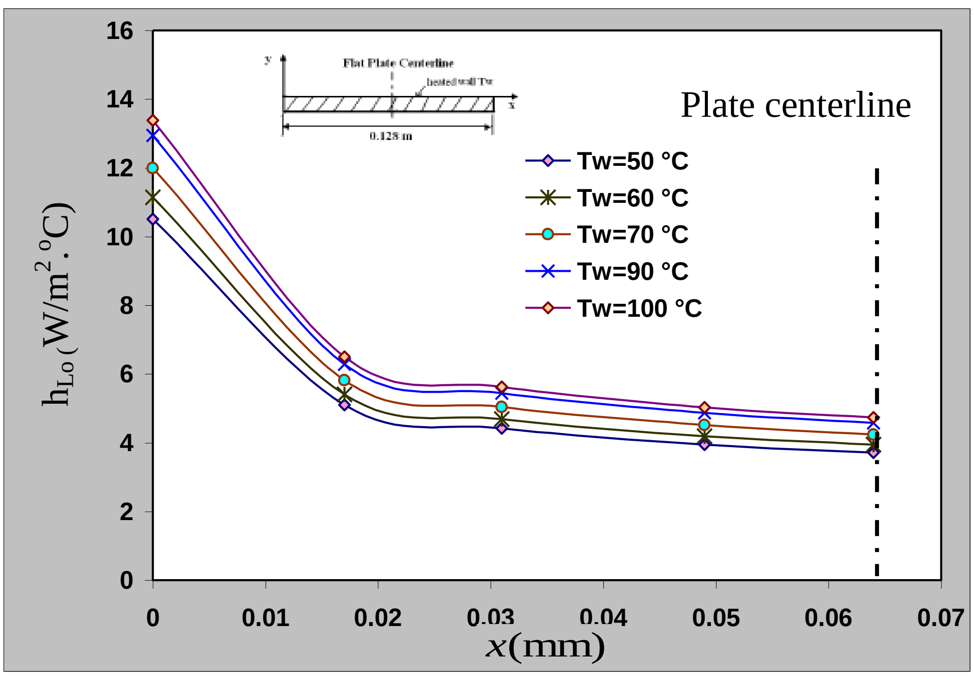

Figure 10. Local heat transfer coefficients vs. x-direction for the model of heated upward rectangle flat plate without perforation (m=0) for a range of wall temperature at horizontal position ($\theta=0^o$).

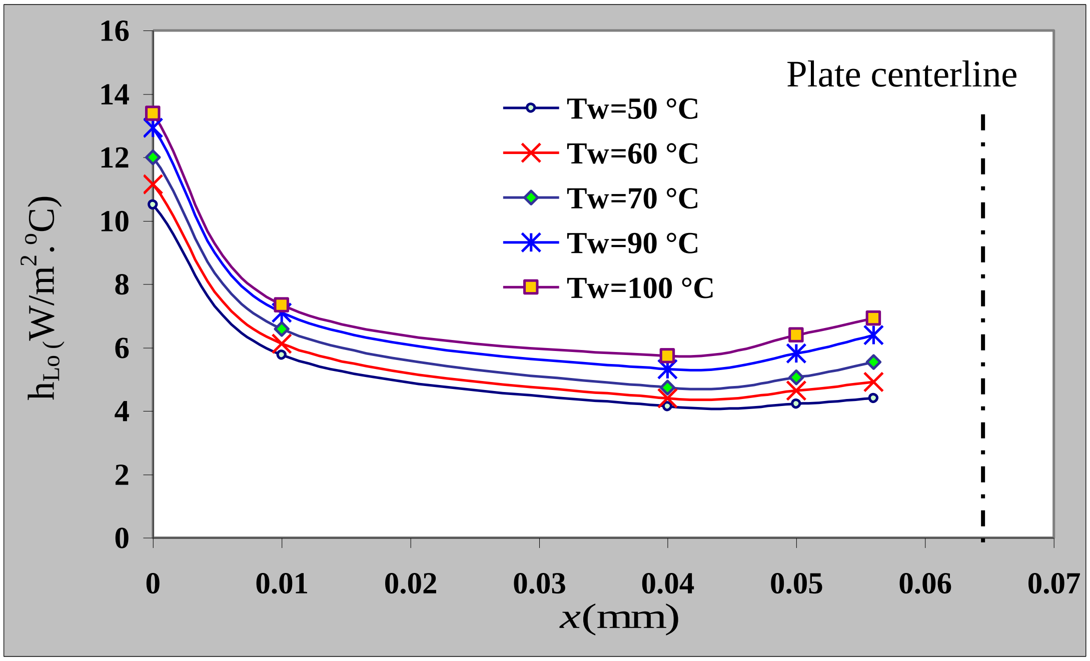

Figure 11. Local heat transfer coefficients vs. x-direction for the model of heated upward rectangle flat plate with central perforation of dimensions (16mm×32mm) (m=0.13) for a range of wall temperature at horizontal position ($\theta=0^o$).

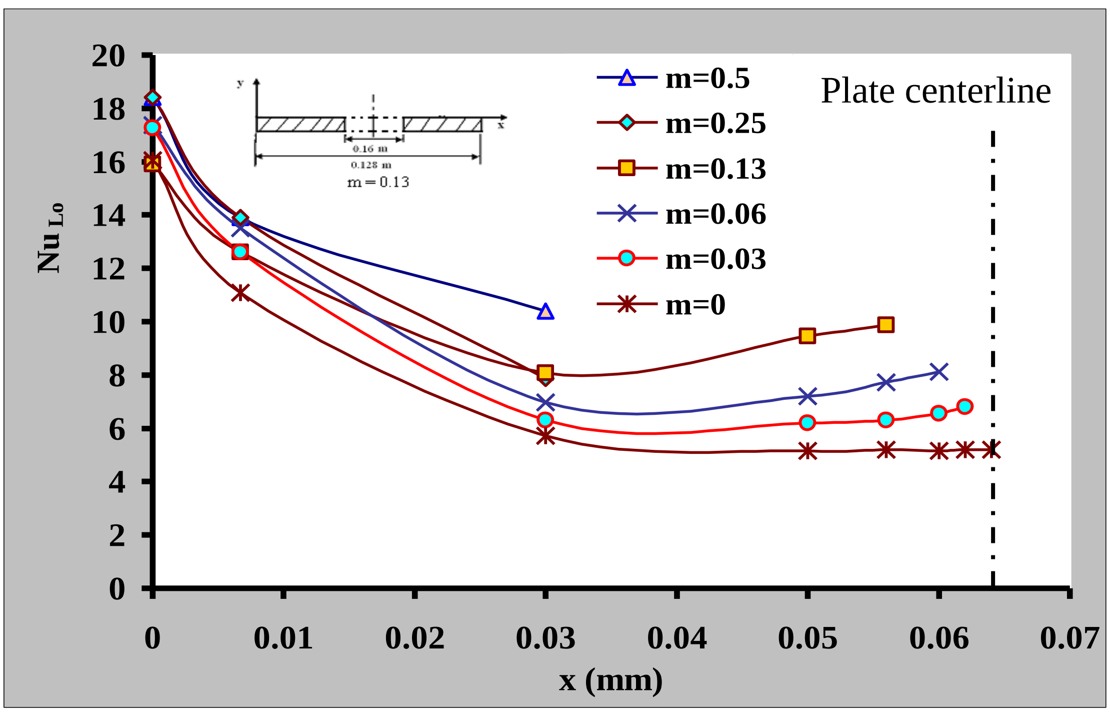

Figure 12. Comparison the distribution local Nusselt number vs. x-direction for all studied models of heated upward rectangle flat plate angle of inclination (0^o).

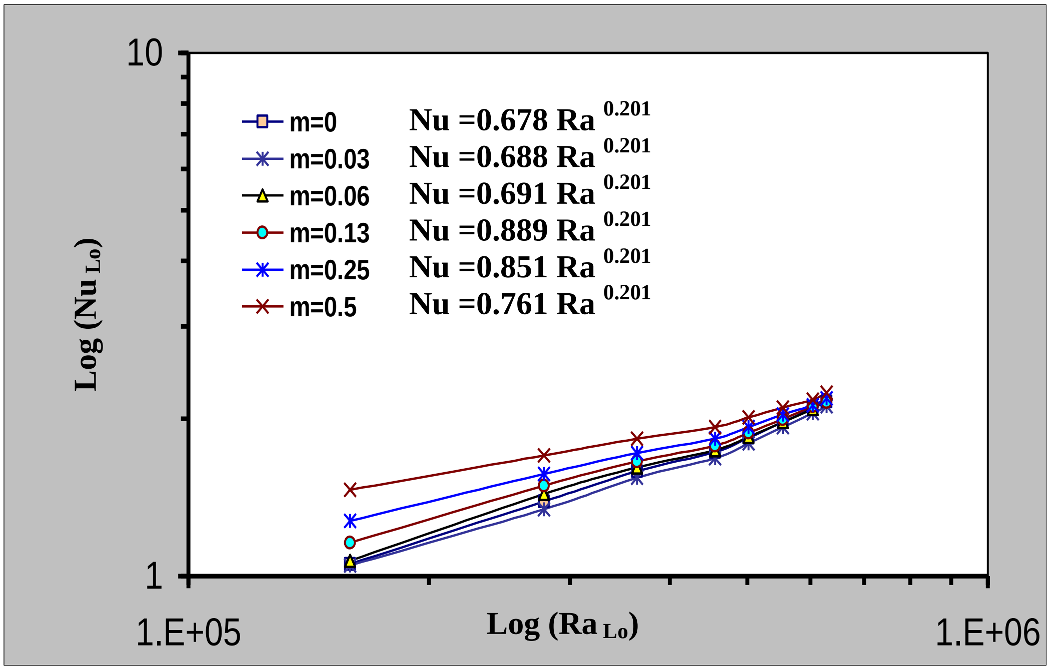

Figure 13. Comparison the distribution the local Nusselt number vs. Raleigh number for all studied models of heated upward rectangle flat plate for horizontal position at angle of inclination (0^o)

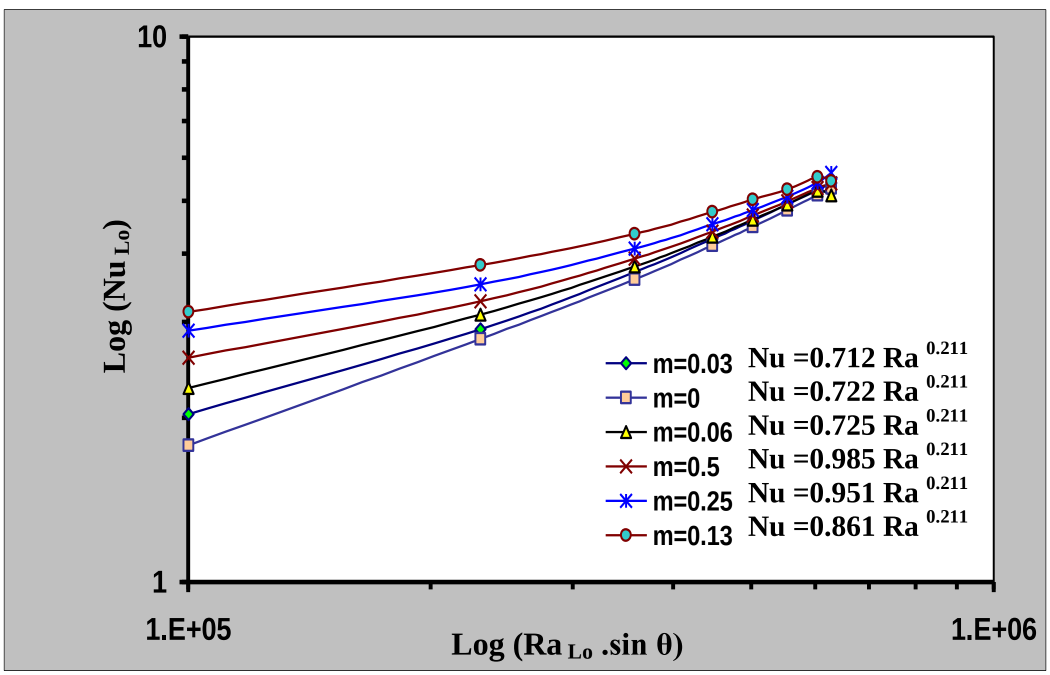

Figure 14. Comparison the distribution the local Nusselt number vs. Raleigh number for all studied models of heated upward rectangle flat plate for horizontal position at angle of inclination (30^o).

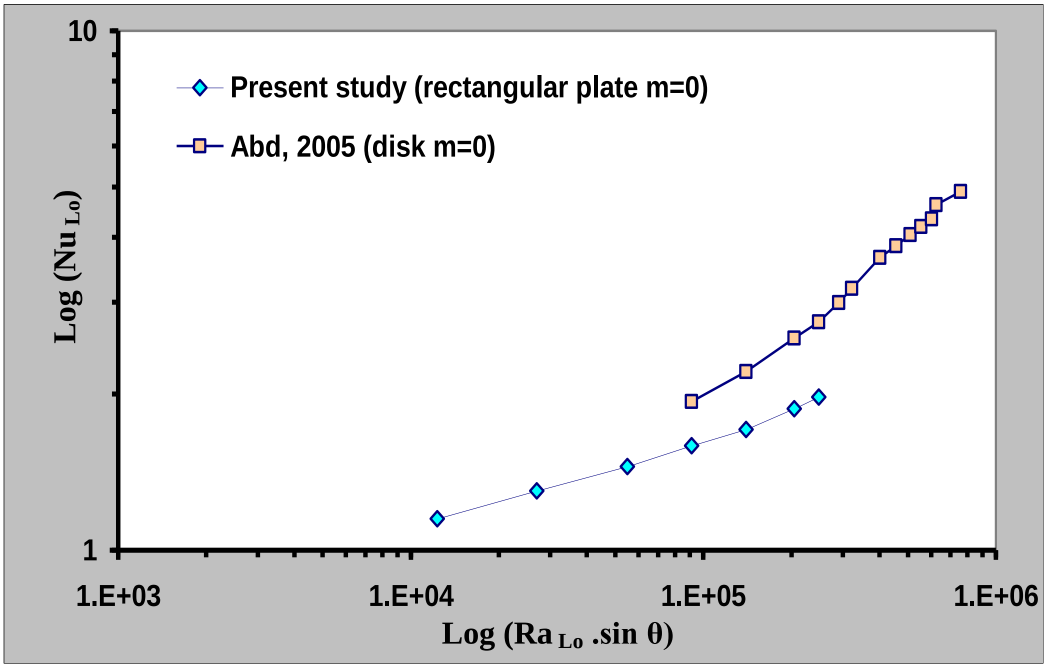

Figure 15. Comparison of the distributions of the logarithm Nusselt number vs. Raleigh number without perforation (m=0) heated upward rectangle flat plate for horizontal position at angle of inclination (0^o).

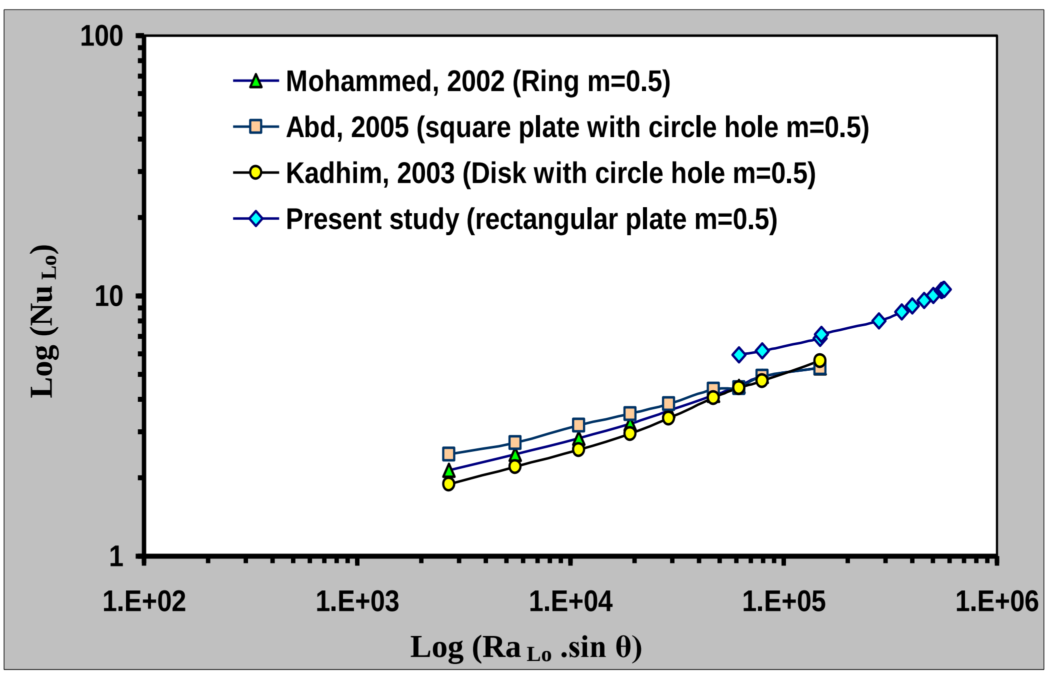

Figure 16. Comparison of the distribution of the local Nusselt number vs. Raleigh number with perforation (m=0.5) heated upward rectangle flat plate for horizontal position at angle of inclination (30^o).

Dynamic Analysis of Fluid – Structure Interaction of Axial Fan System

Dr. Assim Hameed Yousif
Professor
Mechanical Engineering Department-University of Technology
E-mail: assim_yousif20000@yahoo.com

Dr. Wafa Abd Soud Aljanabi
Instructor
Mechanical Engineering Department-UOT
E-mail: wafaabd_92@yahoo.com

Ali Mohammedridha Mahdi
Researcher
Mechanical Engineering Department-University of Technology
E-mail: alimohiraq@yahoo.com

ABSTRACT

Fluid-structure interaction method is performed to predict the dynamic characteristics of axial fan system. A fluid-structure interface physical environment method (monolithic method) is used to couple the fluid flow solver with the structural solver. The integration of the three-dimensional Navier-Stokes equations is performed in the time Doman, simultaneously to the integration of the three dimensional structural model. The aerodynamic loads are transfer from the flow to structure and the coupling step is repeated within each time step, until the flow solution and the structural solution have converged to yield a coupled solution of the aeroelastic set of equations. Finite element method is applied to solve numerically the Navier-Stockes equations coupled with the structural equations The first ten eigenvalue (natural frequency), the first ten eigenvector (mode shape) and effective stress for each part of a rotor system and complete system assembly are predicted.

The validity of the predicted dynamic characteristics of duct fan system was confirmed experimentally by investigating geometrically similar fan system test rig. Good agreement of dynamic characteristics is observed between experimental and numerical results.

Key words: dynamic, fluid-structure interaction, coupling strategies, fan system, natural frequency and mode shape.

تحليل ديناميكي لتداخل المائع والهيكل لمنظومة مروحة محورية

د. عاصم حميد يوسف
أستاذ
قسم الهندسة الميكانيكية - الجامعة التكنولوجية

د. وفاء عبد سعود الجنابي
مدرس
قسم الهندسة الميكانيكية - الجامعة التكنولوجية

علي محمد رضا مهدي
الباحث
قسم الهندسة الميكانيكية - الجامعة التكنولوجية

الخلاصة

استخدمت طريقة تداخل جريان المائع والهيكل للتنبؤ عن المزايا الديناميكية لمنظومة مروحة محورية. تم ربط الحلول العددية لجريان المائع مع الحلول العددية للهيكل باستخدام طريقة البيئة الفيزيائية لتداخل المائع والهيكل.(monolithic method) تم ربط حلول معادلات نفير-ستوك التكاملية ثلاثية البعد مع حلول معادلات الهيكل التكاملية ثلاثية البعد باستخدام طريقة الزمن الحدي. لقد تم نقل الأحمال الديناهوائية من جريان المائع إلى الهيكل وتم إعادة هذه الخطوة المزدوجة مرارا وتكرارا حتى يحصل

الالتئام الكامل لحلول معادلات الجريان ومعادلات الهيكل والذي يقود إلى حلول لمجموعة معادلات المرونة الفضائية. لقد استخدمت طريقة العناصر المحددة لإجراء الحل العددي بشكل مزدوج لمعادلات (نفير-ستوك) التي تحكم المائع مع معادلات تحليل الهيكل. كما استخدمت برامجيات جاهزة لتشغيل طريقة العناصر المحددة وأجراء التحليلات المطلوبة. تم اجراء تحليل ديناميكي لأول عشرة ترددات طبيعية وأول عشرة إشكال نسقيه كذلك الاجهادات الفعالة لأجزاء المنظومة الرئيسية منفردة وللمنظومة مجتمعة.

إن المزايا الديناميكية لمنظومة المروحة التي تم التنبؤ عنها عدديا جرى التأكد من مصداقيتها تجريبيا بإجراء اختبارات عملية على منصة فحص يحاكي شكلها الهندسي نموذج الاختبار العددي لمنظومة مجرى المروحة. ولقد لوحظ إن هناك توافق جيد بين نتائج التنبؤ ونتائج القياسات التجريبية للمزايا الديناميكية للمنظومة.

1. INTRODUCTION

The implementation of a coupled problem (fluid-structure interaction) can be done by using two different strategies, which are the monolithic methods and the partitioned method. In a monolithic method, the discretized fluid-structure system is solved together with the mesh movement system in a single iteration loop, leading to a very large system of nonlinear equations to be solved simultaneously. Some advantages of this method are that it ensures stability and convergence of the whole coupled problem. On the contrary, in simultaneous solution procedures the time step has to be equal for all subsystems, which may be inefficient if different time scales are presented for the problem. An important disadvantage is the considerable high computing time effort required to solve each algebraic system and sometimes the necessity to develop new software and solution methods for the coupling method. A monolithic approach to fluid-structure interaction (FSI) used in the present work is introduced by **Hübner, et al., 2004**.

2. TEST RIG

The experimental test rig designed and manufactured according to the requirement of the present study and its consists of driven motor, static frequency changers, spool shaft, fan, two journal bearing, hollow shaft, eight probes, inlet bow mouth, mesh screen and duct casing. The photograph of the test rig assembly and measuring instruments are shown in **Fig. 1**.

The spooled shaft is made from medium carbon steel (St 60.2), with tensile strength of (600 – 720) N/mm², density (7840) Kg/m^3, Young modulus (210) GN/m^2, modulus of elasticity (80) GN/m^2 and length (544.66) mm with step diameters along its length as shown in **Fig. 2**.

The purpose of using two bearings is to support the load to allow the relative motion being smoothly between two elements of machine, made from porosity bronze alloy. Small holes (2 mm) diameter are made into the bush to allow lubricant oil to pass between shafts and bush bearing to lubricate the contact region and reduce temperature rise. The journal bearing oil film may be idealized into stiffness and damping coefficients which affect the flexibility of the system and introduce damping. The viscosity of the lubricant prevents journal bearing from escaping until pressure is built up in the convergent–divergent film, forcing the lubricant oil to escape and at the same time supporting the load across the film. The load capacity is dependent on the viscosity of the lubricant oil type (SAE. 40) was used as recommended by **Aljanabi, 2007**, in which gave the best dynamic performance.

Two house bearings (bed stall) made from iron (CK 45) there outer diameter is (112.2 mm) and inner diameter is (54 mm). House bearing is used to fix the fan system on test rig stand.

The fan used at present test rig has seven blades (aerofoil section of the blades is NACA 5309), each blade span is (114.35) mm, root chord is (86.64) mm, tip chord (46) mm, and maximum thickness of blade is (6) mm, which is located at 30 % from the leading edge and the leading edge blade twist angle is (10º). The stagger angles of the fan blades can be changed during the test program between (0) to (70º). The fan blades stagger angles are set at (35º) as discovered during the experimental investigation of **Aljanabi, 2007** that give high air speed and uniform flow.

Fine mesh screen fixed behind the fan to smoothing the flow and to minimize the downstream swirls generated by fan rotation.

Hollow shaft has cylindrical shape made from sheet metal (CK 45) has inner diameter (112.2) mm and outer diameter (130.6) mm. Hollow shaft is used to cover the house bearings and to achieve uniform flow of air in the duct test section.

Eight probes were made from (GG18). First four probes are located downstream at a distance (64.14) mm from the fan and the second four probes are located ahead downstream at a distance (415.01) mm from fan, each probe width is (39) mm, thickness is (3) mm and length is (137.7) mm.

Figure 3 shows the schematic diagram of the fan system assembly. The system is isolated in Y-direction from stand frame and ground by four rubber dampers.

AC motor (1.5 KW–50 Hz–3ph) was used to driven the fan system. The motor rotational speed was controlled by using static frequency changer type Hyundai N100.

3. MEASURING INSTRUMENTS

The measuring instruments are flow and dynamic instruments, flow instruments are (Pitot-static tube and micro-manometer), which they used to measure the air flow velocities with respect to the fan rotational speeds. The air velocity obtained for each rotational speed is used as initial input data to the CFD code. Dynamic instruments (accelerometers, vibration transmitters, multiplexer) are also used to measure system dynamic characteristics. Two profile piezoelectric accelerometers (professional vibration sensor), model VB1A4 made by Lutron are used to measure the acceleration and velocity in axial (X) and radial (Y) directions. Two vibration transmitters model TR-VBT1A4 made by Lotrun are used as sensors controller which supply electricity current to excite the sensors in the same time work as an integral circuit that convert the output analog signal (4-20) mv to digital signal. A multiplexor is used to allow the digital signals of two sensors to be record in the same time as sixty reading per second each one. The digital signal then supplied to personal computer. A visual studio program is prepared to represent the output data and to make the analysis required. Data acquisition system was used with a widows-base PC and communication between electrical accelerometers sensor, hardware (card interface), and PC was controlled via software written in Visual studio. The interface precedes raw data transmitted from sensor. Then raw data are digitalized and passed through amplifier to magnify signal before the receiver calculated the time average of the measuring data.

SBS Portable Balancer (SB-1700) is used to permit quick measurements of balance level for various fan system rotational frequency. Laser tachometer (included with the SBS Portable Balance) is used to calibrate the speed indicator of the frequency changer and to check the preciosity of the piezoelectric accelerometers reading.

4. VIBRATION ANALYSIS USING FINITE ELEMENT SIMULATIONS

In the present study the general guideline of the finite element analysis follows the steps described by **Mehdizadeh, et al. 2008**. When finite element method (FEM) applied the solution of eigenvalue, the algebraic eigenvalue problem is exist. Symmetric matrices of order (n) are used as given by **Nakasone, et al. 2006** to fix up the problem. Finite element method also applied to fix the eigenvector problem. Structural systems are very often subjected to transient excitation. A transient excitation is a highly dynamic, time-dependent force exerted on the solid or structure, **Entwistle, 2001**. Time stepping used in finite difference methods are employed in solving transient problems.

Finite element method was tested and extensively developed for structural and solid mechanics problems; it was not admitted as a powerful tool for the solution of fluid mechanics problems until recently reported by **Nakasone, et al. 2006**. The basic concepts associated with the application of the FEM to solve problems in fluid mechanics are summarized in the idealized block diagram given by **Lie,** and **Quek, 2003**. The flow assumed to be three dimensional, steady, incompressible and Newtonian when passing the hollow shaft. The boundary conditions for the problem are specified in terms of pressure and velocity.

5. FLUID–STRUCTURE INTERFACE

Fluid–structure coupled computation is performed by solving the Navier-Stokes equation coupled with the structural equation. The coupled fluid-structure equation is obtained as given by **Vad, et al., 2001,** as follows in Eq. (1) and Eq. (2):

FEM for Structure $$[K_S]\{\delta\} + [M_S]\{\ddot{\delta}\} - [A]^t\{P\} = \{F\} \quad (1)$$

FEM for Fluid $$[K_f]\{P\} + [A]\{\ddot{\delta}\} = 0 \quad (2)$$

For free vibration, the coupled fluid-structure equation is given in Eq. (3):

$$\begin{bmatrix} M_S & 0 \\ A & 0 \end{bmatrix}\begin{Bmatrix} \ddot{\delta} \\ \ddot{P} \end{Bmatrix} + \begin{bmatrix} K_S & -A^t \\ 0 & K_f \end{bmatrix}\begin{Bmatrix} \delta \\ P \end{Bmatrix} = 0 \quad (3)$$

6. NUMERICAL SIMULATION

Soft ware package ANSYS is used to run the finite element method and to make the analysis required. The main complete flow chart for the numerical simulation as given by **Mohammed, 2007** is introduced to do the reprocess step (read geometry and material data, boundary conditions and initial conditions of the problem), to do the processor step (generate finite element mesh, calculate element matrices, assemble element equation and solve the equation) and to do the postprocessors step (compute the solution and it’s derivative at desired paints of the domain and print/plot the result). In the case study analysis for axial fan system all solution is linear except the contact region between shaft and fan.

Air flow load which applied on hollow shaft are non-linear solution. It is essentially the preprocessing is the same for both linear and non-linear analysis, although non-linear analysis might include special elements and non-linear material properties. ANSYS will automatically generate all the nodes and the elements, by specifying:

1- Element attributes include element types, real constants, and material properties.
2- Element size controls the fineness of the mesh.

The next step of finite element analysis involves applying appropriate boundary conditions and the proper loading. The ways used to apply boundary conditions is the same as they used by **Antunes, et al., 2005**.

In this step, the analysis type is defined (static load, transient applies loads, specifying load steps and initiates the finite element solution).

A non–linear analysis will differ from a linear solution in that it often requires load increments and always requires equilibrium iteration. In present study a non-linear static analysis is applied, with convergence criteria, incremental load and specified load step. The main goal of the finite element analysis here is to examine how a structure or component responds to certain loading conditions. The solution of non-linear problems by finite element method is usually attempted by basic techniques given by **Hassan, 2007**.

7. COUPLED-PHYSICS ANALYSIS

When the fluid flowing over a hollow shaft provides pressure loads that can be used in the structural analysis. The pressure loading is a result in a deflection of the hollow shaft. This deflection, in principle, changes the geometry of the flow field around the hollow shaft, but in practice, the change is very small enough and may be regarded to be negligible. Thus, there is no need to iteration. In this problem, fluid element is used for the flow solution and structural elements for the stress and deflection calculations.

ANSYS program performs load transfer coupled the physics analysis by using the concept of a physics environment. The term physics environment applies to both files created which contains all operating parameters and characteristics for a particular physics analysis and to the file’s contents. The data used in the present physics environment method are a single data base and multiplies physics environments as represented by **Daneshmand, 2000**, in which he build a model encompassing all physics requirement. He assign attribute to the model and create physics environment to be used in the analysis. The method starts with (step one) solving the first physics environment, then step two is done with solving next physics environment. The next step is done by solving the current physics environment with the couple-field loads. At last more physics environment are solved, or feedback coupling to physics environment of step two. This feedback close loop is repeated many times until the solution is obtained.

8. MODEL GENERATIONS

The model generations procedure is presented for dynamic modeling of axial fan (rotor-bearing system) by using solid modeling approach method represent by ANSYS drawing key point. Bearing is representing in ANSYS-11 software by using direct generation method, it represent by element COMBIN14 (Combination of spring and damper). The stiffness value of the journal bearings is taken as calculated by **Aljanabi, 2007**.

Air flow is expressed by using solid modeling approach method and meshed by using FLUID142 elements. Element type for each system part is listed in **Table 1**.

9. STRUCTURE MODAL ANALYSIS

The results reported here are the first ten of the structural natural frequency (eigenvalue) and mode shapes (eigenmodes) based upon the behavior of each part of the system (shaft, fan and hollow shaft).

Fig. 4 shows the numerical results of the ten first mode shape of the shaft. The modes titled numbers 1 and 2 show the harmonic motion of the shaft in radial (Y)-direction. These two modes indicated that the oscillatory motion is a function of sine and cosine waves. While mode number 4 shows the shaft oscillatory motion in Z-direction. Modes number 5 and 9 show the transverse vibration in which the shaft is extended and bended, this type of vibration motion indicated that the shaft effected by bending stresses. Modes number 3, 7 and 8 show the torsion vibration in which the shaft is under the influence of the torsion stress. While mode number 6 shows that the shaft is under the torsion vibration and simple harmonic motion (i.e. the shaft is rotate with oscillatory motion in Z-direction). Mode number 10 shows the torsion-transverse vibration due to shaft rotation and the vibration motion appeared to be perpendicular to the shaft axis.

Fig. 5 shows the modal analysis used to determine natural frequency of the fan. Modes number 1, 2, 3, 4, 5, 6 and 7 show that the blades are under the influence of bending, while mode number 8 shows that the fan is under the influence of the torsion and bending together. Mode numbers 9 and 10 showed that the blades are under the influence of twist. As seen in these modes the variation of degrees of freedom is exited in each vibration mode. This may is due to the results of a direct coupling consequence between the degree of freedom in which this explanation is also given by **Ranwala, 2009**. Since blades have to rotate, it must have a lightweight structure as in the present fan, which resulting in their reduced stiffness when compared with other part of a rotor system. Hence blades are quite flexible and can easily bend and twist under the influence of air loads. Although the static air loads on the blades being to twist and bend in a periodic manner, under certain conditions the dynamic air loads may being feeding the elastic motion of the blades, causing its amplitude to grow, which in turn causes increased air loads that eventually exceed the fan strength. Such a catastrophic dynamic coupling between the elastic motion and aerodynamic loading is called flutter. This statement is also in some way has been reported by **Dettmor, 2004**.

Fig.6 shows the first ten mode shape of the hollow shaft. Mode numbers 3, 4, 6 and 7 show that the hollow shaft is vibrated longitudinally in which it is extended and constricted in axial direction. This type of vibration leads to tensile and compressive stresses. Mode numbers 1, 2, 8 and 9 show that the hollow shaft vibrated in transverse direction in which it is extended and bended. This type of vibration is leads to bending stresses. Mode numbers 5 and 10 show torsion vibration in which the hollow shaft is under the influence of the torsion stress.

It can be noticed that the natural frequency for each part of a rotor system was increased with increase of mode number starting from mode number 1 up to mode number 10. The average of the percentage rate of natural frequency is increased for shaft by 44.5%, for fan by 27.32% and for hollow shaft by 12.455%. The highest values of the natural frequency is recorded at shaft and decreased gradually for hollow shaft and fan respectively.

10. FLUID ANALYSIS

The load on the rotor system depends directly on the flow velocity and pressure, when the pressure increase so does the load. The pressure actually fluctuated on the rotor system as the flow passes from fan to the hollow shaft. Five cases of fluid are investigated in this study with respect to the shaft speed.

Fig. 7 shows the summations of velocity distributions for various rotational speeds at the duct exist. The velocity is increased with the increase of rotational speed. At low rotational speed 500 rpm, the velocity distribution is clearly seems to be fully developed. Some deviation is observed from the fully developed flow at the center of blade when the rotational speed increased, this deviations may be exists because the blade twist angle is insufficient enough to produce linear blade loading.

The regions close to the hollow shaft is called **(**fluid-structure regions**)** according to remarkable notes given by **Alzafrany, 2006**. **Fig. 8** shows the pressure distribution along the hollow shaft axis passing through the probe region at difference rotational speed. The pressure exerted on the hollow shaft is reduced gradually in the region just behind the fan. When the air flow passed through the first set of probes, pressure is increased to maximum value at the probes stagnation point and then drops when the flow passes the probes surfaces. Between two set of probes, the pressure distributions became constant. At the second set of probes the pressure increased again to high value because the flow is stagnated at the probes leading edges and then drops when the flow passes on probes surfaces.

According to above discussion one may be decide in the experimental investigation to fix the accelerometer sensors at the mid way along hollow shaft axis in the region when the pressure distribution seems to be approximately constant.

11. STATIC ANALYSIS OF FLUID-STRUCTURE INTERACTION

Figures 9, 10, 11, 12 and **13** show that the fan has maximum stress and higher than the other system parts due to the effect of the generation of the centrifugal stresses, in which these stresses are increased with increase of rotational speed.

The stresses generated along the shaft is maximum at region of sudden change of the cross sectional area (i.e. shaft diameters variations), because all stresses are concentrated at this region, while the minimum stress is recorded at the bearing contact region since the bearing support and carried the shaft.

Fan stress records maximum value at blade roots in which the centrifugal force tend to extirpate the blade from root. While the hollow shaft is influenced by the buildup of pressure of flowing air, and this leads to tensile forces which resist the bursting forces developed across longitudinal and transverse directions.

12. TRANSIENT ANALYSIS

Non-synchronous vibration amplitude is analyzed theoretically and experimentally at various rotational speeds. **Figs. 14, 15, 16, 17** and **18** show the amplitude for a rotor system in axial (X) and radial (Y)-directions. It can be seen that the amplitude in the X-direction is higher than that for Y-direction. This may be due to existent of four dampers in Y-direction used to isolate the system from stand and ground interference. The amplitudes in axial (X) and radial (Y) directions are decreases when the rotational speed is increased. The average of amplitude rate is decreased by 47.949 % in axial-direction and by 47.3 % in radial-direction. The percentage errors between the experimental and the theoretical results of the amplitude components in axial (X) and radial (Y) directions are presented in **Tables 2** and **3**. In spite of that good agreement is observed between experimental and numerical amplitude results in axial (X) and radial (Y) directions as shown in **Figs. 19** and **20** respectively.

13. CONCLUSIONS

According to the adopted data and the obtained results, the present work has reached the following conclusions. The coupling strategies problem (fluid-structure interaction) of duct fan system can be overcome (treated and analyzed) numerically by using finite element method (monolithic method). Experimental investigation of duct fan system satisfied the numerical approach of the coupling problem (fluid-structure interaction). The mode shape depended upon the degree of freedom. The natural frequency for every part of the system and system assembly were increased with increase of mode shape number starting from mode 1 up to 10. Aerodynamic force exerted on the hollow shaft due to air flow is reduced gradually downstream the fan disk of system. The amplitude in axial (X) direction is higher than the amplitude in radial (Y) direction, since the system is isolated in Y-direction from stand frame. The amplitude value decreases when the rotational speed increased.

REFERENCES

- Aljanabi, W. A., 2007, *Theoretical and Experimental Study of an Axial Fan Rotor Bearing System Using Vibration Analysis,* ph. D. Thesis, Mechanical Engineering Department, University of Technology, Baghdad, Iraq.

- Al-Zafrany, A., 2006, *Finite Element Methods*, School of Engineering, Cranfield University, United Kingdom.

- Antunes, A. R., Lyra, P. R., Willmersdorf, R. B., 2005, *A Methodology and Computational System For The Simulation of Fluid-Structure Interaction Problem*, Journal of The Braz. Soc. Of Mech. Sci. and Engineering, Vol. 27, No. 3, PP. 255-265.

- Daneshmand, F., 2000, *Fluid-Structure Interaction Problems and It's Application in Dynamic Analysis*, Ph. D. Thesis, Mechanical Engineering, Shiraz University, Iran.

- Dettmor, W. G., 2004, *Finite Element Modeling of Fluid Flow With Moving Free Surfaces and Interface Including Fluid-Solid Interaction*, Ph. D. Thesis, School of Engineering, University of Wales, United Kingdom.

- Entwistle, K. M., 2001, *Basic Principles of The Finite Element Method*, Alden Press, 1st Published, Oxford, United Kingdom.

- Hassan, A. J., 2007, *Effect of Shape and Location of Cutout on The Dynamic Response of Thin Cylindrical Shell*, M. Sc. Thesis, Nahrain university, collage of engineering, Iraq.

- Hübner, B., Walhorn, E., and Dankler, D., 2004, *A monolithic approach to fluid-structure interaction using space-time finite elements*, Elsevier Journal, Vol. 193, No. 9, PP. 2087-2104.

- Liu, G. R., and Quek, S. S., 2013, *The Finite Element Method: A Practical Course*, Elsevier Butterworth-Heinemann, 2nd Published, Oxford, United Kingdom.

- Mehdizadeh, O. Z., Zhang, C., and Shi, F., 2008, *Flow Induced Vibratory Stress Prediction on Small Turbofan Engine Compressor Vanes Using Fluid-Structure Interaction Analyses*, Alaa Journal, Vol. 4, No. 12, PP. 2431-2483.

- Mohammed, T. F., 2007, *Hot Extrusion with Tilting Dies*, M. Sc thesis, Technical College, Baghdad, Iraq.

- Nakasone, Y., Yoshimoto, S., and Stolarski, T., 2006, *Engineering Analysis With Ansys Software*, Elsevier Butterworth-Heinemann, 1st Published, Oxford, United Kingdom.

- Rangwala, A. S., 2009, *Structural Dynamics of Turbo-machines*, New Age International (p) Ltd., 1st Edition, Delhi, India.

- Vad, J., Bensze, F., Corsini, A., and Pispoli, F., 2001, *Non-Free Vortex Flow Effects in an Axial Flow Rotor*, Periodical Polytechnic Ser. Mech. Eng., Vol.45, No. 2, PP. 201-216.

15. NOTATION

A = fluid-structure interaction matrix.
F = nodal point load vector acting on the structure.
F.E.M = finite element method.
FSI = fluid-structure interaction.
K_f = stiffness matrix of pressure.
K_s = stiffness matrix of the structure.
M_s = mass matrix of the structure.
NACA = the national advisory committee for aeronautics.
P = unknown nodal pressure vector of the fluid.
$\ddot{P}$ = double derivative of nodal pressure after incorporating boundary condition.
X = axial direction.
Y = radial direction.
Z = axis perpendicular to X, Y plane.
δ = unknown nodal displacement vector of the structure.
$\ddot{\delta}$ = normal acceleration vector.
Φ = diameter, mm.

Table 1. Define labeled numbers are as given in **Fig. 3** and element type.

No.	**Discription**	**Element Type**
1	Shaft	SOLID72
2	Hollow Shaft	SOLID72
3	Bush Bearing	COMBIN14
4	House Bearing	COMBIN14
5	Teflon	COMBIN14
6	Fan	SOLID72
7	Probe	FLUID142
8	Fluid	FLUID142
9	Fluid-Strucre	FLUID142- SOLID45
10	Circuler Duct	FLUID142

Table 2. Amplitude values and errors in X-direction.

N (rpm)	**Experimental Work in X-direction (m)**	**Theoretical Work in X-direction (m)**	**% error**
500	2.5532E-4	2.43603E-4	- 4.809
1000	6.38323E-5	6.56559E-5	2.7775
1500	3.64756E-5	4.00810E-5	8.995
2000	2.7356E-5	3.2198E-5	15.038
2500	2.626245E-5	2.8358E-5	7.3896

Table 3. Amplitude values and errors in Y-direction.

N (rpm)	**Experimental Work in Y-direction (m)**	**Theoretical Work in Y-direction (m)**	**% error**
500	2.1885E-4	2.118124E-4	- 3.22814
1000	6.38323E-5	6.40657E-5	0.363
1500	3.6475E-5	3.87487E-5	5.8678
2000	2.62168E-5	3.14019E-5	16.515
2500	2.58962E-5	2.9746E-5	12.9422

Figure 1. Photograph of the fan system and measuring instruments**.**

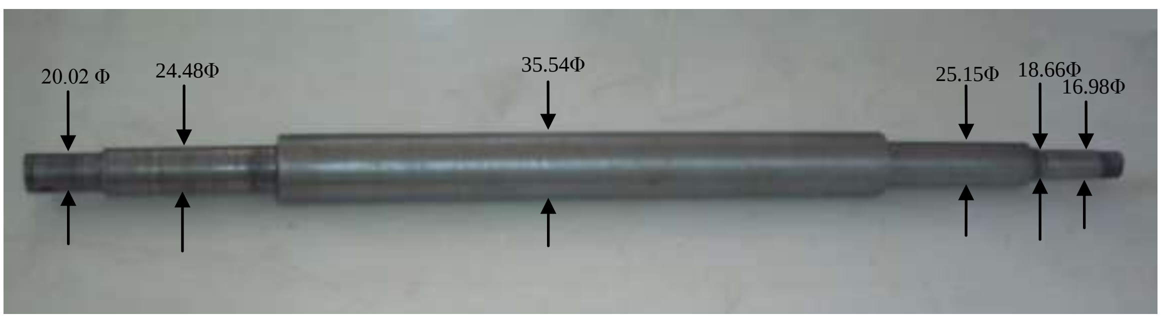

Figure 2. Photograph of the spooled shaft (all dimension in (mm)).

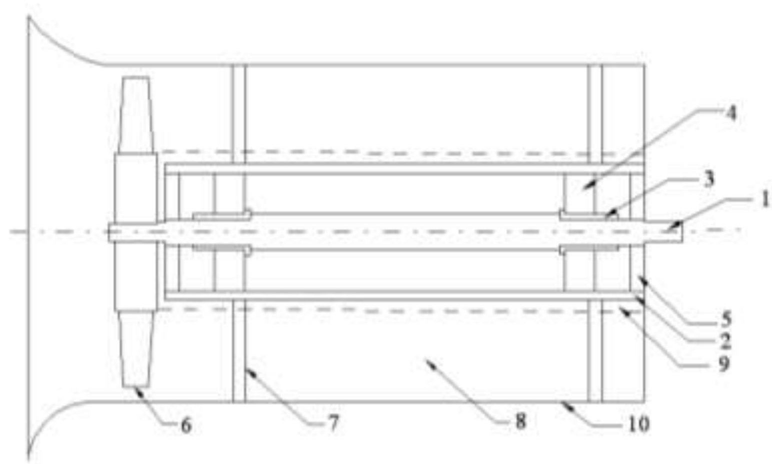

Figure 3. Schematic diagram of the fan system assembly, key of labeled numbers are as given in **Table 1.**

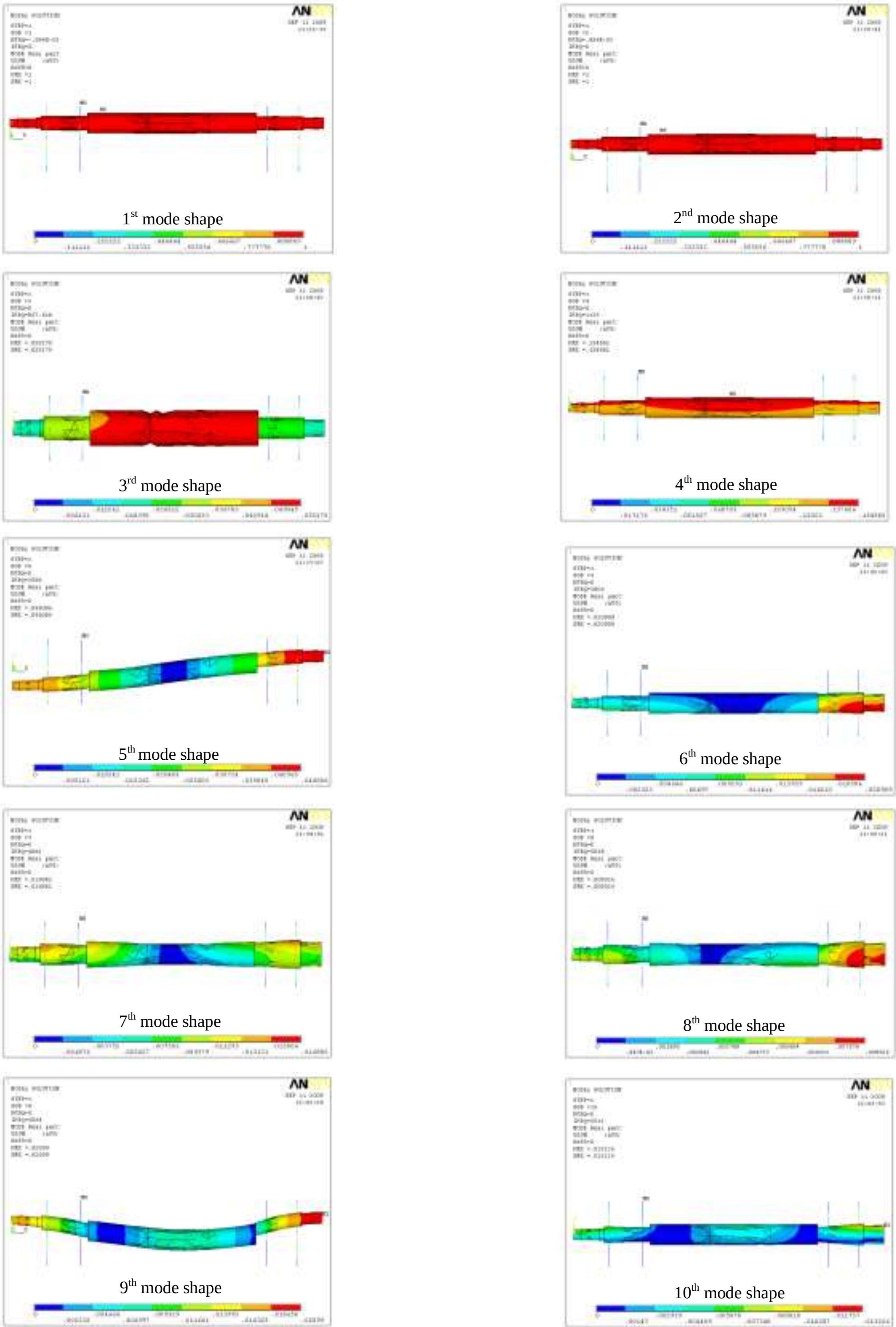

Figure 4. Natural frequency and mode shape for the spooled shaft.

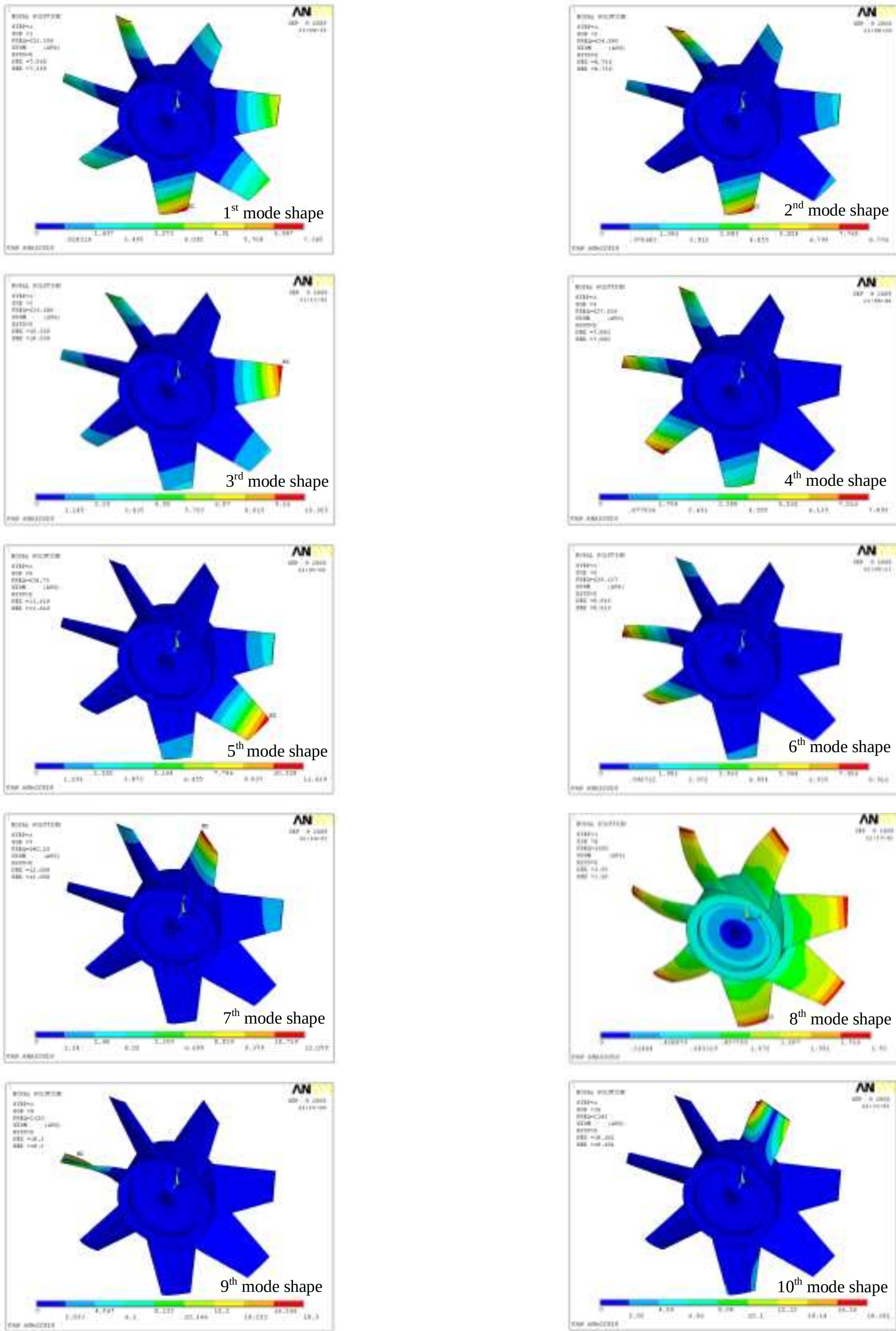

Figure 5. Natural frequency and mode shape for axial fan.

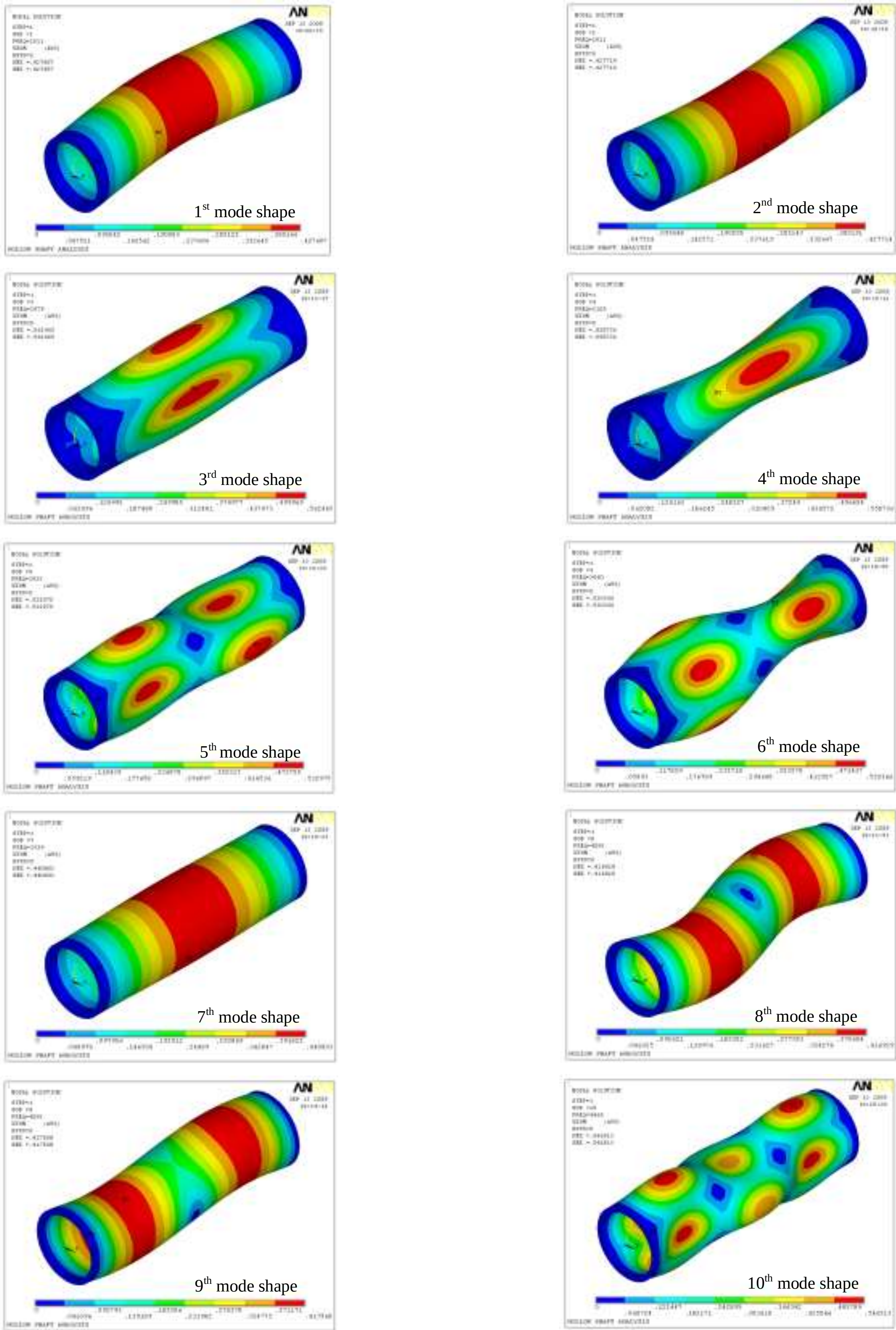

Figure 6. Natural frequency and mode shape for a hollow shaft.

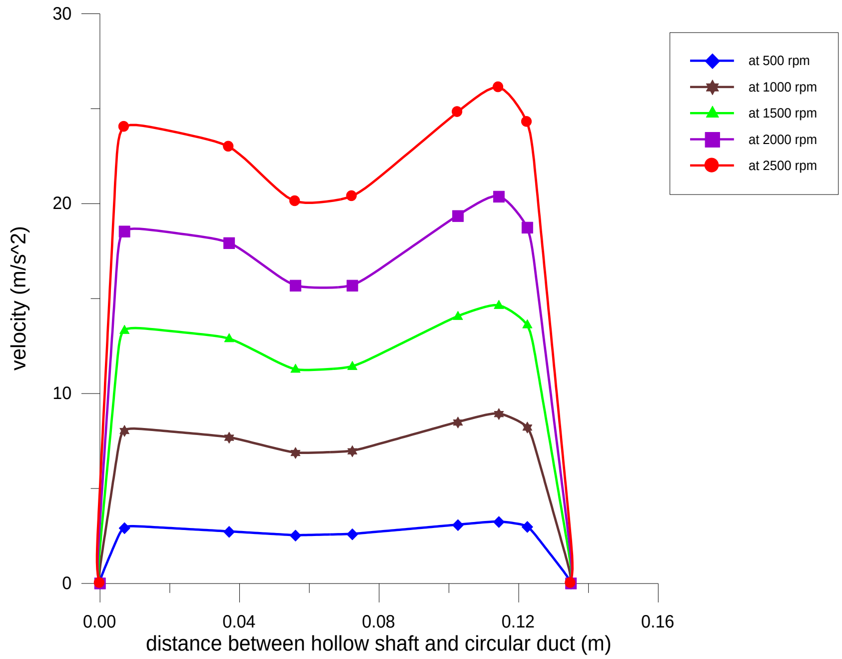

Figure 7. Summation velocity distribution at the outlet of a rotor system at various rotational speeds.

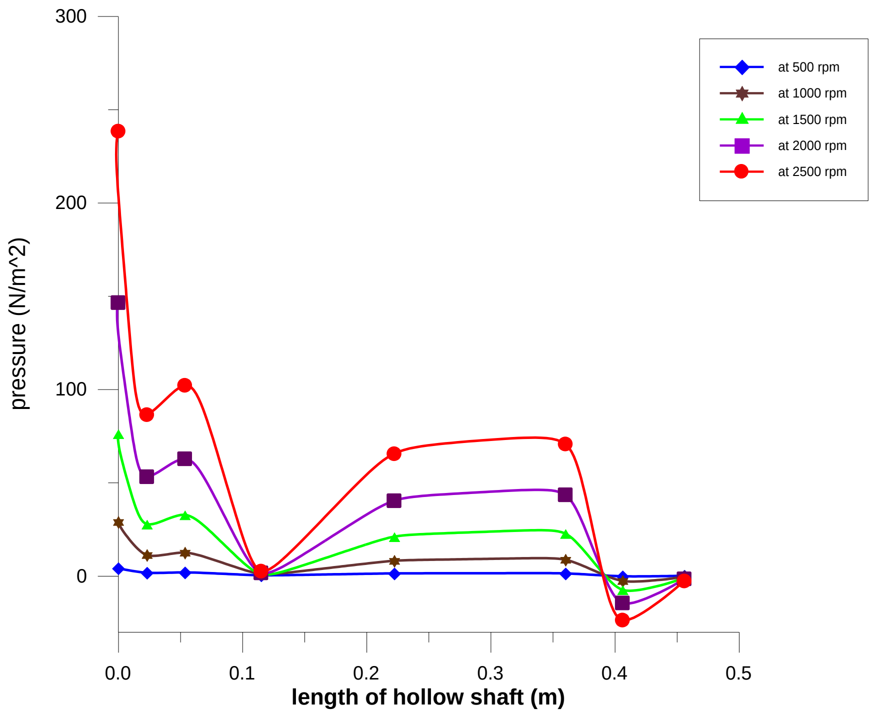

Figure 8. Pressure distribution of fluid-structure interaction at various rotational speeds.

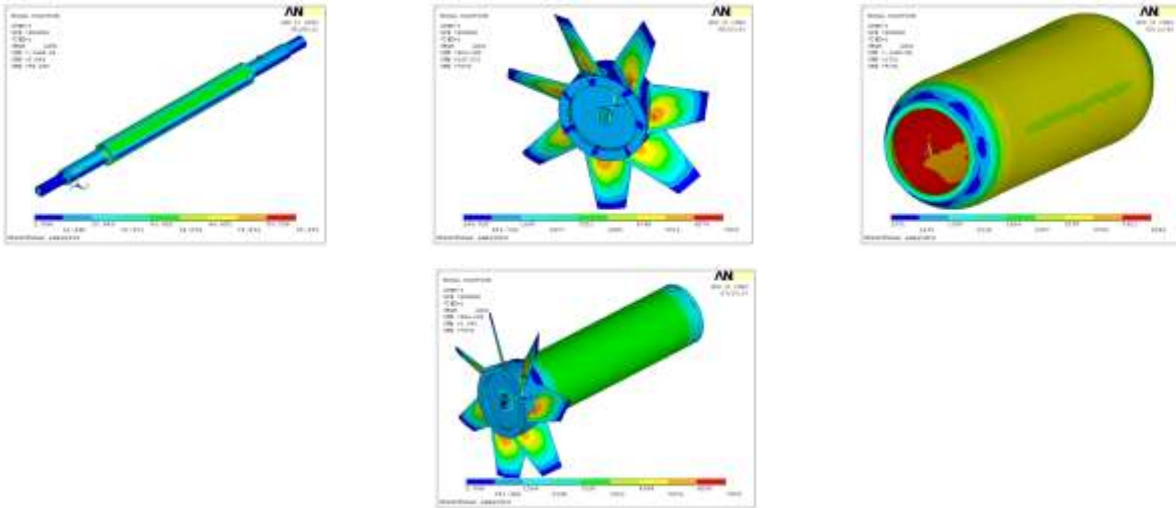

Figure 9. Static stress analysis of system parts and system at rotational speed (500) rpm.

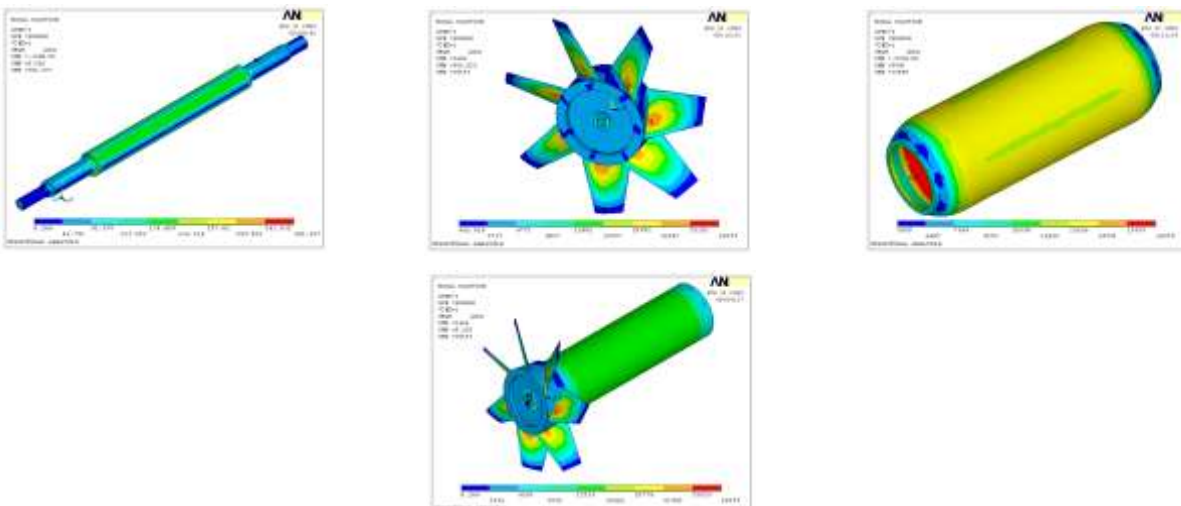

Figure 10. Static stress analysis of system parts and system at rotational speed (1000) rpm.

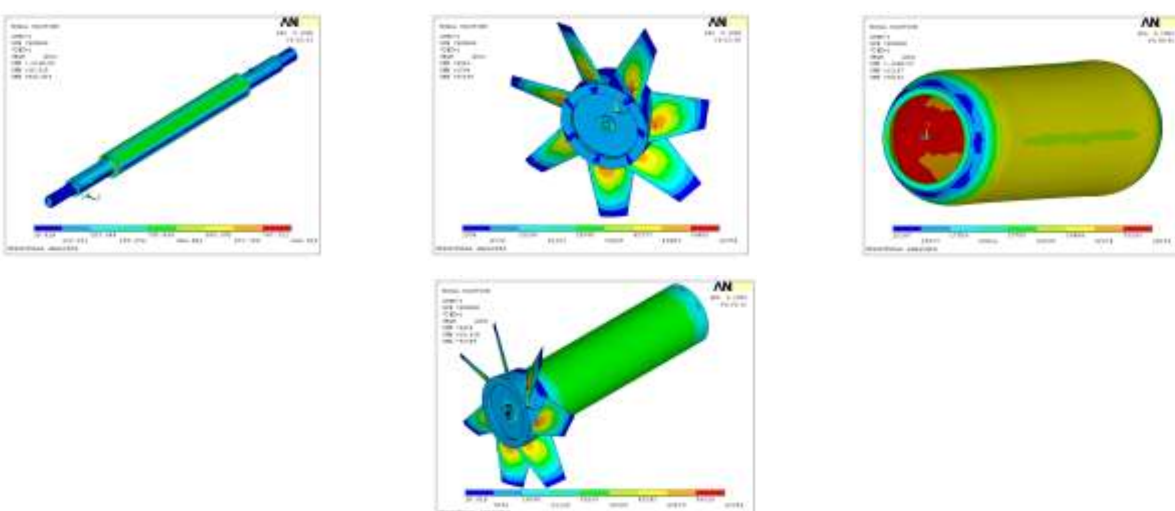

Figure 11. Static stress analysis of system parts and system at rotational speed (1500) rpm.

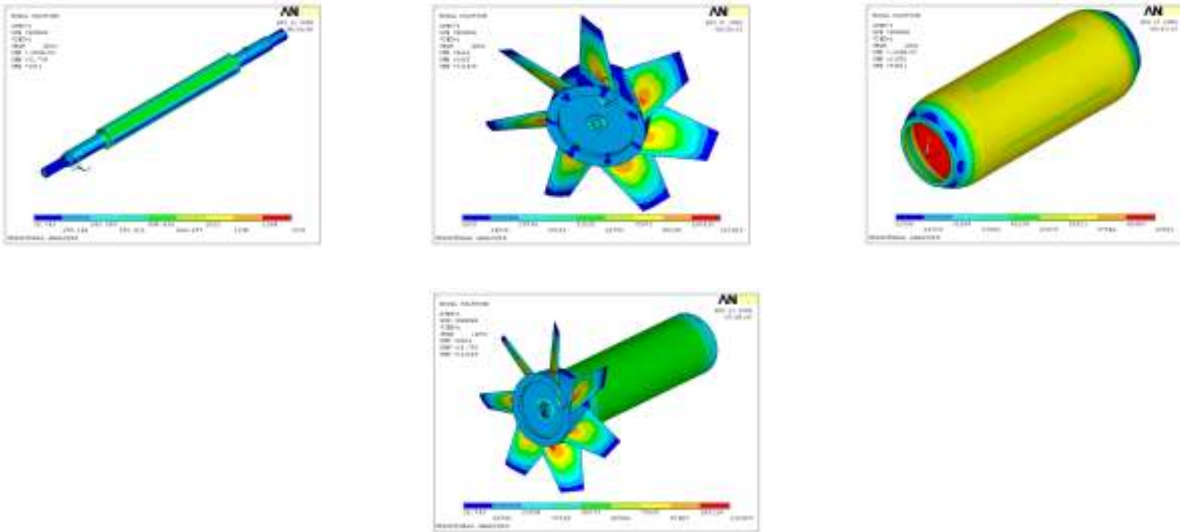

Figure 12. Static stress analysis of system parts and system at rotational speed (2000) rpm.

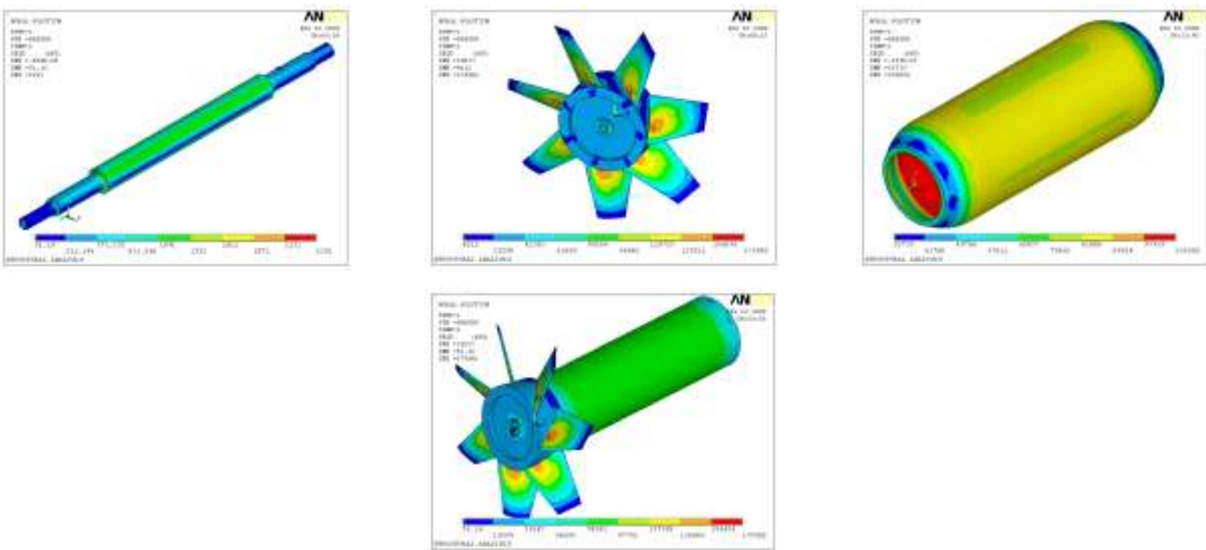

Figure 13. Static stress analysis of system parts and system at rotational speed (2500) rpm.

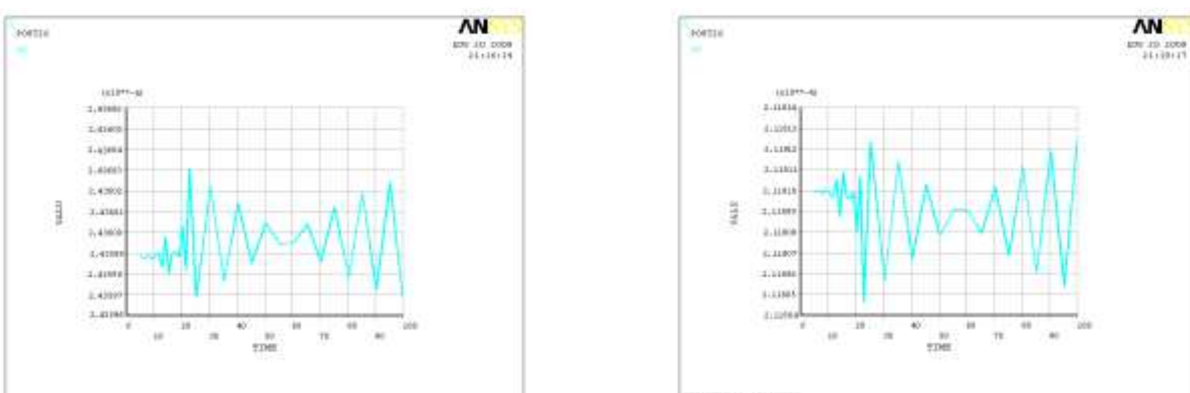

Figure 14. Non-synchronous vibration amplitude for a rotor system in X and Y-directions at (500) rpm.

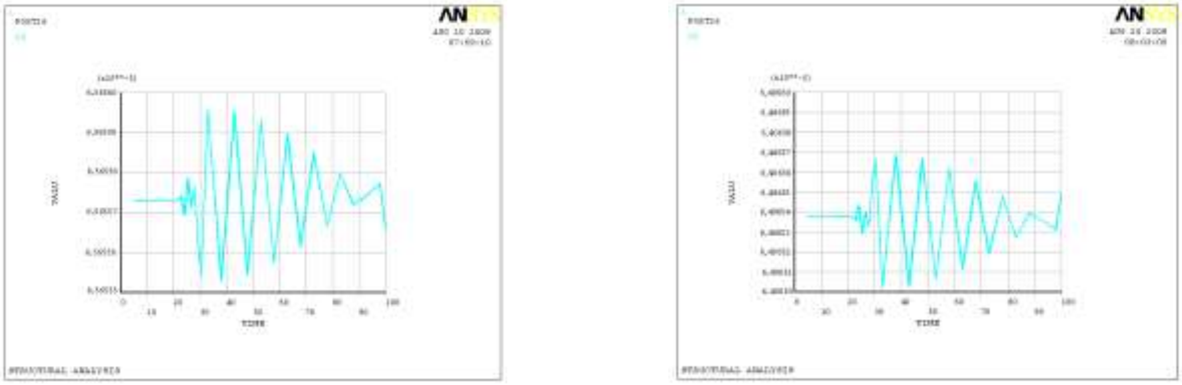

Figure 15. Non-synchronous vibration amplitude for a rotor system in X and Y-directions at (1000) rpm.

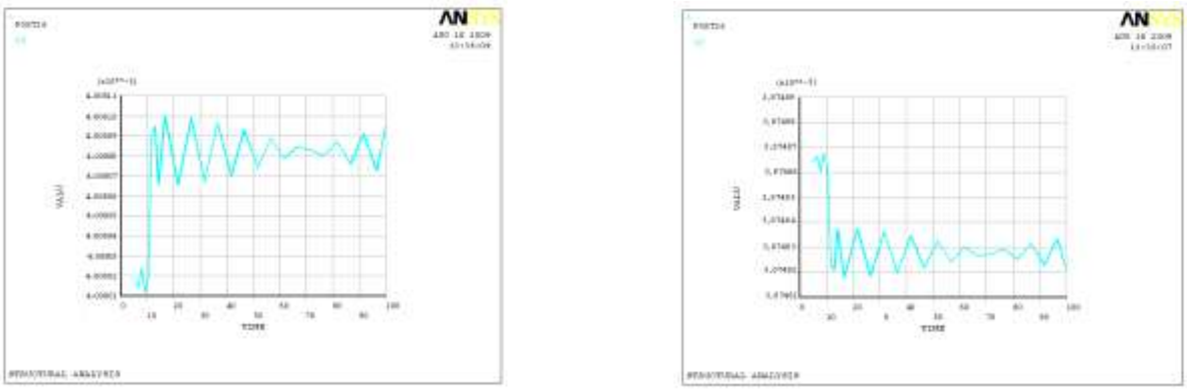

Figure 16. Non-synchronous vibration amplitude for a rotor system in X and Y-directions at (1500) rpm.

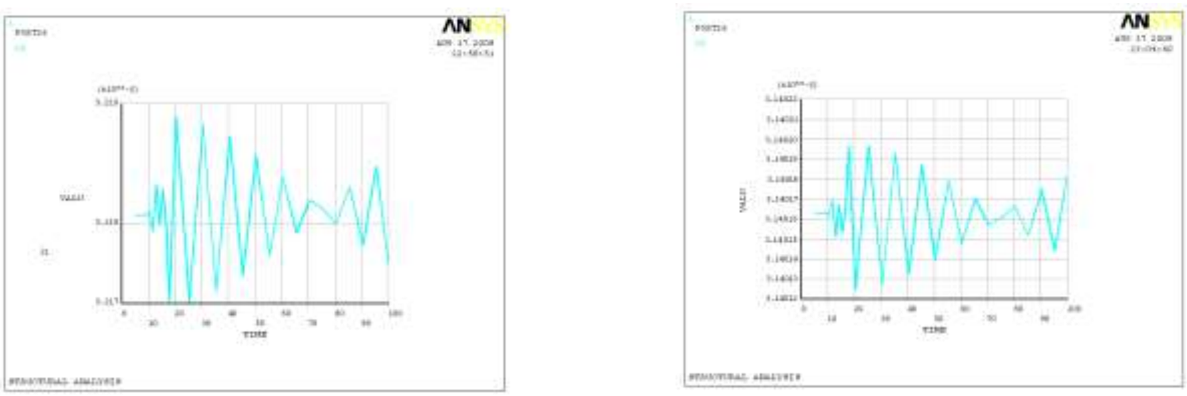

Figure 17. Non-synchronous vibration amplitude for a rotor system in X and Y-directions at (2000) rpm.

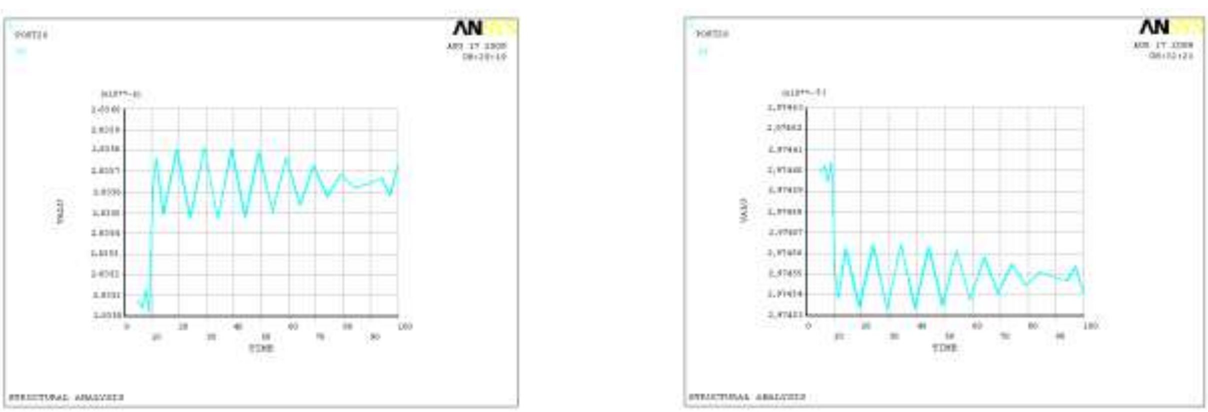

Figure 18. Non-synchronous vibration amplitude for a rotor system in X and Y-directions at (2500) rpm.

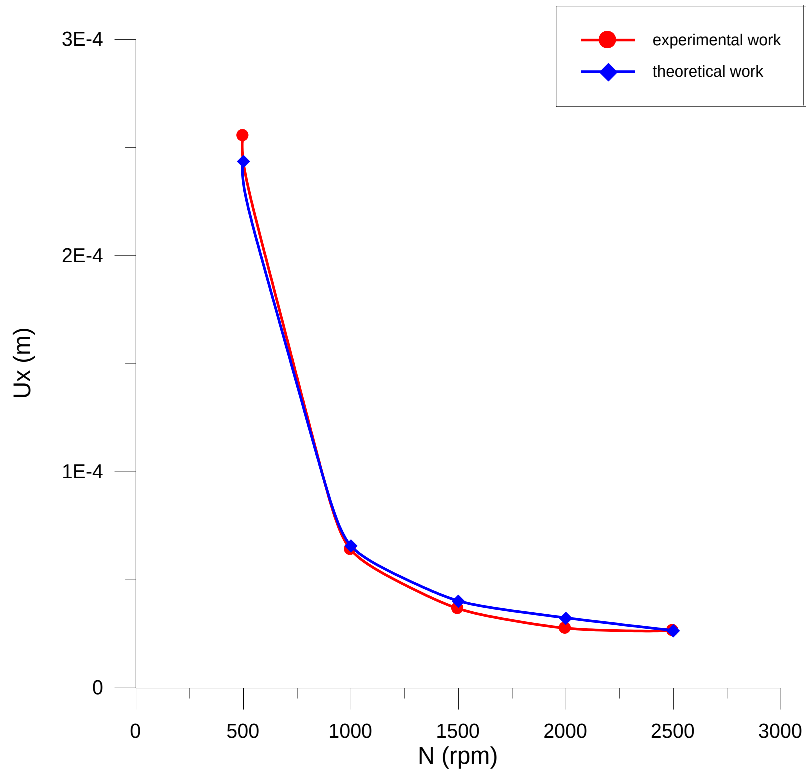

Figure 19. Experimental and theoretical amplitude in X-direction.

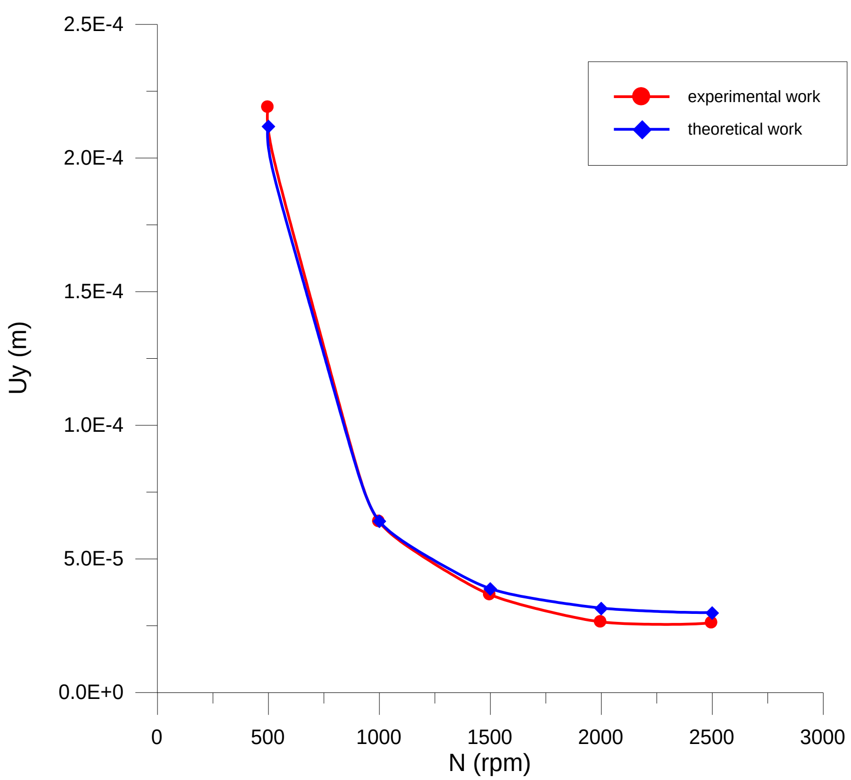

Figure 20. Experimental and theoretical amplitude in Y-direction.

Experimental Study on the Effect of Using Metallic Brushes on the Charging and Discharging Time of Thermal Energy Storage Unit

Asst. Prof. Dr. Rafa Abbas Hassan
Mechanical Engineering Department
College of Engineering
University of Al Mustansiriyah
Email:Rafa_a70@yahoo.com

Lecturer. Dr. Aseel Khaleel Shyaa
Mechanical Engineering Department
College of Engineering
University of Al Mustansiriyah
Email:aseelkhshyaa@yahoo.com

Ban Mohammed Hasan Kadim
Mechanical Engineering Department
College of Engineering
University of Al Mustansiriyah
Email:b.hammendy@yahoo.com

ABSTRACT

Phase change materials are known to be good in use in latent heat thermal energy storage (LHTES) systems, but one of their drawbacks is the slow melting and solidification processes. So that, in this work, enhancing heat transfer of phase change material is studied experimentally for in charging and discharging processes by the addition of high thermal conductive material such as copper in the form of brushes, which were added in both PCM and air sides. The additions of brushes have been carried out with different void fractions (97%, 94% and 90%) and the effect of four different air velocities was tested. The results indicate that the minimum brush void fraction gave the maximum heat transfer in PCM and reduced the time for melting for (ϵ=90%) up to 4.49 times as compare with the case of no brush. It can be seen that the addition of brushes in air side helped to reduce the solidification time and increase the convection heat transfer coefficient as the brush void fraction decreased. Also the minimum velocity (v = 1 m/s) gave maximum outlet temperature.

Keywords: Thermal storage, Phase change materials, Latent heat thermal energy storage and heat transfer enhancement.

دراسة عملية على تأثير استخدام فرش معدنية على المادة المتغيرة الطور الخازنة للطاقة

أ.م.د. رافع عباس حسن
قسم الهندسة الميكانيكية
كلية الهندسة/الجامعة المستنصرية

م.د. اسيل خليل شياع
قسم الهندسة الميكانيكية
كلية الهندسة/الجامعة المستنصرية

بان محمد حسن كاظم
قسم الهندسة الميكانيكية
كلية الهندسة/الجامعة المستنصرية

الخلاصة

المواد المتغيرة الطور تعد من المواد الجيدة المستخدمة في منظومات خزن الطاقة الحرارية الكامنة, ولكن احد عيوبها هو الانصهاروالانجماد ببطء. في العمل الحالي تم دراسة تحسين انتقال الحرارة للمواد المتغيرة الطور خلال عملية الشحن والتفريغ عملياً وذلك بأضافة مادة لها موصلية حرارية عالية مثل النحاس والذي سوف يكون بشكل فرش, وهذه الفرش سوف تضاف في جانب المادة المتغيرة الطور وجانب الهواء. تمت اضافة الفرش بنسب فراغ (97%, 94% و 90%) مع اختبار تأثير اربع سرع مختلفة. وقد بينت النتائج ان اقل نسبة فراغ للفرشاة اعطى اكبر زيادة في نسبة انتقال الحرارة في المادة المتغيرة الطور بحيث قل الزمن اللازم للانصهار لحالة (ϵ = 90%) الى 4.49 مرة بالمقارنة مع حالة عدم وجود الفرشاة. وقد لوحظ ايضاً ان اضافة الفرش في جزء الهواء ساعد في تقليل الزمن اللازم للانجماد وكذلك زادت من معامل انتقال الحرارة بواسطة الحمل بنقصان النسبة الفراغية للفرشاة. وكذلك وجد ان اقل سرعة مستخدمة اعطت اكبر حرارة للهواء الخارج.

الكلمات الرئيسية: الخزن الحراري, مواد متغيرة الطور, خزن الطاقة الحرارية الكامنة و تحسين انتقال الحرارة.

1. INTRODUCTION

Solar energy is one of the most important types of renewable energy because it is one of the cleanest energy and has no impurities into the environment, also it is infinite. Thermal energy storage systems (TESS) are one type of renewable energy systems in which they were developed to use the solar energy in night or in case of dust or clouds. TESS is of critical importance in many engineering applications. The demand for CO_2 reduction to curb global warming considerably increases the interest in utilizing renewable energy sources, especially solar energy **Zhao, et al., 2010**. TESS is one of the most important applications of phase change materials (PCMs). They can be applied conveniently in many fields such as peak shift of electrical demands, solar energy utilization, waste heat recovery, intelligent air-conditioned buildings, and temperature controlled greenhouses, electrical appliances with thermostatic regulators, energy storage kitchen utensils, insulation clothing and season storage **Molefi, 2008.** They can be classified into three main categories according to different storage mechanisms: sensible heat storage, latent heat storage and chemical heat storage. To date most of the studies conducted on storage materials have concentrated on sensible and latent heat storage systems. Studies conducted to compare phase change and sensible heat storages have shown that a significant reduction in storage volume can be achieved using PCM compared to sensible heat storage **Tian**, **2012.**

There are mainly three types of PCMs existing in the solid-liquid category: organic-PCM, inorganic-PCM and eutectic-PCM. In order to be utilized for real applications, PCMs need to meet the thermal, physical, kinetic, chemical and economical requirements **Sunliang, 2010.** Materials to be used for phase change thermal energy storage must have high latent heat of fusion and high thermal conductivity. They should also have a melting temperature lying in a practical range of operation, melt uniformly, chemically inert, low cost, non toxic and non corrosive. As paraffin wax possesses most of these properties it attracts considerable attention as a PCM. However, paraffin waxes have inherently low thermal conductivity and so it takes considerable time to melt and solidify, which reduces the overall power of the thermal storage device and thereby restrict their application **Vadwala, 2011.**

Most PCMs have low thermal conductivity, which led to slow melting and solidification. Different studies have been done to enhance heat transfer in PCMs which include, for example, the addition of water bubbles **Velraj, et al., 1999**, carbon fiber brushes **Fukai, et al., 2002**, longitudinal fins **Castell, et al. , 2006**, metallic powder **Bellah,** and **Ghazy**, **2007,** graphite **Zhang, et al., 2011,** metal foam **Vadwala, 2011**, nanofibers **Sanusi, et al., 2011**and metallic particles **Hasan, 2013**.

Velraj, et al., 1999, investigated three methods of enhancing the heat transfer rate of paraffin wax encapsulated in a cylindrical aluminum tube using internal longitudinal aluminum fins, steel Lessing rings and water bubbles. It found that the best enhancement method was by using of Lessing rings (20% by volume) in which they decrease the freezing time by a factor of 9, and increase thermal conductivity about 10 times than pure paraffin. Also the finned tube with a volume fraction of 7% decrease the solidification time to about 4 times of that of no fins. **Fukai, et al., 2002**, improved the heat transfer rate during the charge and discharge processes by making use carbon fiber brushes combined with n-octadecane. Carbon fiber improves the thermal conductivities of phase-change materials packed around heat transfer tubes. The thermal conductivity increased as the volume fraction and diameter of fibers increased. It was found that the use of brushes improved the charging and discharging rate to about 20% and 30%, respectively, higher than that using no fibers. **Castell, et al., 2006**, study the effect of using longitudinal vertical fins inside a cylindrical water tank which contain cylindrical PCM modules. The experiments were done with three different cases, without fins, with fins of 20mm height and with fins of 40 mm height. It was found that the use of these fins should increase the heat transfer coefficient up to 3 times larger than the ones without fins. Also, they reduced the time which was required for solidification of PCM to about 23.53% and 58.82% for the cases of 20 mm and 40 mm height respectively. **Bellah,** and **Ghazy**, **2007**, made use of 80 μm aluminum powder with PCM in a solar collector. It was found that the addition of 0.5 mass fraction of powder decrease the charging time up to 60% as compare with the case of pure paraffin. **Zhang, et al., 2011**, tried to improve the thermal conductivity of paraffin by using expanded graphite with 7% mass fraction. The results show that the graphite/paraffin composite PCM made 44% reduction in heat storage duration and 69% reduction in the retrieval duration, respectively, as compared with the pure paraffin. **Vadwala, 2011**, placed copper foam (85% porosity) in a rectangular TESS for both PCM (paraffin wax) and air sides. The results show that the thermal conductivity of PCM was increased to about 18 times that of pure paraffin. The time required to melt the same quantity of wax was reduced to 36% of that without foam. Also it was found that the addition of metal foam in the air side decreases solidification time. **Sanusi, et al., 2011,** study experimentally the effect of graphite nanofibers on thermal storage and the solidification time with different aspect ratios. It was found that the addition of these fibers reduce the maximum temperature in the thermal containment unit up to 48%. Also the results showed a reduction in the solidification time up to 61% for the case of 1 aspect ratio. **Hasan, 2013**, made a Comparison between Different Composite PCMs encapsulated for TESS. The thermal conductivity of paraffin had been enhanced by using four different additives which were graphite powder, copper particles, aluminum oxide particles and copper network. The mass ratios of the additives were 3%, 6% and 9%. It was found that copper network with 6% mass ratio gave best enhancement which reduce the time for charging and discharging by 26.4% and 30.3% respectively as compared with pure paraffin. Also thermal conductivity of PCM enhanced by2.57 times than pure paraffin.

The objective of this work is to study experimentally the enhancement of charging and discharging processes by using copper brushes embedded in both PCM and air sides with different void fractions. The effect of air velocity was also observed.

2. EXPERIMENTAL TEST

2.1 Experimental Setup

A small scale thermal energy storage device is fabricated, both with and without copper brush. A paraffin wax grade B (melting temperature equal to 63.7˚C, k= o.214 W/m.˚C) was employed as heat storage media. The experimental setup is shown schematically in **Fig. 1**. It consists of entry section, test section, exit section and transition section. The length of each section is about 1070 mm, 300 mm, 390 mm and 380 mm, respectively. A transition section connects between the entry section and a fan with specification of (0.27 A, 61 W, 3100 rpm). The dimension of the test section was 300 mm × 90 mm × 86 mm (L × W × H). The height of the air side and PCM side were 42 mm and 32 mm, respectively. A Perspex sheet with 9 mm thickness was used to form the test section. A copper plate (2.5 mm thick) is used to separate each side & was placed in two slots (3 mm thick) opposing each other. Other opposing slots of the same thickness of the former ones were in the upper part of the PCM side and another copper plate was placed inside it. In the upper side of this plate, a tape heater (150 W, 260 V) with dimensions of 280 mm× 65 mm, was fixed over it. To ensure good contact between the heater and the copper plate, a heat-conductive paste was used. For each copper plate, a thermocouple type K had been fixed in the middle of them. Other five thermocouples type K were distributed approximately in the center of PCM side with 10 mm distance between adjacent thermocouple. The top thermocouple should be connected to the process controller which works to control the heater to give a constant temperature of 100°c for the upper plate, so that it should be an input to it.

Six thermocouples type K had been distributed in the air passage, one in the entrance, one in the exit and the others are distributed along the centre plane of the air side with equal spaces between them (70 mm spaces). A data logger device (model: BTM-4208SD, Lutron electronic enterprise company) is used to record the data. Fiberglass insulation (12.7 mm thick) with an aluminized outer surface had been used to insulate the test section. The air velocity of 1, 2, 2.5 and 3 m/s is produced by a fan which was controlled by a fan controller by changing the voltages entering to it. These velocities had been measured by a hot wire anemometer (model: YK-2005AH, Lutron electronic enterprise company) fixed in the entrance of the test section.

Two copper brushes had been placed in PCM side which had a diameter equal to the height of the PCM container. So that, each wall was in contact with brushes copper wires. Other two brushes were placed in the air side, and also they had a diameter equal to the air side height. The length of all brushes is equal to the test section length. In each side the tests should be done with three different void fraction 97%, 94% and 90%. The void fraction of each brush had been calculated using standard test method (ASTM C 127). The brushes are weighted with gram unit in air and then in water to get there densities in air and water and then calculate void fraction (ϵ) using Eq. (3). The following equations are using for that purpose:

$$\rho_a = \frac{m_a}{V_b}$$

$$\rho_w = \frac{m_a}{m_a - m_w}$$

$$\epsilon = \frac{\rho_w - \rho_a}{\rho_w}$$

Where;

m_a = mass of weighted material in air, (g).
m_w = mass of weighted material in water, (g).
V_b = bulk volume of used material, (cm^3).
ρ_b = bulk material density, (g/cm^3).
ρ_w = density of material in water, (g/cm^3).
ϵ = void fraction, (%).

Because of the high thermal conductivity of the copper wires (k= 385 W/m.˚C), the PCM brushes work to enhance thermal conductivity and reduce the time for paraffin wax melting. Also the addition of brushes in air side work to decrease the time of solidification.

2.2 Experimental Procedure

Several experimental tests were done with different cases. First of all, the molten paraffin wax was poured into the test rig. After its solidification, a gap of air would be appear in the upper part of the test section because of the decrease in volume of PCM due to differences in solid and liquid densities. After the fixation of the whole TESS, the melting and solidification tests (without brush) should be done for different velocities. A process controller was setup to control the heater to provide constant temperature (100°C) to the top copper plate. The melting time starts from the time the heater turned on, till the lower copper plate reaches a temperature of 63.7◦c. after the heater turned off, the fan turned on and the solidification process starts. The fan was controlled via a fan controller to get the required velocities. This process ended until the whole wax reached its starts temperature. So that, as the charging time is over, the discharging time begins.

The previous processes should be repeated but with the addition of copper brushes in both air and wax sides. Also, the tests should be done with different void fractions (97%, 94% and 90%) to show the effect of the void fraction in charging and discharging processes. **Fig.2** shows these brushes and their position.

3. EXPERIMENTAL DATA REDUCTION

3.1 PCM Side

3.1.1 Latent heat storage

The heat storage in PCM side is in the form of latent heat. The storage capacity can be found from:

$$Q = \int_{T_1}^{T_m} m \, . \, Cp_s \, .dT + m \, . \, a_m \, . \, \Delta \, h_m + \int_{T_m}^{T_2} m \, . \, Cp_l \, . \, Dt$$

$$= m \, [\, Cp_s \, (T_m - T_1) + a_m \, . \, . \, \Delta \, h_m + Cp_l \, (T_2 - T_m)] \qquad (1)$$

Where;

T_m = melting temperature of the storage material, ˚C.
T_1 = initial temperature of the storage material, ˚C.
T_2 = final temperature of the storage material, ˚C.
m = mass, kg.
Cp_l = average specific heat between T_m and T_2, J/kg.˚C.
Cp_s = average specific heat between T_1 and T_m, J/kg.˚C.
a_m = the fraction melted.
$\Delta \, h_m$ = heat of fusion, J/kg.

It can be seen that the second term represents the period in which phase change occurs during it, which means that it is the period for transformation from solid to liquid and vice versa. Conduction heat transfer: The heat transfer inside the PCM occurs due to conduction between its particles. The conduction occurs from the upper surface of PCM to the lower surface of PCM. The following equation represents Fourier's law for heat conduction:

$$Q = k \, A \, \Delta T / \Delta x \qquad (2)$$

Where;

Q = power extracted, W.
A = area, m^2.
ΔT = temperature difference between the upper and lower point of PCM, ˚C.
Δx = distance between the upper and the lower point of PCM, m.

3.2 Air Side

The following procedure was used to calculate mass flow rate, Nusselt number, Reynold number, convection heat transfer coefficient and power extracted. The experimental data includes the measured velocities and thermocouples readings. The air thermo physical properties were taken at bulk mean air temperature;

$$T_b = \frac{Ti+To}{2} \tag{3}$$

Where;

T_b = bulk temperature of air, ˚C.
T_i = inlet air temperature, ˚C.
T_o = outlet air temperature, ˚C.

3.2.1 Mass flow rate

Mass flow rate can be calculated using the following relation;

$$m = \rho\ v\ A_c \tag{4}$$

Where;

v = velocity, m/s.
A_c = crosses sectional area, m^2.

3.2.2 Rate of heat transfer

Value of heat transfer between the hot surface and the moving air can be calculated experimentally from;

$$Q = m\ Cp\ (T_o\text{-}T_i) \tag{5}$$

3.2.3 Convection heat transfer coefficient measurement

Convection occurs between the hot copper plate and the air flow beneath it. It was considered to be constant along the duct length. So that it is given by;

$$h = \frac{Q}{As(\boldsymbol{T_s}-\boldsymbol{T_b})} \tag{6}$$

Where;

T_s = surface temperature, ˚C.
A_s = surface area, m^2.

3.2.4 Reynolds number

It is calculated from;

$$Re = \frac{\rho v \boldsymbol{D_H}}{\mu} \tag{7}$$

Where;

Re = Reynolds number.
μ = dynamic viscosity, kg/m.s.

In which D_H is the hydraulic diameter and can be calculated from;

$$D_H = \frac{2WH}{4(W+H)} \tag{8}$$

Where;

W = width, mm.
H = height, mm.

3.2.5 Nusselt number

It can be calculated using the following equation;

$$Nu = \frac{hD_H}{k} \tag{9}$$

4. RESULTS AND DISCUSSION

This work investigates the effect of copper brush on the melting and solidification time of an organic PCM (paraffin wax grade B). **Fig. 3** shows the lower copper plate temperature variation with time for four cases, without brush, with brush (ϵ=97%), with brush (ϵ=94%) and with brush (ϵ=90%). The time for melting was decreased up to 2.67, 3.71, 4.49 times, respectively, as compare with the pure paraffin case, which means that the heat transfer was enhanced.

Fig. 4 shows the behavior of middle point temperature of PCM in melting and solidification process. It can be seen that the melting and solidification time was decrease in the addition of metal brush as compared with pure paraffin, where the lower void fraction, the lower time for melting and solidification. The copper brushes reduced the solidification time of paraffin up to 1.47, 1.55 and 1.64 when they add in both sides with 3%, 6% and 10% volume percent, respectively, as compared with pure paraffin case.

It can be seen from **Fig. 5** the temperature distribution of five points distributed along PCM in case of brushes with 90% void fraction during melting process. The middle point was melted faster than other points because it was the furthest point from the walls. Also the lower point takes longer time to melt due to its distance to the upper copper plate.

Fig. 6 presents that the lower void fraction of brush in air side gave the maximum outlet temperature. This was due to the increase in contact between the upper copper plate and the brush wires which cause an increase in heat transfer from copper plate and brush to the air flow over them. So that, the decrease in void fraction cause an increase in turbulent which helps to increase the heat exchange between them. The amount of increase in outlet temperature for (ϵ= 97%, 94% and 90%) as compared with the case of no brush were 8.75, 10.32 and 11.99 ˚C, respectively with 2.5 m/s air velocity, in which these values are taken as hourly temperature.

The outlet air temperature vs. time was shown in **Fig. 7** during solidification process with four different velocities in case of brushes (ϵ=90%) in both wax and air side. As compared with the case of no brushes in both sides, it can be seen that the maximum temperature difference reach up to (21.85˚C) occurred in case of minimum void fraction (90%) and minimum velocity (v=1 m/s). That is because at low velocity (v=1 m/s) air will has enough time to acquire heat and make heat exchange with the lower copper plate. While at maximum velocity (v=3 m/s) air will be pass beneath the lower plat quickly.

Also, the higher the velocity, the minimum the outlet temperature and the maximum the temperature gradient. The results show that the decrease in void fraction of brushes in air side cause an increase in Nusselt numbers due to a significant increase in outlet air temperature which resulted in higher Nusselt number for the three void fractions (97%, 94%90%). This increase, as shown in Fig. 8, was up to 2.83, 3.69 and 4.23 times, respectively, as compared with the case of no brush. Fig. 9, 10, shows the relation between velocities with power extracted and convection heat transfer coefficient with different brushes void fractions. As in Nusselt numbers, for lower void fraction, higher power and convection heat transfer coefficient are obtained. The amounts of increase in power for (ϵ=97%, 94%, 90%) were 2.24, 2.49 and 2.83 times, respectively, and 2.9, 3.79 and 4.34 times, respectively, for h as compared with the case of no brush. The results in **Figs. 8, 9** and **10** were taken as an average values for hourly temperature.

5. CONCLUSION

In this work, the thermal conductivity of wax and heat transfer coefficient of flowing air was enhanced by using copper brushes. The enhancement process done to reduce the time for melting and solidification by the addition of brushes in wax and air sides, the following conclusions can be extracted:

The addition of brushes in PCM side reduce the time for melting for (ϵ=90%) by 4.46 times as compare with the case of no brushes. It can be seen that, for lower void fraction, minimum melting time is obtained. The addition of brushes in air side worked to enhance the discharging process, and also reduce the time required for solidification. Lowest void fraction in air side decreases the solidification time and increases the outlet air temperature. The maximum temperature difference reached up to 21.85˚C which occurred in case of minimum void fraction and minimum velocity. The obtained results show that minimum velocity gave maximum outlet temperature. But maximum velocities increased the heat transfer rate especially in the initial period which resulted in minimum time required for freezing. Also, at minimum void fraction and maximum velocity, higher Nu, h and Q for air can be observed. This is because of increase in turbulence which causes an increment in heat transfer rate.

REFERENCES

- Bellah, E., and Ghazy, A., 2007, *Thermal Conductivity Enhancement in Latent Heat Storage System*, Solar Energy, Vol. 81, 839–845.

- Castell, A., Solé, C., Medrano, M., Roca, J., García, D.,and Cabeza, L., F., 2006, *Effect of Using External Vertical Fins in Phase Change Material Modules for Domestic Hot Water Tanks*.

- Fukai, J., Hamada, Y., Morozumi, Y., and Miyatake, O., 2002 , *Effect of Carbon Fiber Brushes on Conductive Heat Transfer in Phase Change Materials*, International Journal of Heat and Mass Transfer, Vol. 45, 4781-4792.

- Hasan, A. H., 2013, *Comparison Between Different Composite Phase Change Materials for Latent Heat Encapsulated Thermal Energy Storage*, M.Sc Thesis, University of Al Mustansiriyah.

- Molefi, J. A., 2008, *Investigation of Phase Change Conducting Materials Prepared from Polyethylenes, Paraffin Waxes and Copper*, PhD thesis, university of the free state.
- Sanusi, O., Warzoha, R., and Fleischer, A. S., 2011, *Energy Storage and Solidification of Paraffin Phase Change Material Embedded with Graphite Nanofibers*, International Journal of Heat and Mass Transfer, 54 4429–4436.
- Sunliang, C., 2010, *State of the Art Thermal Energy Storage Solutions for High Performance Buildings*, M.Sc Thesis, University of Jyväskylä, Finland.
- Tian, Y., 2012, *Heat Transfer Enhancement in Phase Change Materials (PCMs) by Metal Foams and Cascaded Thermal Energy Storage*, PhD Thesis, University of Warwick.
- Vadwala, P. H., 2011, *Thermal Energy Storage in Copper Foams Filled with Paraffin Wax*, Msc Thesis, University of Toronto.
- Velraj, R., Seeniraj, R. V., Hafner, B., Faber, C., and Schwarzer, K., 1999, *Heat Transfer Enhancement in a Latent Heat Storage System,* Solar Energy, 65(3), pp. 171- 180.
- Zhang, P., Xia, L., and Wang, R. Z., 2011, *the Thermal Response of Heat Storage System with Paraffin and Paraffin/Expanded Graphite Composite for Hot Water Supply*, World Renewable Energy Congress.
- Zhao, C. Y., Lu, W., and Tian, Y., 2010, *Heat Transfer Enhancement for Thermal Energy Storage Using Metal Foams Embedded within Phase Change Materials (PCMs),* Solar Energy , 84(8), pp. 1402-1412.

NOMENCLATURE

a_m = the fraction melted**.**
A_c = crosses sectional area, m^2.
A_s = surface area, m^2**.**
Cp = specific heat of air, J/kg.˚C.
Cp_l = average specific heat between T_m and T_2, J/kg.˚C.
Cp_s = average specific heat between T_1 and T_m, J/kg.˚C.
D_H = hydraulic diameter, m.
h = convection heat transfer coefficient, W/m^2.˚C.
Δh_m = heat of fusion, J/kg.
H = height, mm.
K = thermal conductivity, W/m.˚C.
L = length, mm.
m = mass, kg.
m_a = mass of weighted material in air, (g).
m_w = mass of weighted material in water, (g).
Nu = Nusselt number, dimensionless.
Q = power extracted, W.
Re = Reynolds number.

t = time, minute.
T = temperature, ˚C.
ΔT = temperature difference between the upper and lower point of PCM, ˚C .
T_b = bulk temperature of air, ˚C.
TC = thermocouple.
T_i = inlet air temperature, ˚C.
T_m = melting temperature of the storage material, ˚C.
T_{mid} = middle temperature of the storage material, ˚C.
T_o = outlet air temperature, ˚C.
T_s = surface temperature, ˚C.
T_1 = initial temperature of the storage material, ˚C.
T_2 = final temperature of the storage material, ˚C.
v = velocity, m/s.
V_b = bulk volume of used material, (cm^3).
W = width, mm.
Δx = distance between the upper and the lower point of PCM, m.

Greek symbols.

ϵ = void fraction, %.
μ = dynamic viscosity, kg/m.s.
ρ = density, kg/m^3.
ρ_b = bulk material density, (g/cm^3).
ρ_w = density of material in water, (g/cm^3).

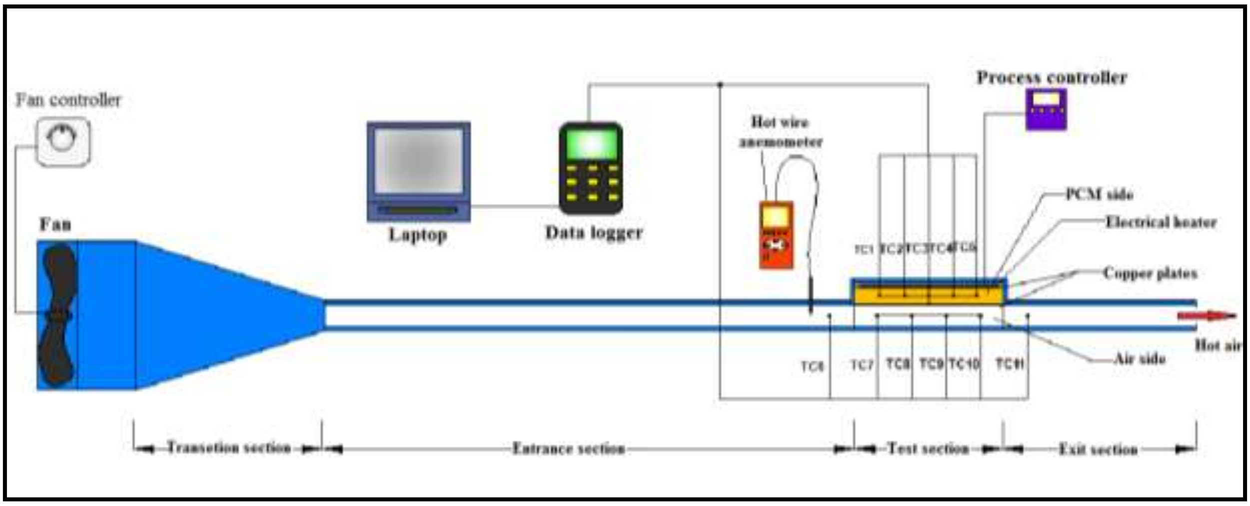

Figure1. Schematic diagram of experimental apparatus.

-a- -b-

Figure 2. a) PCM and air brushes, b) Test section with brushes.

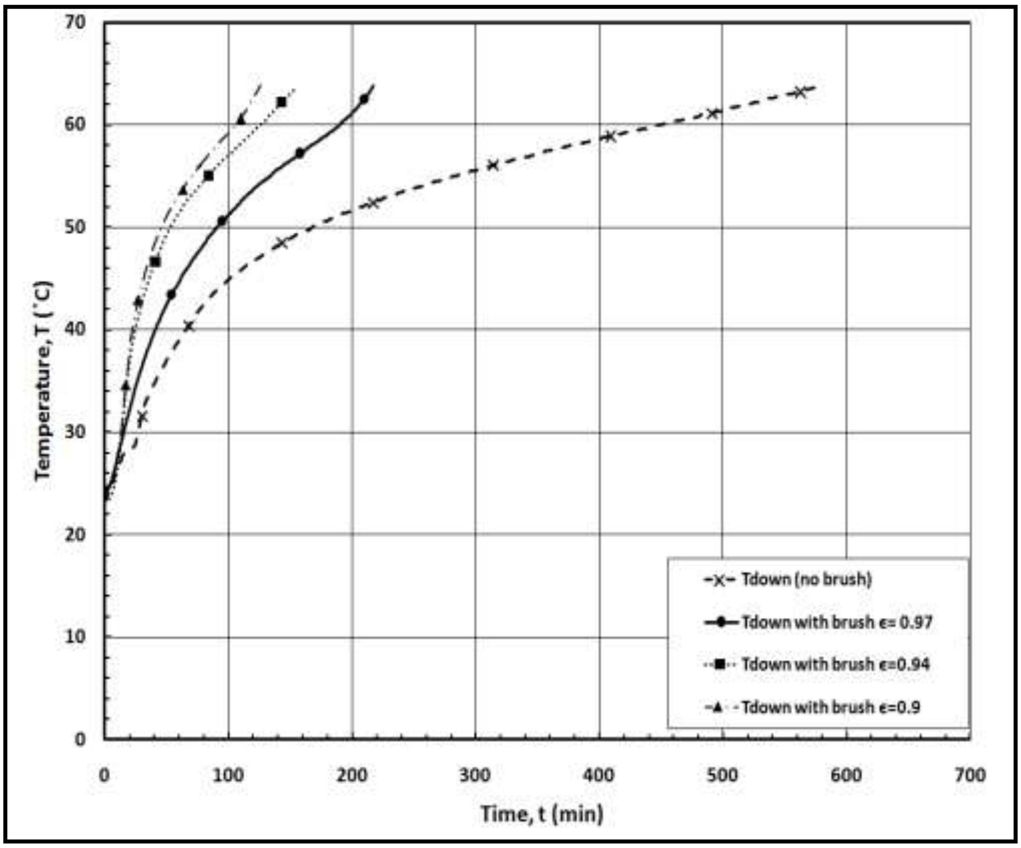

Figure3. Temperature variation of bottom point of paraffin wax vs. time during melting process for the cases of brushes with different void fractions.

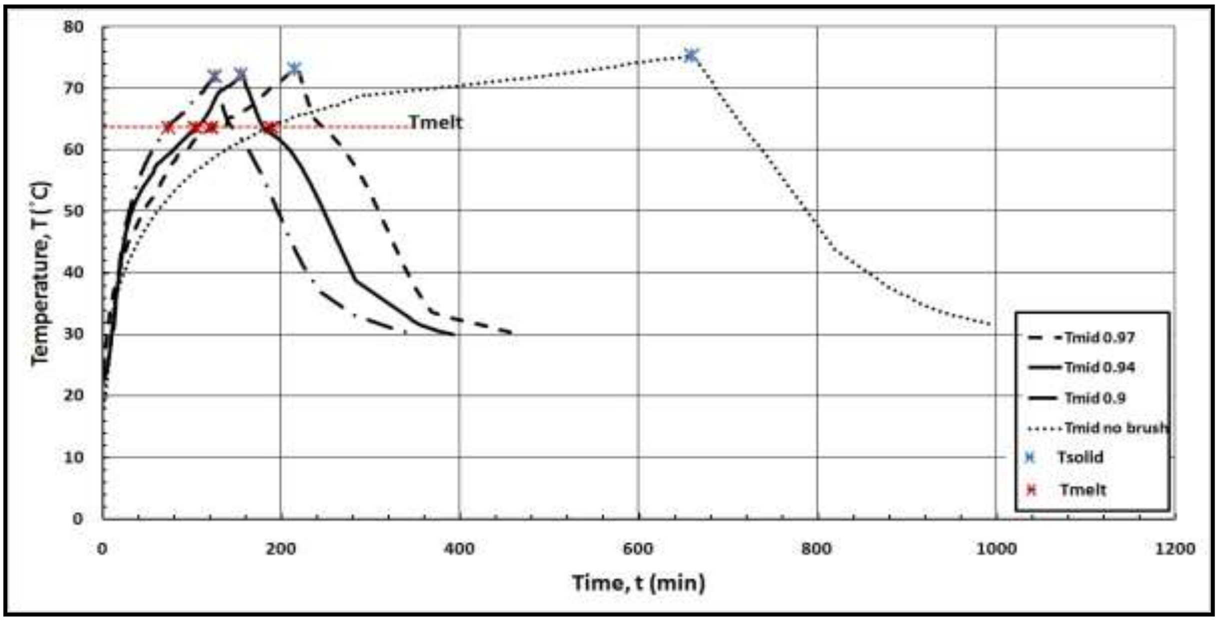

Figure 4. Temperature variation and the melting and solidification point of middle PCM point in charging and discharging processes with and without brushes for different void fractions. The discharging process is conducted for velocity of 2.5 m/s.

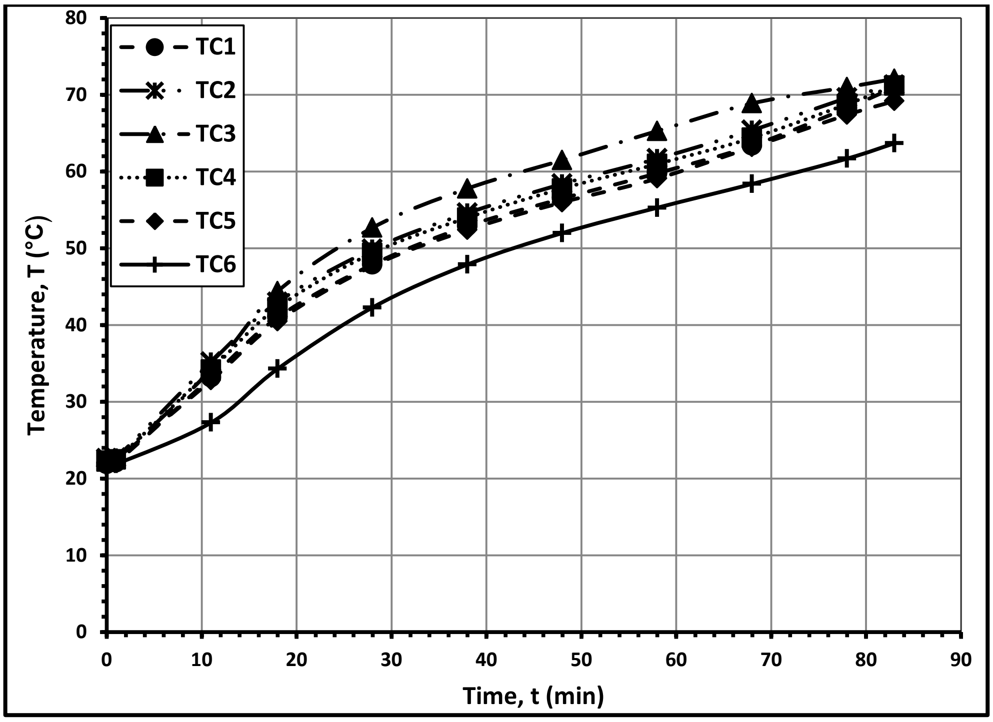

Figure 5. Temperature distribution for different points along the axial center line of PCM during melting process in case of brushes with 90% void fraction.

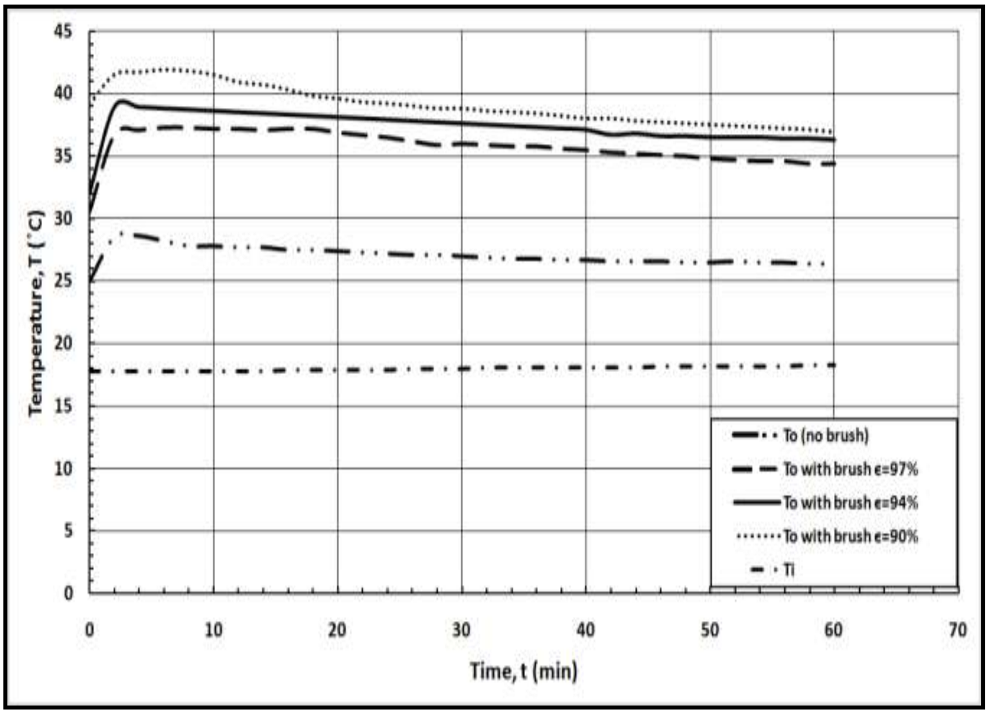

Figure 6. The change in outlet air temperature vs. time in cases of brushes in both wax and air side with three void fractions brushes compared with the case of no brush for an air velocity of 2.5 m/s for an hour.

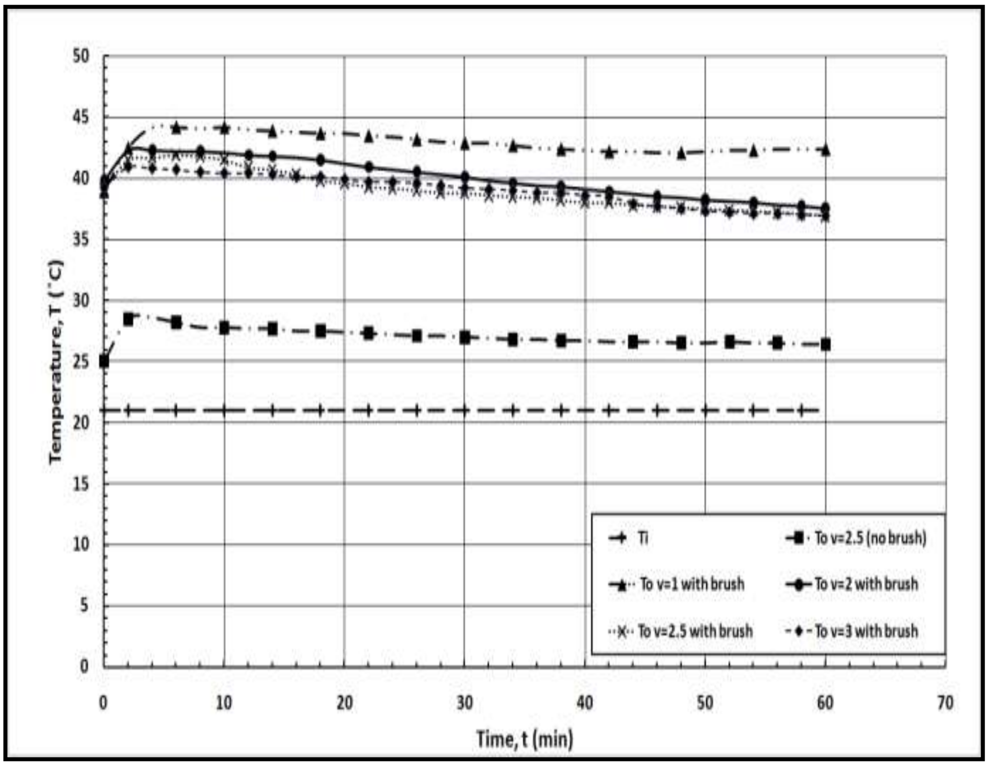

Figure 7. Change with time in outlet air temperature with brushes in both sides for different velocities compared with the case of no brushes for an air velocity of v=2.5 m/s for an hour.

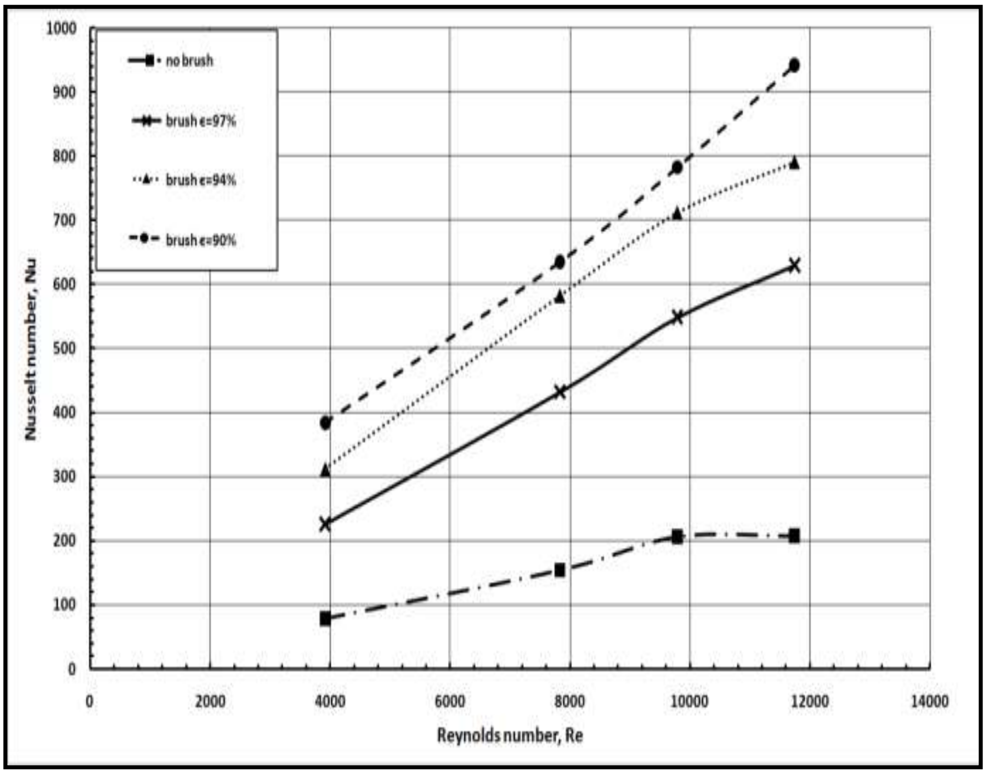

Figure 8. The computed Nusselt numbers with respect to Reynolds number for the cases of different void fractions brushes on both sides compared with the case of no brushes.

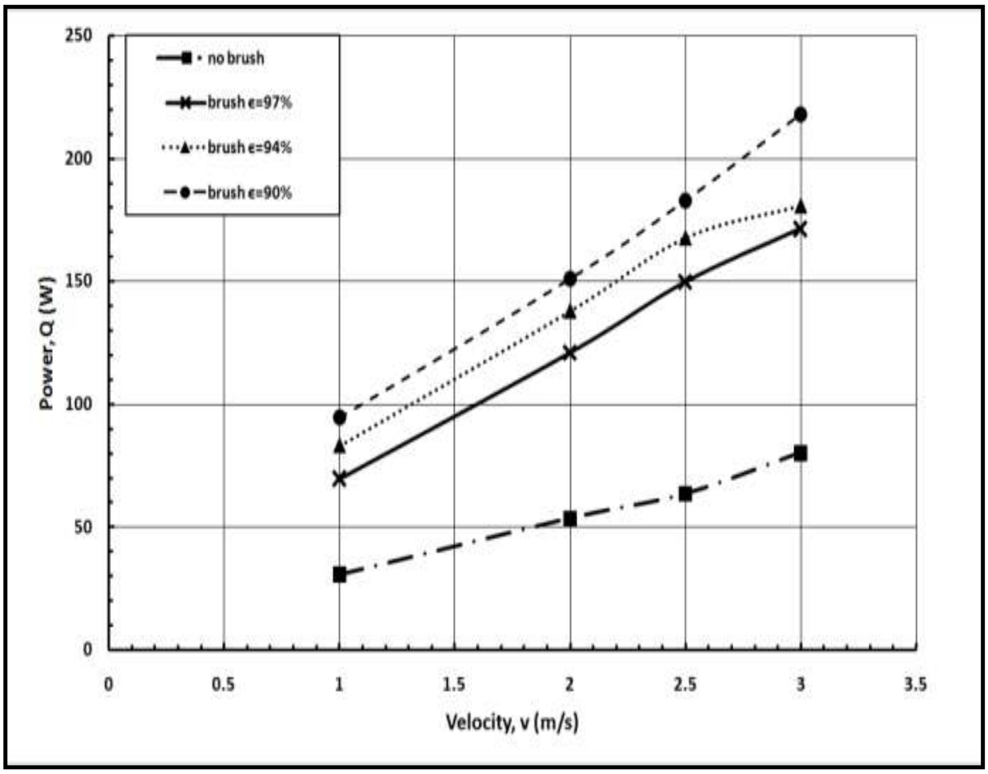

Figure 9. The calculated power extracted vs. velocities for the case of brushes in both sides with different void fractions compared with the case of no brushes.

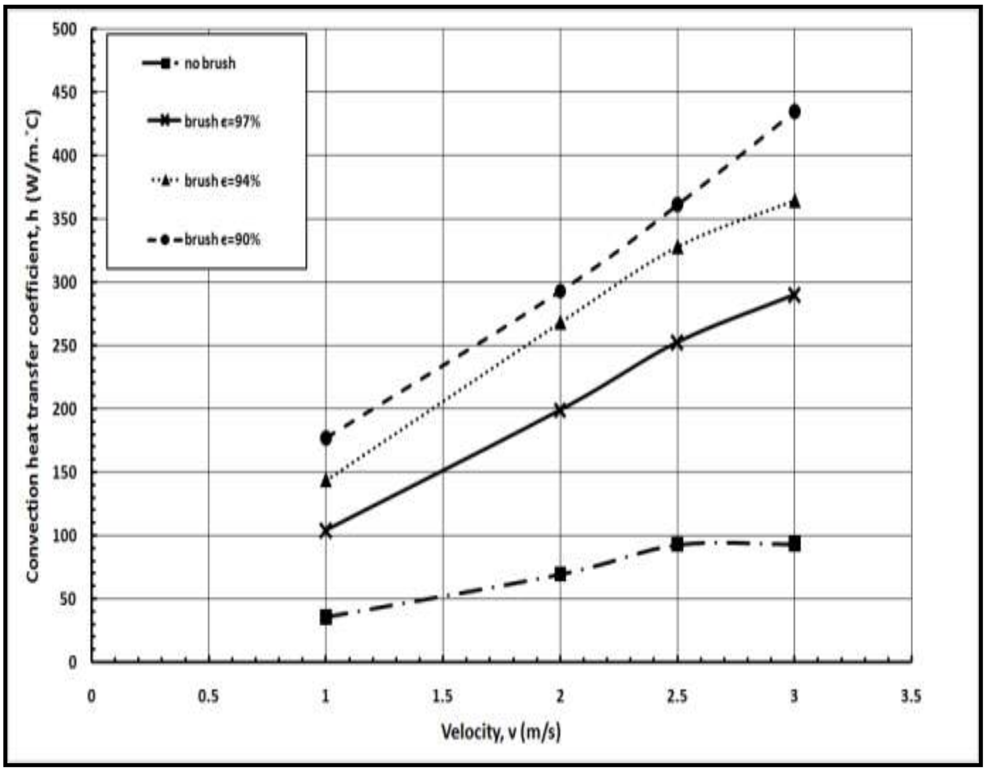

Figure 10. The computed convection heat transfer coefficients vs. velocities for the cases of brushes in both sides with different void fractions compared with the case of no brushes.

Application of Box-Behnken Method Based ANN-GA to Prediction of wt.% of Doping Elements for Incoloy 800H Coated by Aluminizing-Chromizing

Dr.Abbas Khammas Hussein
Assistant Professor
University of Technology ,Department of Materials Engineering
Email: abbas2000x@yahoo.com

ABSTRACT

In this work , an effective procedure of Box-Behnken based-ANN (Artificial Neural Network) and GA (Genetic Algorithm) has been utilized for finding the optimum conditions of wt.% of doping elements (Ce,Y, and Ge) doped-aluminizing-chromizing of Incoloy 800H . ANN and Box-Behnken design method have been implanted for minimizing hot corrosion rate k_p ($10^{-12}g^2.cm^{-4}.s^{-1}$) in Incoloy 800H at 900^{o}C . ANN was used for estimating the predicted values of hot corrosion rate k_p ($10^{-12}g^2.cm^{-4}.s^{-1}$) . The optimal wt.% of doping elements combination to obtain minimum hot corrosion rate was calculated using genetic algorithm approach . The predicted optimal values for minimizing hot corrosion rate for Incoloy 800H coated by (Ce-Y-Ge) doped-aluminizing-chromizing are (3wt.%Ce, 3wt.%Y, and 3wt.%Ge) , the hot corrosion rate k_p ($10^{-12}g^2.cm^{-4}.s^{-1}$) value at these conditions was found to be 71.701 . The results have been verified by confirmation experiment , results obtained by GA method match closely with experimental values (R^2=98.30) . EDS and XRD results show that the formation of protective layers Al_2O_3 and Cr_2O_3 during hot corrosion tests.

Keywords: Box-behnken design, GA, ANN, Hot Corrosion , Pack cementation .

تطبيق طريقة بوكس-بينكن ذات أساس شبكات عصبونية إصطناعية-خوارزمية وراثية للتنبأ بالنسب الوزنية المثالية لعناصر الإضافة لسبيكة Incoloy 800H المغطاة بالالمنة-كرمنة

د.عباس خماس حسين
أستاذ مساعد
الجامعة التكنولوجية،قسم هندسة المواد

الخلاصة

يتضمن هذا البحث إستخدام الإسلوب الفعّال من خلال طريقة بوكس-بينكن ذات أساس شبكات عصبونية إصطناعية-خوارزمية وراثية لتحديد الظروف المثلى للنسب الوزنية لعناصر الإضافة (سيريوم-يتيريوم-جرمانيوم) لعملية الألمنة-كرمنة لسبيكة Incoloy 800H . و أستخدمت كل من طريقة التصميم بوكس-بينكن و الشبكات العصبونية لخفض معدل التآكل الساخن في سبيكة Incoloy 800H عند 900^{o}C ، حيث أستخدمت الشبكات العصبونية للتنبأ بقيم معدل التآكل الساخن ، أما بالنسبة لمزيج النسب الوزنية المثالي لعناصر الإضافة اللازمة للحصول على القيمة الدنيا لمعدل التآكل الساخن فقد تم تحديدها بواسطة الخوارزمية الوراثية . و لوحظ أن القيم المثلى التي تم التنبأ بها لخفض معدل التآكل الساخن لسبيكة Incoloy 800H المغطاة بعناصر الإضافة (سيريوم-يتيريوم-جرمانيوم) لعملية الألمنة-كرمنة هي (3wt.%Ce, 3wt.%Y, and 3wt.%Ge) أما قيمة معدل التآكل الساخن عند هذه الظروف فقد كانت $71.701X10^{-12}g^2.cm^{-4}.s^{-1}$. و قد تم التحقق من هذه الظروف من خلال تجربة التحقق (التأكد) ، و لوحظ أن النتائج التي تم الحصول عليها من خلال طريقة الخوارزمية الوراثية تتطابق بشكل دقيق مع القيم التجريبية (معامل التحديد= 98.30) . و أظهرت نتائج EDX و XRD تكون طبقات الحماية الأوكسيدية Al_2O_3، Cr_2O_3 خلال إختبارات التآكل الساخن .

الكلمات الرئيسية: تصميم وكس بينكن، الجينات الوراثية، الشبكات العصبونية، التاكل الساخن ، تغليف السمنتة .

1.INTRODUCTION

High-temperature oxidation, hot corrosion and erosion are the main failure modes of components in the hot sections of gas turbines, boilers, etc. Incoloy 800H have been developed for high temperature applications . This material finds application in the gas turbine industry, constituting over fifty percent of the gas turbin weight due to their good mechanical properties at high temperatures . In general, hot corrosion increases due to the transport in liquid phase of complex mixtures of molten sodium sulfate which cause catastrophic hot corrosion .,**Lin-Chang Tsai1,et. al., 2015, Fahamsyah H.,et al, 2015, Subhash Kamal, et. al.,2015** . Hot corrosion refers to an accelerated corrosion, resulting from the presence of salt such as (Na_2SO_4), NaCl ,V_2O_5 …ect that combine to form molten deposits, which damage the protective surface oxides . This type of corrosion occurs when metals are subjected to the temperature range 700–900°C in the presence of sulphur deposits formed as a result of the reaction between sodium chloride and sulphur compounds in the presence of gas phase surrounding the metals .The Deposits of (Na_2SO_4) are molten at higher temperatures (m.p. 884°C) and can cause accelerated corrosion on Ni- and Co-based superalloys. This type of corrosion is commonly called ‘hot corrosion’.**, Subhash Kamal, et al., 2010, T. S. Sidhu,et al.,2006** . Coating techniques play a important role in the operation at high temperatures, particularly for hot section parts, which are subjected to complex thermal and mechanical strain/stress cycling. Coatings are applied with a specific aim to improve the base material resistance by provide a barrier against high temperatures., **Marta Kianicova ,et al., 2011, W.H Lee and R.Y Lin ,2003** . Pack cementation using aluminum, chromium or silicon is one of the easiest and cheapest processes to obtain the protective coatings to improve the corrosion resistance at high temperature ., **LIN Nai-ming, et al., 2010, Bruce M., et al., 2001**. The diffusion Coating method is used for surface alloying of protective coatings on the substrate surface, for example aluminizing, siliconizing, chromizing, simultaneousaluminizing-siliconizing,`simultaneous-aluminizing-siliconizing-chromizing and forms a thin oxide scale, which works as the diffusion barrier and reduces the oxidizing speed of the base material. , **A. ESLAMI, et al., 2009, I.M. Edmonds,et al., 2008, H. R. KARIMI ZARCHI,et al., 2013** . High temperature oxidation resistance is usually improved by the addition of some amount of oxygen reactive elements (doping elements) like Y and rare earth elements (REE) Ce, La, Er and others into surface metal. These elements is introduced through surface treatment techniques such as pack cementation. The incorporation *via* surface treatment acts in favour of doping elements concentration at the surface where the oxide will form and thus may have the most benefit, **Chao-Chi Jain and Chun-Hao Koo,2007, Ranjan Sinha, et al.,2013, Hongyu Wang ,et al., 2010.**

In this work, it has been reported the effects of amounts of oxygen reactive elements (Ce, Y,Ge) on the parabolic rate constant (Hot corrosion rate k_p ($10^{-12}g^2.cm^{-4}.s^{-1}$)) through the hot corrosion experiment of Aluminized-Chromized Superfer 800H (Incoloy 800H) . Recently many statistical experimental design methods have been employed such Box-Behnken design . These methods involve mathematical models for designing which can be processed using Artificial Neural Network (ANN) and Genetic Algorithm (GA) . The main objective of (GA) is to determine the optimum operational conditions for the coating system .

2.MATERIALS AND COATING FORMULATIONS

The experimental work was performed by using samples of Superfer800H (Incoloy800) . The spectrochemical analysis of candidate material is shown in Table 1. Samples were cut into squares shapes with dimensions of (10mm× 10×mm×4mm). All surfaces , including the edges were wet ground using 120, 220, 320, 600, 800, and 1200 grit silicon carbide papers. These samples were then cleaned with water, degreased with acetone, and then ultrasonically cleaned for 30 minutes using ethanol as a medium. After drying, the samples were stored in polyethylene zip-lock bags. The dimensions of all samples were measured. The pack mixture used for aluminum-chromium diffusion coating consisting of 20 Wt.%Al powder (40–45 μm in particule size) as an aluminum source, 10 Wt.%Cr powder (50-55 μm in particule size) as a chromium source, 2Wt.% NaF and 4Wt.%NaCl as activator and the balance was alumina-powder (80-110 μm in particule size). All pack powders were sized by sieving method and 1-3Wt.% of the pack alumina filler was replaced by reactive elements (Ce,Y,Ge) according to a standard response surface methodology (RSM) design called Box-Behnken Design (BBD) . The samples was placed in a sealed stainless steel cylindrical retort of 50mm in a diameter and of 80mm in a height in contact with the pack mixture. The retort was then put in another stainless steel cylindrical retort of 80mm in a diameter and 140mm in a height. The outer retort has a side tube through which argon gas passes and second in the top cover for argon gas outlet. Type-k calibrated thermocouple was inserted through the cover of the outer retort for recording real temperature near inner retort. Figure 1 shows the apparatus used for pack cementation (University of Technology / Department of Production Engineering & Metallurgy). Pack cementation process was carried out at 1050 ^{o}C for 6 h under an Ar atmosphere according to **Robert A.Rapp et al procedure, 1991**. In order to examine the microstructure of the coatings before and after hot corrosion test at the optimum conditions, the coated and tested samples were mounted and ground up to 1000 grit with SiC paper and then polished using 1μm diamond paste. The samples were then analyzed using energy dispersive spectroscopy(EDS) , x-ray diffraction (XRD), and optical microscope .

3.HOT CORROSION TEST

For hot corrosion tests, 75% wt.Na_2SO_4 and 25%wt. NaCl powders were selected as a corrosive salts. Samples were deposited with each of these salts until a total coating weight of 5 mg/cm^2 was reached according to **A.Anderson et. al procedure,2012** .The samples were measured and weighed first , then placed on a hot plated heated to 110^{o}C. An air gun sprayed on the saturated aqueous –salt solutions in air mist and a coat of fine salt particles formed on the samples surfaces after the mist settled and the water evaporated. The process was repeated until the dry particles were deposited up to 5 mg/cm^2. Hot corrosion test was performed in a static air at (900^{o}C) for 50 hr at 1 hr cycle in a programmable tube furnace . The experimental setup is shown in Figure 2 (University of Technology / Department of Production Engineering & Metallurgy). After testing the samples were cleaned in an ultrasonic bath, first in distilled water and then in ethanol. They were then weighed on a digital balance to determine the change in weight. The parabolic rate constant (Hot Corrosion Rate) K_P is calculated by a linear-square algorithm to a function in the form of $(\Delta W/A)^2=K_P \times t$, where $\Delta W/A$ is the weight gain per unit surface area (mg/cm^2) ant t is the hot corrosion time in seconds .

4.EXPERIMENTAL DESIGN

Response surface methodology (RSM) is a technique that uses quantitative data from appropriate experiments to determine regression model equations and operating conditions. RSM is a collection of mathematical and statistical techniques for modeling and analysis of problems in which a response of interest is influenced by several variables, **Douglas C.Montgomery,2009** . A standard RSM design called Box-Behnken Design (BBD) was applied in this work to study the variables for hot corrosion rate k_p ($10^{-12}g^2.cm^{-4}.s^{-1}$) . BBD for three variables (wt.%Ce, wt.%Y, and wt.%Ge) each with two levels (the minimum and maximum), was used as experimental design model. The model has advantage that it permits the use of relatively few combinations of variables for determining the complex response function . A total of 15 experiments are needed to be conducted to determine 10 coefficients of second order polynomial, **Douglas C.Montgomery,2009** . In the experimental design model, wt.%Ce, wt.%Y, and wt.%Ge were taken as input variables. hot corrosion rate k_p ($10^{-12}g^2.cm^{-4}. s^{-1}$)was taken as the response of the system. The experimental design matrix derived from BBD is given in Table 2**.**

The output and input variables can be expressed as follow:

$$Y = f (X_1, X_2, X_3, X_4........, X_n) \quad (1)$$

Where Y is the response of the system and Xi is the variables of action called factors where the goal is to optimize the response variable (Y). It is assumed that the independent variables are continuous and controllable by experiments with negligible errors. It is required to find a suitable approximation for the true functional relationship between independent variables and the response surfaces. The optimization of hot corrosion rate k_p ($10^{-12}g^2.cm^{-4}.s^{-1}$) was carried out by using Box-Behnken design with 12 unique runs including 3-replicates at center points. The quadratic equation model for predicting the optimal point was expressed according to Eq(2).

$$Y = \beta_0 + \sum_{i=1}^{k} \beta_i x_i + \sum_{i=1}^{k} \beta_{ii} x_i^2 + \left(\sum_{i=1}^{k-1} \sum_{j=i+1}^{k} \beta_{ij}\ x_i x_j \right)_{i<j} \quad (2)$$

Three factors were studied and their low and high levels are given in Table 3. hot corrosion rate k_p ($10^{-12}g^2.cm^{-4}.s^{-1}$) was studied with a standard RSM design called Box-Behnken Design (BBD). Fifteen experiments were conducted in duplicate according to the scheme mentioned in Table 2. Minitab and Matlab program was used for regression and graphical analysis of the data obtained. The optimum values of the selected variables were obtained by solving the regression equation and by analyzing the response surface contour plots. The variability in dependent variables was explained by the multiple coefficient of determination, R^2 which is can be calculated according to equation (3), where n is the number of data pairs, x is independent variable , and y is dependent variable . and the model equation was used to predict the optimum value and subsequently to elucidate the interaction between the factors within the specified range, **Douglas C.Montgomery,2009**.

$$R^2 = \left(\frac{n(\sum xy) - (\sum x)(\sum y)}{\sqrt{[n(\sum x^2) - (\sum x)^2][n(\sum y^2) - (\sum y)^2]}} \right)^2 \tag{3}$$

5. RESULTS AND DISCUSSIONS

The results of the each experiments are given in Table 2. Empirical relationships between the response and the independent variables have been expressed by the quadratic model as shown in Figure 3 . Regression coefficient of full polynomial model is also shown in this Figure .

Analysis of variance has been calculated to analyze the accessibility of the model. The analysis of variance for the response has been predicted in Figure 4 . In general, ANOVA table is used to evaluate the goodness of the model , as a rule , if p-value is less than 0.05, model parameter is significant . On the basis of analysis of variance, the conclusion is that the selected model adequately represents the data for hot corrosion rate k_p ($10^{-12}g^2.cm^{-4}.s^{-1}$) . The Experimental values and the predicted values are in perfect match with R^2 value of 0.983 (Figure 5). This methodology could therefore be successfully employed to study the importance of main and interaction effects of the test variables in hot corrosion test

6. DEVELOPING THE ANN MODEL

Artificial neural network (ANN) is a network with nodes or neurons analogous to the biological neurons. The nodes are interconnected to the weighted links. The weights are adjustable and can be trained by learning and training process and training treatments. ANN is able to receive inputs patterns in order to produce a pattern on its outputs that are correct for that class i.e. The ANN modeling can be an excellent approach in simulating the out-put results, **Daniel Graupe, 2007**. The three variables (wt.%Ce, wt.%Y, and wt.%Ge) each play important roles in influencing hot corosion properties like hot corrosion rate k_p ($10^{-12}g^2.cm^{-4}.s^{-1}$). The target of this research is to establish nonlinear relationships between the input parameters and the output parameters by the usage of ANN networks. So to model the hot corrosion kinetics, the three variables (wt.%Ce, wt.%Y, and wt.%Ge)has been defined as input and hot corrosion rate k_p ($10^{-12}g^2.cm^{-4}.s^{-1}$) as outputs in network. In this work, three input layers, ten hidden layers and one output layer, are used for predicting hot corrosion rate k_p ($10^{-12}g^2.cm^{-4}.s^{-1}$) according to Figure 6 . Sigmoid and pureline transfer function was employed for hidden layers and output layer, respectively. After neural networks are trained successfully, all output results is stored as shown in Figure 7. Figure 8 presents the comparison between measured and predicted results for hot corrosion rate k_p ($10^{-12}g^2.cm^{-4}.s^{-1}$). The agreements between the predicted and measured values (R^2=0.94) indicate that this approach can be very useful in modelling the hot corrosion properties of hot corrosion rate k_p ($10^{-12}g^2.cm^{-4}.s^{-1}$) in hot corrosion kinetics.

7. GENETIC ALGORITHM (GA)

The genetic algorithm approach provides the solution for the global optimization i.e. to find the "best possible" solution in decision models that frequently have a number of sub-optimal (local) solutions. The genetic algorithm solves optimization problems by mimicking the principles of biological evolution, repeatedly modifying a population of individual points using rules modelled on gene combinations in biological reproduction, **David A. Coley,1999.** Due to its random nature, the genetic algorithm improves the chances of finding a global solution. Thus

they prove to be very efficient and stable in searching for global optimum solutions. The mathematical model that best describes the relationship between Input and output parameters has to be developed in order to be used as objective function in GA to aid the global optimization. The Mathematical model was obtained using the Regression function in Minitab software.The proposed mathematical model was used to formulate the objective functions, which was the pre-requisite of genetic algorithm. The objective function was solved using MATLAB software as shown in Figure 9 . The optimized process parameter level of Genetic algorithm was obtained from this Figure . Figure 10 shows the plot of variation of hot corrosion rate k_p ($10^{-12}g^2.cm^{-4}.s^{-1}$) with the number of generation which is obtained by MATLAB program . The initial variation in the curve is due to the search for optimum solution . It is evident that the minimum hot corrosion rate k_p ($10^{-12}g^2.cm^{-4}.s^{-1}$) is 71.701.
The optimal values of input variables from regression equations using GA for the hot corrosion rate k_p ($10^{-12}g^2.cm^{-4}.s^{-1}$) were shown in Table4 . The optimum values of weight percentages (Wt.%) of Ce, Y, and Ge from Box-Behnken design were found to be 3,3 and 3 respectively. The minimum predicted value of hot corrosion rate k_p ($10^{-12}g^2.cm^{-4}.s^{-1}$) was found to be 71.701 .

The hot corrosion rate k_p ($10^{-12}g^2.cm^{-4}.s^{-1}$) was studied by Wt.%Ce and Wt.%Y. The results have been depicted in Figure 11a . The results indicated that the minimum hot corrosion rate k_p ($10^{-12}g^2.cm^{-4}.s^{-1}$)has been occurred in the 3wt.% Ce and 3wt.%Y . The combined effect of wt.%Ce and wt.%Ge has been presented in Figure 11b . The results show that the minimum hot corrosion rate k_p ($10^{-12}g^2.cm^{-4}.s^{-1}$) was recorded at the 3wt.% Ce and 3wt.%Ge. In the same way, the effect of wt.%Y and wt.%Ge on the hot corrosion rate k_p ($10^{-12}g^2.cm^{-4}.s^{-1}$) , the minimum hot corrosion rate k_p ($10^{-12}g^2.cm^{-4}.s^{-1}$) was 71.701 for 3wt.%Y and 3wt.%Ge as shown in Figure 11c .

The microstructure using optical microscope for coating (a) and hot corrosion(b) systems is shown in Figure 12 . Figure 13 shows the EDAX (a), and XRD (b) analysis. These analyses show that the coated layer at the optimum conditions consists of Ce-Y-Ge doped (Al+Cr) . The addition of Ce,Y, and Ge to the coated layer improve bond strength of the coatings to the substrate [14] . The formation of oxides of aluminum and chromium contribute to the development of hot corrosion resistance of this coating . XRD analysis indicate a scale consisting of a layer containing oxides of aluminum (Al_2O_3) and chromium (Cr_2O_3) , thus Al-Cr diffusion coatings on superfer 800H in molten salt environments at 900^oC are found effective in decreasing corrosion rate in molten salt , due to the formation of protective oxide scales of Al_2O_3 and Cr_2O_3 .

8. CONFIRMATION TEST FOR GENETIC ALGORITHM

The confirmation test for Genetic algorithm approach at the optimized process parameter levels (3Wt.%Ce, 3Wt.%Y, 3Wt.%Ge) was done and the hot corrosion rate k_p ($10^{-12}g^2.cm^{-4}.s^{-1}$) exhibited by the hot corrosion test of Superfer 800H was found to be 72.113×10^{-12} $g^2.cm^{-4}.s^{-1}$ i.e. there is a good agreement between GA and experimental results .

9. CONCLUSIONS

The results obtained in this study lead to the following conclusions:

1. Response surface methodology using Box-Behnken design prove very effective model for studying the influence of wt.% of doping elements on hot corrosion rate .
2. The experimental values and predicted values are perfect match with R^2 value of 98.30 .
3. ANN model has been developed for predicting Kp as function of wt.% of doping elements (Ce,Y,Ge) . The model has been proved to be successful in terms of agreements with experimental results.
4. The developed GA model can be used to find the optimal wt.% of doping elements (Ce,Y,Ge) which minimize the hot corrosion rate during the hot corrosion tests . A confirmation experiment was also conducted and verified the effectiveness of GA method.
5. EDS and XRD reveal the presence of elements of mixture in coating layer and the formation of the dense and continuous protective Al_2O_3 and Cr_2O_3 scale on surface during hot corrosion tests .

REFERENCES

- Lin-Chang Tsai1, Hung-Hua Sheu, Cheng-Chieh Chen, Ming-Der Ger, *The Preparation of the Chromized Coatings on AISI 1045 Carbon Steel Plate with the Electroplating Pretreatment of Ni or Ni/Cr-C Film*, Int. J. Electrochem. Sci., 10 (2015) 317 – 331.

- Fahamsyah H. Latief, El-Sayed M. Sherif, Koji Kakehi, *Role of Aluminide Coating on Oxidation Resistance of Ni-Based Single Crystal Superalloy at 900 °C*, Int. J. Electrochem. Sci., 10 (2015) 1873 – 1882 .

- Subhash Kamal , Korada Viswanath Sharma , A. M. Abdul-Rani, *Hot Corrosion Behavior of Superalloy in Different Corrosive Environments*, Journal of Minerals and Materials Characterization and Engineering, 2015, 3, 26-36 .

- Subhash Kamal, R. Jayaganthan, S. Prakash , *High temperature cyclic oxidation and hot corrosion behaviours of superalloys at 900°C* , Bulletin of Materials Science, June 2010, Volume 33, Issue 3, pp 299-306 .

- T. S. Sidhu, S. Prakash and R. D. Agrawal , *Hot corrosion and performance of nickel-based coatings*, CURRENT SCIENCE, VOL. 90, NO. 1, 10 JANUARY 2006 , pp 41-47 .
- Marta Kianicova , Karel Slamecka , Jaroslav Pokluda , *Damage Of Diffusion Coatings On Turbine Blades*, Brno, Czech Republic, EU18. 2011,20- 5 .
- W.H Lee, R.Y Lin, *Hot corrosion mechanism of intermetallic compound Ni_3Al*, Materials Chemistry and Physics, Volume 77, Issue 1, 2 January 2003, Pages 86-96 .
- LIN Nai-ming, , XIE Fa-qin, ZHOU Jun, ZHONG Tao, WU Xiang-qing, TIAN Wei, *Microstructures and wear resistance of chromium coatings on P110 steel fabricated by pack cementation*, J. Cent. South Univ. Technol. (2010) 17: 1155−1162 .

- Bruce M. Warnes, Nick S. DuShane, Jack E. Cockerill, *Cyclic oxidation of diffusion aluminide coatings on cobalt base superalloys*, Surface and Coatings Technology 148 (2001) 163–170.
- A. ESLAMI, H. ARABI and S. RASTEGARI, *Gas Phase Aluminizing Of A Nickel Base Superalloy By A Single Step Htha Aluminizing Process,* Canadian Metallurgical Quarterly, Vol 48, No 1., 2009, pp 91-98.
- I.M. Edmonds,, H.E. Evans, C.N. Jones, *Oxidation & Coating Evolution In Aluminized Fourth Generation Bladealloys*, The mineral, metal materials society , superalloy2008, pp.661-670.
- H. R. Karimi Zarchi, M. Soltanieh, M. R. Aboutalebi, X. Guo2, *Thermodynamic study on pack aluminizing systems of pure titanium and nickel* , Trans. Nonferrous Met. Soc. China 23(2013) 1838−1846 .
- Chao C. Jain and Chun H. Koo, *Creep and Corrosion Properties of the Extruded Magnesium Alloy Containing Rare Earth*, Materials Transactions, Vol. 48, No. 2 (2007) pp. 265 to 272.
- Rajesh Ranjan Sinha, Dr. Brahm Deo Tripathi, Dr. Mahendra Yadav, Mines, Dhanbad, *Effect of rare earth additions on high-temperature oxidation resistance of V and Mo alloyed steels*, steel-grips.com 2013,pp.14-18.
- Hongyu Wang , Dunwen Zuo, Gang Chen,, Guifang Sun ,, Xiangfeng Li,, Xu Cheng, *Hot corrosion behaviour of low Al NiCoCrAlY cladded coatings reinforced by nano-particles on a Ni-base super alloy*, Corrosion Science 52 (2010) 3561–3567.
- Rober A.Rapp, Mark A.Haper and Robert Bianco, *Codepostion elements by Halide Activated Pack Cementation*, JOM, Vol3, No.14,Nov.1991,pp.20-25.
- Anderson and S.Ramachandran, A. *Analysis of Corrosion at Hot Environment of Plasma Sprayed Stainless Steels* , European Journal of Scientific research, ISSN1450-216X Vol.76 No.2 (2012) , pp. 300-308.
- Douglas C.Montgomery , *Design and Analysis of Experiments*, John Wily &Sonc, Inc., 2009 .
- Daniel Graupe, *Principles Of Artificial Neural Networks*, 2nd Edition, World Scientific Publishing Co. Pte. Ltd., 2007.

- David A. Coley, *An Introduction to Genetic Algorithms for Scientists and Engineers*,World Scientific Publishing Co. Pte. Ltd.1999.

Table 1. Chemical composition of substrate material.

Element	Co	Cr	Ti	Al	W	Ta	C	B	Mo	Ni
Wt.%	8.4	16	3.31	3.23	1.07	0.59	013	0.05	1.02	bal

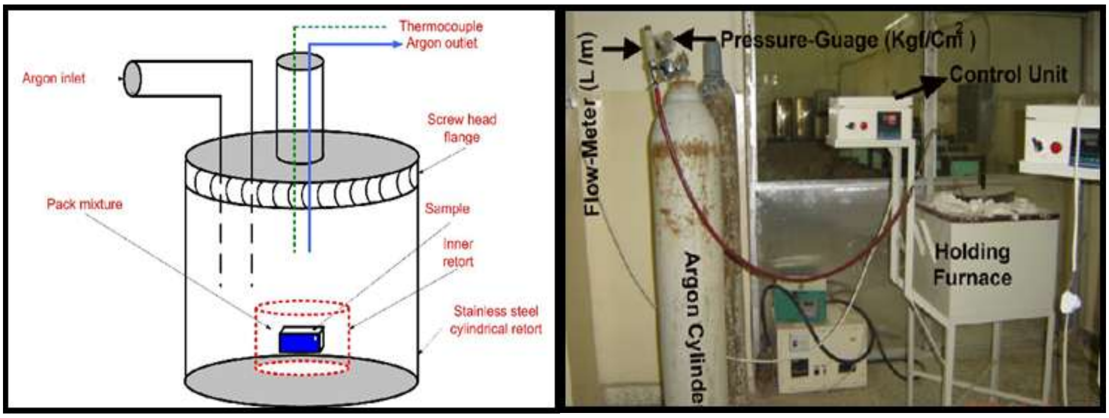

(a) Pack Cementation retort **(b) Pack Cementation Furnace**

Figure 1. Apparatus used for pack cementation .

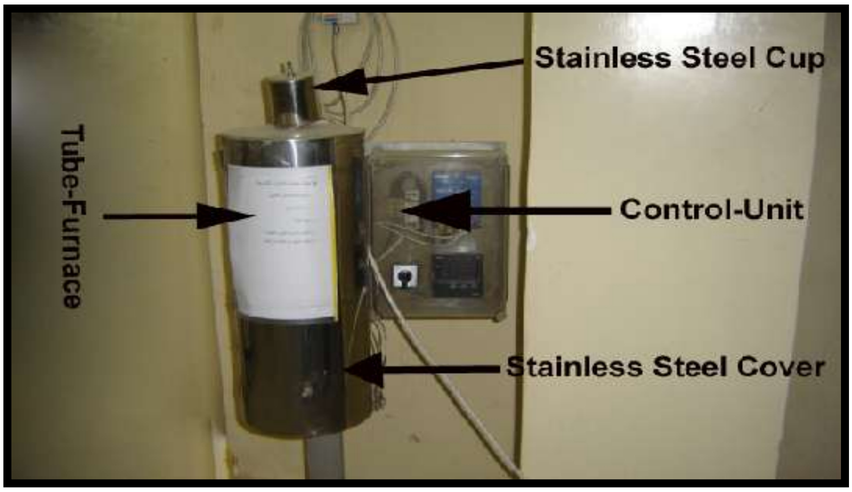

Figure 2. A programmable tube furnace of hot corrosion test.

Table 2. Experimental design and results for hot corrosion rate k_p ($10^{-12} g^2.cm^{-4}. s^{-1}$)

Run	Coded Values			Actual Values			k_p ($10^{-12} g^2.cm^{-4}. s^{-1}$)	
	X_1	X_2	X_3	X_1	X_2	X_3	observed	Predicted
1	0	1	1	2	3	3	74.81	74.64
2	1	1	0	3	3	2	75.76	75.51
3	1	-1	0	3	1	2	77.65	77.46
4	0	1	-1	2	3	1	76.39	76.62
5	1	0	-1	3	2	1	80.55	80.57
6	-1	-1	0	1	1	2	81.19	81.44
7	-1	1	0	1	3	2	79.35	79.54
8	0	0	0	2	2	2	83.33	83.55
9	0	-1	-1	2	1	1	78.28	78.45
10	0	0	0	2	2	2	83.43	83.55
11	-1	0	1	1	2	3	82.7	82.68
12	1	0	1	3	2	3	77.04	77.46
13	-1	0	-1	1	2	1	83.76	83.34
14	0	-1	1	2	1	3	76.89	76.66
15	0	0	0	2	2	2	83.88	83.55

Table 3. Coded and actual values of variables of the experimental design

Factor		Coded levels of variables		
		-1	0	+1
Wt.%Ce	X_1	1	2	3
Wt.%Y	X_2	1	2	3
Wt.%Ge	X_3	1	2	3

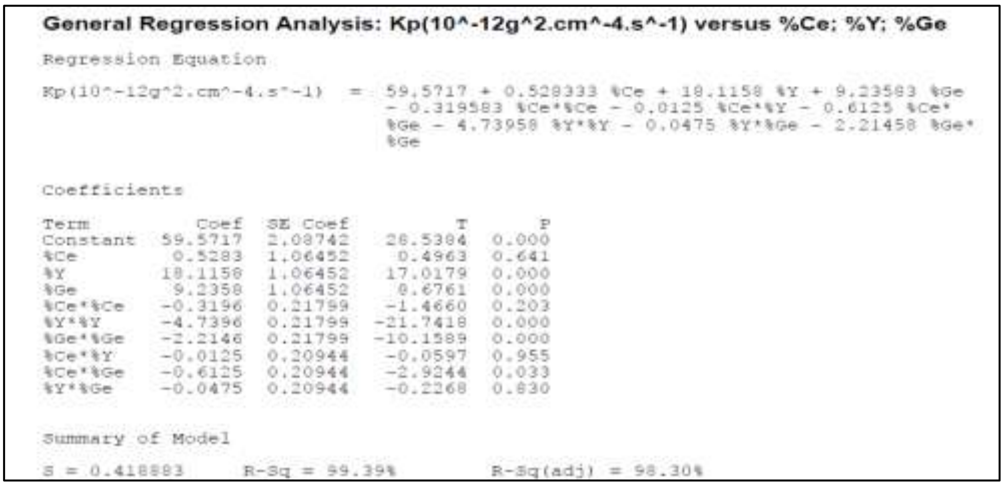

```
General Regression Analysis: Kp(10^-12g^2.cm^-4.s^-1) versus %Ce; %Y; %Ge

Regression Equation

Kp(10^-12g^2.cm^-4.s^-1)  =  59.5717 + 0.528333 %Ce + 18.1158 %Y + 9.23583 %Ge
                             - 0.319583 %Ce*%Ce - 0.0125 %Ce*%Y - 0.6125 %Ce*
                             %Ge - 4.73958 %Y*%Y - 0.0475 %Y*%Ge - 2.21458 %Ge*
                             %Ge


Coefficients

Term          Coef  SE Coef         T      P
Constant   59.5717  2.08742   28.5384  0.000
%Ce         0.5283  1.06452    0.4963  0.641
%Y         18.1158  1.06452   17.0179  0.000
%Ge         9.2358  1.06452    8.6761  0.000
%Ce*%Ce    -0.3196  0.21799   -1.4660  0.203
%Y*%Y      -4.7396  0.21799  -21.7418  0.000
%Ge*%Ge    -2.2146  0.21799  -10.1589  0.000
%Ce*%Y     -0.0125  0.20944   -0.0597  0.955
%Ce*%Ge    -0.6125  0.20944   -2.9244  0.033
%Y*%Ge     -0.0475  0.20944   -0.2268  0.830


Summary of Model

S = 0.418883      R-Sq = 99.39%        R-Sq(adj) = 98.30%
```

Figure 3. MINITAB session show the results of general regression.

Analysis of Variance

Source	DF	Seq SS	Adj SS	Adj MS	F	P
Regression	9	143.800	143.800	15.9778	91.060	0.000053
Error	5	0.877	0.877	0.1755		
Total	14	144.677				

Figure 4. MINTAB session for ANOVA of regression model.

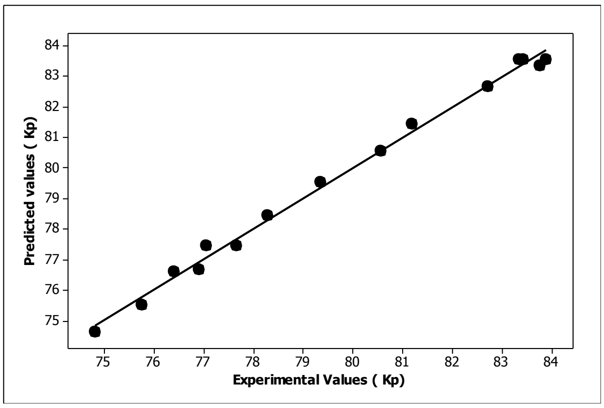

Figure 5. Comparison between predicted and experimental values.

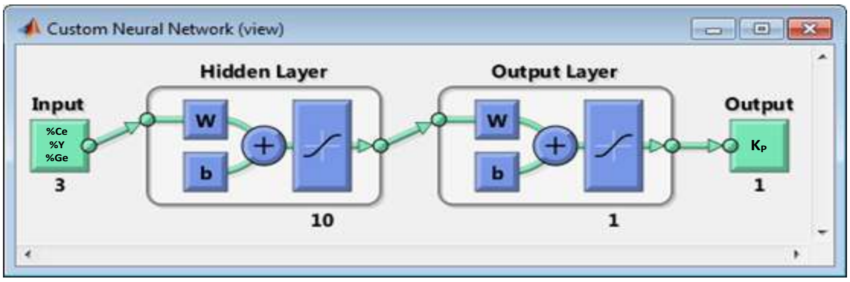

Figure 6. ANN Structure for input, hidden and output layers.

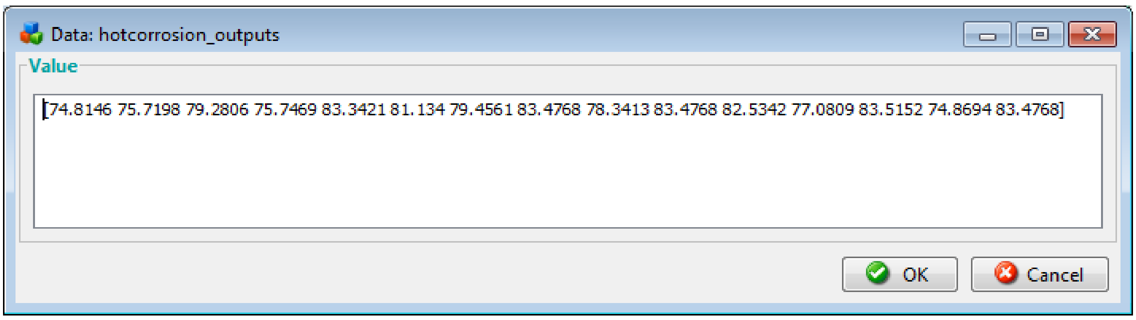

Figure 7. Results of ANN-outpouts.

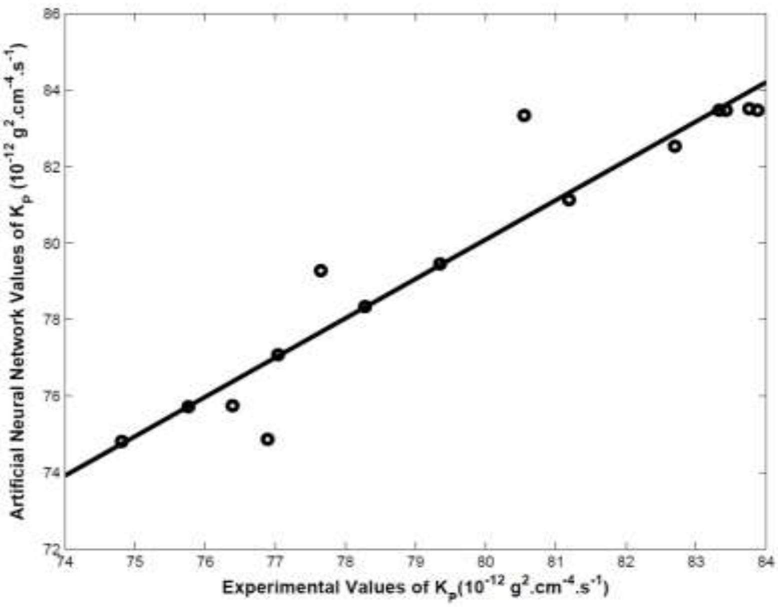

Figure 8. Comparison of the experimentation and calculation.

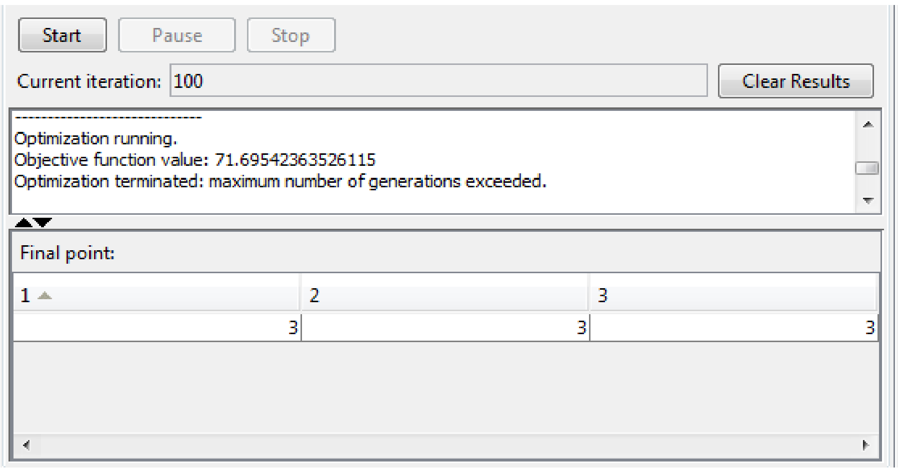

Figure 9. Solver showing the results in MATLAB.

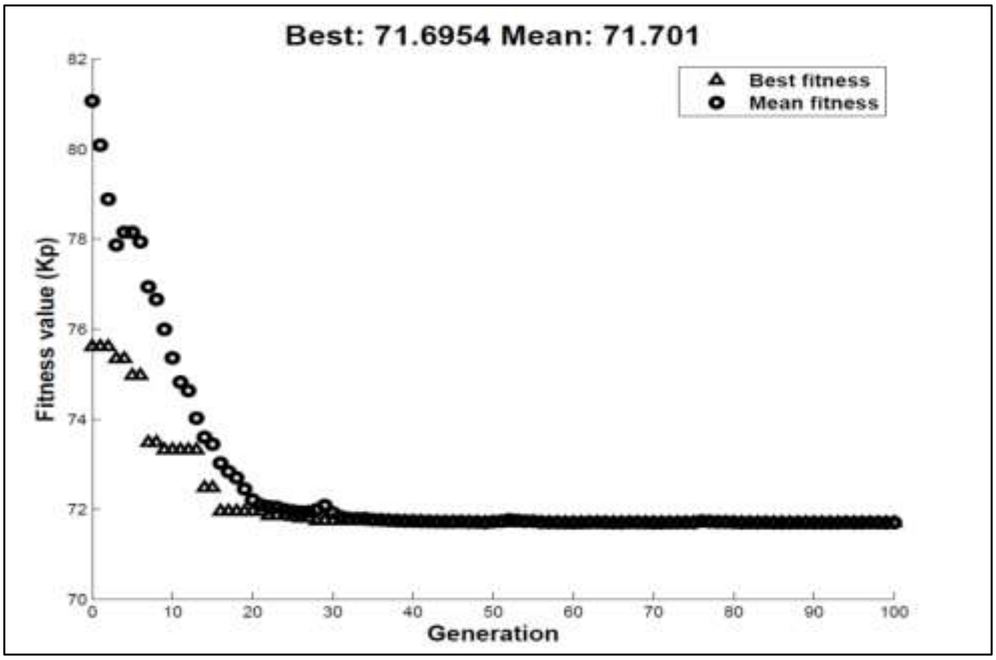

Figure 10. Variation of hot corrosion rate k_p ($10^{-12}g^2.cm^{-4}.s^{-1}$) with number of generation.

Table 4. Optimum values of variable obtained from GA of regression model

No.	parameter	Optimum value	Minimum predicted k_p $10^{-12}g^2.cm^{-4}.s^{-1}$
1	Wt.%Ce	3	71.701
2	Wt.%Y	3	
3	Wt.%Ge	3	

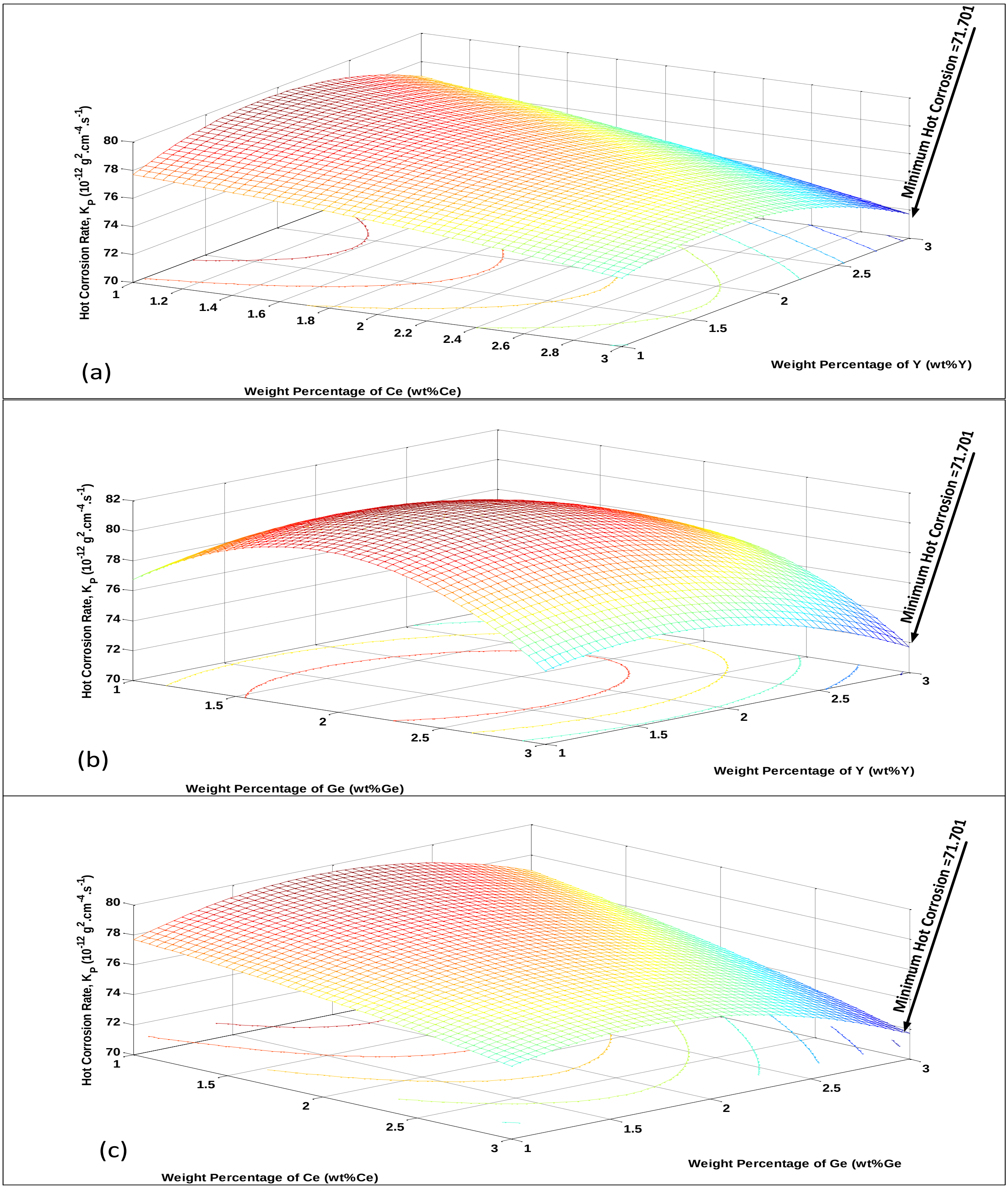

Figure 11. Response surface of 3D plot indicating the effect of interaction between (a) wt.%Ce and wt.%Y on hot corrosion rate k_p ($10^{-12}g^2.cm^{-4}.s^{-1}$) while holding wt.%Ge at 3wt.% (b) wt.%Ce and wt.%Ge on hot corrosion rate k_p ($10^{-12}g^2.cm^{-4}.s^{-1}$) while holding wt.%Y at 3wt.% (c) wt.%Y and wt.%Ge on hot corrosion rate k_p ($10^{-12}g^2.cm^{-4}.s^{-1}$) while holding wt.%Ce at 3wt.%

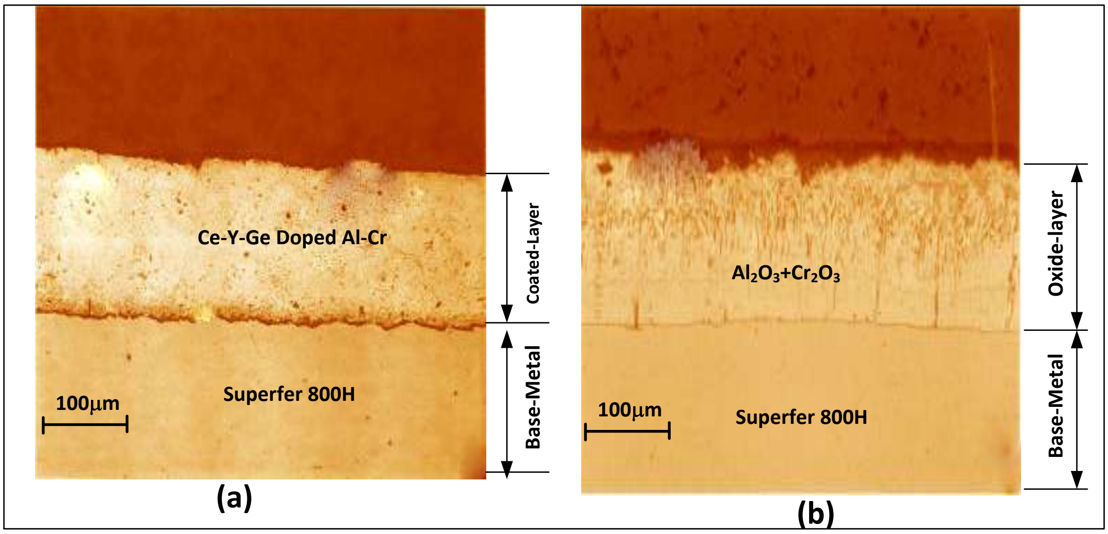

Figure 12. The microstructure using optical microscope for coating (a) and hot corrosion(b) systems

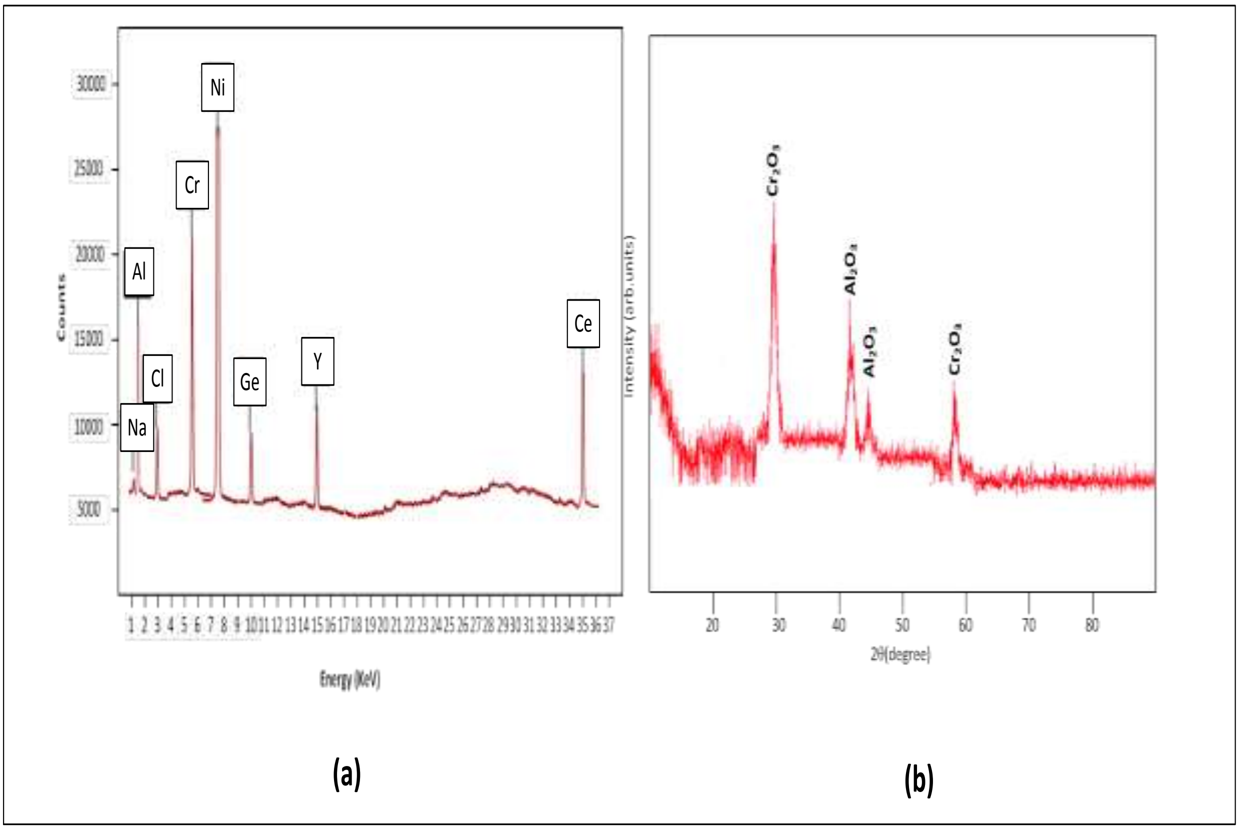

Figure 13. The EDAX (a), and XRD (b) analysis.

Performance Enhancement of a Piezoelectric Harvester Included into an Autonomous System

Waleed Al-Ashtari
Instructor
College of Engineering - University of Baghdad
E-mail: waleedalashtari@yahoo.com

ABSTRACT

Autonomous systems are these systems which power themselves from the available ambient energies in addition to their duties. In the next few years, autonomous systems will pervade society and they will find their ways into different applications related to health, security, comfort and entertainment. Piezoelectric harvesters are possible energy converters which can be used to convert the available ambient vibration energy into electrical energy. In this contribution, an energy harvesting cantilever array with magnetic tuning including three piezoelectric bi-morphs is investigated theoretically and experimentally. Other than harvester designs proposed before, this array is easy to manufacture and insensitive to manufacturing tolerances because its optimum operation frequency can be re-adjusted after fabrication. In this array, each bimorph has its own rectification circuit in order to prevent the interference of its operation with the others. Two electrical connections are investigated: the series connection and the parallel connection. These connections are tested under several cases such as moderate and high excitation level and large and small connected load. The theoretical and experimental works show that each connec-tion has characteristics and can be used to enhance the harvester output power and/or its frequen-cy bandwidth. These characteristics are highly related to the excitation level and the connected load together.

Key words: piezoelectric bimorph, cantilever array, frequency tuning, electrical connections

تحسين اداء حاصدة كهروضغطية تستعمل لتوليد الطاقة الكهربائية اللازمة لتشغيل جهاز ذاتي العمل

وليد خالد خيري الاشتري
مدرس
كلية الهندسة-جامعة بغداد

الخلاصة

الاجهزة ذاتية العمل هي تلك الاجهزة التي تستعمل الطاقة الموجودة في البيئة المحيطة لتحويلها الى الطاقة الكهربائية اللازمة لاداء عملها. في السنين القليلة القادمة, تلك الاجهزة ستتوفر بكثرة في المجتمع و سيوجد لها تطبيقات كثيرة متعلقة بالصحة و الرفاهية. الحاصد ات لكهروضغطية هي احدى الوسائل المستخدمة لتشغيل هذه الاجهزة حيث يمكن لهذه الحاصدات تحويل طاقة الاهتزاز الى طاقة كهربائية. في هذا البحث, تم تصميم حاصدة تحتوي ثلاث عتبات المصنوعة من مواد كهروضغطية. كل عتبة تم تثبيتها من طرف واحد و الطرف الاخر ترك حرا. كل عتبة يمكن توليف ترددها الطبيعي باستخدام مغانط ثابتة. تمتاز هذه الحاصدة الجديدة بانه يمكن تجاوز التاثيرت السلبية لسماحات التصنيع بعد تصنيعها وذلك لانه يمكن اعادة توليف ترددها الامثل الذي عنده تحصد اكبر طاقة ممكنة. تم ربط لكل عتبة في هذه الحاصدة دائرة كهربائية تستخدم لتحويل الفولطية المتناوبة المتولدة الى فولطية مستمرة وذلك لمنع التاثير السلبي لكل عتبة كهروضغطية على الاخرى. لقد تم تصنيع هذه الحاصدة و دراستها نظريا و عمليا.تم بحث نوعين من الربط الكهربائي لهذه العتبات الكهروضغطية: ربط على التوالي و ربط على التوازي. هذان الربطان تمت دراستهما بعدة حالات مثلا تمت دراستهما عند تسليط اهتزاز ذو سعة متوسطة و عالية و كذلك عند ربط حمل كهربائي صغير او كبير. نتائج النظري و العملي بينت تحسن كبير في اداء الحاصدة المقترحه مقارنة مع

التصميم المعروف للحاصدات الكهروضغطبة. حيث لوحظ ازدياد كبير في الفولطية المتولدة و كذلك توسع مدى الترددات التي ممكن ان تعمل به الحاصدة.

1. INTRODUCTION

Energy harvesting commonly refers to the process of converting the available energy from the environment into electrical energy. The concept of this process can be found in many real-life applications and on different scales. For example, wind turbines and solar panels are used for high amount of energy conversion and solar cells or piezoelectric materials are used for low amount of electrical energy conversion.

The new challenge since about a decade ago is how to exploit this process to design systems which have the abilities to achieve their requirements (duties) and in addition power themselves from the available ambient energies. Such systems are called autonomous systems. In the next few years, autonomous systems will pervade society and they will find their ways into different applications related to health, security, comfort and entertainment.

In the last few years, piezoelectric harvester has received the most attention concerning its potential to power electronic devices; numerous related scientific journals and conferences have investigated this subject intensively.

The basic configuration of an autonomous system typically contains three elements in addition to the piezoelectric harvester: a full-wave rectifier, a reservoir capacitor and an electronic device performing the primary task. **Fig.1** schematically shows the typical arrangement of such systems. It is clear that the autonomous system has two parts: the electrical part and the electromechanical part. These two parts effect on each other and they can prevent the autonomous system from functioning if they are not properly matched.

One major limitation of piezoelectric energy harvester, discussed before by **Al-Ashtari et al., 2012a**, is that it operates effectively at a single excitation frequency. This excitation frequency must match the optimal frequency of the piezoelectric harvester. The optimal frequency is defined as the frequency at which the harvester generates the maximum voltage. It is determined by the harvester properties, geometry and the connected load (electronic device). For example, for a low damped harvester, experiments show that a 5% difference between the excitation frequency and the optimal frequency causes a drop of the harvested energy by about 90%.

Tang et al., 2010 presented a comprehensive review contains most of the techniques developed over the past years to overcoming the bandwidth limitation of piezoelectric harvesters mentioned above. This review classified the known solutions into two main categories: optimal frequency tuning and multimodal energy harvesting. Optimal frequency tuning was sub-classified into mechanical methods, magnetic methods and piezoelectric methods; multimodal energy harvesting is divided into hybrid energy harvesting schemes and cantilever arrays.

Optimal frequency tuning techniques can be classified more conveniently into manual and self-tuning methods. The self-tuning methods also should be subdivided into active tuning and passive tuning techniques. Active tuning techniques continuously consume power while passive tuning techniques require power only initially for tuning the harvester frequency. Up to now, there is no robust self-tuning harvester that can power its tuning process independently.

This contribution focuses on the cantilever array approach either for increasing the magnitude of the generated voltage or extending the bandwidth of an energy harvester. A cantilever array consists of multiple piezoelectric cantilevers integrated in one harvester in order to increase its frequency bandwidth and/or output power. Increasing voltage is achieved when all the piezoelectric cantilevers have equal optimal frequency. While, extending the frequency bandwidth is accomplished if each piezoelectric cantilever has a certain optimal frequency so that at a certain range

of excitation frequency all (or a group) of the piezoelectric cantilevers operate together to generate the required voltage.
Throughout the literature, it can be found that many attempts to design and model cantilever arrays. For example**, Shahruz, 2006a, b, and c** introduced so-called mechanical band-pass filters which consist of multiple cantilevers. Dimensions and proof masses are calculated from the predefined optimal frequency. These works generally do not consider the electrical characteristics and thus cannot investigate the electrical effect of each cantilever on the others. **Xue et al., 2008** presented another design of an array with cantilevers of different optimal frequencies. Each cantilever includes two piezoelectric layers and its resonance frequency is adjusted by varying their thickness. The authors concluded that connecting multiple bimorphs in series increased not only the harvested power but also the harvester bandwidth. They used 10 piezoelectric bimorphs of different thicknesses to harvest power across a bandwidth of 25 Hz. The mathematical model given in this work ignores the electrical effect of the bimorphs on each other. Also, the effect of connecting multiple bimorphs in parallel or in series on the optimal load of the complete harvester is not investigated. **Ferrari et al., 2007** designed a multi-frequency piezoelectric harvester which consists of three cantilever bimorphs of the same dimension. The authors determined the resonance frequency of each bimorph by adjusting the tip mass. They modeled the piezoelectric harvester as a voltage source in series with a branch consisting of a resistor and a capacitor connected in parallel. This allows describing the effect of the bimorphs on each other. In this setup, a half-wave AC-DC rectifier was used for each bimorph for two main reasons: The electronic application needs DC power and power transfer between the bimorphs shall be prevented.
It is hard to realize any of the harvesters presented in the aforementioned works in industrial applications. The setups in those works require very accurate manufacturing processes and careful handling, and operate at an unchangeable frequency band. If the frequency spectrum of the host changes, for example due to wear or changed operating conditions, those arrays will be useless. Another fact worth mentioning is that the characteristic frequencies of piezoelectric elements might also change due to aging temperature, vibration level etc. **Al-Ashtari et al, 2013** introduced a cantilevers array have no such limitations. This cantilever array is developed basing on their magnetic tuning technique addressed in **Al-Ashtari et al., 2012b**. The optimal frequency is tuned by changing the attraction force between two permanent magnets by adjusting the distance between the magnets. The optimal frequency and bandwidth can be re-adjusted at any time. This makes the proposed cantilever array insensitive to the effects of manufacturing tolerances of both the piezoelectric elements and the harvester structure on the optimal frequency of the system.
In this contribution, a new cantilever array is designed based on that proposed by **Al-Ashtari et al., 2013**. This array was used as the energy harvester in an autonomous system similar to that shown in **Fig. 1**. In such systems, the electrical connections between the piezoelectric elements of the energy harvester, as well as the electromechanical characteristics of each one, are the important parameters which can be adjusted in order to increase the generated power, enhance the frequency bandwidth or make the system more reliable. There are two primary possible electrical connections to connect the piezoelectric elements together: the series connection and the parallel connection. Each one of these connections has its own characteristics and is suitable for different requirements. The model describing the operation of such system is derived and its operation is analyzed. This theoretical work is supported by the corresponding experimental results. The results of these two sections show good agreement between them.

2. AUTONOMOUS SYSTEM

It has been mentioned above that the autonomous system has two parts: the electrical part and the electromechanical part. In this section, these parts will be discussed in details.

2.1 Electrical Part

In this paper the, behavior of an energy harvester connected to a rectifier circuit is introduced. As shown in **Fig. 2**, the rectifier circuit consists of four diodes: D_1, D_2, D_3 and D_4. These diodes are connected in the standard arrangement to convert the generated AC voltage from the harvester $u(t)$ into an output DC voltage U_{dc}.

Fig. 3a shows the generated AC voltage $u(t)$ during the first two periods of operation, where t_p is the period. The corresponding output DC voltage is shown in **Fig. 3b**. These two figures show that the first period of operation is very important and it includes four intervals; these intervals are dependent on the design of the autonomous system components and their properties. Thus, the autonomous system should be designed with this in mind to operate successfully. These intervals are: the dead zone interval t_0, the diode transient conduction interval t_{tr}, the open circuit interval t_{op} and finally the diode steady-state conduction interval t_{ss}.

The rectification process starts when the dead zone interval ends. This interval is defined as that time interval during which the AC voltage is applied and there is no corresponding output DC voltage. That's because the input AC voltage amplitude is less than that required to overcome the diode barrier voltage U_d. The dead zone interval exists only in the first quarter of the first period of operation (between 0 and t_0) as shown in **Fig. 3b**.

At the end of the dead zone interval t_0, the transient conduction interval t_{tr} will start when the amplitude of the generated AC voltage rises to be greater than the diodes' barrier voltage. Within this interval, either the first pair of diodes (D_2 and D_4) is on and the other pair (D_1 and D_3) is off or vice-versa. This causes the current to flow from the harvester into the parallel loads C_R and R_l. The size of the reservoir capacitor C_R should be calculated carefully so that it will be is fully charged at the end of this interval; otherwise the transient conduction time will continue over into the next periods until the capacitor is fully charged. When the capacitor voltage rises higher than the amplitude of generated AC voltage, the diodes will be off because the capacitor will try to discharge its stored energy through them in their reverse direction.

This means the harvester is now disconnected from the load side i.e. it is in open-circuit condition. This will continue until the amplitude of the input AC voltage becomes greater than the capacitor voltage. This happens in a time interval called the open circuit interval t_{op}. The load R_l in this interval is electrically powered only by the energy stored in the capacitor and the harvester in open-circuit condition.

When the capacitor voltage becomes smaller than the amplitude of the applied AC voltage $u(t)$, then this interval will be ended and the steady-state conduction interval t_{ss} starts. Within this interval, the other pair of diodes that were not conducting earlier will do so and the first conducting pair will not. Within this time, the capacitor should be recharged.

The second and also all the next periods of operation have only the open circuit interval and the diodes steady-state conductions intervals i.e. the system will be in its steady state operation as shown in **Fig. 3b**.

In most real-life applications, the required charging time of the reservoir capacitor is much smaller than required time for its discharging. This enables us to assume that almost all the generated current flows into the connected load during the diodes steady-state conductions intervals i.e. during the steady state operation the harvester will serve two different loading conditions: the open-circuit condition and resistive load condition. In this article, the connected load is chosen to be large enough in order the generated voltages have almost the characteristics during these alternative intervals.

2.2 Electromechanical Part

The electromechanical part (the piezoelectric harvester) has related mechanical and electrical characteristics. These characteristics are determined by the mechanical and electrical boundary conditions of the harvester. The open circuited condition refers to the case when the electrodes of the included piezoelectric elements are not connected. The resistive load condition means that the electrodes of the piezoelectric harvester are connected to each other via a resistive load.

2.2.1 **Open circuit condition**

The system representing the piezoelectric harvester of the autonomous system in an open circuited condition is shown in **Fig. 4** (the electrical subsystem has been removed for purposes of clarity). Based on the model introduced by **Al-Ashtari et al., 2012a,** the equivalent systems (mechanical and electrical) of the harvester in this condition are shown in **Figs. 5a** and **5b**, respectively. All the parameters in the figures are the same as defined previously. $u_o(t)$ and $x_o(t)$ are the generated open voltage and the corresponding harvester deflection resulting from force application $F(t)$, respectively. If the excitation force $F(t)$ shown in **Figs. 5a** and **5b** is described by

$$F(t) = F\sin\omega t, \tag{1}$$

then the generated AC voltage can be expressed as

$$u_o(t) = U_o\sin(\omega t + \varphi_{uo}) \tag{2}$$

where ω is the excitation frequency in rad/s, F and $U_o$the amplitudes of the excitation force and the generated AC voltage, and φ_{uo} is the phase difference between them. The governing equation of such system is

$$M\ddot{x}_o(t) + B\dot{x}_o(t) + Kx_o(t) = F(t) - \alpha u_o(t) \tag{3}$$

For the electrical side, the following equation can be derived:

$$\alpha\dot{x}_o(t) = C_p\dot{u}_o(t) \tag{4}$$

Therefore, the transfer function between the excitation force and the generated voltage is

$$\frac{U_o(s)}{F(s)} = \frac{\alpha}{MC_ps^2 + BC_ps + KC_p + \alpha^2} \tag{5}$$

where $F(s)$ and $U_o(s)$ are the Laplace transforms of the excitation force and generated AC voltage, respectively. In terms of the series resonance frequency ω_s, the parallel resonance frequency ω_p and the system damping ratio ζ, it becomes

$$\frac{U_o(s)}{F(s)} = \frac{(\alpha/MC_p)}{s^2 + 2\zeta\omega_s s + \omega_p^2} \tag{6}$$

Where,**Al-Ashtari, 2012a**

$$\omega_s = \sqrt{\frac{K}{M}}, \tag{7a}$$

$$B = 2\zeta M\omega_s\,, \tag{7b}$$

$$\alpha^2 = M\left(\omega_p^2 - \omega_s^2\right)C_p \tag{7c}$$

The generated AC voltage amplitude can be expressed as

$$U_o = \frac{\left(\alpha/MC_p\right)F}{\sqrt{\left(\omega_p^2 - \omega^2\right)^2 + (2\zeta\omega_s\omega)^2}} \tag{8}$$

and the phase difference is

$$\varphi_{uo} = -\tan^{-1}\left(\frac{2\zeta\omega_s\omega}{\omega_p^2 - \omega^2}\right) \tag{9}$$

2.2.2 Resistive load condition

Resistive load condition refers to the condition in which the electrodes of the piezoelectric element in a harvester are connected by a resistive load R_l as shown in **Fig. 6**. All the parameters of the systems are as defined previously. $x_R(t)$ is the beam deflection from the external force $F(t)$ applied to the system. $u_R(t)$ and $q_R(t)$ are the corresponding generated voltage and charge across the connected resistive load. **Figs. 7a** and **7b** respectively show the equivalent mechanical and electrical systems of a piezoelectric harvester at resistive load condition.

Now, the first goal is to calculate the generated voltage as a function of the connected load R_l and the excitation frequency ω, and then to derive the relationship between these two variables in order to determine the condition at which the maximum power can be generated. The governing equation is the same as that for the open circuited condition, thus

$$M\ddot{x}_R(t) + B\dot{x}_R(t) + Kx_R(t) = F(t) - \alpha u_R(t) \tag{10}$$

for the mechanical side; for the electrical side, we have

$$\alpha\dot{x}_R(t) = C_p\dot{u}_R(t) + \dot{q}_R(t) \tag{11}$$

and

$$\dot{q}_R(t) = \frac{u_R(t)}{R_l} \tag{12}$$

As before, the transfer function between the excitation force and the generated voltage is

$$\frac{U_R(s)}{F(s)} = \frac{\alpha R_l s}{MR_lC_ps^3 + (M + BR_lC_p)s^2 + (B + KR_lC_p + \alpha^2 R_l)s + K} \tag{13}$$

In terms of series resonance frequency ω_s, parallel resonance frequency ω_p and damping ratio ζ, which are defined by Eqs. (7a) ,(7b) and (7c), then Eq. (13) can be rewritten as

$$\frac{U_R(s)}{F(s)} = \frac{(\alpha R_l/M)\,s}{R_lC_ps^3 + (1 + 2\zeta\omega_sR_lC_p)s^2 + (2\zeta\omega_s + \omega_p^2R_lC_p)s + \omega_s^2} \tag{14}$$

This gives the amplitude of the generated AC voltage as

$$U_R = \frac{(\alpha R_l\omega/M)\,F}{\sqrt{\left[\omega_s^2 - (1 + 2\zeta\omega_sR_lC_p)\omega^2\right]^2 + \omega^2\left[2\zeta\omega_s + R_lC_p(\omega_p^2 - \omega^2)\right]^2}} \tag{15}$$

and the phase difference is

$$\varphi_{uR} = -\tan^{-1}\left(\frac{\omega\left[2\zeta\omega_s + R_lC_p(\omega_p^2 - \omega^2)\right]}{\omega_s^2 - (1 + 2\zeta\omega_sR_lC_p)\omega^2}\right) \tag{16}$$

Usually, a piezoelectric harvester is an electromechanical device that is located in or on a vibrating host structure to generate AC voltage, which can be used to power an electronic application. Therefore, the base of the piezoelectric harvester is excited, thus exciting the entire structure. The derived model can be valid if the force F is replaced by the force MA_b. Where A_b is the amplitude of the base acceleration. The generated DC voltage of a harvester U_{dc} in an autonomous system can be expressed as

$$U_{dc} = U_R - 2U_d \tag{17}$$

where U_R is the generated voltage under R_l conditions.

3. CANTILEVER ARRAY

There are two main connections can be used to connect electrically multiple piezoelectric elements: the series connection and the parallel connection. Also, each of these connections can be performed by two different ways as will be shown later: direct connection and indirect connection.

3.1 Series Connection

The series connection of the piezoelectric elements can be classified into two types: the direct and the indirect series connections.

3.1.1 **Direct series connection**

The direct series connection is when the electrodes of all the piezoelectric elements are connected together in series before the rectification process – for example, the system that is shown in **Fig. 8**. For this connection, all the piezoelectric elements should have exactly the same optimal

frequency in order to gain an output voltage equal to the generated voltage of one element, times the total number of elements (i.e., the ideal output).
If the harvester includes n number of piezoelectric elements and all are excited by the applied force $F(t)$, then the amplitude of the generated voltage by the i^{th} element during steady-state operation can be expressed as (based on Eq. (15))

$$U_i = \frac{(\alpha_i R_l \omega / M)\, F}{\sqrt{\left[\omega_{si}^2 - \left(1 + 2\zeta_i \omega_{si} R_l C_{pi}\right)\omega^2\right]^2 + \omega^2\left[2\zeta_i \omega_{si} + R_l C_{pi}\left(\omega_{pi}^2 - \omega^2\right)\right]^2}} \quad (18)$$

If all the elements have the same optimal frequency, then the amplitude of the total generated voltage is

$$U_g = n \cdot U_i \quad (19)$$

and the total output DC voltage can be calculated as

$$U_s^d = U_g - 2U_d \quad (20)$$

For this connection, if the piezoelectric elements have different optimal frequencies, then the generated voltages of each one will have different amplitudes and be in different phases. This will cause them to overlap and may lead to not achieving any enhancement.

3.1.2 **Indirect series connection**
The indirect series connection means that the piezoelectric elements in the harvester are connected together in series, but after the rectification process is carried out, as for example in the system shown in **Fig. 9**.
If this harvester also includes n number of piezoelectric elements, and these elements all have small differences in their optimal frequencies, and if the excitation frequency matches the optimal frequency of one piezoelectric element, then the other piezoelectric elements should be able to generate voltage amplitudes equal to or more than that dropped through the diodes, so the total DC voltage will be

$$U_s^i = \sum_{i=1}^{i=n} (U_i - 2U_d) \quad (21)$$

This connection can be used to expand the frequency bandwidth within which the harvester can supply enough power to the connected load.
It is not practical to use the indirect connection if the piezoelectric elements have large differences in their optimal frequencies. That is because the losses of voltage across the diodes will be very large. Thus, if a harvester includes n number of piezoelectric elements, and is excited by a harmonic acceleration of frequency that activates on piezoelectric element, which then generates voltage while the others do not, then the total DC voltage U_s^l at that case can be expressed as

$$U_s^l = \sum_{i=1}^{i=n} [U_i - (2\, n. U_d)] \quad (22)$$

It seems to be that if a large number of piezoelectric elements are used then this may result in there being no generated voltage anymore.

3.1.3 **Tuning strategy for series connection**

To achieve an expanded frequency bandwidth, each piezoelectric element should be tuned to a different optimal frequency. The spread between the different frequencies defines the bandwidth and the minimum voltage generated in this frequency range. In this paper, the tuning strategy is developed so that at a frequency f_h where two neighbouring piezoelectric elements generate the same DC voltage, the voltage generated by each element is half the mean peak voltage of the two elements.

Fig. 10 shows an example with three piezoelectric elements with approximately equal peak voltages (the solid line curves). It is clear that these elements are tuned in such a way as to ensure that at the frequencies f_{h1} and f_{h2}, the neighboring piezoelectric elements share equally in generating the total voltage. The total generated voltage is similar to that shown in **Fig. 10** in the dashed black line. It seems that the peak voltage that can be generated by a single piezoelectric element at a single excitation frequency is extended across a considerable range as shown in **Fig. 10**.

This tuning strategy has been tested theoretically and experimentally, as will be shown later, and the results show that this strategy is very effective for enhancing the frequency bandwidth of a piezoelectric harvester.

3.2 Parallel Connections

If a harvester includes piezoelectric elements with different optimal frequencies which are connected in parallel, then only the element that generates the higher voltage powers the load, while the other elements do not. In a direct parallel connection, the other elements which are not generating voltage at the moment behave as additional parallel loads. Therefore, these elements cause the generated voltage to decrease. This is because these parallel elements reduce the overall load connected to the operating element.

In indirect parallel connections, the voltage generated by the operating element prevents the rectifier circuits of the other elements from conducting. Therefore, it is not advisable to use either parallel connection type if the piezoelectric elements have different optimal frequencies.

If all the piezoelectric elements have the same optimal frequency and are connected in parallel (direct or indirect), then the generated current increases. This case is not examined further because it is interested in replacing batteries with piezoelectric harvesters in currently commercial electronic applications. In such applications, achieving the required voltage is necessary to ensure achieving of the required power for the operation; the current is therefore uninteresting for this purpose.

4. EXPERIMENTAL VERIFICATION

Fig. 11 shows the experimental cantilever array harvester that was constructed to validate the analytical model presented above. This harvester consists of three piezoelectric bimorphs (SITEX-Module 427.0085.11Z from Johnson Matthey; specifications in Table 1). Magnetic stiffening **Al-Ashtari et al., 2012b** can be used to tune each bimorph individually. The bimorphs are electrically isolated from each other and from the aluminum base by plastic parts. Magnets with a face area of 8.5 x 2 mm² and a thickness of 1.5 mm (from HKCM Engineering, manufacturing code Q08.5x02x01.5Ni48H) were used. The distance between the two magnets is adjusted using a knurled screw.

This harvester is connected to a bridge full-wave rectifier consisting of four Schottky diodes and reservoir capacitor of size 200 μF. The used electrical application is a temperature sensor (TFA Dostmann GmbH & Co. KG Kat. Nr. 30.2018). This sensor requires 1.5 V DC voltage and has a total resistance of 360 kΩ. This system was excited with a harmonic acceleration of amplitude equal to $5.5\ \mathrm{m/s^2}$ and frequency of 250 Hz matches to the harvester parallel-resonance frequency.

Fig. 12 schematically shows the setup that used in the experimental work. The piezoelectric harvester is excited from its base by a harmonic acceleration supplied by an electro-dynamic shaker. In order to keep this acceleration on the desired value, it is monitored by using a laser vibrometer (vibrometer #1) and an oscilloscope. The amplitude and frequency of this acceleration are manually adjusted by manipulating the used signal generator and amplifier.

A second vibrometer of two laser probes is used to measure the deflection of the piezoelectric element included in the used harvester. This deflection is monitored and measured by using also an oscilloscope as shown in **Fig. 12**.

Fig. 13 shows a comparison between the obtained output DC voltages for three cases all excited by the same harmonic acceleration as before ($5.5\ \mathrm{m/s^2}$): the first case when the harvester includes a single bimorph, the second case when the harvester includes three identical bimorphs of the same operational frequency (250 Hz) and connected in indirect series and finally the third case when these three bimorphs are connected in direct series.

It is clear that connecting identical bimorphs of same operational frequency in series directly gives the greater DC voltage and it is more than the required voltage for making the temperature sensor operates. Therefore, this connection can be used to achieve one of two requirements: the first that such harvester of three bimorphs can be excited only by acceleration of amplitude $1.9\ \mathrm{m/s^2}$ to generate the DC voltage required for the temperature sensor operation. This makes such type of harvesters are relevant for small excitation level. The second is that such harvester can be designed not to operate at its parallel-resonance frequency and that causes a considerable reduction in the deflection of the bimorph and so increases the life time of the piezoelectric harvester. For example the autonomous system implemented before which was excited by an acceleration of frequency 250 Hz, if the harvester of this autonomous system includes a single bimorph, then this bimorph should have a parallel-resonance frequency matching the excitation frequency and is deflected 95.2 μm to generate 1.5 V DC voltage. But if the harvester includes three bimorphs, then each bimorph should have a parallel-resonance frequency of 242.6 Hz or 257 Hz and deflects with amplitude of 35.7 μm in order to be the total output DC voltage of 1.5 V.

If it is required from using the multiple bimorphs to enhance the frequency bandwidth of the harvester, then operations of the bimorphs should be integrated by tuning each one to a different frequency, as discussed earlier in tuning strategy. **Fig. 14** shows that the single bimorph can generate 1.5 V DC voltage only at a single frequency (250 Hz), but using three bimorphs can extend this frequency into a considerable range of frequencies. It seems for the first moment that using three bimorphs in direct series connection gives a larger range of operational frequencies, but unfortunately the fluctuation in the generated voltage is too large due to the overlap of the generated AC voltages (amplitudes and phases) of three bimorphs. Connecting the bimorphs in indirect series also offers a considerable enhancement in the harvester frequency bandwidth from 243 Hz to 256 Hz with a reasonable fluctuation in output DC voltage.

5- CONCULSION

The feasibility of using harvester with multiple piezoelectric elements has been investigated. For this purpose a cantilever array with three piezoelectric bimorphs was constructed to be used in experimental verification. The results show good agreement between the theoretical and the experimental works. Strategies for connecting multiple bimorphs to increase the maximum generated power and/or enhance the bandwidth compared to a single bimorph harvester were also investigated.

The results show that the harvester with three bimorphs of identical optimal frequency can be used either if the excitation amplitude is small or if it is required to generate higher voltage. The result shows that the generated DC voltage of harvester with three bimorphs can be reached to four times that generated of the harvester of single bimorph.

The results also show that using the proposed strategy of the optimal frequency tuning extends the harvester frequency bandwidth considerably. The harvester of three bimorphs can generate 1.5 V DC for a range 13 Hz instead of generating this voltage at only single frequency.

ACKNOWLEDGMENT

The author gratefully acknowledge the support of Prof. Dr. Walter Sextro and the staff at the Chair of Mechatronics and Dynamics / University of Paderborn.

REFERENCES

- Al-Ashtari, W., Hunstig, M., Hemsel, T., and Sextro, W., 2012a, *Analytical Determination of Characteristic Frequencies and Equivalent Circuit Parameters of a Piezoelectric Bimorph*, Journal of Intelligent Material Systems and Structures, Vol. 23, PP. 15-23.

- Al-Ashtari, W., Hunstig, M., Hemsel, T., and Sextro, W., 2012b, *Frequency Tuning of Piezoelectric Energy Harvesters by Magnetic Force*, Smart Mater. Struct., Vol. 21, PP. 035019.

- Al-Ashtari, W., Hunstig, M., Hemsel, T., and Sextro, W., 2013, *Enhanced Energy Harvesting Using Multiple Piezoelectric Elements: Theory and Experiments*, Sensors and Actuators A, Vol. 200, PP. 138-146.

- Ferrari, M., Ferrari, V., Guizzetti, M., Marioli, D., and Taroni, A., 2008, *Piezoelectric Multifrequency Energy Converter for Power Harvesting in Autonomous Microsystems*, Sensors and Actuators A, Vol. 142 PP. 329-335.

- Shahruz, S. M., 2006a, *Design of Mechanical Band-Pass Filters for Energy Scavenging*, J. Sound and Vibration, Vol. 292, PP. 987-998.

- Shahruz, S. M., 2006b, *Design of Mechanical Band-Pass Filters with Large Frequency Bands for Energy Scavenging*, Mechatronics, Vol. 16, PP. 523-531.
- Shahruz, S. M., 2006c, *Limits of Performance of Mechanical Band-Pass Filters Used in Energy Scavenging*, J. Sound and Vibration, Vol. 293, PP. 449-461.

- Tang, L., Yang, Y., and Soh, C. K., 2010, T*oward Broadband Vibration-based Energy Harvesting*, J. Intelligent Material Systems and Structures, Vol. 21, PP. 1867-1896.

- Xue, H., Hu, Y., and Wang, Q., 2008, *Broadband Piezoelectric Energy Harvesting Devices Using Multiple Bimorphs with Different Operating Frequencies*, IEEE Transactions on Ultrasonics, Ferroelectrics and Frequency Control, Vol. 55, PP. 2104-2108.

NOMENCLATURE

B = equivalent mechanical damping of a piezoelectric device, Ns/m

C_p = equivalent capacitance of the piezoelectric material, F

C_R = reservoir capacitor, F

$F(t)$ = applied excitation force, N

f_a = frequency at which piezoelectric element generates maximum voltage, Hz

f_h = frequency at which piezoelectric element generates half maximum voltage, Hz

K = equivalent mechanical stiffness of a piezoelectric device, N/m

M = total equivalent mass of a piezoelectric device, kg

n = number of used piezoelectric elements included in the harvester

$q_R(t)$ = generated charge of the piezoelectric harvester at resistive load condition, V

R_l = connected Resistive load, Ω

t = time, s

t_p = period

t_0 = dead zone interval, s

t_{tr} = transient conduction interval, s

t_{ss} = steady-state interval, s

t_{op} = open circuit interval, s

U_d = diode drop barrier voltage, V

U_g = amplitude of the total generated voltage of a harvester included multiple piezoelectric elements connected directly in series, V

U_i = amplitude of the generated voltage of the i^{th} piezoelectric element at resistive load condition, V

U_o = amplitude of the generated voltage at open circuit condition, V

$u_o(t)$ = generated AC voltage of the piezoelectric harvester at open circuit condition, V

$u_R(t)$ = generated AC voltage of the piezoelectric harvester at resistive load condition, V

U_s^d = generated DC voltage of a harvester included multiple piezoelectric elements connected directly in series, V

U_s^i = generated DC voltage of a harvester included multiple piezoelectric elements connected indirectly in series, V

U_s^l = generated DC voltage of a harvester included multiple piezoelectric elements when excitation frequency match the optimal frequency of one element, V

$u(t)$ = generated AC voltage of the piezoelectric harvester (general), V

$x_o(t)$ = displacement of the piezoelectric harvester at open circuit condition, m

$x_R(t)$ = displacement of the piezoelectric harvester at resistive load condition, m

α = conversion factor between the mechanical and electrical domains of a piezoelectric device, N/V

ζ = equivalent damping ratio of the piezoelectric device

φ_{uo} = phase difference between the excitation force $\mathrm{F}(t)$ and the generated voltage $u_o(t)$, rad

φ_{uR} = phase difference between the excitation force $\mathrm{F}(t)$ and the relative velocity $u_R(t)$, rad

ω = Angular frequency of the excitation, rad/s

ω_n = natural frequency of piezoelectric harvester, rad/s

ω_s = series frequency of piezoelectric harvester, rad/s

ω_p = parallel frequency of piezoelectric harvester, rad/s

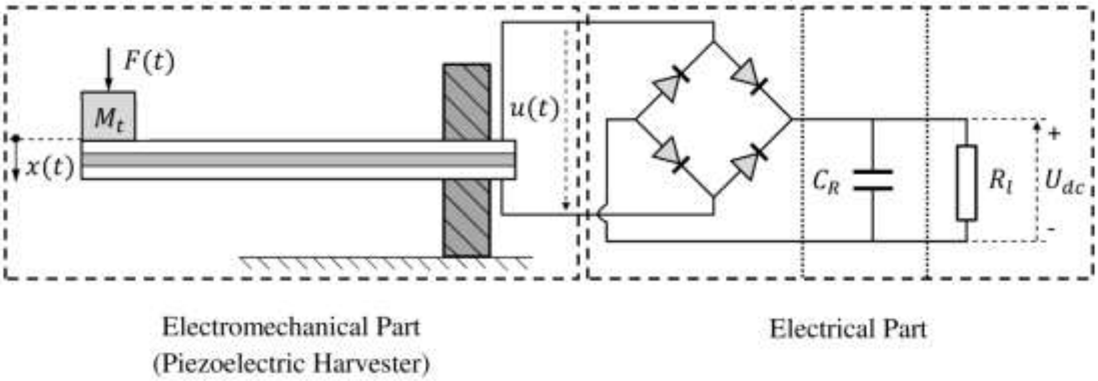

Figure 1. Basic autonomous system.

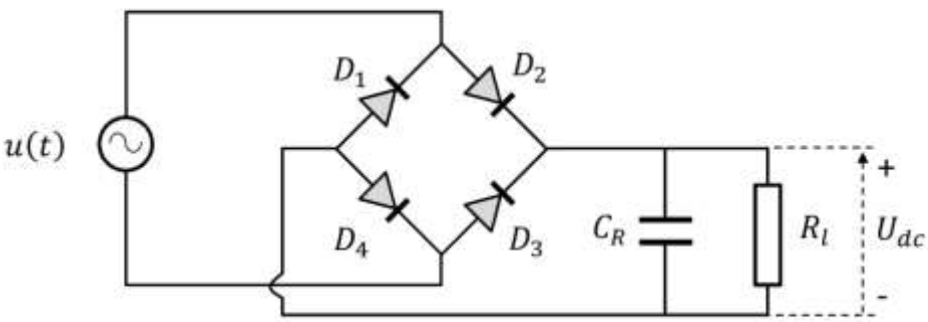

Figure 2. Electrical representation of a basic autonomous system.

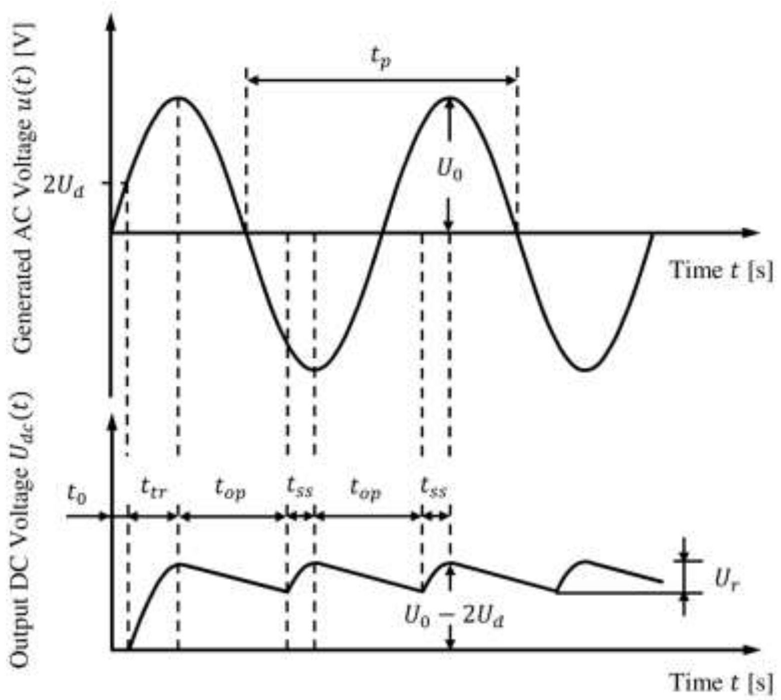

Figure 3. (a) Applied AC voltage $u(t)$ and **(b)** the output DC voltage across the connected load U_{dc}.

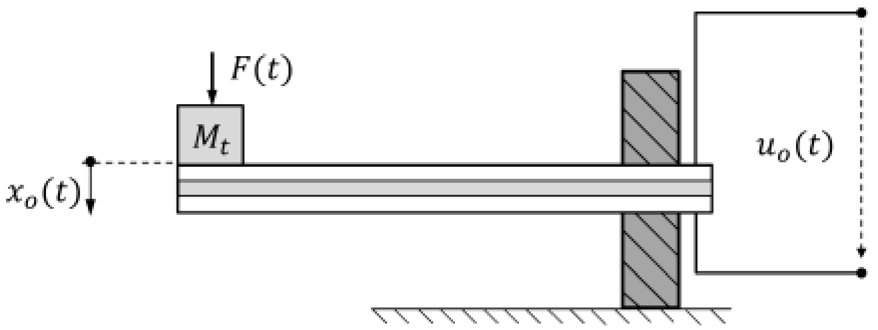

Figure 4. Piezoelectric Harvester in open circuited condition.

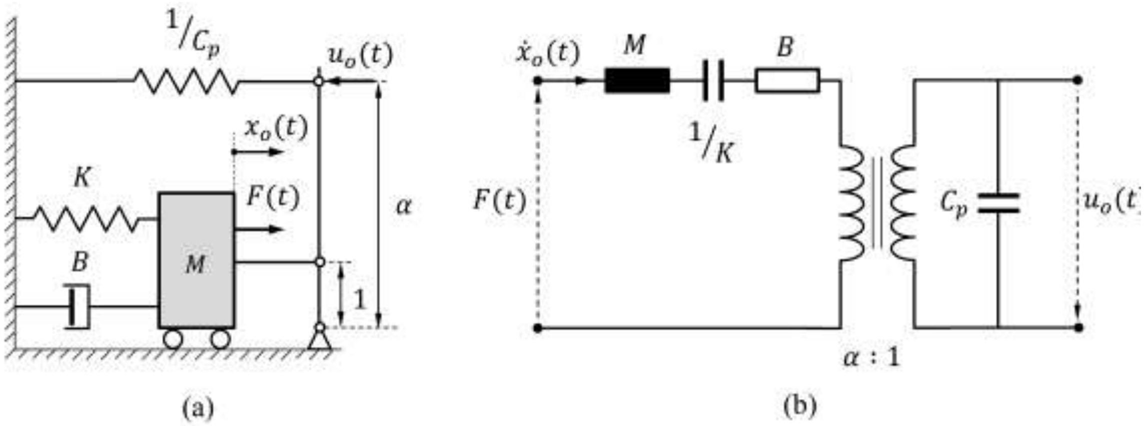

Figure 5. Equivalent systems of the piezoelectric harvester for autonomous system **(a)** mechanical **(b)** electrical

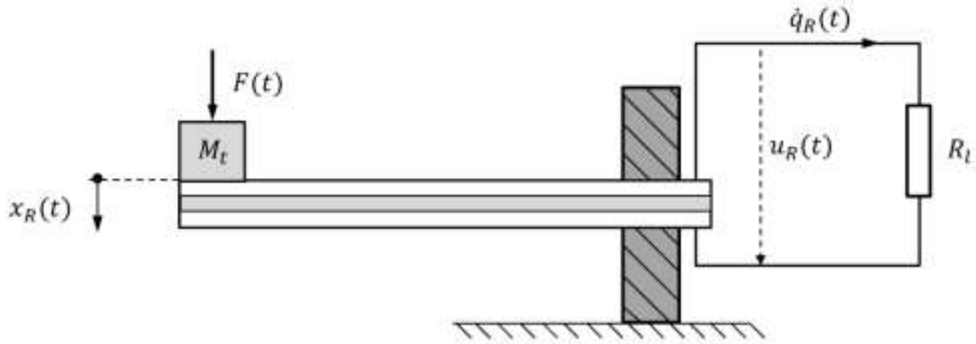

Figure 6. Piezoelectric harvester connected to a resistive load.

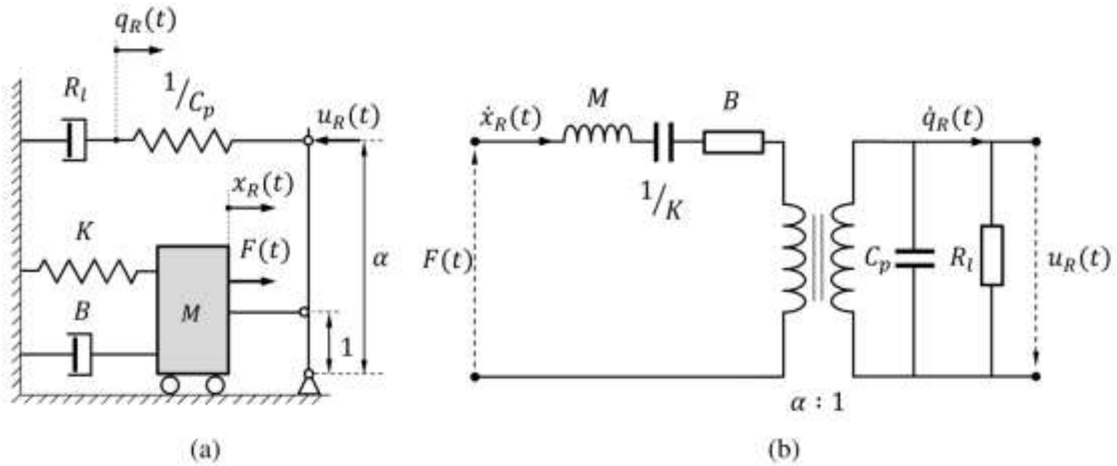

Figure 7. Equivalent systems of piezoelectric harvester connected to resistive load **(a)** mechanical and **(b)** electrical.

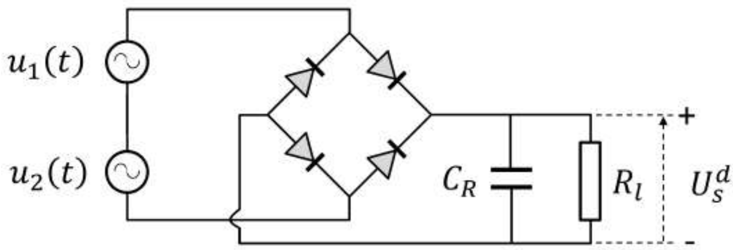

Figure 8. Autonomous system including a harvester with two piezoelectric elements connected in direct series.

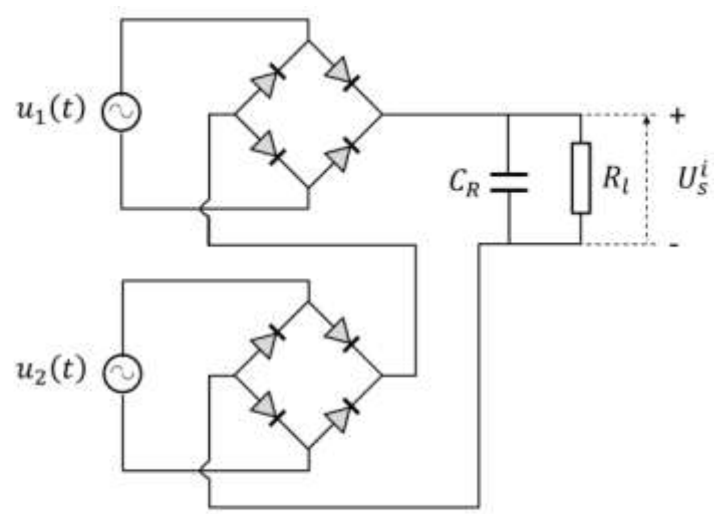

Figure 9. Autonomous system including a harvester with two piezoelectric elements connected in indirect series.

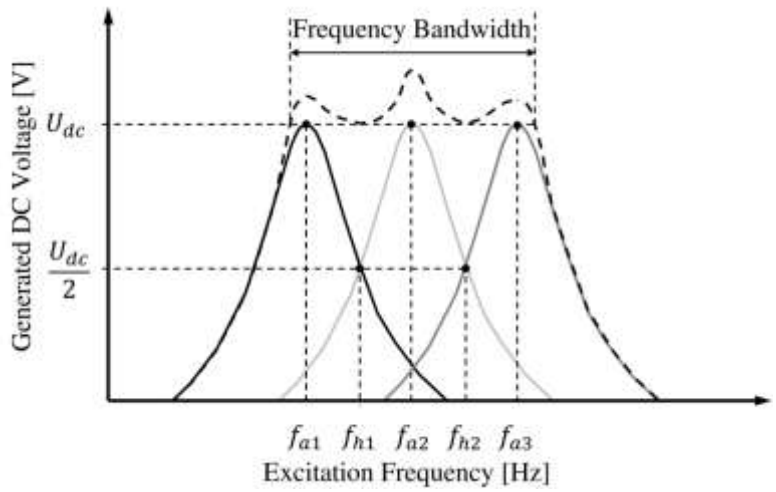

Figure 10. Tuning strategy for bandwidth enhancement.

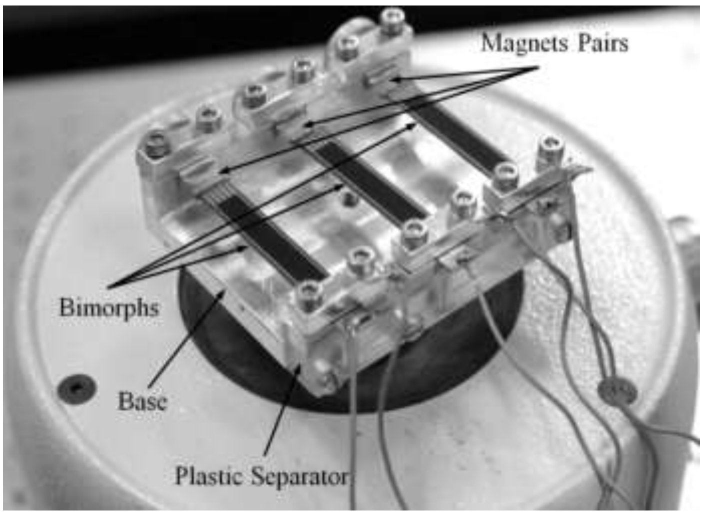

Figure 11. Experimental rig showing a cantilever array of three piezoelectric bimorphs**.**

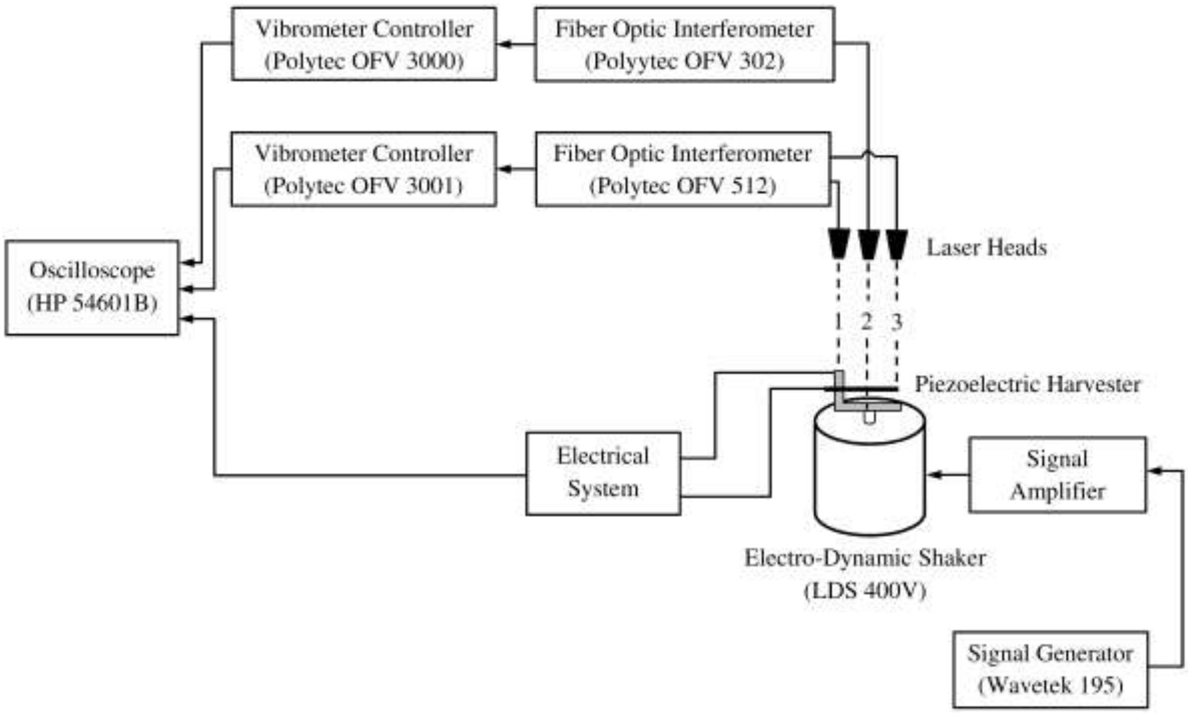

Figure 12. Schematic diagram of the experimental setup.

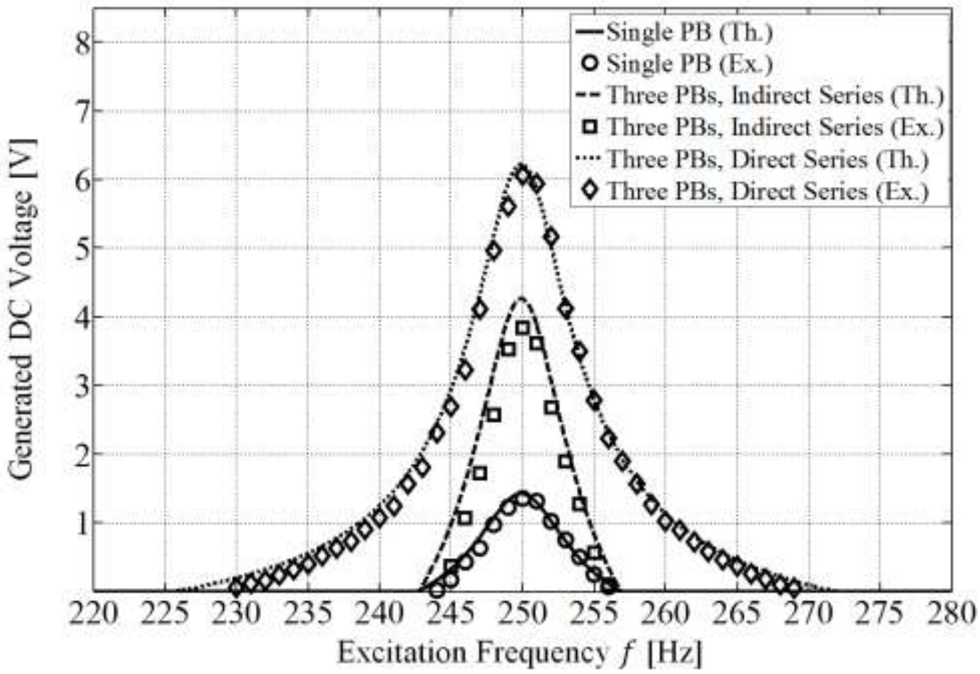

Figure 13. Generated DC voltages of harvesters of differenet number of bimorphs and different electrical connection, all bimorhs are tunned to have same optimal frequency.

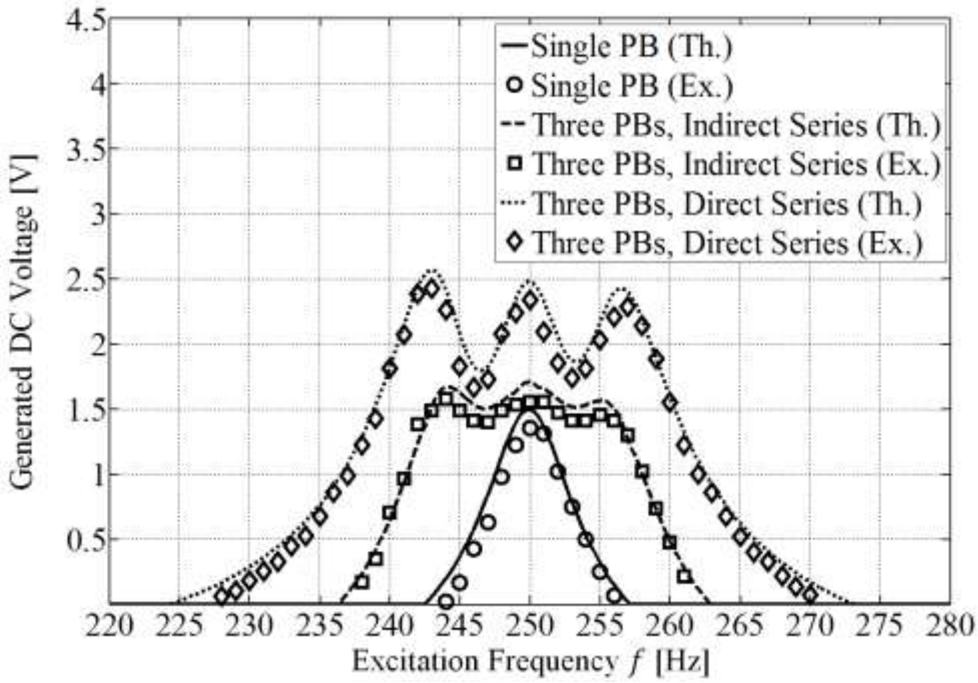

Figure 14. Generated DC voltages of harvesters of differenet number of bimorphs and different electrical connection, bimorphs are tunned using the propsed tuning strategy.

Table 1. Bimorph Specifications.

Parameter	Value
Total length of piezoelectric layers	$45.00\ \pm 0.1$ mm
Beam width	$7.20\ \pm 0.1$ mm
Total beam thickness	$0.78\ \pm 0.03$ mm
Shim layer thickness	$0.28\ \pm 0.05$ mm
Piezoelectric layer density	$8000\ \mathrm{kg/m^3}$
Shim layer density	$1800\ \mathrm{kg/m^3}$
Piezoelectric coupling factor	0.38
Piezoelectric compliance	$15.8 \times 10^{-12}\ \mathrm{m^2/N}$
Piezoelectric dielectric constant	$61.95\ \mathrm{nF/m}$
Beam mechanical quality factor	45
Shim layer modulus of elasticity	$120 \times 10^9\ \mathrm{N/m^2}$

Reduction of Noise and Vibration of Spur Gear by Using Asymmetric Teeth Profiles with Tip Relief

Mohammad Qasim Abdullah
Professor
Engineering College, University of Baghdad
Email:mohq1969@yahoo.com

Adnan Naji Jameel
Professor
Engineering College, University of Baghdad
Email: adnanaji51@coeng.uobaghdad.edu.iq

Husam Saad Hasan
PHD Student
Engineering College, University of Baghdad
Email:hussamsaad82@yahoo.com

ABSTRACT

Reduction of noise and vibration in spur gear experimentally by using asymmetric teeth profiles with tip relief was presented. Both of classical (symmetric) and asymmetric (with and without tip relief) spur gears are used in this work. Gear test rig was constructed to achieve torsional vibration measuring, and two modified cutters are designed and manufactured to achieve tooth profile modifications. First to cut asymmetric gear tooth with pressure angles ($14.5^{o}/25^{o}$) without tip relief for loaded and unloaded tooth sides respectively, and second to cut asymmetric gear tooth with pressure angles ($14.5^{o}/25^{o}$) for loaded and unloaded tooth sides respectively with tip relief to achieve best dynamic performance. Dynamic load factor, transmission error and noise level are carried out in this work. Final results showed improvement in dynamic load factor and noise level for asymmetric gear (with and without tip relief) compared with classical spur gear .

Key words: dynamic load factor, tooth transmission error, asymmetric tooth profile , tooth tip relief.

اختزال الضوضاء والاهتزاز للمسننات العدلة بواسطة جانبيات الاسنان غير المتناضرة مع تشذيب الحواف

محمد قاسم عبد الله
استاذ
جامعة بغداد / كلية الهندسة

عدنان ناجي جميل
استاذ
جامعة بغداد /كلية الهندسة

حسام سعد حسن
طالب دكتوراة
جامعة بغداد / كلية الهندسة

الخلاصة

تم تقديم اختزال الضوضاء والاهتزاز للمسننات العدلة عمليا بواسطة استخدام جانبيات اسنان غير متناضرة مع تشذيب الحواف في هذا البحث. كلا من الاسنان المتناضرة والغير متناضرة (مع تشذيب الحواف وبدونها) تم استخدامه في هذا العمل. منصة اختبار المسننات بنيت خصيصا لتحقيق قياس الاهتزاز الدوراني وتم تصميم وتصنيع قاطعات مسننات محورة لتحوير جانبيات الاسنان. الاولى لقطع مسنن غير متناظر ذو زوايا ضغط (25/14.5) درجة بدون تشذيب الحواف. والثانية لقطع مسنن غير متناضر ذو زوايا ضغط (25/14.5) درجة ذو خاصية على تشذيب حواف المسنن وذلك لضمان افضل اداء

ديناميكي . في هذا البحث تم استخراج معمل الحمل الديناميكي وخطا النقل الديناميكي ومستوى الضوضاء . النتائج النهائية اظهرت تحسين في معمل الحمل الديناميكي ومستوى الضوضاء للمسننات غير المتناضرة (بوجود وعدم وجود تشذيب لحافات الاسنان) مقارنة بالاسنان التقليدية .

الكلمات الرئيسية : معامل الحمل الديناميكي , خطأ النقل لسن المسنن ,اسنان غير متناضرة الجانبيات , تشذيب حواف الاسنان.

1. INTRODUCTION

Dynamic loads, vibration and noise level have been considered as a major problem in transmitting machines especially at high speeds and heavy loads .Tooth transmission error (Tm) and non linear mesh stiffness have been represented a major excitation sources for vibration and noise in gear drive system, as the tooth transmission error defined as the difference between actual and ideal position of driven gear . The aim of this paper is reducing of dynamic load factors, transmission error and noise level by modifying gear tooth profiles experimentally by using asymmetric teeth profiles with tip relief, where relief defined as removing metal from the tip or the root of the teeth or from both, **Smith, 1999**. Little literature attempted to investigate dynamic characteristics of spur gear system experimentally. **Munro, 1962** measured dynamic transmission error in spur gear pair, he selected high precision spur gears with manufacturing errors much smaller than tooth deflection, and he applied tooth profile modifications to achieve minimum static transmission error at design load. **Kubo, 1962** designed gear test rigs which were heavily damped, he measured dynamic root stress and then estimated the dynamic factor. **Smith, 1999** used two smaller optical rotary encoder made by Heidenhain Ltd. which had become readily available and used extensively for rotary positioning system on tooth geared system. His results indicated error below 0.1 second of arc at operating speed. **Kang ,2009** indicted the shaft compliance effect on dynamic Tranmission error, he used tangential accelerometer for measuring the gear motions in rotational, torsional and translitional axis, he used spur and helical gears in his experimental work. In this work gear test rig was built to achieve torsional vibration measuring, and two modified cutters was designed and manufactured to achieve tooth profile modifications such as asymmetric tooth profile with and without tip relief to improve dynamic load factor, transmission error and noise level.

2. PROBLEM FORMULATION

Simple dynamic model with single degree of freedom has been employed in this work ;therfore , equation of motion will be, **Hasan, et al,2014** :

$$m_e \ \ddot{x} \ + c_m \dot{x} \ + k_m \ (t) \ x = \ F \qquad (1)$$

Where *x(t)* refers to dynamic transmission error of a gear pair along its line of action which defined as:

$$x(t) = \ r_{b1} \theta_1 - r_{b2} \theta_2 - e(t) \qquad (2)$$

r_{b1} & r_{b2} represented base radius for pinion and gear respectively , θ_1 & θ_2 represented angular displacement for gear and pinion respectively, and *e(t)* represented periodic static transmission error , m_e equivalent mass, k_m non linear mesh stiffness , c_m non linear mesh damping and F static load .

Dynamic load factor in gear drive system defined as the ratio of dynamic mesh load to static load under operating speed :

$$DLF = \ \frac{F_d}{F} \qquad (3)$$

Dynamic mesh load in Eq. (3) defined as, **Duboswky and Freudenstein, 1971**:

$$Fd = c_m \dot{x} + k_m (t)\, x \tag{4}$$

Sub. Eq. (4) in Eqs. (1) and (3). Dynamic load factor has been written in terms of second derivative of transmission error as:

$$DLF = 1 - \frac{m_e \ddot{x}}{F} \tag{5}$$

Where ($\ddot{x}$ & x) measured by gear test rig experimentally as shown in next section .

3. GEAR TEST RIG

Test rig was constructed to analyze dynamic performance in gear drive system such as dynamic load factor, transmission error and noise level. Three types of steel spur gear pairs with a unity speed ratio (1:1) and a fixed center distance of 98 mm had been selected to be under the test. The first type was symmetric spur gear with classical pressure angles ($20^{o}/20^{o}$). The second type was asymmetric spur gear with pressure angles ($14.5^{o}/25^{o}$) for loaded and unloaded tooth sides respectively. Third type was asymmetric spur gear with pressure angles ($14.5^{o}/25^{o}$) for loaded and unloaded tooth sides respectively but with tip relief. All design parameters of the symmetric and asymmetric spur gear drives with and without tip relief are listed in table (1). The chemical composition of the spur gears (pinion and gear) and shafts material are inspected in “Specialized Institute for Engineering Industries/Ministry of Industry & Minerals/Iraq” that was listed in Appendix (A) .

A gear milling operation had been adopted to manufacture the test specimens (prototypes) of all spur gears by using standard and modified gear milling cutters.

A standard HSS gear milling cutter of disc type had been adopted to cut symmetric prototypes of spur gears (pinion and gear). According to the design specifications of DIN 3972, the cutter number can be selected by depending on the gear design parameters to be cut, where each cutter number was designed to cut a range of teeth number for certain pressure angle and module, therefore; with gear design parameters $\phi = 20^{\circ}$, $m_o = 7$ mm and $z = 14$ teeth, cutter No.2 in Appendix (B) had been selected, where this cutter can be used to cut three gears with different number of teeth ($z = 14$, 15 and 16 teeth) .

A modified HSS gear milling cutter of disc type with asymmetric involute profiles with optimal fillet radii and without tip relief had been designed by **Abdullah and Jweeg, 2012,** depending on the tooth profiles geometry. Asymmetric tooth profiles with tip relief had been design depending on reduction in static transmission error by selecting appropriate amount and location of tip relief on asymmetric tooth profile (tip amount 40 micron , start relief lied on 0.33 base pitch on involute profile) as shown in **Fig.1** ,amount and extent of tip relief achieved theoretical basis of spur gear profile relief design that established by **Munro et ,al ,1990** and **palmer ,1999** .

The workshop drawings and manufacturing of these cutters had been achieved by “Acedes Gear Tools Company (division of Furzeland Ltd.) / UK-England”. Final products of these cutters are shown in **Fig.2**. Test rig (gear-shaft-bearing system) as shown in **Fig.3** had been constructed precisely to indicate dynamic load factor, transmission error and noise level under certain external load and rotational speed values for symmetric , asymmetric and asymmetric with tip relief spur gear . Two steel gears (pinion and gear) of the same diameter of 98 mm are fixed on two steel shafts with diameter of 49 mm; where two ball bearings supported each shaft. AC motor (3 KW, 2880 rpm, Three-phases, 220~230 Volt, 50~60 Hz, MeZ Electric Motors Ltd./Czech Rep.) was used to provide sufficient amounts of the required torque to overcome the overall inertias of mechanical components of test rig and steel flywheels with masses (5 kg , 15 kg , 25kg , 35 kg) respectively. Speed control was automated by using a controller speed device

(Variable Frequency Drive , Power range: from 0.4 to 3.75 KW, Three phase, 220~230 Volts, 50~60 Hz, Delta Industrial Systems Co. Ltd./ Taiwan) . A thick steel plate with dimensions (700 × 300 × 20 mm) was used as a platform for fixing the motor by using four bolts with diameter of 10 mm and the fixed four housings by using four bolts with diameter of 12 mm for each housing. The measurement system was designed to perform measuring torsional vibration components ($\theta 1$ and θ_2) for both pinion and gear. Uni-axial tangential accelerometer was devised. Accelerometers (PCB Piezotronics, Model: 353B18, sensitivity: nearly 10 mV/g, frequency range: 0 to 10 kHz) can be mounted tangentially at pinion and gear respectively as shown in **Fig4**.

The accelerometers data are fed to the fixed frame through the end-of-shaft by using slip rings (Jinapat SR, Model: LPT038). Signals transmitted from the slip rings are fed into a multi-channel signal conditioner (PCB Piezotronics ICP Model 482C64) to condition and amplify the data. Then, the signals are fed to Digital storage Oscilloscope that digitizes the analog signals at a user defined sampling rate and monitoring signals in voltage amplitudes, **Fig. 5** shows the flow chart for measurement system .

Sound intensity levels can be measured by using a sound level meter *(*Model: SL-4022, IEC 61672 class 1, Microphone type: Electrical condenser, Measurement range: from 30 to 130 dB, Lutron Electronic Enterprice Co. Ltd./Taiwan*)* by putting meter microphone vertically with a distance 15 Cm above the gears engagement location to obtain purest sound signal as shown in **Fig. 6** .

4. RESULTS AND DISCUSSION

Digital storage oscilloscope shows accelerometers signals, but in voltage amplitudes, so these data should be converted to acceleration values in (m/s^2) by using accelerometer conversion scale. Dynamic transmission error defined as the difference between axial displacement of pinion and gear ; therefore, Sigview software (V 2.6) analyzed storage signals and integrated it twice to carry out dynamic transmission error and dynamic load factor.

Fig. 7 shows the variation of noise levels (sound intensity level in dB) with rotational speed of motor for both of asymmetric gear teeth with and without tip relief. Generally Tip relief in asymmetric gear teeth reduced the noise levels of spur gear by around (10 -20) % in low speeds (less than 1000 rpm) and by around (2 -5) % in high speeds (more than 3000 rpm).

Fig.8 shows dynamic load factors with rotational speed of motor for symmetric gear teeth with pressure angles (20^{o} /20^{o}) and asymmetric gear teeth with pressure angles (14.5^{o} /25^{o}) without tip relief . Generally asymmetric gear tooth with tip relief shows improvement in dynamic load factors at all speeds except at super harmonic frequency which occurred at 1000 rpm .In high speeds (more than 2000 rpm) the dynamic load factor became greater compared with low speeds and symmetric gear tooth recorded high peak of dynamic load factor at 2200 rpm which approximate 6 for dynamic load factor .

Fig. 9 shows comparison between dynamic load factors with rotational speed of motor for asymmetric tooth gear with and without tip relief , this figure shows convergence in results but with improvement for asymmetric tooth without tip relief at low speeds (less than 1000 rpm) and improvement for asymmetric tooth with tip relief at high speeds (more than 1200 rpm) .

Fig. 10 shows the effect of different inertial loads on dynamic load factors for asymmetric gear tooth with tip relief. (5kg, 15 kg and 25 Kg) fly wheels are used in gear test rig. In low speeds (less than 1500 rpm) both of (5 and 25 kg) flywheels showed improvement in dynamic load factors compared with 15 kg flywheel . In high speeds (more than 1500 rpm) 15 kg flywheel showed improvement in dynamic load factors compared with 25 kg flywheel which was increased while 5kg inertia still better compared with both of (15 &25 kg) flywheels.

Fig. 11 shows dynamic load factors for symmetric gear tooth with loaded pressure angle (20^0) and asymmetric gear tooth with tip relief and loaded pressure angle (25^0) with rotation speed . Results showed improvement by around (51%) in asymmetric gear tooth at most speeds (higher than 500 rpm) although loaded pressure angle in symmetric gear tooth lower than asymmetric gear (25^0) due to modified loaded tooth side by medium tip relief.

Fig.12 shows dynamic transmission error for symmetric and asymmetric tooth gear with rotation speed, it's clear that asymmetric gear tooth showed improvement by around (50 %) in dynamic transmission error compared with symmetric tooth gear at all speeds except (1000 rpm) .

Fig. 13 shows improvement by around (50%) in dynamic transmission error for asymmetric gear tooth without tip relief compared with asymmetric gear tooth with tip relief at low speeds (less than 1100 rpm) ,for other speeds tip relief modification in asymmetric tooth profile improve dynamic transmission error in spur gear by around (20-66 %) .

Fig. **14** shows the effect of different inertias on dynamic transmission error for asymmetric tooth gear with tip relief , and three regions were remarked in this figure. In low speeds (less 1000 rpm) (5kg and 25 kg) flywheels showed improvement in results compared with 15 kg flywheel , at speeds (1000 -2000 rpm) (15kg and 25 kg) flywheels show improvement in results compared with 5 kg flywheel , at high speed (more than 2000 rpm) 15 kg flywheel shows improvement in results compared with (5 kg and 25 kg) flywheels .

Table 2 showed maximum dynamic load factors and maximum dynamic transmission errors that were recorded in previous figures.

5. CONCLUSION

Noise level, Dynamic load factor and dynamic transmission error are carried out experimentally in this paper. Results showed that the noise radiated from asymmetric gear drive system was improved when asymmetric profiles modified by appropriate tip relief by around (10 -20) % in low speeds and by around (2 -5) % in high speeds .

Asymmetric gear teeth with and without tip relief showed improvement in dynamic load factor and dynamic transmission error compared with symmetric gear tooth where percentage improvement reach (50 – 80) % in different rotations speed. Minimum flywheel (5 kg) used in asymmetric gear drive showed lowest dynamic load factor compared with other flywheels while (15) kg flywheel showed lowest dynamic transmission error compared with other flywheels.

REFRENCES

- Abdullah ,M.Q., and Jweeg ,M.J. ,2012, *Simulation of Generation Process for Asymmetric Involute Gear Tooth Shape with and without Profile Correction*, Innovative Systems Design and Engineering , Vol.3 ,No. 6 ,pp19-35.

- Duboswky S., and Freudenstein F., 1971, *Dynamic Analysis of Mechanical Systems with Clearance Part1and Part 2* ", ASME journal of Engineering for Industrial, pp 305 – 306.
- Husam, S. H. , Adnan ,N. J. , and Abdullah , M. Q. , 2014, *A Novel Method for Evaluating The Dynamic Load Factor of An Involute Tooth Gear with Asymmetric Profiles* , Innovative Systems Design and Engineering ,Vol. 5 , No.10 , pp 17-30.
- Kubo, A., Yamada, K., Aida, T. and Sato S., 1972, Research *on Ultra High Speed Gear Devices (reports 1-3)* ,Transactions of Japanese Society of Mechanical Engineers 38, 2692-2715.

- Kang , Ma Ru , 2009, *Measurement of Vibrations of Gears Supported by Compliant Shafts*, MS.C Thesis , university of ohio state .
- -Munro, R. G, 1962, *The Dynamic Behavior of Spur Gears*, Ph. D. Dissertation, Cambridge University.
- -Munro, R.G., Yildirim, N. , and Hall, D.M.1990, *Optimum Profile Relief and Transmission Error in Spur Gears*, I Mech E Conference on Gearbox Noise and Vibration, Paper C404/032, 35–41.
- -Palmer D., 1999,*The Effects of Profile Relief on Narrow Face Width Parallel Axis Gears*, Ph.D. Dissertation, Huddersfield University.
- - Smith J.D., 1999, *Gear Noise and Vibration*, by Marcel Dekker Inc., New York, USA , 1st Edition.

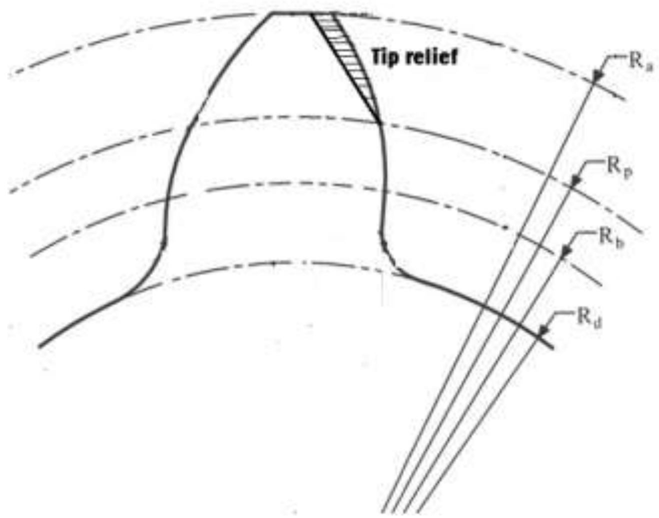

Figure 1 . Asymmetric tooth profile with tip relief.

Figure 2. Asymmetric gear milling cutter.

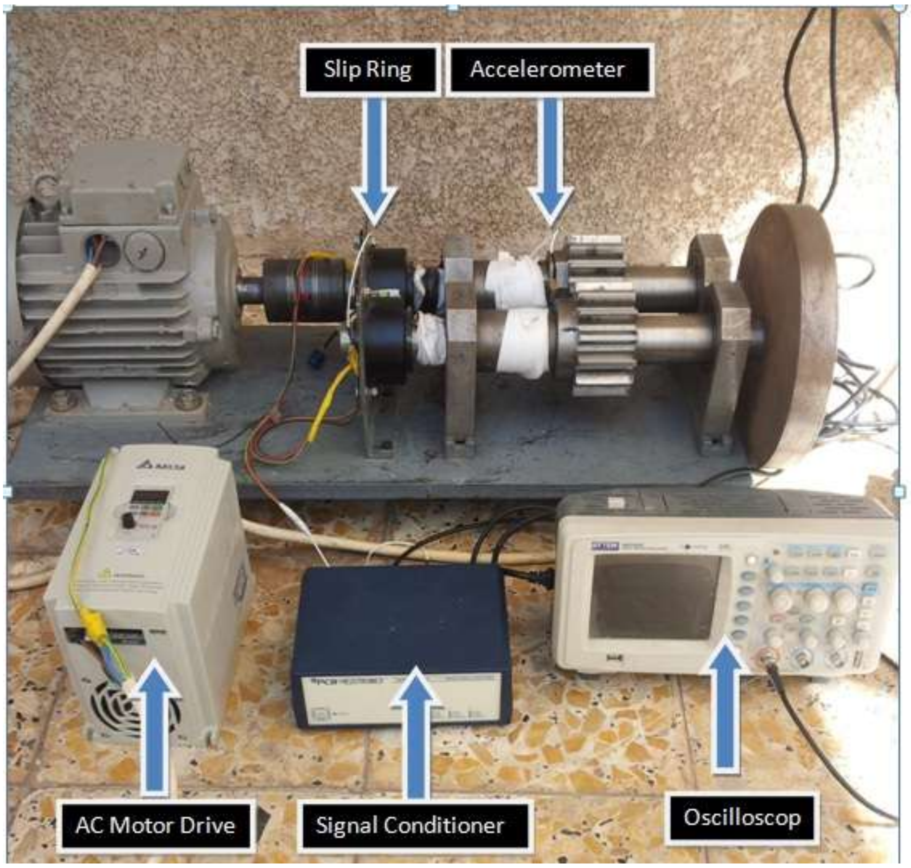

Figure 3. Gear test rig.

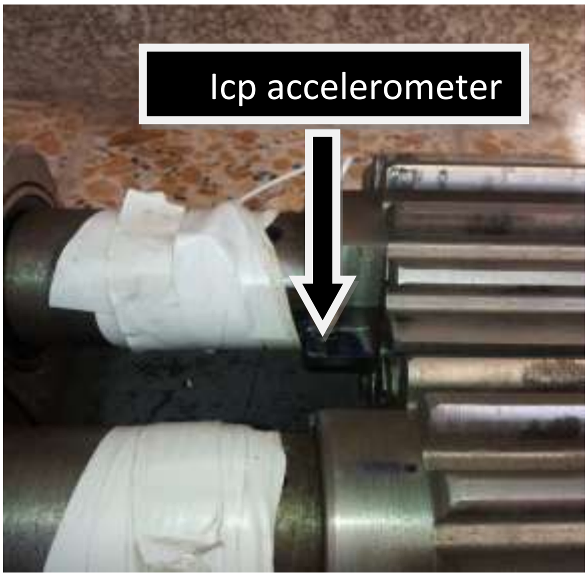

Figure 4. Tangential accelerometer.

Figure 5 . Noise measurement .

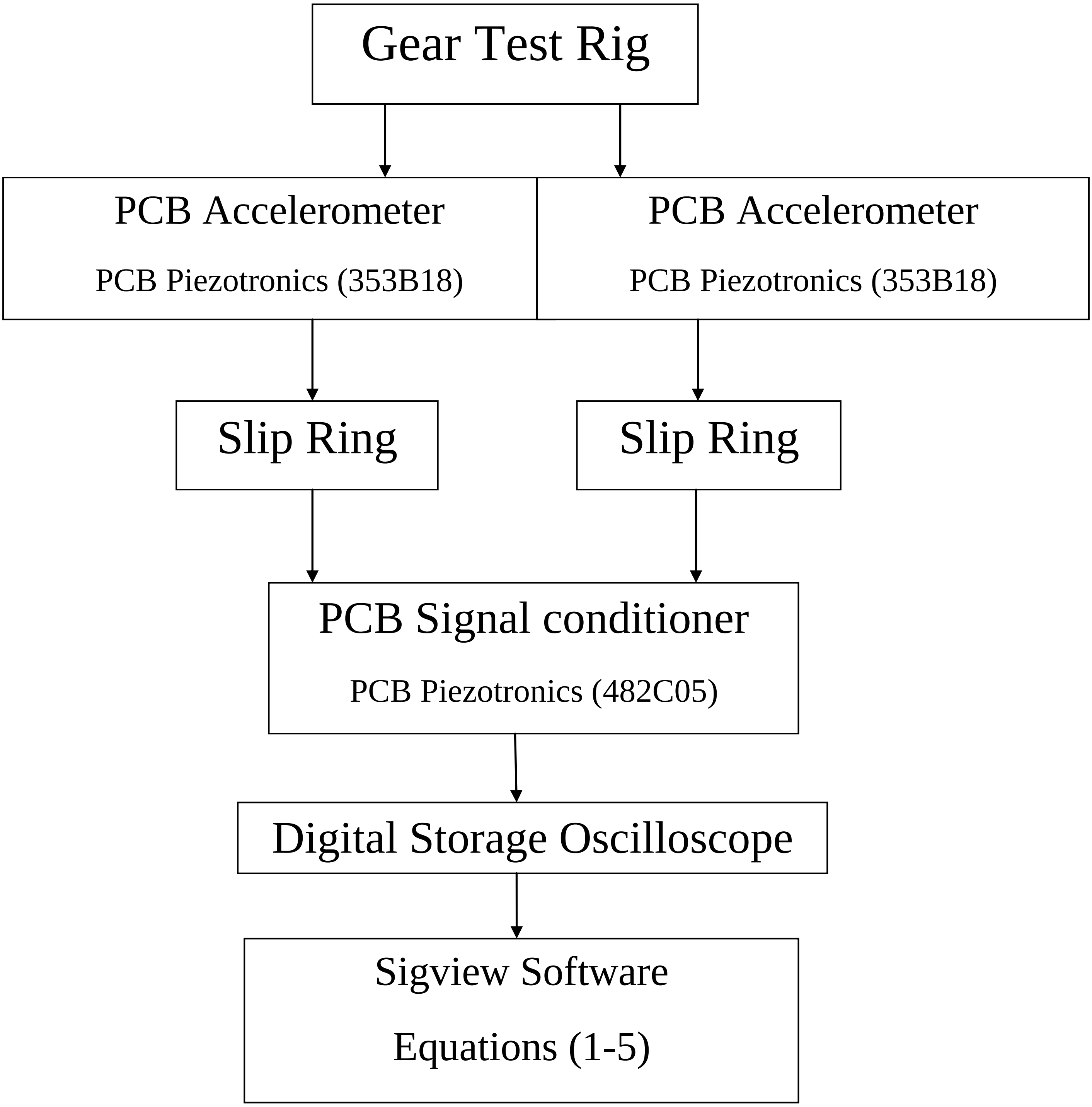

Figure 6. Flow chart for measurement system.

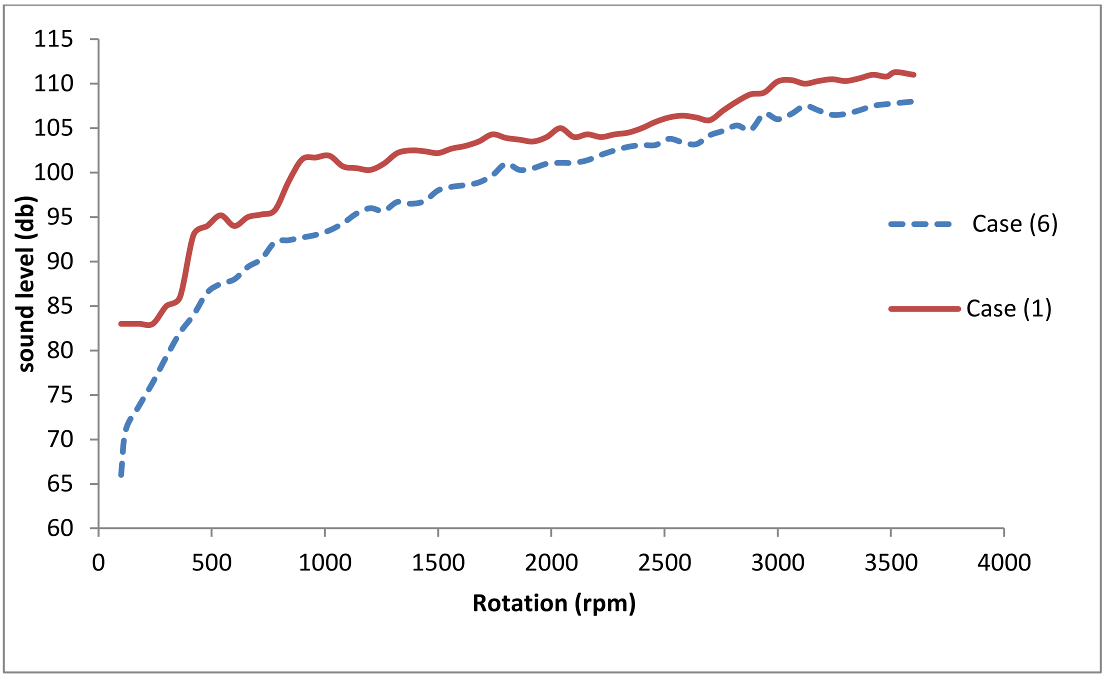

Figure 7.The Variation of sound intensity level for asymmetric gear with and without tip relief.

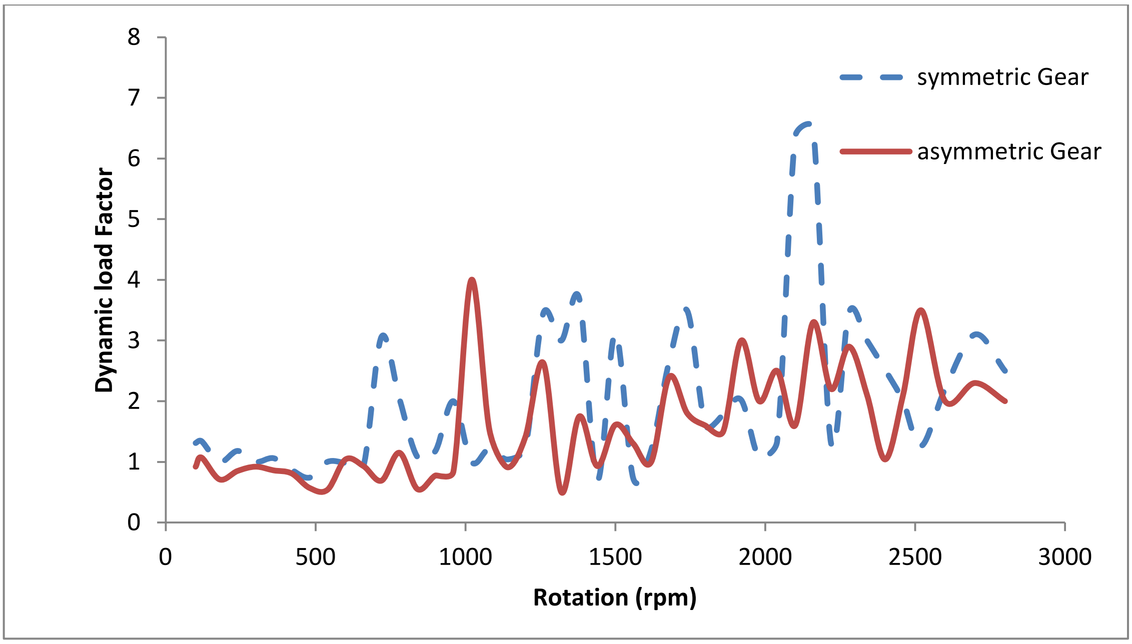

Figure 8. Dynamic load factor for symmetric& asymmetric gears.

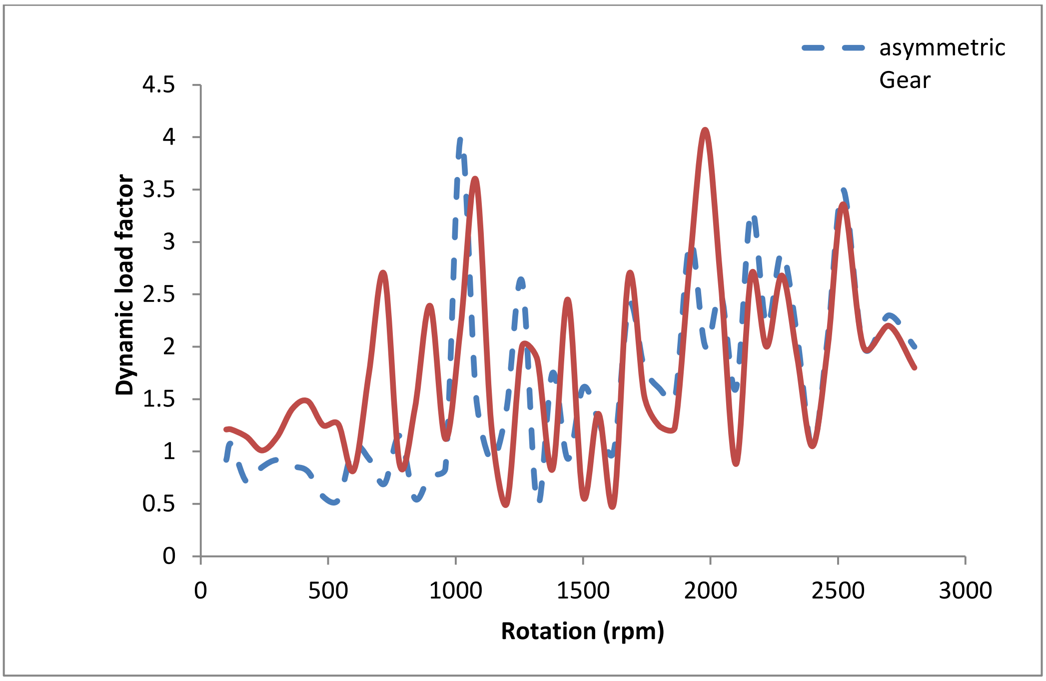

Figure 9. Dynamic load factor for asymmetric gears with and without tip relief.

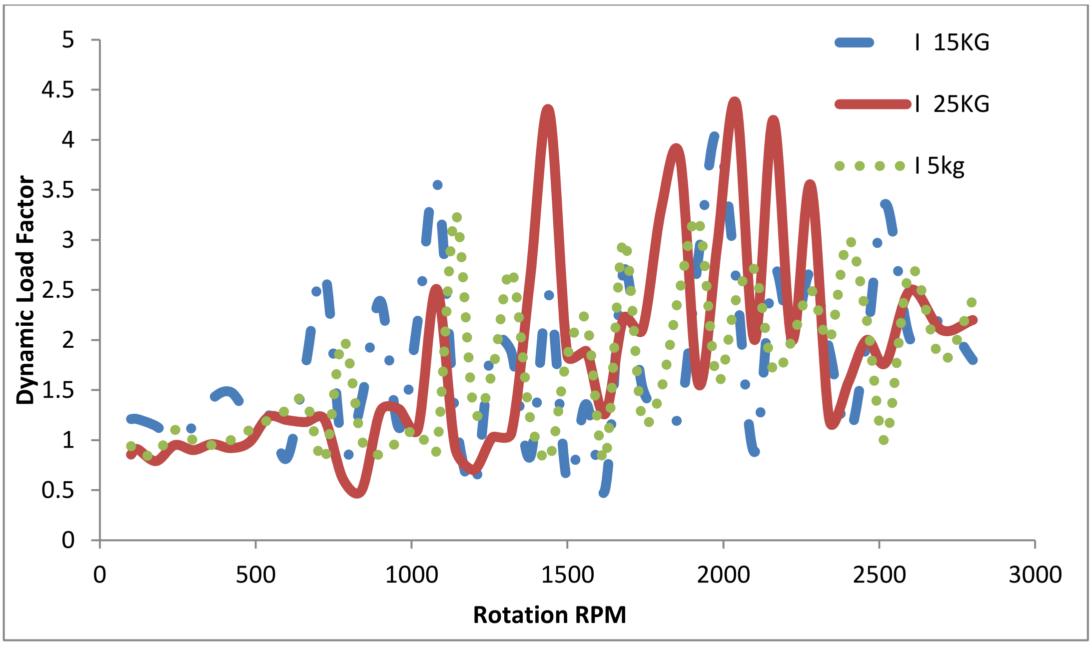

Figure 10. The effect of different inertia on dynamic load factor for asymmetric tooth gear with tip relief.

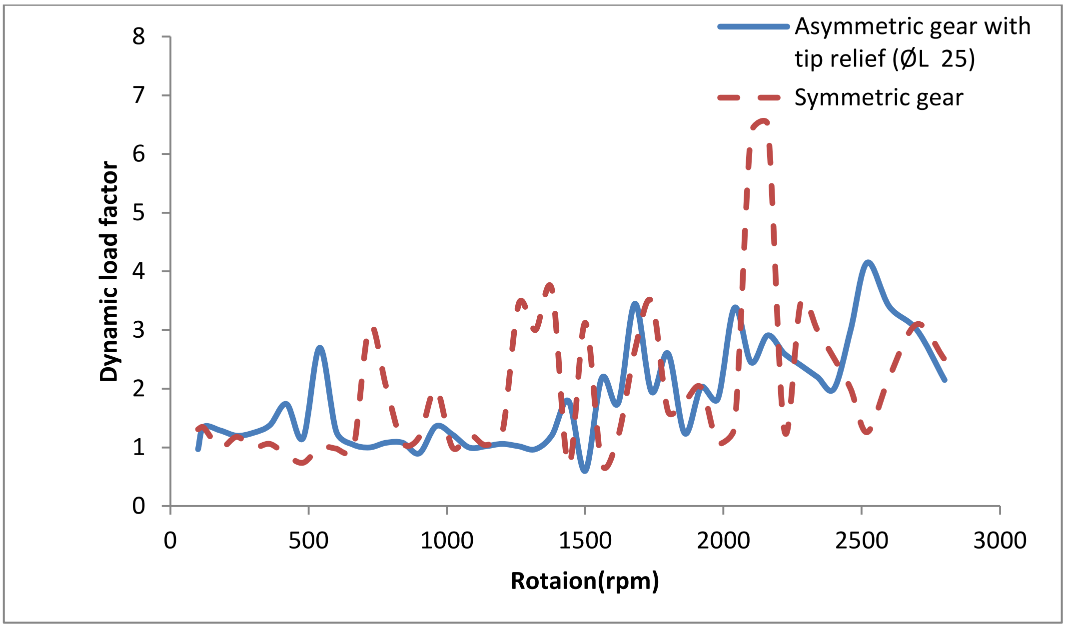

Figure 11. Dynamic load factor for symmetric gear and asymmetric gear with tip relief and loaded pressure angle (25^0).

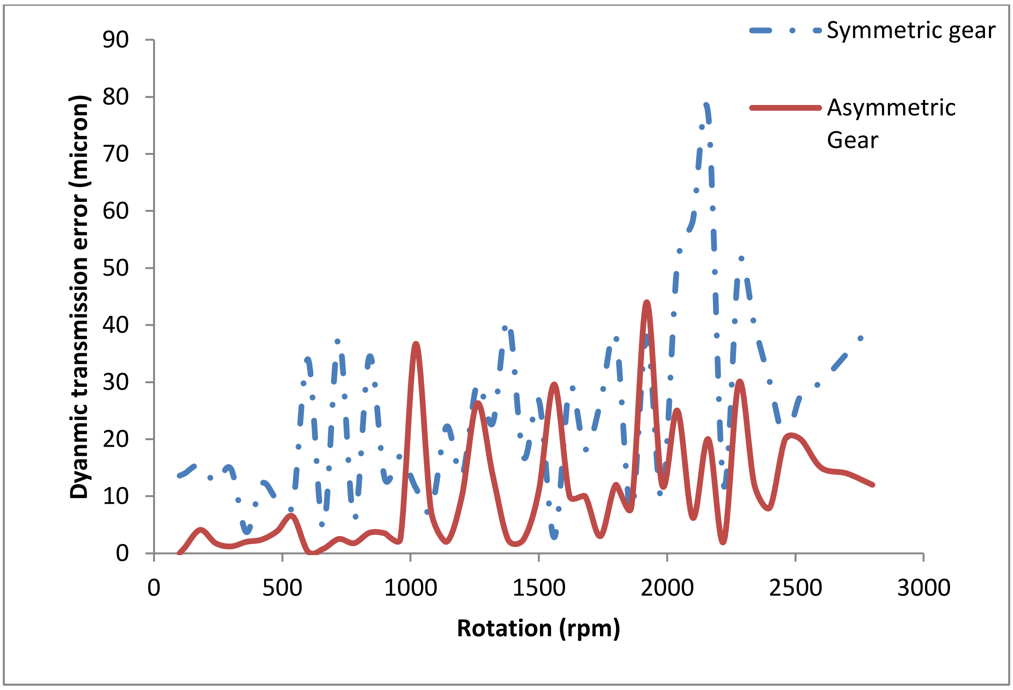

Figure 12. Dynamic transmission error for symmetric and asymmetric gear.

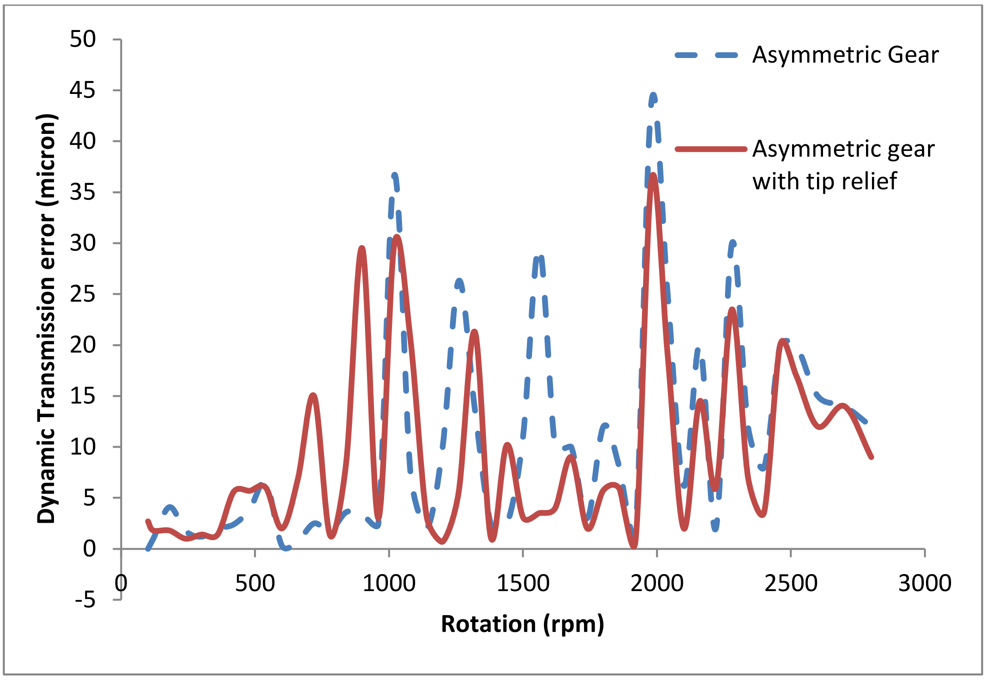

Figure 13.Dynamic transmission error for asymmetric gears with and without tip relief.

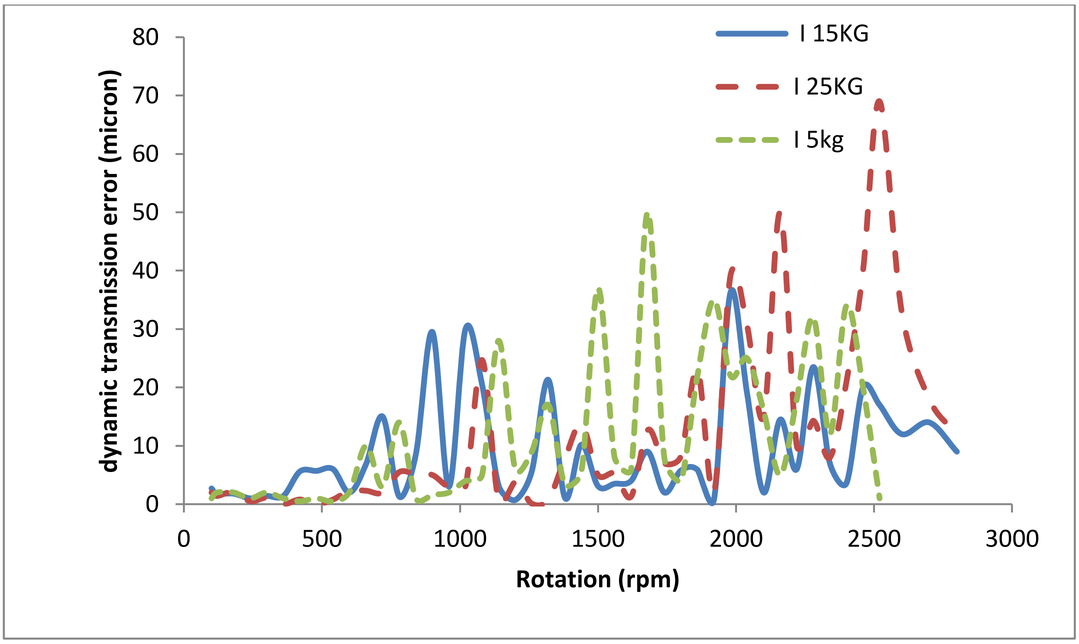

Figure 14. The effect of different inertia on dynamic transmission error for asymmetric tooth gear with tip relief.

Table 1. Design parameters of symmetric, asymmetric and asymmetric with tip relief of spur gear drive.

Gear parameter	Symmetric gear drive (pinion and gear)	Asymmetric gear drive (pinion and gear)	Asymmetric gear drive with tip relief (pinion and gear)
Pressure angle	$20^{o}/20^{o}$	$14.5^{o}/25^{o}$	$14.5^{o}/25^{o}$
Module	7 mm	7 mm	7mm
Face width	60 mm	60 mm	60 mm
Teeth number	14	14	14
Tooth addendum height	7 mm	7 mm	7 mm
Tooth dendum height	8.16 mm	8.16 mm	8.16 mm
Fillet radius	2.1 mm	2.1 mm	2.1 mm
Relief amount	-	-	40 micron
Relief specification	-	-	0.33 pb

Table 2. Maximum dynamic load factor and maximum dynamic transmission error for different gear types.

Gear type	Maximum Dynamic load Factor	Maximum Dynamic Transmission Error (micron)
Symmetric	6.1	75
Asymmetric	4	40
Asymmetric with tip relief (I 5kg)	3.2	45
Asymmetric with tip relief (I 15kg)	3.3	35
Asymmetric with tip relief (I 25kg)	4.2	65
Asymmetric with tip relief (I 35kg)	3.4	32

Internal Convective Heat Transfer Effect on Iraqi Building Construction Cooling Load

Khalid Ahmed Joudi
Professor
College of Engineering-University of Baghdad
E-mail: Khalid47joudi@yahoo.com

Ali Naser Hussien
Lecturer
department of Mechanical engineering -University of Technology
E-mail: aaali_n@yahoo.com

ABSTRACT

This work involves the calculation of the cooling load in Iraqi building constructions taking in account the effect of the convective heat transfer inside the buildings. ASHRAE assumptions are compared with the Fisher and Pedersen model of estimation of internal convective heat transfer coefficient when the high rate of ventilation from ceiling inlet configuration is used. Theoretical calculation of cooling load using the Radiant Time Series Method (RTSM) is implemented on the actual tested spaces. Also the theoretical calculated cooling loads are experimentally compared by measuring the cooling load in these tested spaces. The comparison appears that using the modified Fisher and Pedersen model when large ventilation rate is used; modify the results accuracy to about 10%.

Key words: surface conductance, Iraqi building cooling load calculation.

تأثير انتقال الحرارة الداخلي بالحمل على حمل التبريد لأبنية عراقية التركيب الإنشائي

خالد أحمد جودي
أستاذ
كلية الهندسة- جامعة بغداد

علي ناصر حسين
مدرس
قسم الهندسة الميكانيكية- الجامعة التكنولوجية

الخلاصة

العمل الحالي يتضمن حساب حمل التبريد في تراكيب البناء العراقي مع الأخذ في الاعتبار تأثير انتقال الحرارة بالحمل داخل البناية. فرضية اشري قورنت مع طريقة فيشر وبدرسن في تخمين معامل انتقال الحرارة الداخلي عند استخدام معدلات عالية للتهوية لحالة تجهيز الهواء من السقف. تم احتساب حمل التبريد نظريا باستخدام طريقة السلسلة الزمنية للإشعاع (RTSM) لفضاءات اختبار حقيقية. كذلك فان حمل التبريد المحسوب نظريا تم مقارنته عمليا بقياس حمل التبريد في هذه الفضاءات. المقارنة أظهرت ان استخدام طريقة فيشر وبدرسن المعدلة لمعدلات كبيرة من التهوية, يحسن دقة النتائج لحدود تصل ل 10%.

الكلمات الرئيسيه: مواصلة السطوح, حساب حمل التبريد لأبنية عراقية.

1. INTRODUCTION

The nature of air motion in the air-conditioned space is one of the important features to provide a uniform temperature, humidity, and velocity distributions to insure a comfort sense in this space. In the other hand the air conditioning equipment energy cost as a result from the variation of heat transfer by convection through the construction is influenced by the velocity and the configuration of air movement in the space. Many efforts are made in this field to estimate the essential parameters affect, to achieve the actual conception of the relation between the air movement and heat transfer.

The internal heat transfer coefficient can be combined as the conductance in the inside of the structure which is one component of overall heat transfer coefficient (U value). ASHRAE assumes that the flow of internal air near walls and roofs by buoyancy only and sometimes called "still air", **ASHRAE, 2009** and according to this assumption the values of the inside surface conductance h_i and the resistance R_i given by ASHRAE assuming natural convection heat transfer. These values indicated in **table 1** are satisfied for many cases of air-conditioning, but the new studies of convective heat transfer in buildings, showed that for other cases, natural convection film coefficients significantly underpredict the rate of surface convective heat transfer, especially at high rate of air movement. Results of experimental convective heat transfer validation inside room found from **Ferguson, 1979**, and investigation of forced convective heat transfer coefficient at high flow rate of air ventilation introduced by **Kooi and Forch 1985**, both works appear that the convective heat transfer coefficient is impacted by the volumetric air flow rate and the air inlet temperature.

Experimental cooling load calculations for the room done by **Spitler et al. 1987** showed that the assumption of an adiabatic floor and free convection from ceiling in air conditioning spaces were incorrect. Convection coefficients correlated with twenty-seven data point by multi regression as a function of temperature difference between air and building interior surface was introduced by **Khalifa and Marshall 1990** and these coefficients are differ from ASHRAE data. **Alamdari 1991** studied the thermo-fluid analysis of the building environment using CFD model. Effect of air inlet location on the thermal comfort and inside air motion were analyzed by **Vazques et al. 1991**, and found that the temperature and flow field are greatly related to the air inlet location. A convective internal heat transfer correlations were experimentally investigated by **Spitler et al. 1991** depending on the ventilation rate by momentum number of air inlet, the correlations include roof, wall, and floor internal convective heat transfer coefficients and for wall grille air inlet.

The study of **Fisher and Pedersen, 1997** was correlated the value of the internal convective heat transfer coefficient for ceiling inlet configuration as a function of an enclosure air change rate per hour (ACH) within the range ($3 < ACH < 100$). The correlations are indicated in **table 2** for roofs, walls and floors. Fisher and Pedersen concluded that the error resulted in cooling load using ASHRAE assumption of h_i under predict the actual measuring values by more than 10%.

Djuneady 2000, Djuneady et al. 2003; Djuneady et al. 2004; Djuneady et al. 2005 simulated the air flow pattern in the air conditioned room using the coupling between the Building Energy Simulation (BES) and Computational Fluid Dynamics (CFD) (Fluent) model compared with experimental measurement; they concluded that the inlet conditions of the air have significant effect on the flow pattern.

The summary of concepts can be concluded from the above works that, the inlet air temperature, velocity, and configuration are greatly affected the indoor air movement and the convective heat transfer in the air conditioned spaces and then the accuracy of cooling load estimation. Also the adoption of ASHRAE model of Inside surface conductance h_i and the resistances R_i given by assumed natural convection heat transfer that illustrated in **Table 1** are underestimate the cooling load calculation in many cases of high rate air movement.

Therefore the suitable correlations such as Fisher and Pedersen correlations that relate the inside surface heat transfer coefficient to the air change per hour (ACH) should be adopted in cooling load calculation at high rate of ventilation, these correlations gave practical estimation to inside surface heat transfer coefficient and easy to use for ceiling inlet configuration (air supply from ceiling diffusers).

The objectives of the present work are:

1. Using Fisher and Pedersen correlation of internal convective heat transfer coefficient for ceiling inlet configuration listed in **Table 2** in calculating of cooling load for three air conditioned spaces with high rate of ventilation.
2. Repeat cooling load calculation in 1 above for the same spaces but using ASHRAE model of convective heat transfer coefficient illustrated in **Table 1**.
3. Using Radiant Time Series (RTS) method which is the latest ASHRAE method of cooling load calculation in 1 and 2 above.
4. Compare the results in 1 and 2 above with the actual experimental measurement of cooling load for the three test spaces mentioned in 1 above, to explore the accuracy of these results.

2. CALCULATION PROCEDURES IN RTS METHOD

2.1 Heat Gain Calculations in RTS Method

Wall and roof conductive heat input at the exterior at *n* hours ago is defined by the familiar conduction equation:

$$Q_{i,t-n} = UA(T_{e,t-n} - T_i) \quad (1)$$

where T_i is the indoor temperature and $T_{e,t-n}$ is the sol-air temperature at *n* hours ago and is expressed as:

$$T_{e,t-n} = T_{o,t-n} + \frac{\mu}{h_o} I_{t,t-n} - \frac{\varepsilon \Delta R(t)}{h_o} \quad (2)$$

Conductive heat gain through walls or roofs can be calculated using conductive heat inputs for the current hour and past 23 hours and conduction time series **, ASHRAE 2009.**

$$Q_t = c_{f0} Q_{i,t} + c_{f1} Q_{i,t-1} + c_{f2} Q_{i,t-2} + c_{f3} Q_{i,t-3} + \ldots + c_{f23} Q_{i,t-23} \quad (3)$$

c_{f0}, c_{f1}, etc. represent the conduction time factors. Multiplying of the conduction time factors by the U value gives the periodic response factors, p_r and Eq. (3) may be rewritten as:

$$Q_t = p_{r0} A\left(T_{e,t} - T_i\right) + p_{r1} A\left(T_{e,t-1} - T_i\right) + \cdots + p_{r23} A\left(T_{e,t-23} - T_i\right) \quad (4)$$

Periodic response factors, p_r can be evaluated by using Periodic Response Factor / Radiant Time Factor (PRF/RTF) Generator software published by **Iu and Fisher in 2001.** at Oklahoma state university. The program yields the conduction transfer function coefficients, the periodic response factors, and the U value, by giving the physical properties of any structure with any number of layers. These physical properties include; thickness, thermal conductivity, density, and specific heat for each layer of a homogeneous material constituting the wall or roof. For non-homogeneous materials and for air gaps and air films in and outside the structure, the equivalent thermal resistance is the input instead of other physical properties.

The heat gain from glass and the other components in the space can be calculated by reviewing **chapters 15 and 18 of ASHRAE Handbook of Fundamentals 2009**.

2.2 Conversion of Heat Gain to Cooling Load

The heat gains of all components are divided into convective and radiative heat gain portions. **Table 14 in chapter 18 of ASHRAE Handbook of Fundamentals 2009** illustrates the recommended radiative / convective splits for each component heat gain. The hourly convective portion heat gain is directly converted to hourly convective cooling load, whereas the appropriate radiant time series are applied to the hourly radiant portion heat gains to account for time delay in conversion to cooling load.

The radiant time series or Radiant Time Factors (RTF) are the series of 24 factor denoted by r in the present study and generated from heat balance procedures between interior surfaces radiant heat gain and room air for different types of structures, fenestrations, and furnishing. These factors are tabulated for specific cases, (as indicated in **table 19 and 20 in chapter 18 of ASHRAE Handbook of Fundamentals 2009**) to use them directly for the certain application instead of performing inside surface and room air heat balances. Converting the radiant portion of hourly heat gains into hourly cooling loads is accomplished by the following equation **ASHRAE 2009**:

$$Q_{clr,t} = r_0 Q_{r,t} + r_1 Q_{r,t-1} + r_2 Q_{r,t-2} + r_3 Q_{r,t-3} + \ldots + r_{23} Q_{r,t-23} \quad (5)$$

The hourly radiant portion cooling load calculated in Eq. (5) above is then added to the hourly convective cooling load to obtain the total hourly cooling load for a certain component.

2.3 Inside Surface Heat Transfer Coefficient (h_i)

The convective heat transfer coefficients in Fisher and Pedersen correlations are based on a reference temperature measured in the supply air duct, which are calculated from the rate of convective heat transfer and the temperature difference between the interior surface temperature T_{si} and the supply air temperature T_s as follows (**Fisher and Pedersen 1997**):

$$h_{i(supply)} = q_i/(T_{si} - T_s) \quad (6)$$

The use of supply temperature as the reference temperature provides larger temperature differences between the surface and the air reference temperature, which enables the development of more accurate exponents and convection correlations, as proposed by **Spitler et al. , 1991a, 1991b)**.

Also the internal convective heat transfer coefficient can be calculated based on the room air temperature T_i as a reference temperature as follows ,**Goldstein and Novoselac 2010**.

$$h_{i(room)} = q_i/(T_{si} - T_i) \quad (7)$$

The choice of reference temperature, as either room temperature (T_i) or air supply temperature (T_s), is dependent upon the dominant mode of convection within the room. If natural convection dominates, then room temperature is appropriate as a reference as long as the air is well mixed. However, as room air can be stratified due to the effect of buoyancy when natural convection dominates, the temperature must be taken at multiple points vertically from floor to ceiling, and averaged for an accurate reading. Whereas the choice of air supply temperature (T_s) as a reference temperature is more appropriate when forced convection dominates ,**Goldstein and Novoselac 2010**.

For building energy simulation programs or load calculation methods that utilize the room temperature as the reference, the correlations developed as a function of supply air temperature can easily be converted to correlations that utilize room air temperature as follows ,**Goldstein and Novoselac 2010**.

$$h_{i(room)} = h_{i(supply)} * \left(\frac{T_{si}-T_s}{T_{si}-T_i}\right) \tag{8}$$

3. EXPERIMENTAL VERIFICATION OF RTSM

Figs. 1, 2, and 3 show the schematic floor plans of the three test spaces and the distribution of temperature sensor that measured the inside and outside temperature. These figures also illustrate the semi-conditioned space that neighbored to the test spaces and have temperatures higher than the test spaces. The heat gain resulted due to this temperature difference denoted by due T.D. The test spaces are 24 hr air-conditioned and have ceiling air inlet diffusers in the medical city in Baghdad (33.3^o N latitude and 44.4^o E longitude), the three test spaces were as follows:

1. Statistics office in the maintenance building, which will be called space A.
2. Pharmacy store in the pharmacy department buildings, named space B.
3. Meeting room in burns care building designated space C.

Table 3 illustrates the shape of diffusers and the average air velocity across them, whereas the construction component details of three spaces are listed in **Table 4a** for the external construction of each space that exposed to external heat sources**,** and **Table 4b** for the internal construction of each space that exposed to Temperature Difference T.D. only.

The air change per hour of ventilation of each space has ceiling inlet configuration and the corresponding inside heat transfer coefficients h_i are indicated in **Table 5**. These values of h_i (T_S) are calculated based on Fisher and Pedersen model using the supply air temperature as a reference value. But h_i (T_i) that calculated based on average room air temperature as a reference value is required. Therefore Eq. (8) is used for this purpose. A shaded boarded value in **Table 5** will be used as a modified surface resistance values.

Periodic response factors (PRFs) that are needed to calculate the heat gain of the roofs and walls included R_i of ASHRAE assumption and PRFs of roofs of spaces A, and B, and the ceiling and walls of space C according to the new modified R_i shaded boarded values in **Table 5**. PRFs are calculated by inserting the thermal properties of the building materials in addition to the surface resistances in the dialog box of PRF/RTF Generator program mentioned in section 2.1.

Thus, the theoretical cooling load can be calculated by apply Eqs. (2, 4, and 5). And the values of *r*s are selected from **Table 19 in chapter 18 of ASHRAE Handbook of Fundamentals 2009** for heavy weight, no carpet and 10% of glass to wall ratio.

The experimental verification of the calculated cooling load was accomplished by measuring the average indoor air temperature, the supply air temperature and the flow rate. The sensible heat extraction was calculated as **ASHRAE 2009**:

$$Q_{s.h} = \dot{m}_a * c_p * (T_i - T_s) \tag{9}$$

where $\dot{m}_a = p\dot{V}_s/RT_s$ (10a)

$$\dot{V}_s = \upsilon_a * A_c \tag{10b}$$

and $c_p = 1.006 + 1.840 * w_s$ (10c)

where the specific heat of dry air and water vapor were taken as 1.006, and 1.840 kJ/kg.K respectively for the range of air conditioning temperatures and w_s is the moisture content. The approximated value of c_p is equal to 1.012 kJ/kg.K.

The heat extraction rate is equal to the cooling load if the indoor temperature of the space is constant. The latent load inside the space was zero for no occupancy.

4. RESULTS AND DISCUSSION

Cooling load calculations by ASHRAE and modified Fisher and Pedersen convective heat transfer models appear that the average increase in cooling load of each hour calculated by modified model is about 15.5 W (about 7%) for the roof of space A as shown in **Fig. 4**. This value of increasing is low relative to the value of ventilation ratio which is 20.7 ACH and 7.5 ^oC temperature differences between internal room surface and air supply. The low effect of the inside surface conductance on the cooling load value of the roof of space A is due to the high overall resistance and the thick material of this roof which weaken the h_i effect.

For the roof of space B, **Fig. 5** shows that the raising in cooling load of each hour is about 90 W (about 16.6%). This significant raising resulting from the difference in inside surface conductance of ASHRAE model compared with that of modified model. According to ASHRAE model inside surface conductance (h_i) of the metal sheet suspended ceiling of space B is 2.1W/m^{2}K (notes under **Table 1**) because of this metal surface is reflective and has low emittance value, where h_i is 15.44 W/m^{2}K according to modified model at 13.19 air changes per hour and the difference between internal room surface and air supply temperature of 8 ^oC.

Space C of 18.77 air change per hour and 9 ^oC surface temperature over than supply air temperature is exposed to heat flow from the ceiling and all the external and internal walls. The augmentation of cooling load components of each hour due to the modifying of interior heat transfer coefficient model were: ceiling/ 39 W (about 17.9%), NE shaded wall/ 18 W (about 6.23%), NW wall/ 33.2 W (about 6.29%), and internal walls/ 41W (about 9.4%). The increase of modified h_i of the ceiling resulted in a significant increase in cooling load. The percentage of increasing the cooling load of internal walls is higher than that of the external walls because of the difference in overall resistance between them. The increase in thickness of the layers of building materials increases the overall resistance of the roof or the wall and reduces the variation effects in surface conductance. The overall increase in cooling load of each hour is 131.2 W (about 10%). **Fig. 6** shows the cooling load components that calculated by both ASHRAE and modified model of estimating h_i.

Figs. 7 to 9 show the variation of total cooling load of all components of three spaces which are calculated theoretically based on baseline ASHRAE model and modified Fisher and Pedersen model in addition to a measured heat extraction rate from the three tested spaces. On these figures the variation of outdoor temperature, the average room air temperature, and supply air temperature are graphed. Also the daily average indoor temperature T_i which is used in theoretical calculation and assumed as a constant temperature is written on figures.

The average theoretical cooling loads which are calculated by base (ASHRAE) and modified Fisher and Pedersen model and the average measured heat extraction are mentioned on each figure denoted by LCBav, LCMav and QMav respectively. These represent the daily average values that calculated by summing the values for each hour along 24 hours and divided by 24.

The percentage difference ratios between measured and theoretical base cooling load and between measured and theoretical modified cooling load are calculated as: ((LCBav - QMav)/ QMav)% and ((LCMav - QMav)/ QMav)% respectively. These percentage difference ratios are used to discuss the results of **Figs. 7 to 9** in the following**.**

Fig. 7 shows the theoretical cooling load for all components calculated by ASHRAE baseline model and modified model in addition to measured cooling load for space A. The difference between the average measured value and the average calculated value in this space is (-8.6%) compared with modified model and (-9.3%) compared with ASHRAE model. These values represent the underestimation of the calculated cooling load compared to that measured.

Fig. 8 shows the baseline and modified model theoretical cooling load of space B in addition to measured cooling load. The difference between the average measured heat extracted and the average theoretical load is (-0.45%) in comparison with modified cooling load and (-2.8%) with ASHRAE model.

For space C, the modified and baseline theoretical models cooling load compared with the measured cooling load is shown in **Fig. 9**. The modified model that take in account the effect of modified h_i of ceiling and walls has the average modified result higher than average baseline result by about 10 %. Whereas the average measured values of heat extracted are higher than average theoretical results. The error values are about (-9.7%) for modified model and (-19.8%) for ASHRAE model.

5. CONCLUSIONS

The following conclusions are found from the present work and pertinent for the variation of the internal surface conductance and its effect on cooling load calculations:

1. A 20.7 air changes per hour with 7.5 ^oC temperature differences between internal room surface and air supply increases the internal heat transfer coefficient of the non-reflective roof surface according to modified model by about 14.6 W/m^2K more than ASHRAE model which in turn increases the heat gain value of heavy weight concrete roof with insulation and roofing material by about 7%.
2. A 13.19 air changes per hour with the difference between internal room surface and air supply temperature by 8 ^oC increases the internal heat transfer coefficient of the reflective roof surface according to modified model by about 13.9 W/m^2K higher than ASHRAE model. And then increases the heat gain value of heavy weight concrete roof with insulation and roofing material painted steel sheet suspension ceiling by about 16.6%.
3. The rate of air change per hour of 18.77 and 9 ^oC surface temperature over than supply air temperature magnify the internal surface conductance by about 24.5 W/m^2K of non- reflective roof surface and 3.6 W/m^2K of wall surfaces more than ASHRAE model. And thus increases the heat gain by about 17.9% of heavy weight concrete roof with insulation and roofing material, and 6.3% and 9.4% of double row perforated brick with stone sheathing of external wall and hollow block interior partitions respectively.
4. The increasing in cooling load calculated by modified model lessen the underestimation of the overall calculated cooling load values depending on ASHRAE model from the actual measured values by o.7% , 2.35%, and 10.1% as in cases of spaces A, B, and C respectively.

REFERENCES

- ASHRAE, 2009, Handbook of Fundamentals.
- Alamdari, F. 1991, *Microclimate Performance of An Open Atrium Office Building: A Case Study in Thermo-fluid Modeling*. Computational Fluid Dynamics-Tool or Toy? Proceedings of the 1991 IMechE Conference, pp. 81-92. London, UK: The Institute of Mechanical Engineers.
- Djunaedy Ery, 2000, *Numerical Modeling of Supply Openings For Room Air Distribution*, M.sc. Thesis, Thesis National University of Singapore.

- Djunaedy, E., Hensen, J.L.M., Loomans, M.G.L.C. 2003, *Toward External Coupling of Building Energy and Airflow Modeling Programs*, ASHRAE Transactions, Vol. 109, No. 2, pp. 771-787.
- Djunaedy, E., Hensen, J.L.M., Loomans, M.G.L.C. 2004. *Comparing Internal and External Run-Time Coupling of CFD And Building Energy Simulation Software*, Proc. Room vent 2004, Coimbra, Portugal.
- Djunaedy, E., Hensen, J.L.M., Loomans, M.G.L.C. 2005, *External Coupling Between CFD and Energy Simulation: Implementation and Validation*, ASHRAE Transactions, 111 (1), pp. 612-624.
- Fisher, D.E., and C.O. Pedersen. 1997. *Convective Heat Transfer in Building Energy and Thermal Load Calculations*, ASHRAE Transactions, vol. 103, pt. 2, pp. 137-148.
- Ferguson Jeffry Don, 1979, *Experimental Convective Heat Transfer Facility, Testing and Validation*. M.sc. Thesis, Oklahoma State University.
- Goldstein, K., and Novoselac, A., 2010 *Convective Heat Transfer in Rooms with Ceiling Slot Diffusers*. www.ASHRAE.org
- Iu Ip seng and Fisher D.E. ,2001.www.hvac.okstate.edu
- Khalifa A.J.N. and Marshall R.H.,1990., *Validation of Heat Transfer Coefficients on Interior Building Surfaces Using a Real-Sized Indoor Test Cell*, Int. J. Heat and Mass Transfer, vol. 33 (10), pp. 2219-2236.
- Kooi van der, J., and E. Forch. 1985. *Calculation of the Cooling Load by Means of a "More-Air-Points-Model."* Proceedings of the CLIMA 2000 World Congress on Heating, Ventilating and Air-Conditioning 4: 395-40l.
- Spitler, J.D., C.O. Pedersen, and R.J. Bunkofske. 1987, *Experimental Study of Interior Convective and Radiative Heat Transfer in Buildings.* Heat Transfer in Buildings and Structures, ASME HTD, Vol. 78, pp. 67- 76. New York: American Society of Mechanical Engineers
- Spitler, J., C. Pedersen, D. Fisher, P. Menne, and J. Cantillo. 1991a. *Design of an Experimental Facility For Investigation of Interior Convective Heat Transfer Under Ventilative Cooling Conditions*. ASHRAE Transactions 97(1).
- Spitler, J., C. Pedersen, and D. Fisher. 1991b. *Interior Convective Heat Transfer in Buildings with Large Ventilative Flow Rates*. ASHRAE Transactions 97(1).
- Vazquez, B., Samano, M., and Yianneskis, M. (1991), *The Effect of Air Inlet Location on the Ventilation of an Auditorium*. Computational Fluid Dynamic-Tool orToy? Proceedings of the 1991 IMechE Conference, pp. 56-66. London, UK: The Institute of Mechanical Engineers.

NOMENCLATURE

A	area	m^2
c_p	specific heat of air	kJ/kgK
c_f	conduction time factor	
hi, ho	inside, outside heat transfer coefficient	W/m^2K
I	solar radiation	W/m^2
$\dot{m}_a$	air mass flow rate	kg/s
p	atmospheric pressure	pa
p_r	periodic response factor	W/m^2K
Q	heat	W
R	gas constant of air	kJ/kgK
R_i	internal surface thermal resistance	m^2K/W

ΔR the difference between the long wave radiation incident on the surface from the sky and surroundings, and the radiation emitted by a black body at the outdoor air temperature W/m^2
r radiant time factor
T temperature °C
t time sec
U overall heat transfer coefficient W/m^{2}K
υ_a air supply velocity m/s
$\dot{V}_s$ air supply volume flow rate m^3/s
w_s moisture content kg_{water}/kg_{air}

Greek Symbols
e emittance of the surface
m absorptivity of the surface

Subscripts
a air
c cross sectional (diffuser area)
e sol-air (Temperature)
i indoor
o outdoor
s supply
t total (solar radiation), time (others)

Abbreviations
ACH Air Change per Hour
due T.D due temperature difference
LCBav average Calculated Baseline Load W
LCMav average Calculated Modified Load W
PRF Periodic Response Factor W/m^{2}K
QMav average Measured Load W
RTS Radiant Time Series
RTSM Radiant Time Series Method
tot. calc.base total cooling load calculated according to base (ASHRAE) model W
tot. calc.Mod. total cooling load calculated according to modified model W

Table 1. Surface conductances and resistances for air, **ASHRAE 2009.**

Position of surface (assume still air)	Direction of heat flow	Nonreflective surfaces		Reflective surfaces			
		Emittance,* ε= 0.90		Emittance,ε=0.20		Emittance,ε=0.05	
		h_i W/m^{2}K	R_i m^{2}K/W	h_i W/m^{2}K	R_i m^{2}K/W	h_i W/m^{2}K	R_i m^{2}K/W
Horizontal	Upward	9.26	0.11	5.17	0.19	4.32	0.2
Sloping at 45°	Upward	9.09	0.11	5.00	0.20	4.15	0.24
Vertical	Horizontal	8.29	0.12	4.20	0.24	3.35	0.30
Sloping at 45°	Downward	7.50	0.13	3.41	0.29	2.56	0.39
Horizontal	Downward	6.13	0.16	2.10	0.48	1.25	0.80

* Surface emittance of ordinary building materials is 0.9 and for metals and metal paint between 0.05 and 0.5

Table 2. Heat transfer coefficients for ceiling inlet configuration (air supply from ceiling diffuser) **,Fisher and Pedersen 1997.**

Surface type	Correlation
Walls	$h = 0.19 \cdot ACH^{0.8}$ (W/m^2K)
Floor	$h = 0.13 \cdot ACH^{0.8}$ (W/m^2K)
Ceiling	$h = 0.49 \cdot ACH^{0.8}$ (W/m^2K)

Table 3. Diffuser shapes, dimensions, and air flow measuring data.

Space	A	B	C
Average velocity m/s	6	7.133	1
Diffuser shapes	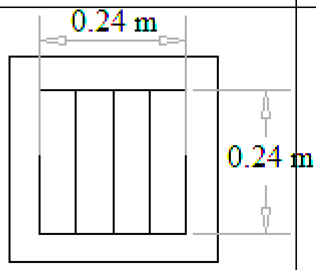	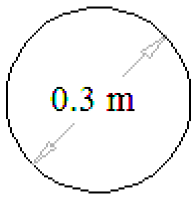	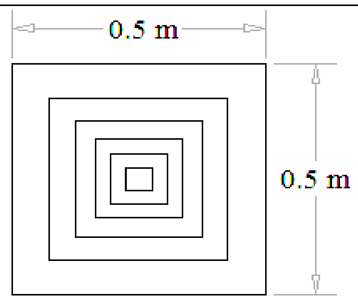

Table 4a. External wall, roof and floor construction details of tested spaces.

Spaces		Constructions (from outside to inside)	Direction and area m^2
A	Wall	External air conductance +3 cm of cement plaster +30 cm thermo-stone +1.5cm juss plaster +1 cm gypsum plaster + internal air conductance	NE=8.32 NW=15.05
	Roof	External air conductance +4 cm of cement shtyger +5 cm of sand +1cm of felt and membrane +5 cm of sty-rubber + 15 cm of high density concrete + air gap +acoustic tiles in suspended ceiling + internal air conductance	22.25
B	Wall	External air conductance +2.5 cm of cement plaster +20 cm hollow block +1.5cm juss plaster +1 cm gypsum plaster + internal air conductance	SW=34.65 SE=18
	Roof	External air conductance +4 cm of cement shtyger +5 cm of sand +1cm of felt and membrane +5 cm of sty-rubber + 20 cm of high density concrete + air gap + metal plates in suspended ceiling + internal air conductance	51
C	Wall	External air conductance +5 cm of helan stone+ 5 cm of cement mortor +24 cm perforated brick +1.5cm juss plaster +1 cm gypsum plaster + internal air conductance	SW=17.2 SE=14.74

Table 4b. Internal wall, roof and floor construction details of tested spaces.

Spaces		Constructions (from outside to inside)	Area m^2
A	Wall	Internal air conductance +1 cm gypsum plaster +1.5cm juss plaster +20 cm hollow block +1.5cm juss plaster +1 cm gypsum plaster + internal air conductance	7.92
	floor	Internal air conductance +20 cm of high density concrete+3cm cement mortar+2.5cm mozaek tile +internal air conductance	22.25
B	Wall	Internal air conductance +2mm of steel sheet +air gap+ 2mm of steel sheet + internal air conductance	40.635
C	walls	Internal air conductance +1 cm gypsum plaster +1.5cm juss plaster +20 cm hollow block +1.5cm juss plaster +1 cm gypsum plaster + internal air conductance	20.87
	ceiling	Internal air conductance +2.5cm granite tile+3cm cement mortar +30 cm of high density concrete+ air gap +1.5cm suspended ceiling +internal air conductance	17.76
	door	Internal air conductance+5cm wood+ Internal air conductance	1.7

Table 5. Interior conductance according to Fisher and Pedersen model for the tested spaces.

spaces	ACH	T_s ^oC	T_i ^oC	Surface	T_{si} ^oC	$h_i(T_s)$ W/m^2K	$h_i(T_i)$ W/m^2K	$R_i(T_i)$ m^2K/W
A	20.7	17	22.5	Ceiling	24.5	5.53	20.74	0.048
				Walls	24.5	2.145	8	0.12
				floor	24	1.47	6.86	0.146
B	13.19	17	23	Ceiling	25	3.86	15.44	0.065
				Walls	25	1.5	6	0.16
				floor	24	1.023	7.16	0.14
C	18.77	15.5	23	Ceiling	24.5	5.12	30.7	0.0325
				Walls	24.5	1.98	11.88	0.084
				floor	23.5	1.36	21.76	0.046

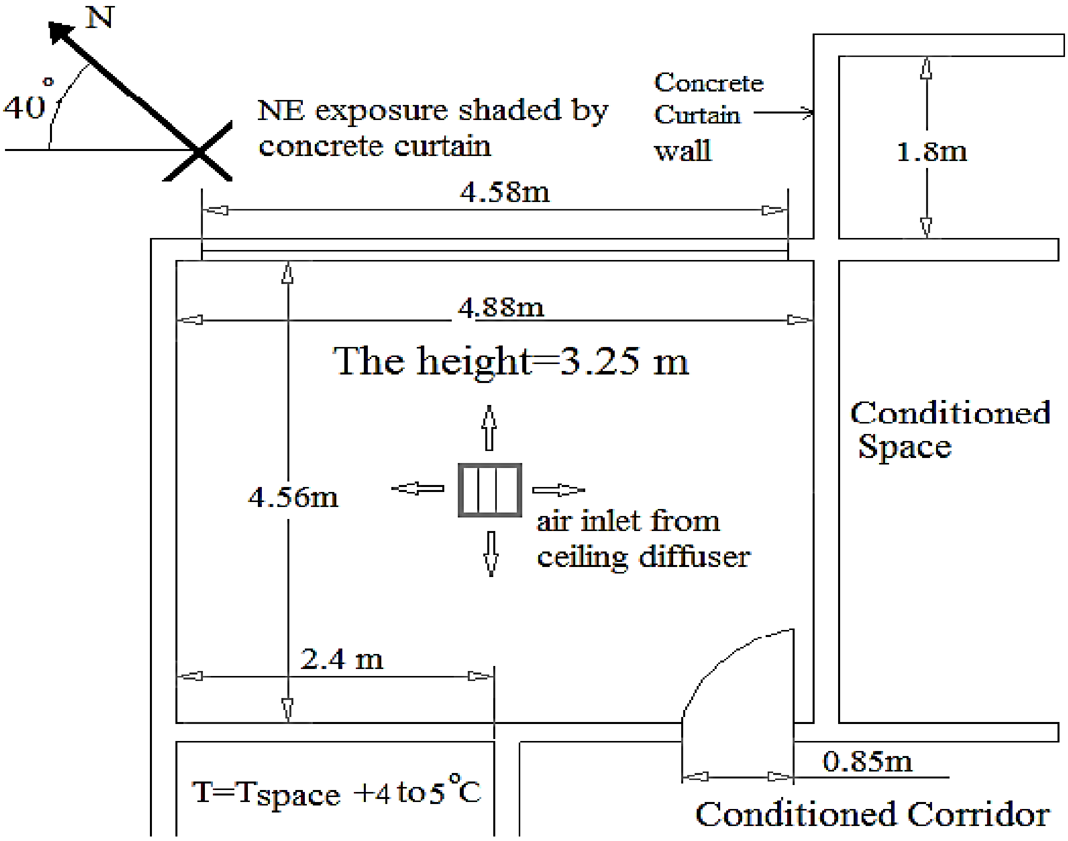

Figure 1. Schematic floor plan of tested space A.

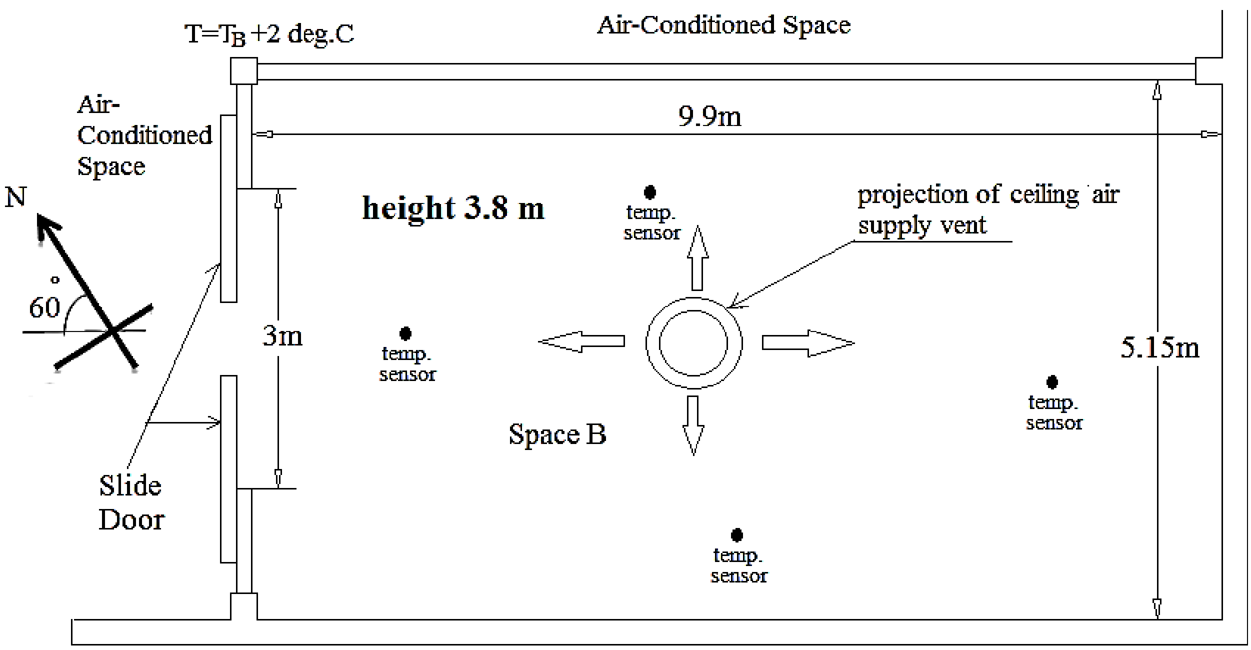

Figure 2. Schematic floor plan of space B .

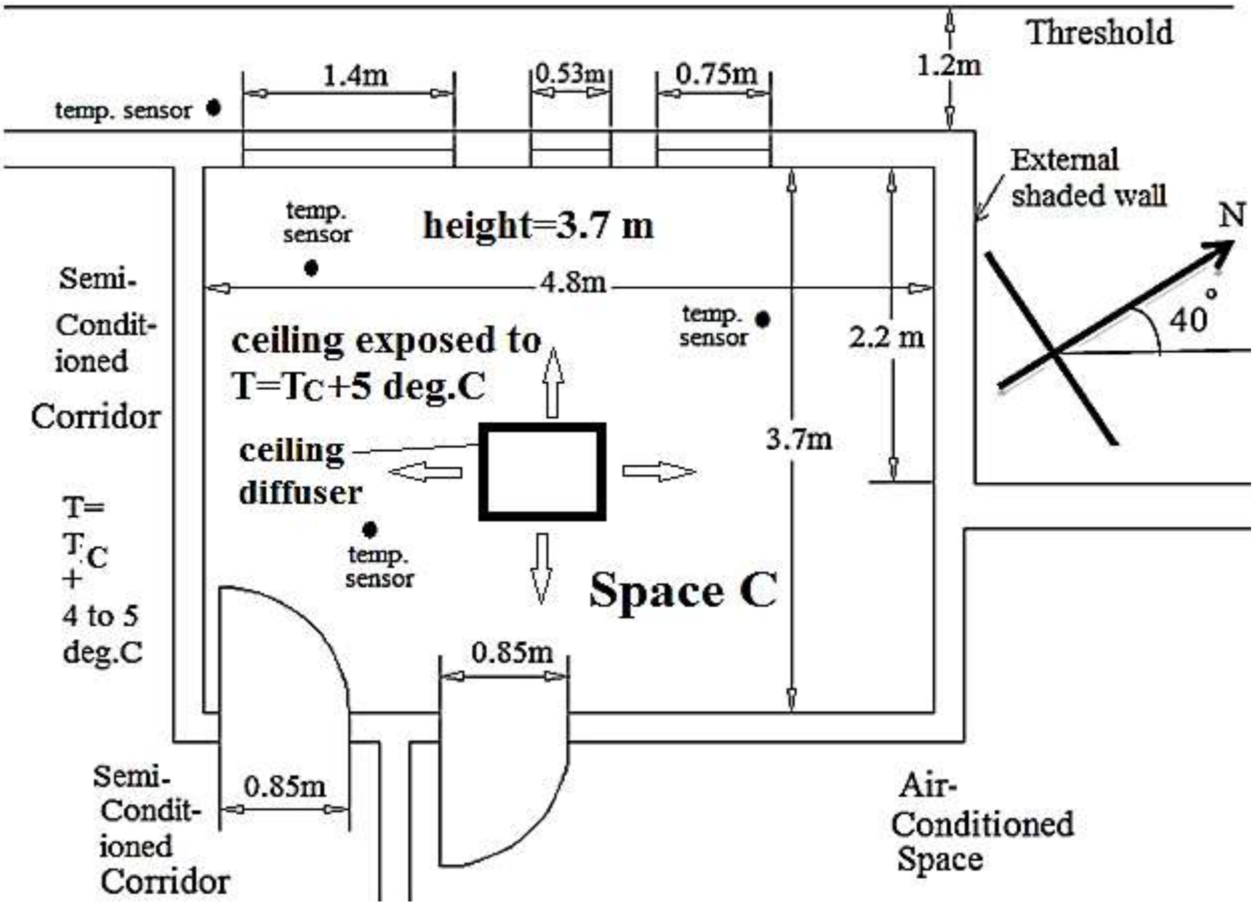

Figure 3. Schematic floor plan of space C.

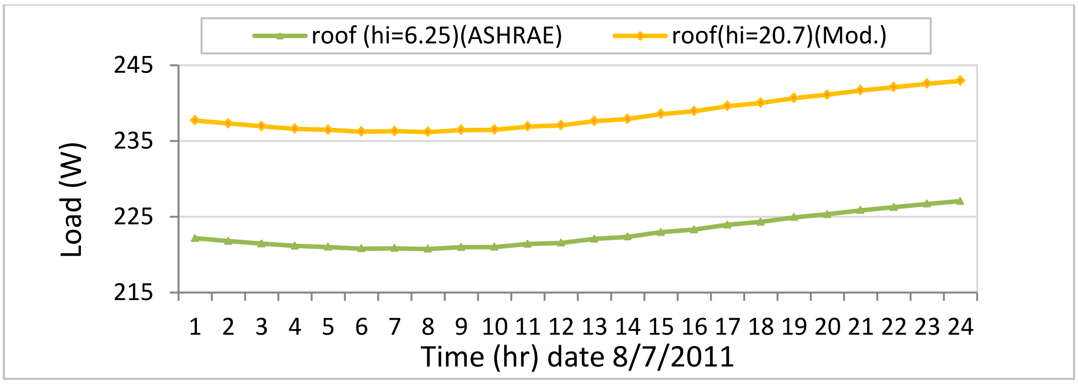

Figure 4. The effect of h_i model on the cooling load of the roof of space A on 8th July 2011.

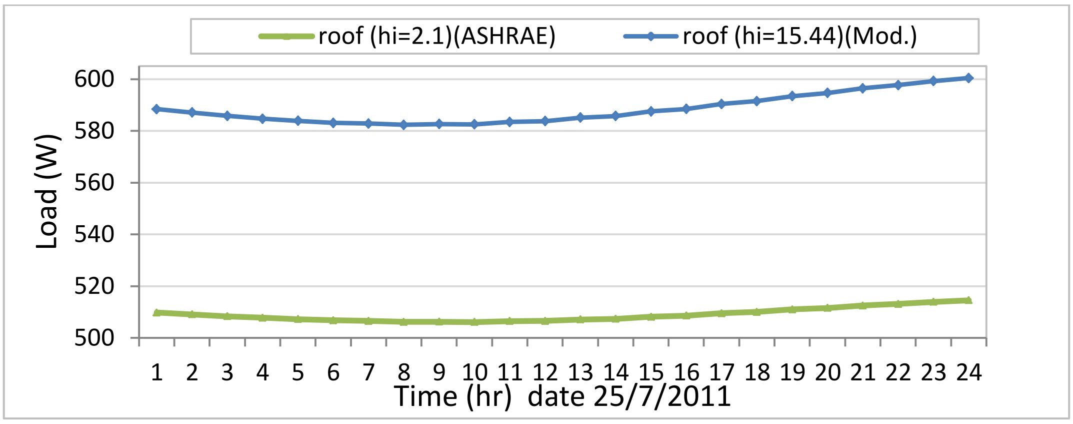

Figure 5. The effect of h_i model on the cooling load of roof of space B on 25th July 2011.

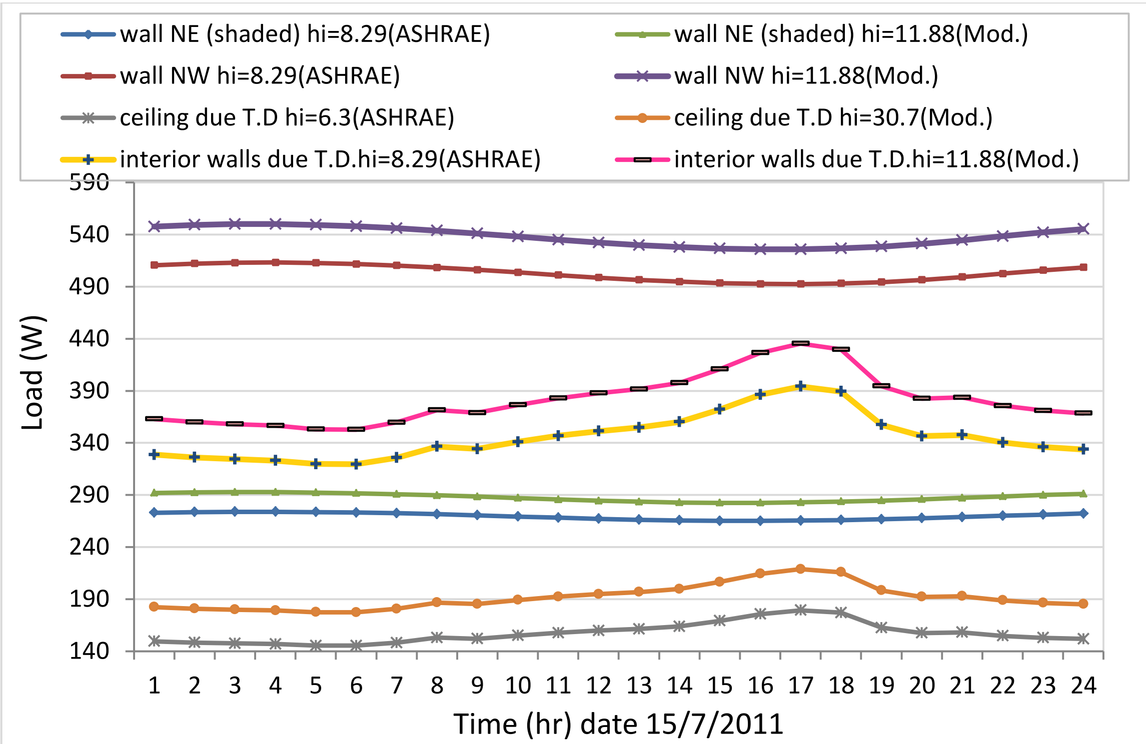

Figure 6. The effect of h_i model on the cooling load of the ceiling and walls of space C on 15th July 2011.

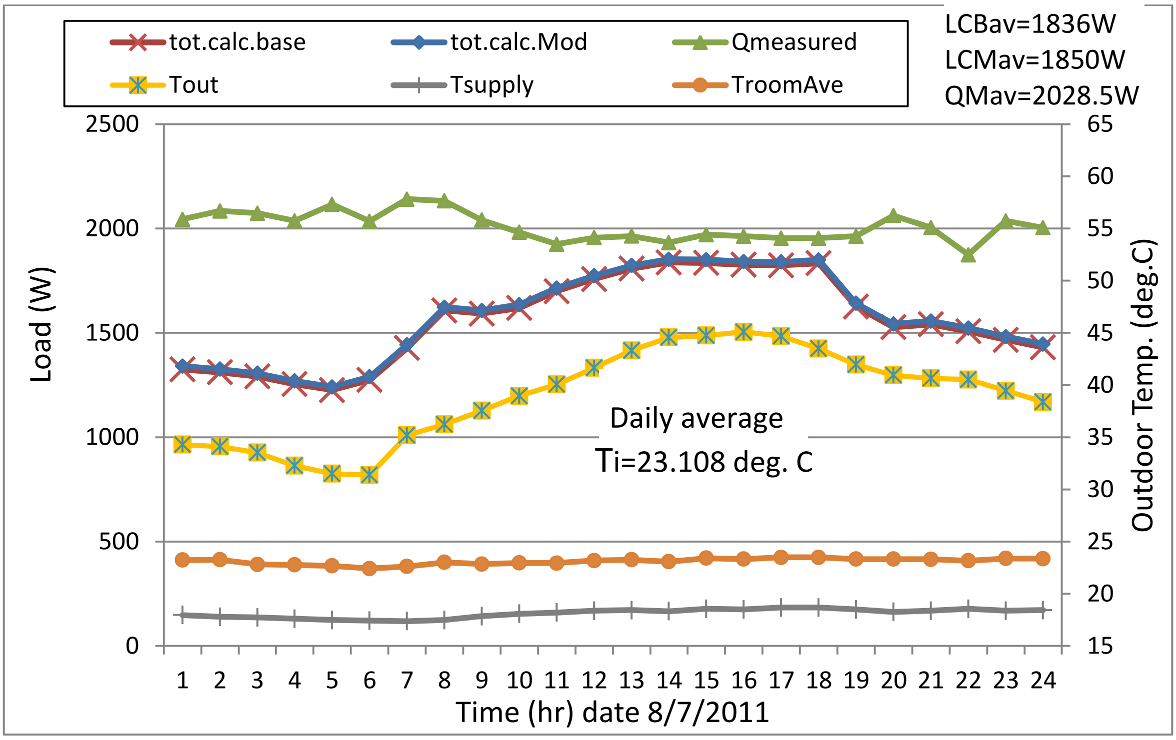

Figure 7. Cooling load comparison for the calculated baseline and modified model with the measured load of space A on 8th July 2011.

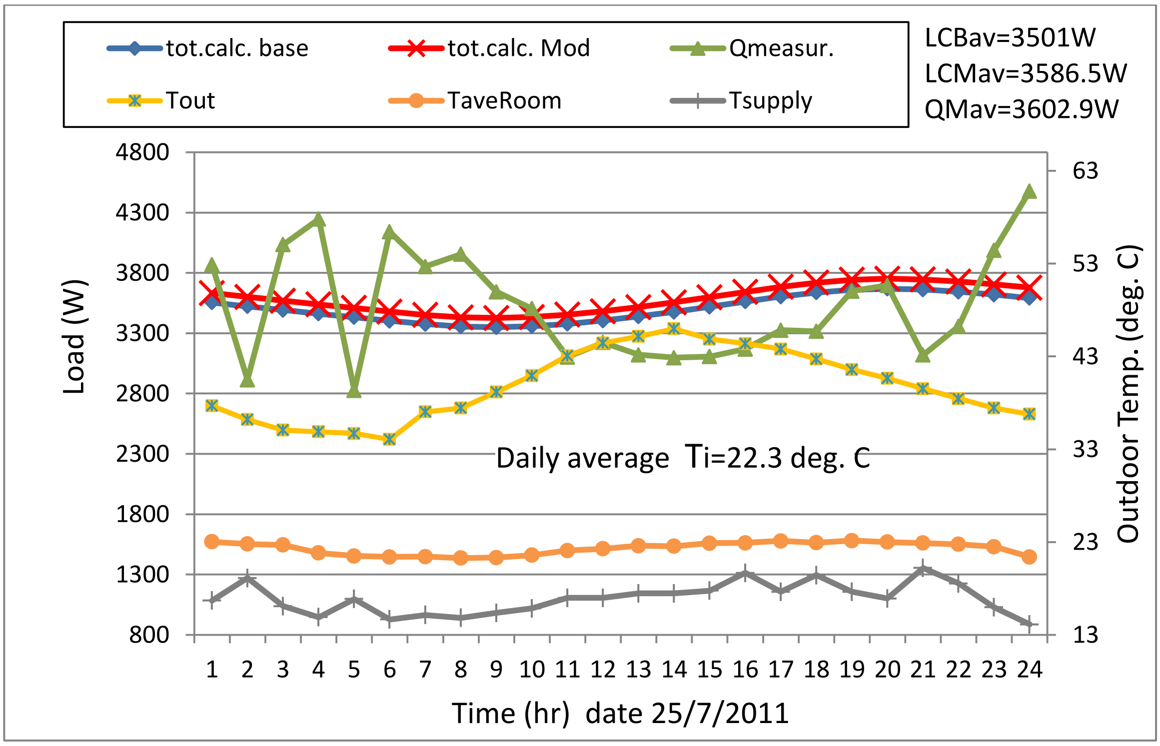

Figure 8. Cooling load comparison for the calculated base and modified model with the measured load of space B on 25th July 2011.

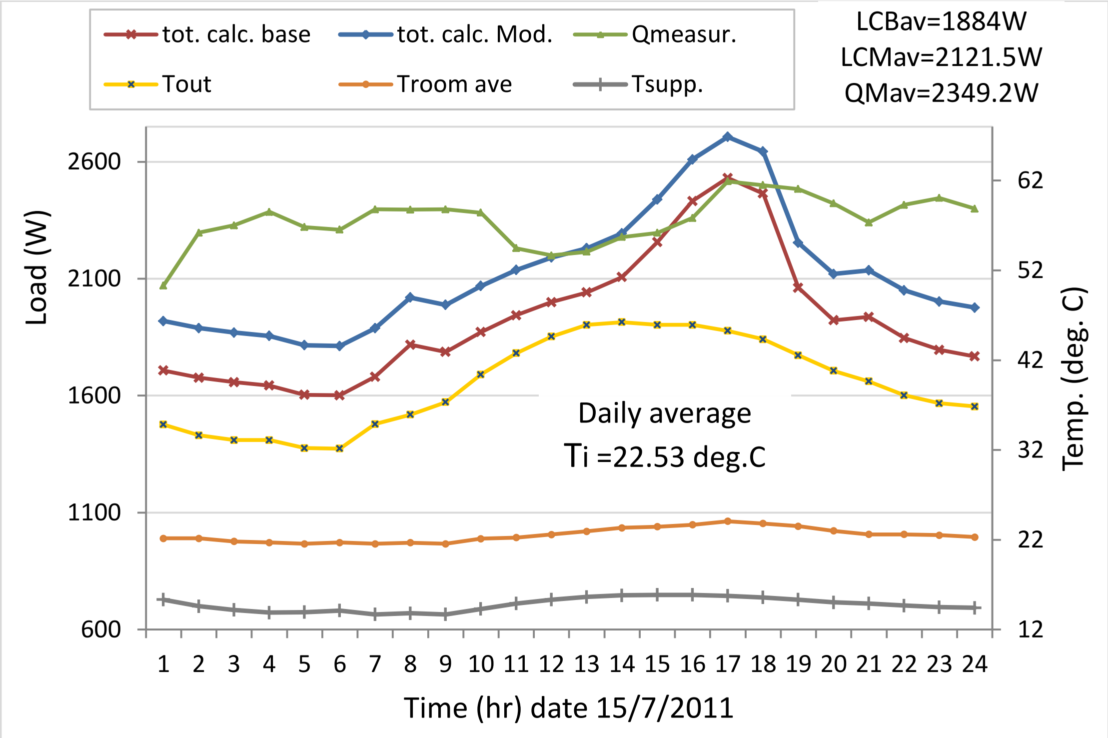

Figure 9. Cooling load comparison for the calculated base and modified model with the measured load of space C on 15th July 2011.

Mixed Convection Heat Transfer in a Vertical Saturated Concentric Annulus Packed with a Metallic Porous Media

Dr. Mohammed A. Nima
Lecturer
Mechanical Engineering Department
College of Engineering- Baghdad University
E-mail: dralsafi@uobaghdad.edu.iq

Sarmad A. Abdal Hussein
Asst. Lecturer
Mechanical Engineering Department
Engineering College - Baghdad University
E-mail: sarmadaziz402@gmail.com

Saud S.Hameed
Mechanical Engineering Department
Engineering College - Baghdad University
E-mail: saudswedan@yahoo.com

ABSTRACT

Mixed convection heat transfer in a vertical concentric annulus packed with a metallic porous media and heated at a constant heat flux is experimentally investigated with water as the working fluid. A series of experiments have been carried out with a Rayleigh number range from Ra=122418.92 to 372579.31 and Reynolds number that based on the particles diameter of Re_d=14.62, 19.48 and 24.36. Under steady state condition, the measured data were collected and analyzed. Results show that the wall surface temperatures are affected by the imposed heat flux variation and Reynolds number variation. The variation of the local heat transfer coefficient and the mean Nusselt number are presented and analyzed. An empirical correlation has been proposed for computing the Nusselt number for the geometry and boundary conditions under investigation.

Key words: mixed convection, concentric annulus, metallic porous media, constant heat flux.

انتقال الحرارة بالحمل المختلط في تجويف حلقي عمودي مشبع ذو أسطوانتين متمركزتين تم حشوه بوسط مسامي معدني

المدرس الدكتور محمد عبد الرؤوف نعمة
قسم الهندسة الميكانيكية
كلية الهندسة – جامعة بغداد

المدرس المساعد سرمد عزيز عبد الحسين
قسم الهندسة الميكانيكية
كلية الهندسة – جامعة بغداد

سعود سويدان حميد
قسم الهندسة الميكانيكية
كلية الهندسة – جامعة بغداد

الخلاصة

انتقال الحرارة بالحمل المختلط في تجويف حلقي عمودي ذو أسطوانتين متمركزتين تم حشوه بوسط مسامي معدني قد تم دراسته بصورة عملية مع استخدام الماء كمائع مشغل. تم اجراء عدد من التجارب العملية لمدى رقم رالي من 122418.92 الى 372579.31 و مدى رقم رينولد على اساس قطر الجسيمات 14.62, 19.48 و 24.36. عند وصول حالة الاستقرار تم جمع البيانات وتحليلها. اظهرت النتائج تأثر درجات حرارة السطح تتأثر بتغير الفيض الحراري المسلط وتغير رقم رينولد. تغير معامل انتقال الحرارة الموضعي ومتوسط رقم نسلت قد تم اظهارها و دراستها. تم اقتراح معادلة تجريبية لحساب رقم نسلت للشكل الذي تم دراسته مع الظروف الحدية المحيطه به.

الكلمات المفتاحية: الحمل المختلط، أسطوانتين متمركزتين، وسط مسامي معدني، فيظ حراري ثابت.

1. INTRODUCTION

Heat transfer in porous media received great interest for many years because of the improved in the heat transfer performance without proportionate increase in hydraulic resistance. It is well known that the porous structure reduces the thickness of the boundary layer, increases the surface area that in contact with the fluid and intensifies the mixing of the flowing fluid, and thus enhances the thermal heat transfer. Flow and heat transfer through channels packed with porous media are widely studied because of their potential applications in thermal management such as compact heat electronic exchanges, solar collector, nuclear reactor cooling and regenerators. Packed bed has been developed for different types of porous materials with specific intent to enhance the heat transfer from the thermally loaded surfaces. Because of the random structures of porous media, they will be different in engineering, physical and thermal properties, **Venugopal, et al., 2010**. As a result, flow and heat transfer characteristics in these media also greatly differ. **Renken and Poulikakos**, **1990** investigated experimentally and numerically the forced convection heat transfer in the packed bed areas of an occupied parallel plate channel whose walls maintain a constant temperature. Based on this study, porous media needs to be considered as a viable alternative for the transfer of heat enlarge in forced convection heat transfer in channels. **Pu, et al., 1999,** used R-113 loop in performing the experiments of mixed convection heat transfer in a vertical packed channel with asymmetric heating of opposing walls. Chrome steel beads of 6.35 mm in diameter were used as a porous media. The experiments were carried out in the range of $2<Pe<2200$ and $700<Ra<1500$. The measured temperature distribution indicated the existence of a secondary convective cell inside the vertical packed channel in the mixed convection regime. A correlation equation for Nusselt number in terms of Peclet number Pe and Rayleigh number Ra was obtained from experimental data. They found that the following three convection regimes exist: natural convection regime: $105< Ra/Pe$, mixed convection regime: $1<Ra/Pe<105$, and forced convection regime: $Ra/Pe< 1$. **Dirker, 2000** presented a comparison of the literature that involving heat transfer in the ring. Their comparison showed that there was a need for more research in the field of links convection heat transfer in concentric ring as they found a little agreement among the existing relationship. Empirical relationship for predicted Nusselt number in the ring had been developed with water as the working fluid. **Boomsma and Poulikakos, 2002** showed the results of experimental studies performance to assess the hydraulic characteristics of open cell aluminum foam of different pore diameters and pore in each of the compressed and non-compressed format. The study was done mainly to predict important parameters permeability coefficient foam, precisely in order to describe the pressure drop versus the flow behavior in the porous media. **Hussein, et al., 2009** experimentally and theoretically studied the convective heat transfer in vertical concentric annulus where the two cylinders filled with porous medium. They concluded that the behavior of temperature profile were the same for any diameters ratio and any different heat flux. The relation between Nu and Ra was proposed and the results showed good agreement between experimental and theoretical studies. The potential of a simple and inexpensive porous insert was experimentally investigated by **Venugopal, et al., 2010**. The porous inserted consists of a stack of metallic perforated plates that used to enhance the heat transfer from the heated wall of a vertical rectangular duct under forced flow conditions. The characteristic features of the porous medium model on the hydrodynamic and heat transfer behavior were investigated. The key novelty in this work was the development of a new correlation for the Nusselt number that did not require any information from hydrodynamic studies. The largest increase in the average Nusselt number of 4.52 times that for clear flow was observed with a porous material of porosity of 0.85. **Andrea, et al., 2012,** investigated experimentally the air forced convection through electrically heated open-cells copper foams with different number of pores per unit of length (PPI) with constant porosity (ε=0.93) and foam core height of 40 mm. The experimental heat transfer coefficient and pressure drop measurements permitted to understand the effects of the pore density on the heat transfer and fluid flow performance of the foams. They compared different enhanced surfaces, which can be considered suitable for electronic thermal management against present author's experimental measurements for 40 mm high aluminum foams at the same operative test conditions.

To the best of the authors' knowledge, there is no existing experimental study on the mixed convection heat transfer in a saturated concentric annulus that filled with metallic porous media. So we proposed the present study to cover this shortage in the understanding of the flow and heat transfer in porous enclosure with mixed convection effects.

In the present work, mixed convection heat transfer in a vertical saturated concentric porous annulus subjected to a constant heat flux, is examined experimentally with water as the working fluid. The main objective is to study the influence of mixed convection heat transfer on the flow field and the associated heat transfer process in such system. The influence of heat flux and mass flux variation on wall temperatures and Nusselt number are investigated and analysed then a general relation that describe the overall process is presented.

2. EXPERIMENTAL APPARATUS AND PROCEDURE

2.1 Experimental Apparatus

The experimental investigation is carried out in an apparatus shown in **Figs. 1** and **3**. The apparatus has been constructed to achieve the requirements of the present study and it consists of the following major assemblies:

1- Test section

As shown in **Fig. 2**, the test section consists of two stainless steel cylinders that form a concentric annulus of length L=63 cm. The inside and outside diameters of inner cylinder are (D_i=40 mm, D_o=41mm) and the inside and outside diameters of outer cylinder are (D_i=80 mm, D_o=82 mm). The inner and the outer cylinders are assembling together by means of two Teflon flanges to form the concentric annulus test section. The Teflon flanges is used to reduce the dissipative heat transfer from the test section ends and to support the inner and outer cylinders in one concentric annulus by pushing them between the Teflon flanges inner and outer diameters (D_i=39 mm, D_o=83 mm). The wall thickness of each Teflon flange is 1.5 cm. Four holes are drilled in each

Teflon flange as shown in **Fig. 2** but with different purposes. The holes in the lower flange are used to distribute the incoming water from the liquid splitter and guide it uniformly to inter the test section, while the holes in the upper flange are used as an exit passage for the thermocouples extension wires that used to measure inner cylinder wall temperatures. The upper flange holes are filled with a relatively high temperature adhesive material to support the thermocouples extension wires and to prevent water infiltration. The concentric annulus is packed with stainless steel beads, essentially spherical in shape with an average particles diameters of d_p=6 mm. A metallic O-Ring with holes (less than 6mm in diameter) is used to support the metallic porous media 13.5 cm far from the test section lower end and to form an entrance length to achieve a uniform inlet water velocity profile to the porous packing. The length of the porous packing was designed to be 40 cm as shown in **Fig. 2**, and the water was then derived out of the test section by a tube that mounted at 9.5 cm far from the test section upper end. A uniform heat flux is provided on the outer surface of the concentric annulus by a nickel-chrome wire of 1 mm in diameter, which is electrically insulated and warps around the outer surface of the concentric annulus along the test section part that filled with the metallic porous media (40 cm). This steel wire is supplied with AC-current from a voltage regulator, to control the incoming current according to the heat flux desired. The test section is well insulated outside with asbestos and fiber glass wool layers of 15 mm and 50 mm thickness, respectively. The concentric annulus outer surface and inner surface temperatures are measured by (18 K-type) thermocouples, which were distributed equally within nine sections along the outer surface and inner surface of the concentric annulus as shown in **Fig. 2**. Another (5 K –type) thermocouples were used to measure the water bulk temperature distribution by inserting these thermocouples inside the test section through holes on the outer surface of the concentric annulus as shown in **Fig. 2**. These holes are filled with a relatively high temperature adhesive material to support the thermocouples extension wires and to prevent water infiltration. The temperature distribution on the outer surface of the insulation shield are measured using (4 K-type) thermocouples distributed in an equal pitch, to calculate the heat lost during the experiment by referring to the temperature difference between the heater wall and the ambient. The heat lost is found to be approximately 6% during the whole range of the imposed heat flux. A digital electronic thermometer (type IDC-420042), is connected in parallel to the thermocouples by leads through a selector switches, to record the temperature measurements.

2- Water supply

As shown in **Fig. 1**, the liquid supply assembly consists of water tank, valve, filter, flowmeter (0.8 LPM full range) and liquid splitter, which are placed adjacent to the test section. A drain reservoir was placed at the test section exit to collect the water. When the water exit from the test section, it was forced to flow through a flexible tube that raise the water to a higher elevation (ΔH) before it collected in the drain reservoir. The purpose of this arrangement at the test section exit is to control the test section pressure and to ensure that the water pressure inside the test section is higher than the atmospheric pressure.

3- Electrical power measurement

The constant heat flux is supplied by using electrical circuit of alternating current that includes:

A) Voltage regulator.
B) Transformer.
C) Voltmeter.
D) Ammeter.

2.2 Experimental Procedure

Before starting the experimental measurements and in order to degas the air from the packed annulus, the valve is opened in such a manner that the water flow at the flowmeter full range (0.8 LPM) and a moderate heat flux is applied for two to three hours. Then, the valve is adjusted to give the required water flow rate. Each experiment is performed using the following procedure:

1) The valve that connected to the water tank is adjusted to give the required water flow rate which is measured by the flowmeter.
2) The electrical power is switched on, and the heater input voltage is adjusted by a voltage regulator to give the required voltage and current.
3) The supplied voltage and current to the heater are recorded to calculate the required electrical power in accordance to the heat flux required.
4) The apparatus is left for two to three hours to establish the steady state condition. The thermocouples readings are collected every half an hour. When the difference between two readings became almost constant, the steady state condition is fixed and a final reading is recorded.

To obtain a new set of experiments under the same water flow rate, a new electrical power is selected, and the procedure from step 2 to 4 is repeated.

The net heat flux to the saturated porous media is determined from recording the electrical power supplied to the heater and applying the following equation:

$$q_w = P_o/A \tag{1}$$

where;

P_o= electrical power consumed by heater = $I \times V$.

I = current flow through the heater.

V = voltage across the heater.

A = surface area of the annulus outer cylinder.

Heat losses from the heater across asbestos and fiber glass wool layers are calculated to be 6% while the heat losses from the axial direction through the Teflon flanges are found to be small and neglected. These losses are subtracted from the electric power to obtain the net heat transfer rate.

3. HEAT TRANSFER CALCULATIONS

It is important to calculate the absolute permeability (K), the effective thermal conductivity (k_{eff}) and the porosity (ε) of the saturated porous media, as they are used in the dimensionless groups that govern the fluid flow and heat transfer calculations.

According to **Nield and Bejan, 2006**:

$$K = \frac{\varepsilon^3 d_p^2}{180(1-\varepsilon)^2} \tag{2}$$

$$k_{\text{eff}} = \varepsilon k_l + (1-\varepsilon)k_s \tag{3}$$

where k_l and k_s are the thermal conductivities of the water and the solid porous media, respectively. The porosity of the packed stainless steel beads is found experimentally using the expression, **Nield and Bejan, 2006:**

$$\varepsilon = \frac{Vol_{total} - Vol_{solid}}{Vol_{total}} \tag{4}$$

3.1 Reynolds Number

The Reynolds number can be defined according to the particle diameter and the fluid velocity at the inlet as:

$$Re_d = \frac{\mathrm{U_{in} d_p}}{v} \tag{5}$$

3.2 Grashof and Rayleigh Number

The Grashof number can be defined as:

$$Gr = \frac{\mathrm{g}\beta K q_w D_h^2}{k_{\mathrm{eff}}\, v^2} \tag{6}$$

then Rayleigh number (*Ra*) can be calculated using the following equation:

$$Ra = Gr\ Pr \tag{7}$$

3.3 Local and mean Nusselt Number

The local heat transfer coefficient at the heated wall can be defined as:

$$h = \frac{q_w}{T_w - T_b} \tag{8}$$

Hence, the local and the mean Nusselt number can be calculated as, **Nield and Bejan, 2006** :

$$Nu = \frac{h\, D_h}{k_{\mathrm{eff}}} = \frac{q_w\, D_h}{k_{\mathrm{eff}}\,(T_w - T_b)} \tag{9}$$

$$Nu_m = \frac{1}{L}\int_0^L Nu\ dy \tag{10}$$

The thermophysical properties of the water-stainless steel beads that used in the present study are listed in **Table 1** and the physical parameters for the stainless steel beads are listed in **Table 2**.

4. RESULTS AND DISCUSSION

A series of experiments have been carried out with a heat flux range from q_w = 3912 W/m^2 to 11907 W/m^2 (Ra=122418.92 to 372579.31) and volumetric flow rate of Q = 0.3, 0.4 and 0.5 L/min (Re_d=14.62, 19.48 and 24.36). The temperature distribution along the inner and the outer annulus surfaces is measured and presented. The influence of heat flux variation and Reynolds number variation on the local and mean heat transfer coefficient is discussed and analyzed. Finally, a general correlation for the mean Nusselt number Nu_m as a function of the parameters (*Ra*/*Re*) is derived to describe the overall fluid flow and heat transfer behavior in the porous annulus.

4.1 The Influence of Heat Flux and Reynolds Number on the Surface Temperature Distribution.

Figs. 4-6 show the influence of the imposed heat flux variation on the distribution of the outer annulus surface temperature for Re_d=14.62, 19.48 and 24.36, respectively. A general trend can be seen from **Figs. 4-6**, that the outer annulus surface temperature increases as the heat flux is increased for the same Reynolds number value. When the imposed heat flux is increased (with a constant Reynolds number), the buoyancy effect increases and causes a faster growth in the thermal boundary layer along the porous annulus surface that will be associated with an increased in the outer annulus surface temperature values.

Figs. 7-9 show the influence of the imposed heat flux variation on the distribution of the temperature difference between the outer and the inner annulus surface temperature [$\Delta T_w = T_{w,\ outer\ annulus\ surface} - T_{w,\ inner\ annulus\ surface}$] for Re_d=14.62, 19.48 and 24.36, respectively. **Figs. 7-9** show that the temperature difference (ΔT_w) increases as the imposed heat flux is increased for the same Reynolds number. It is clear from **Fig. 7,** that for a low Reynolds number (Re_d=14.62) the fluctuation in the temperature difference (ΔT_w) values with the axial distance is mild except for q_w = 11907 W/m^2. When the heat flux is supplied on the outer annulus surface, the buoyance force will caused an induced mass flux that will oppose the incoming cold-fluid and drive the hot fluid from the vicinity of the outer heated wall towards the inner insulated wall and rising its temperature. For low Reynolds number values, the buoyance effect increases and results in a faster heat transfer from the outer to the inner annulus surface and as a consequence a smaller temperature difference (ΔT_w) as shown in **Fig. 7**.

While for a higher Reynolds numbers of Re_d=19.48 and 24.36 **Figs. 8** and **9**, the temperature difference (ΔT_w) increases with the axial distance and reaches its maximum value at Z=0.2 m from the annulus entrance section and then it decreases downstream up to the annulus exit section. This behavior can be explained based on the interaction between the buoyancy force and the inertia force of the incoming cold-fluid. In the annulus entrance region the buoyancy force is still limited in comparison with the inertia force of the incoming cold-fluid, and this will caused a retreat in the thermal boundary layer growth from the outer annulus surface towards the inner annulus surface. The domination of the incoming cold-fluid effect in the entrance region will cause a faster temperature rise in the outer annulus surface and continues increased in the temperature difference (ΔT_w) with the axial distance to a point located at Z=0.2 m from the annulus entrance section as shown in **Figs. 8** and **9**. In the region downstream of Z=0.2 m, the buoyancy force becomes stronger due to the continuous heating and it will be able to overcome the inertia force of the incoming cold-fluid. This will result in mobilizing more hot fluid from the vicinity of the outer heated wall towards the inner insulated wall to rise its temperature and consequently we observe a remarkable decreased in the temperature difference (ΔT_w) as shown in **Figs. 8** and **9**. Another observation is made from **Figs. 7-9**, that for higher Reynolds numbers (Re_d=19.48 and 24.36) the temperature difference (ΔT_w) increases suddenly at the annulus exit section. This can be attributed to the higher fluid mixing at the annulus exit section as the hot fluid try to find its way out through the drain tube and this caused a reduction in the inner annulus surface temperature and an increased in the temperature difference (ΔT_w) at the annulus exit.

Figs. 10-14 show the influence of Reynolds number variation on the distribution of the outer annulus surface temperature for q_w = 3912 W/m^2 to 11907 W/m^2. The figures show that the surface temperature decreases as the Reynolds number increased for the same heat flux value. When the Reynolds number increased the thermal boundary layer retreat along the heated wall and as a consequence a higher heat transfer rate can be expected that associated with a decrease in the outer annulus surface temperature.

Figs. 15-19 show the influence of Reynolds number variation on the distribution of the temperature difference between the outer and inner annulus surface temperature [$\Delta T_w = T_{w,\ outer\ annulus\ surface} - T_{w,\ inner\ annulus\ surface}$] for q_w = 3912 W/m^2 to 11907 W/m^2. Two different relationships between the temperature difference curves (ΔT_w) can be seen depending on the magnitude of the imposed heat flux.

At low heat fluxes, q_w = 3912 W/m^2 and 5511 W/m^2 **,Figs. 15** and **16**, the temperature difference (ΔT_w) decreases as the Reynolds number is increased except at Z=0.2m. For low heat fluxes the buoyancy effect is limited and the thermal boundary layer will grow in the vicinity of the heated wall only, and as a result the inner annulus surface temperature will mainly effected by the incoming cold-fluid. As the Reynolds number increased, the heated wall (outer annulus surface) temperature will decreases due to the incoming cold-fluid effect and the temperature difference (ΔT_w) between the outer and inner annulus surface will decrease as shown in **Figs. 15** and **16**.

While for higher heat fluxes, q_w = 7382 W/m^2 to 11907 W/m^2 **,Figs. 17-19**, a gradual inversion can be seen in which the temperature difference (ΔT_w) decreases as the Reynolds number is decreased. For high heat fluxes the buoyancy force is dominant over the inertia force of the incoming cold-fluid throughout the porous annulus. As the Reynolds number is decreased, the buoyancy effect more increases and causes a rapid movement of the hot fluid from the vicinity of the outer heated wall towards the inner insulated wall rising its temperature and reducing the temperature difference (ΔT_w) as shown in **Figs. 17-19**.

Figs. 15-19 also show that the temperature difference (ΔT_w) values at the annulus exit section are always higher for Re_d= 24.36 and then decreases as the Reynolds numbers is decreased. As mentioned earlier, when the hot fluid try to find its way out from the annulus exit section through the drain tube, a reduction in the inner annulus surface temperature is recorded due to the reduction in the hot fluid amount that mobilized from the vicinity of the outer heated wall towards the inner wall. This reduction in the inner annulus surface temperature increases for higher Reynolds numbers and causes the temperature difference (ΔT_w) at the exit section to be maximum at Re_d= 24.36.

4.2 Local Heat Transfer Coefficient.

A general behavior can be seen from the distribution of the local heat transfer coefficient in **Figs. 20-25**, that the local heat transfer coefficient decreases from the channel inlet to a point where it reaches its minimum value and then it increases downstream up to the channel exit. At the channel inlet, the small thickness of the thermal boundary layer results in high temperature gradients at the heated wall and high heat transfer coefficient. As the thickness of the thermal boundary layer increases downstream, the heated wall temperature gradients decreases and causes a reduction in the heat transfer. As a result, the local heat transfer coefficient reaches its minimum value, after which the porous media plays a crucial role in the enhancement of heat transfer by conducting more heat from the heated wall to increase the fluid bulk temperature and as a consequence increases the local heat transfer coefficient values up to the channel exit.

Figs. 20-22 show the influence of the imposed heat flux variation on the distribution of the local heat transfer coefficient at the heated wall for Re_d=14.62, 19.48 and 24.36. It can be seen from these figures that the local heat transfer coefficient increases as the heat flux is increased for the same Reynolds number value. This can be attributed to the fact that for higher heat fluxes the buoyancy effect increases and the thermal boundary layer growth is more rapidly and causes a smaller temperature difference between the fluid bulk temperature and the heated wall temperature and as a result a higher local heat transfer coefficient will be attended.

Figs. 23-25 show the influence of Reynolds number variation on the distribution of the local heat transfer coefficient at the heated wall for q_w = 3912 W/m^2, 7382 W/m^2 and 11907 W/m^2. It can be seen from these figures that the local heat transfer coefficient increases as the Reynolds number is increased for the same heat flux value. When the Reynolds number is increased, a reduction in the thermal boundary layer thickness occurs with the domination of the incoming cold-fluid effect and this will cause a larger fluid mixing and higher local heat transfer coefficient values.

Another observation is made from **Figs. 23-25**, that the point of the minimum value of local heat transfer coefficient is moving towards the channel inlet as the imposed heat flux is increased. At q_w = 3912 W/m^2 **,Fig. 23**, the the local heat transfer coefficient curves reaches its minimum value at Z=0.2 m from the annulus entrance section, while this point is moving to Z=0.1 m at q_w = 7382 W/m^2 **,Fig. 24** and Z=0.05 m at q_w = 11907 W/m^2 **,Fig. 25**. As the heat flux increases, the buoyancy force increases and its effect start to arise from the channel inlet and causes an increase in the local heat transfer coefficient values and as a consequence a retreat in the point of the minimum value of local heat transfer coefficient towards the channel inlet.

4.3 Mean Nusselt Number.

The relationship between mean Nusselt number and Rayleigh number are plotted in **Fig. 26** for Re_d=14.62, 19.48 and 24.36. It shows an increase in the mean Nusselt number as Rayleigh number is increased for the same Reynolds number value. This can be attributed to the increase of the buoyancy effect for higher Rayleigh number values which improves the heat transfer process.

The relationship between mean Nusselt number and Reynolds number are plotted in **Fig. 27** for Ra=122418.92 to 372579.31, which shows an increase in the mean Nusselt number as Reynolds number is increased for the same Rayleigh number value. This can be attributed to the higher fluid mixing that associated with the domination of the incoming cold-fluid effect, which causes a clear heat transfer enhancement for higher Reynolds number values.

4.4 Correlation of Average Heat Transfer Data.

The values of the mean Nusselt number (Nu_m) are plotted in **Fig. 28** against (Ra/ Re_d) for the range of Ra=122418.92 to 372579.31, and Re_d=14.62 to 24.36. All the points as can be seen are represented by linearization of the following equations:

$$Nu_m = c(Ra/Re_d)^m \quad [c = 2.227 \;\&\; m = 0.144] \tag{11}$$

It can be seen from **Fig. 28** that the correlated mean Nusselt number increases with the increasing of Rayleigh number and Reynolds number.

5. COMPARISON WITH PREVIOUS EXPERIMENTAL RESULTS

K. Muralidhar, 1988 conducted a theoretical study on the mixed convective heat transfer in saturated porous annulus, where the inner cylinder is heated and the outer cylinder is cooled. This work is the closest previous published work that found in the literature using the same setup with mixed convection except that it is a theoretical study and the fluid is heated at a constant temperature along the inner cylinder. The average Nusselt number of a vertical annulus as a function of Rayleigh number for different Peclet numbers is shown in **Fig. 29**. It can be seen from **Fig. 29** that the average Nusselt number increases when the Rayleigh number is increased and when the Peclet number increased. The behavior shown in **Fig. 29** agrees with the present work results that shown in **Fig. 26** (the mean Nusselt number increases as Rayleigh number is increased for the same Reynolds number value) and in **Fig. 27** (the mean Nusselt number increases as Reynolds number is increased for the same Rayleigh number value).

6. CONCLUSIONS

The main conclusions of the present work are:

1- The temperature difference (ΔT_w) increases as the imposed heat flux is increased.
2- For low Reynolds number (Re_d=14.62) and with higher buoyance effect, the temperature difference (ΔT_w) exhibit a moderate fluctuation with the axial distance.
3- For high Reynolds numbers (Re_d=19.48 and 24.36) and with higher effect of the inertia force of the incoming cold-fluid, the temperature difference (ΔT_w) increased with the axial distance and reached a maximum value at Z=0.2m from the annulus entrance section and then it decreased downstream up to the annulus exit section.
4- At low heat fluxes [q_w = 3912 W/m^2 and 5511 W/m^2], the temperature difference (ΔT_w) decreased as the Reynolds number increased. On the other hand, for higher heat fluxes [q_w = 7382 W/m^2 to 11907 W/m^2] a gradual inversion can be seen in which the temperature difference (ΔT_w) decreased as the Reynolds number decreased due to the domination of the buoyancy force over the inertia force of the incoming cold-fluid.
5- The local heat transfer coefficient increased with the increased of the imposed heat flux and Reynolds number.
6- Mean Nusselt number is increased with the increased of Rayleigh number and Reynolds number.

REFERENCES

- Andrea, D., Simone, M., Claudio, Z., Luisa, R., 2012, *Experimental Measurements of Air Forced Convection through Copper Foams*, International Refrigeration and Air Conditioning Conference at Purdue, July 16-19, 2312.
- Boomsma, K., and Poulikakos, D., 2002, *The effects of compression and pore size variations on the liquid flow characteristics in metal foams*, ASME J. Fluids Eng. 124, pp. 263–272.
- D. A. Nield, A. Bejan, 2006, *Convection in porous media*, New York, Springer.
- Dirker. J., and Vyver. H. V. 2004, *Convection Heat Transfer in Concentric Annuli*. Experimental Heat Transfer, Volume 17, Issue 1, pp. 19 - 29.
- Hussein, M. A., Tahseen, A. T., and Jasim, H. A., 2009, *Convection Concentric Annulus Vertical Cylinders Filling Porous Media*, Journal of Kirkuk University-Scientific Studies, vol.4, No.2, pp. 55–71.
- K. Muralidhar, 1988, *Mixed convection flow in a saturated porous annulus,* International Journal of Heat Mass Transfer,Vol. 32, pp. 881–888.
- Pu, W. L., Cheng, P., Zhao, S. T., 1999, *An Experimental Study of Mixed Convection Heat Transfer in Vertical Packed Channels*, ALAA Journal of Thermo Physics and Heat Transfer, Vol. 13 (4), pp. 517 – 521.
- Renken, K. J., and Poulikakos, D., 1990, *Mixed convection experiments about a horizontal isothermal surface embedded in a water-saturated packed bed of spheres*, International Journal of Heat Mass Transfer,Vol. 33, pp. 1370–1373.
- Venugopal, G., Balaji, C., Venkateshan, S. P., 2010, *Experimental Study of Mixed Convection Heat Transfer in a Vertical Duct Filled with Metallic Porous Structures*, International Journal of Thermal Sciences, Vol. 49, pp. 340-348.

8. NOMENCLATURE

A = area, m^2.
β = expansion coefficient, K^{-1}.
d_p = mean diameter, m.
D_h = hydraulic diameter, m.
ε = porosity.
K = absolute pearmability, m^2.
k_{eff} = effective thermal conductivity, W/m^2. K.
Gr = Grashof number.

h = local heat transfer coefficient, W/m^2.K.
L = effective heating length, m.
Nu = Nusselt number.
Pr = Prandtl Number.
ρ = density, kg/m^3.
Ra = Rayleigh number.
q_w = heat flux, W/m^2.
Q = volumetric flow rate, L/min.
Re_d = Reynolds number based on the particle diameter.
T = temperature, K.
U_{in} = inlet velocity, m/s.
v = kinematic viscosity, m^2/s.
Vol_{solid} = volume of the metallic porous media, m^3.
Vol_{total} = total volume of the concentric annulus, m^3.

Subscript Meaning
b = bulk.
m = mean.
w = wall.

Table 1. Thermophysical properties of the water- stainless steel beads system.

Property	Symbol	Solid	Liquid
Density	ρ kg/m^3	7833	988.1
Thermal conductivity	k W/m K	15.1	0.644
Expansion coefficient	β, K^{-1}	---	0.451×10^{-3}
Dynamic viscosity	μ kg/m.s	---	0.547×10^{-3}
Prandtl Number	Pr	---	3.55

Table 2. Physical parameters for each size of the copper beads.

Mean diameter d_p (mm)	Porosity† ε	Permeability †† K (m^2)
6	0.4	3.556×10^{-6}

† Calculated experimentally with the use of Eq. (4).
†† Calculated from Eq. (2).

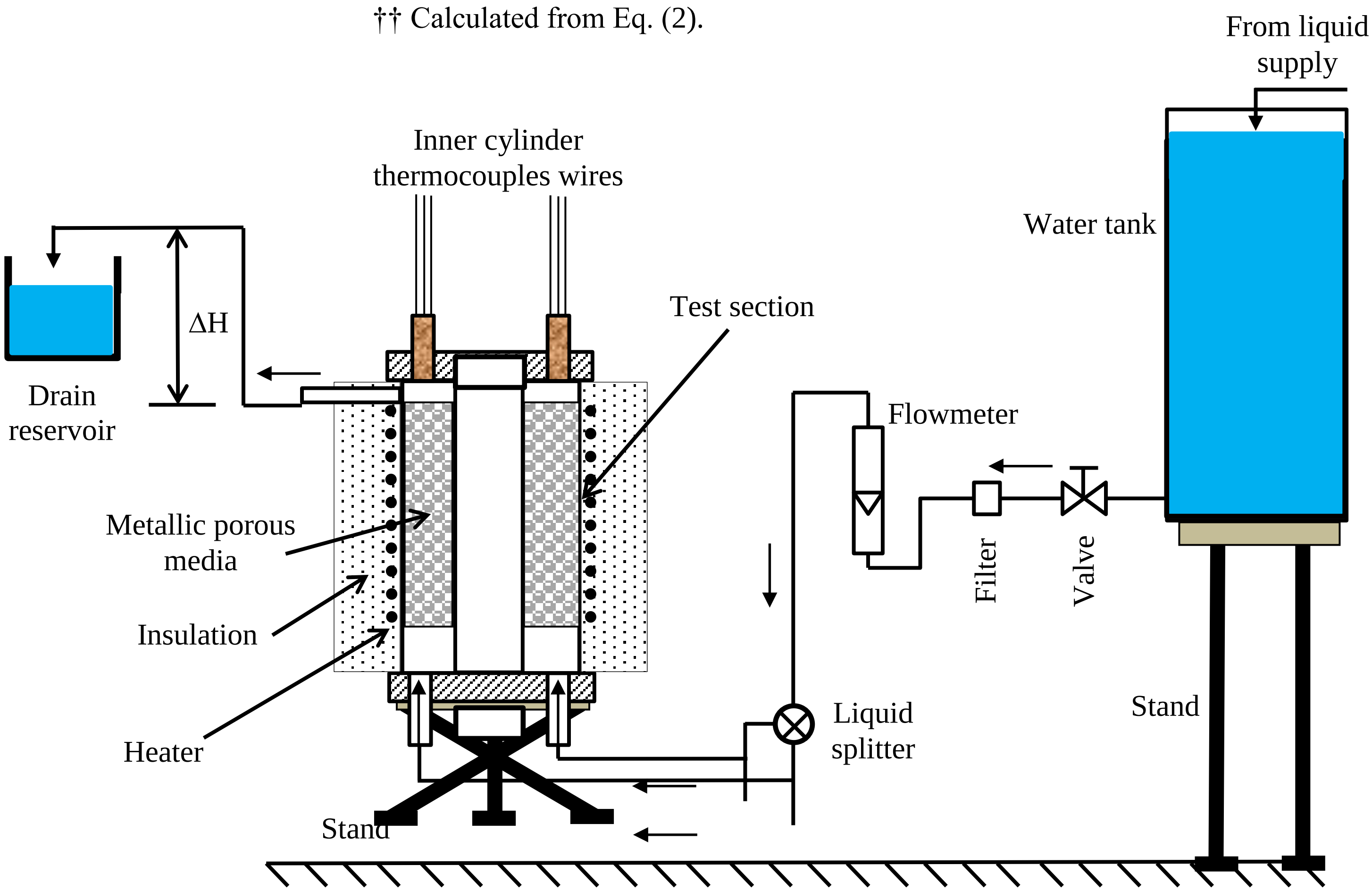

Figure 1. Schematic of the experimental apparatus.

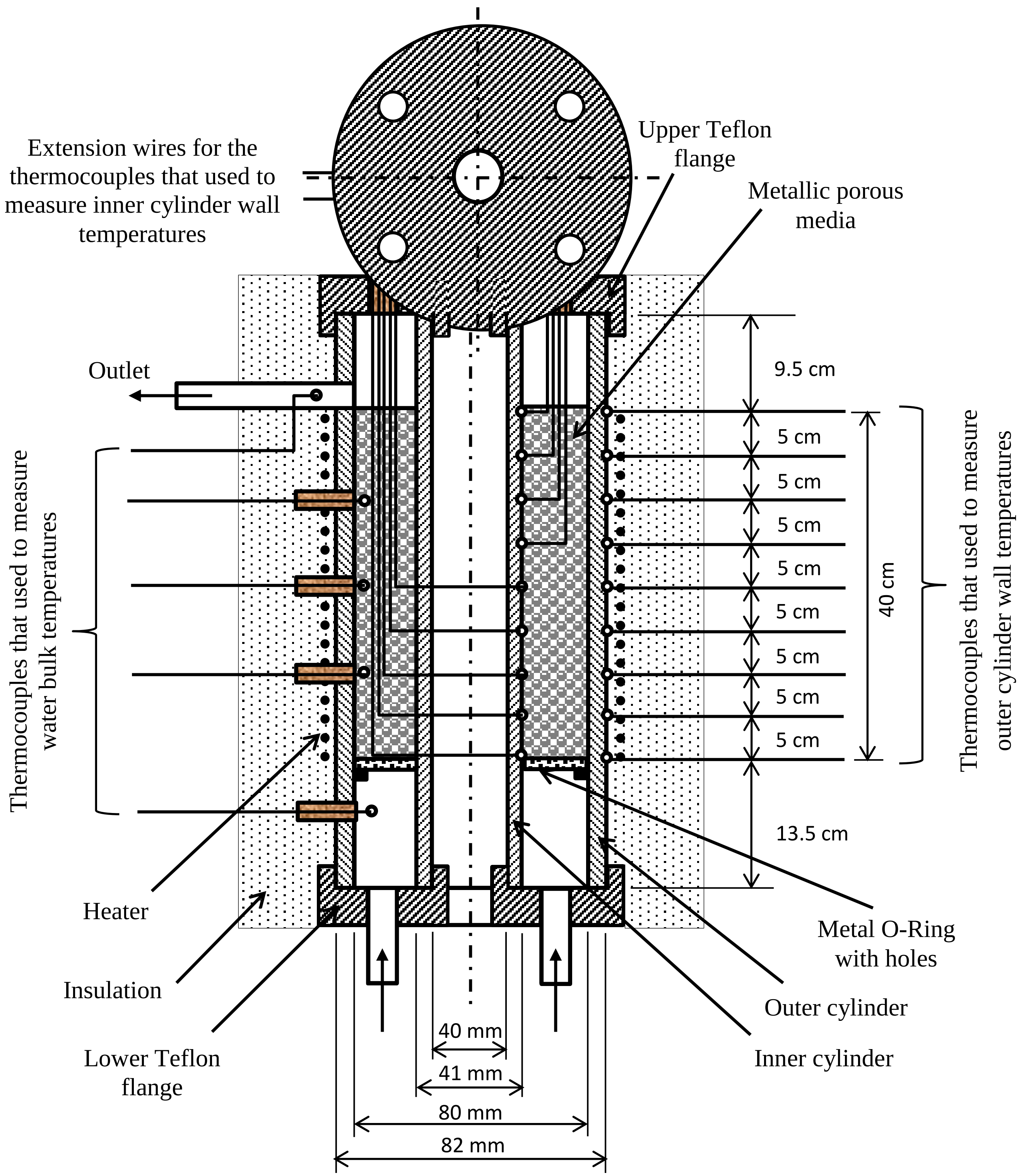

Figure 2. Arrangement and the locations of thermocouples.

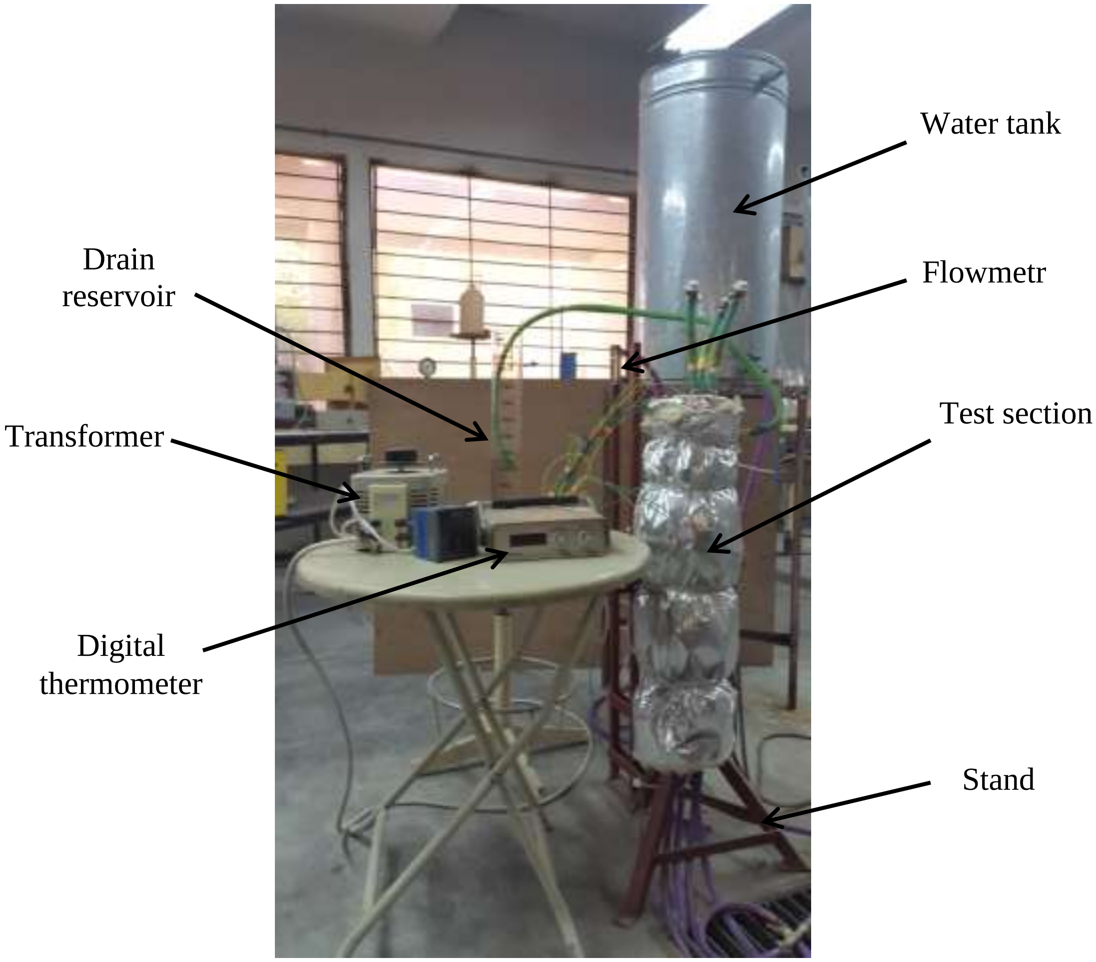

Figure 3. Photograph of the experimental apparatus.

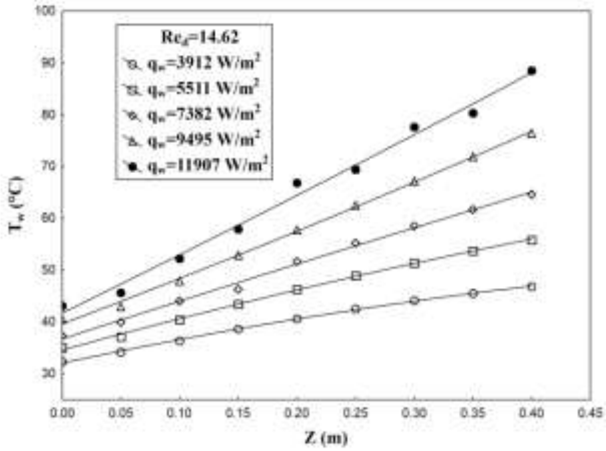

Figure 4. Variation of the outer annulus surface temperature with the axial distance for different heat fluxes and Re_d=14.62.

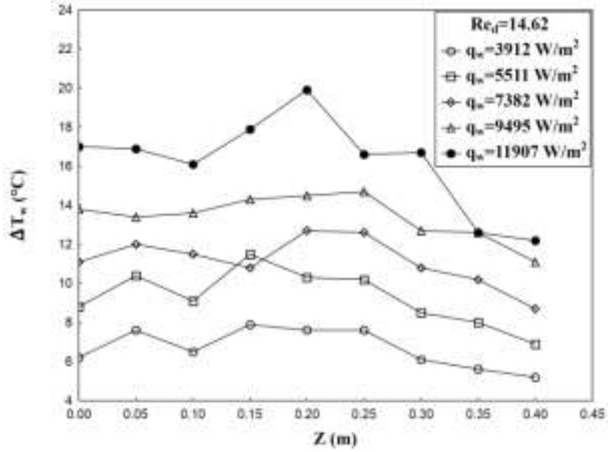

Figure 7. Temperature difference between inner and outer annulus surfaces with the axial distance for different heat fluxes and Re_d=14.62.

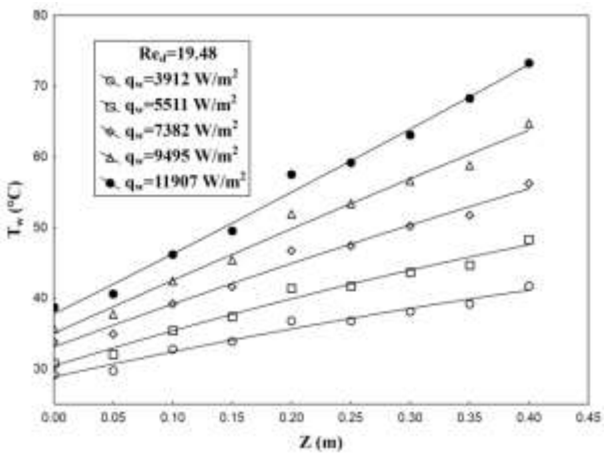

Figure 5. Variation of the outer annulus surface temperature with the axial distance for different heat fluxes and Re_d=19.48.

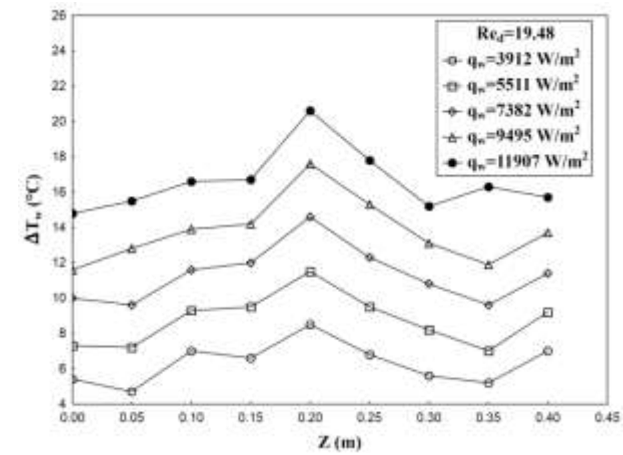

Figure 8. Temperature difference between inner and outer annulus surfaces with the axial distance for different heat fluxes and Re_d=19.48.

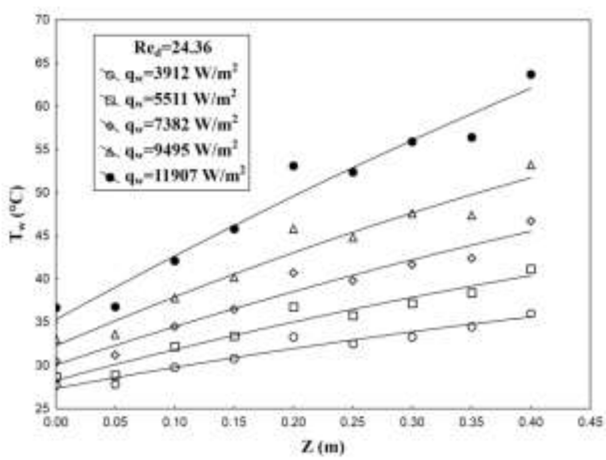

Figure 6. Variation of the outer annulus surface temperature with the axial distance for different heat fluxes and Re_d=24.36.

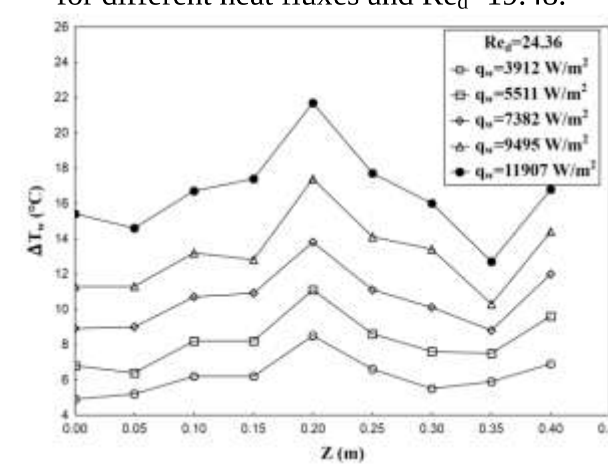

Figure 9. Temperature difference between inner and outer annulus surfaces with the axial distance for different heat fluxes and Re_d=24.36.

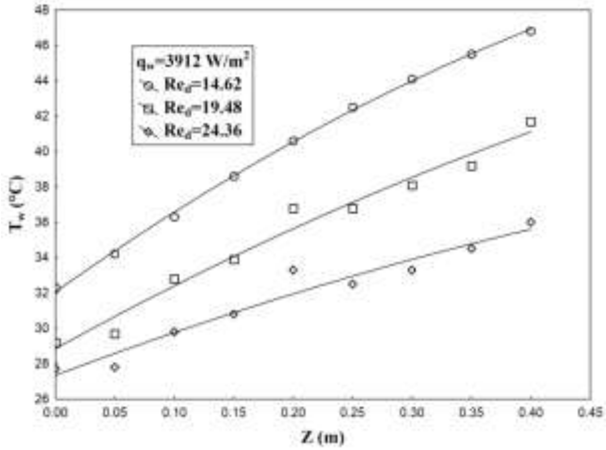

Figure 10. Variation of the outer annulus surface temperature with the axial distance for different Reynolds numbers and q_w=3912 W/m^2.

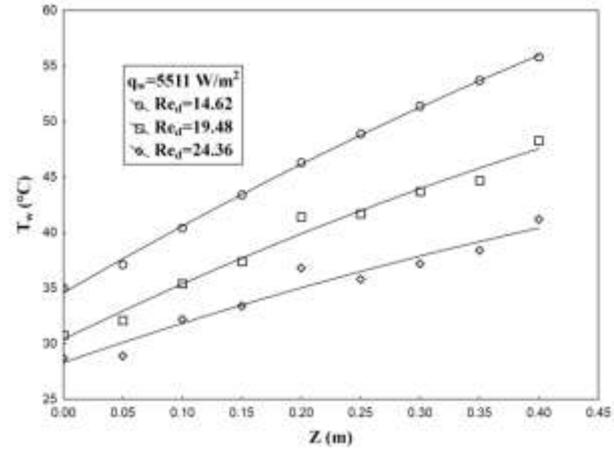

Figure 11. Variation of the outer annulus surface temperature with the axial distance for different Reynolds numbers and q_w=5511 W/m^2.

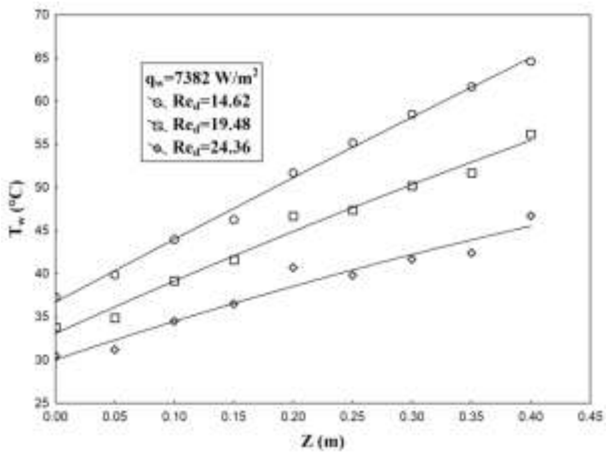

Figure 12. Variation of the outer annulus surface temperature with the axial distance for different Reynolds numbers and q_w=7382 W/m^2.

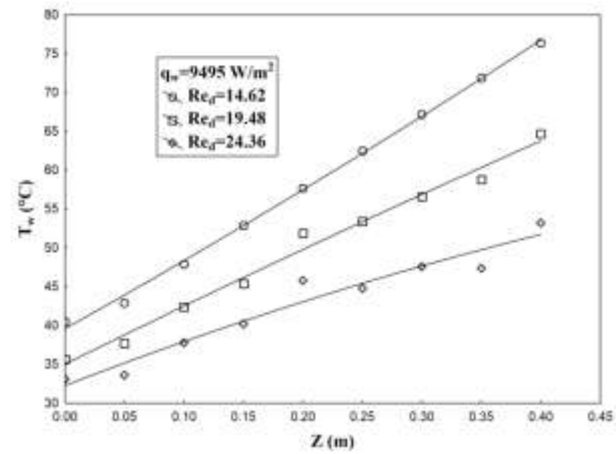

Figure 13. Variation of the outer annulus surface temperature with the axial distance for different Reynolds numbers and q_w=9495 W/m^2.

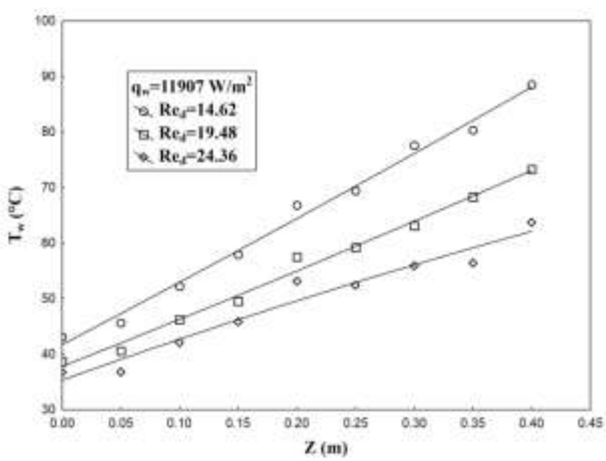

Figure 14. Variation of the outer annulus surface temperature with the axial distance for different Reynolds numbers and q_w=11907 W/m^2.

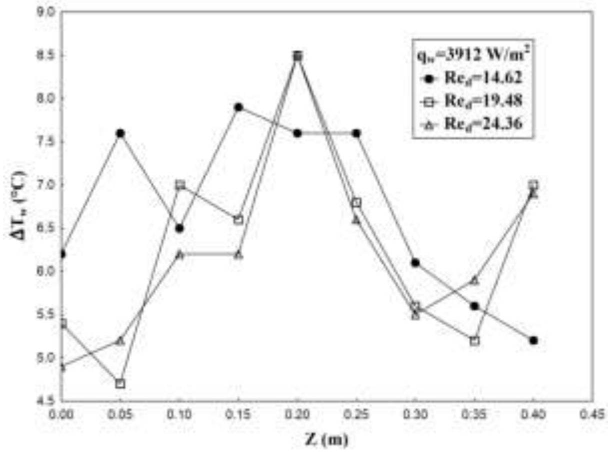

Figure 15. Temperature difference between inner and outer annulus surfaces with the axial distance for different Reynolds numbers and q_w=3912 W/m^2.

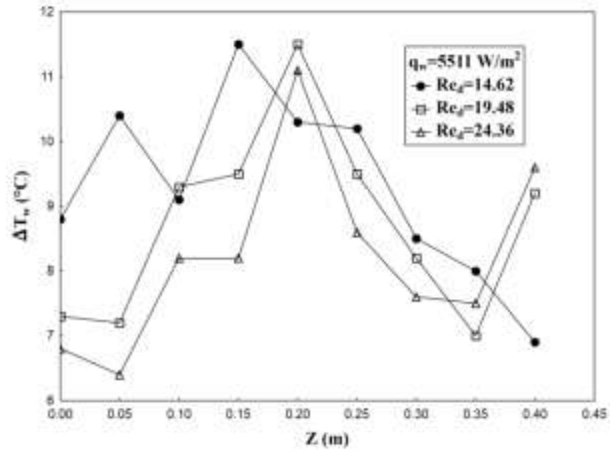

Figure 16. Temperature difference between inner and outer annulus surfaces with the axial distance for different Reynolds numbers and q_w=5511 W/m^2.

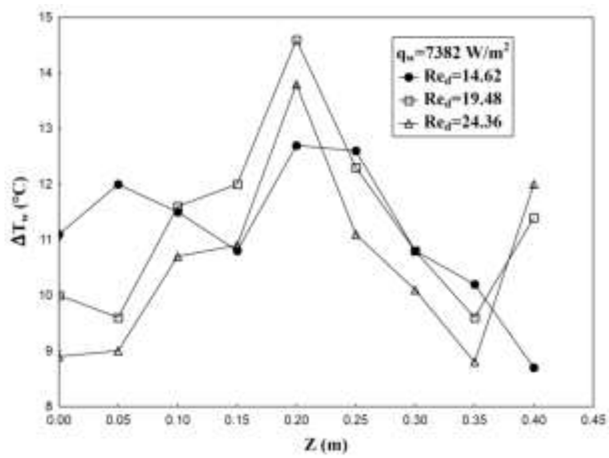

Figure 17. Temperature difference between inner and outer annulus surfaces with the axial distance for different Reynolds numbers and q_w=7382 W/m^2.

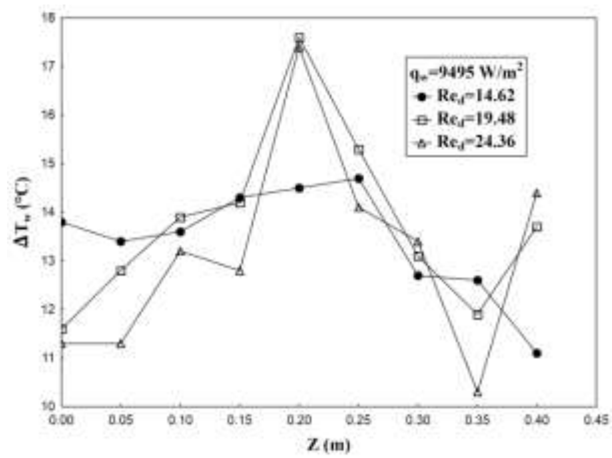

Figure 18. Temperature difference between inner and outer annulus surfaces with the axial distance for different Reynolds numbers and q_w=9495 W/m^2.

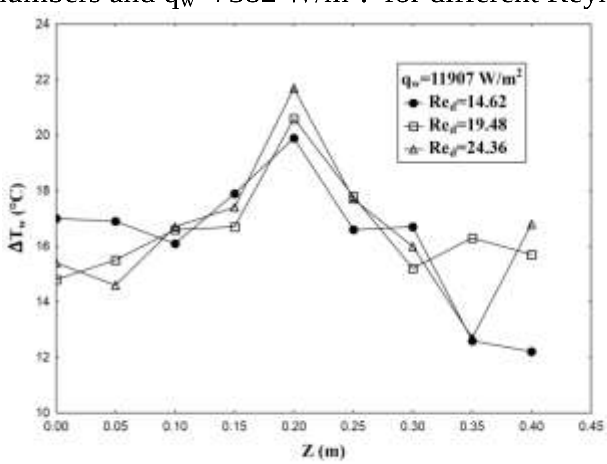

Figure 19. Temperature difference between inner and outer annulus surfaces with the axial distance for different Reynolds numbers and q_w=11907 W/m^2.

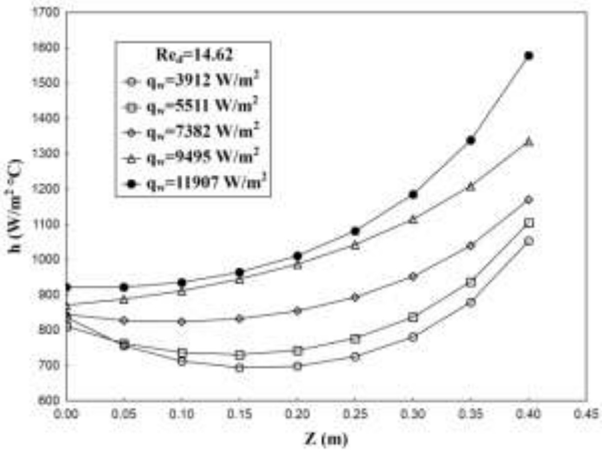

Figure 20. Local heat transfer coefficient with the axial distance for different heat fluxes and Re_d=14.62.

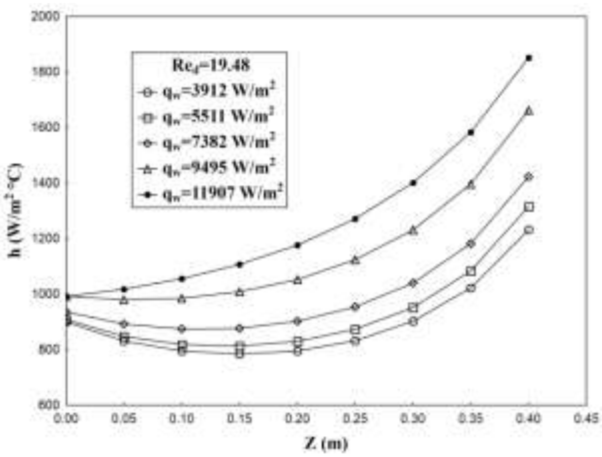

Figure 21. Local heat transfer coefficient with the axial distance for different heat fluxes and Re_d=19.48.

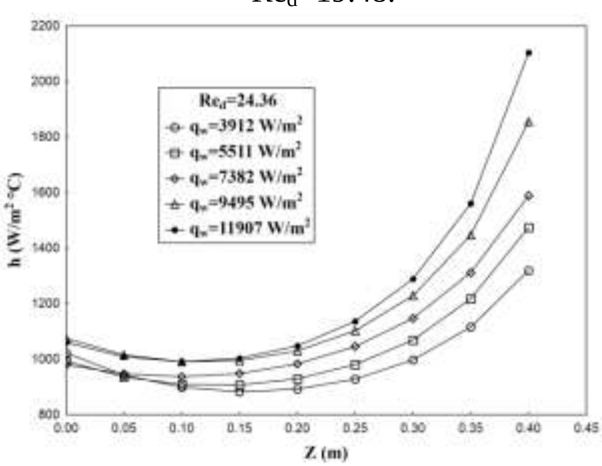

Figure 22. Local heat transfer coefficient with the axial distance for different heat fluxes and Re_d=24.36.

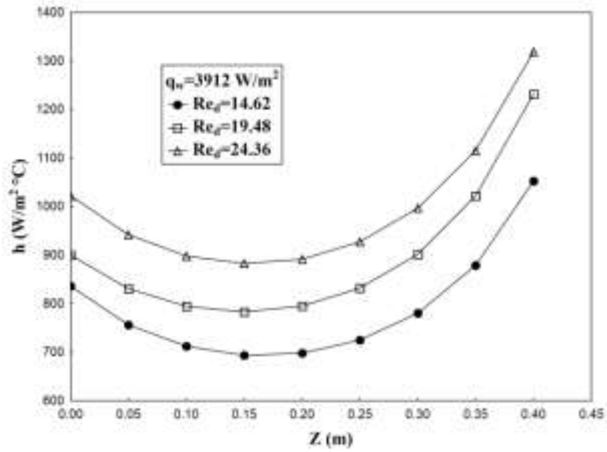

Figure 23. Local heat transfer coefficient with the axial distance for different Reynolds numbers and q_w=3912 W/m^2.

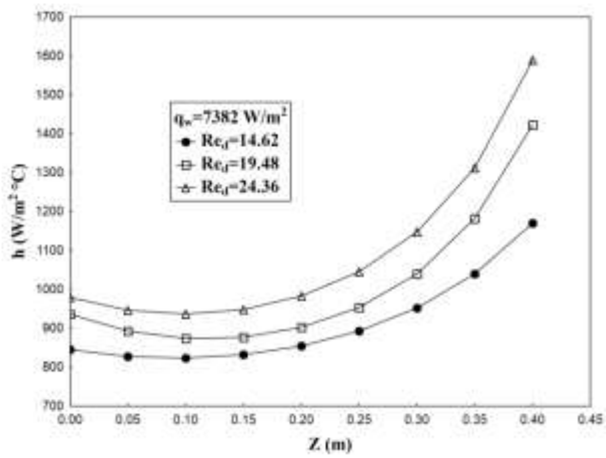

Figure 24. Local heat transfer coefficient with the axial distance for different Reynolds numbers and q_w=7382 W/m^2.

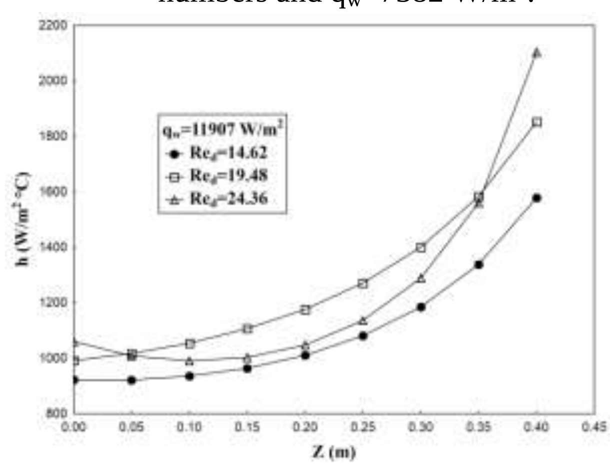

Figure 25. Local heat transfer coefficient with the axial distance for different Reynolds numbers and q_w=11907 W/m^2.

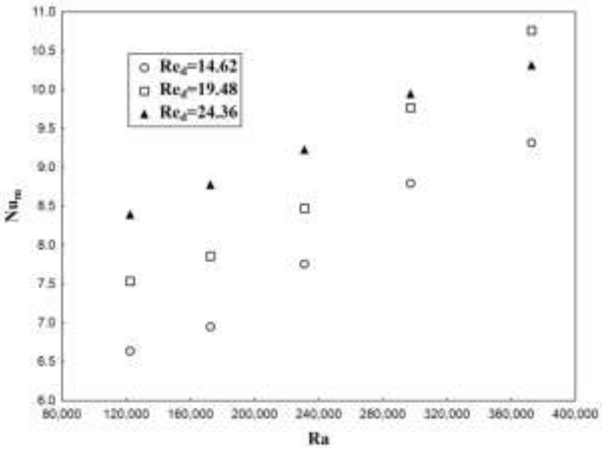

Figure 26. Mean Nusselt number versus Rayleigh number for different Reynolds numbers.

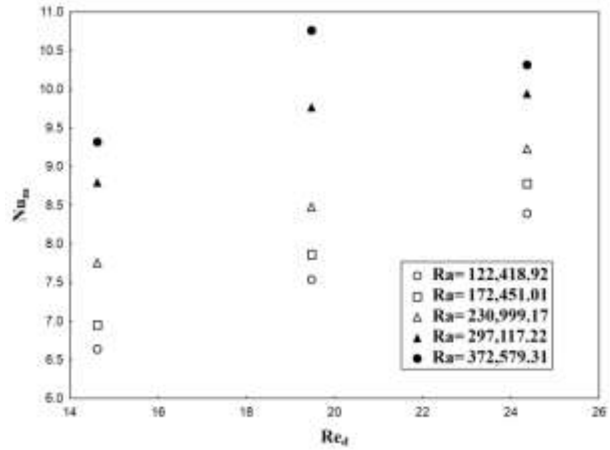

Figure 27. Mean Nusselt number versus Reynolds number for different Rayleigh numbers.

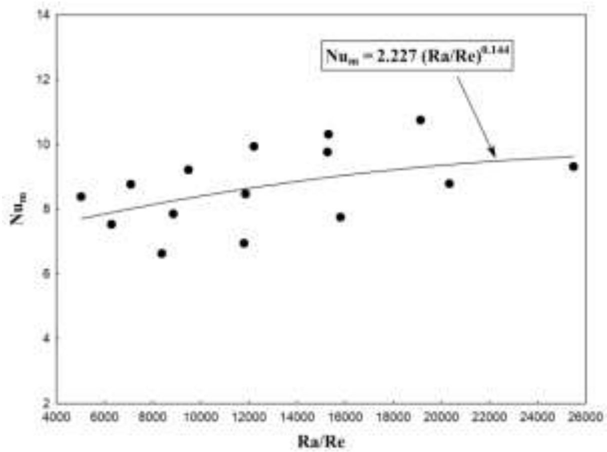

Figure 28. Mean Nusselt number versus Ra/Re.

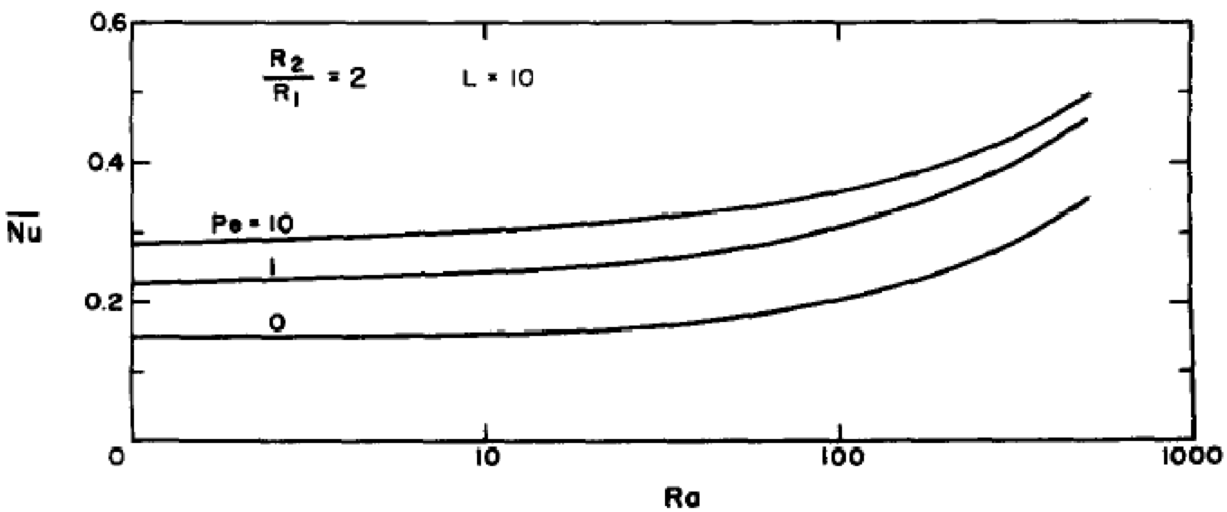

Figure 29. Average Nusselt number of a vertical annulus as a function of Rayleigh number (**K. Muralidhar, 1988**).

Effect of Recirculation Ratio on the Uniformity Flow in a High Area Ratio of Outlets Pipe at Different Entrance flow rates

Dr. Wissam H. Alawee
Lecture
Center of truuing-Univ. of tecnology
Wissam_772005@yahoo.com

Dr. Jafar M. Hassan
professor
Mech. Eng. Dep.- Univ.of Technology
Jafarmehdi1951@yahoo.com

Dr. Wahid S. Mohammad
professor
Mech. Eng. Dep.- Univ. of Technology
Wahid_1953@Yahoo.com

ABSRTACT

The uniform flow distrbiution in the multi-outlets pipe highly depends on the several parameters act togather. Therefor, there is no general method to achieve this goal. The goal of this study is to investigate the proposed approach that can provide significant relief of the maldistribution. The method is based on re-circulating portion of flow from the end of the header to reduce pressure at this region . The physical model consists of main manifold with uniform longitudinal section having diameter of 152.4 mm (6 in), five laterals with diameter of 76.2 mm (3 in), and spacing of 300 mm. At first, The experiment is carried out with conventional manifold, which is a closed-end. Then, small amount of water is allowed by controling the valve located at the end of the manifold slowly. The pressure and the flow distribution among the lateral pipes were recorded. Different inlet flows have been tested and the values of these flows are (625, 790, and 950) l/min. The result reveals that the conventional header give high non-uniform flow distrbution and the distribution of flow is greatly improved by using the perposed methods . When the recircluting ratio is of 15%, the non-uniform coefficient (the stander devation) is reduced from 0.48 to 0.13 which means improves in the flow distribution by 75%.

Keyword: Flow distribution**,** manifold**,** uniform

تأثير نسبة إعادة التدوير على توحيد التدفق في انبوب متعدد المنافذ ذو نسبة مساحة عالية عند معدلات تدفق مختلفة

د. وسام حميد عليوي
مدرس
مركز التدريب- الجامعة التكنولوجية

د. جعفر مهدي حسن
استاذ
قسم الهندسة الميكانيكية- الجامعة التكنولوجية

د. وحيد شاتي محمد
أستاذ
قسم الهندسة الميكانيكية- الجامعة التكنولوجية

الخلاصة

التوزيع المنتظم للجريان خلال الانابيب متعددة المنافذ يعتمد بشكل كبير على العديد من المتغيرات التي تؤثر بشكل مجتمع. لذلك لا توجد هناك طريقة محددة لتحقيق هذا الهدف. البحث الحالي هو تطوير لطريقة مقترحة يمكن ان تقلل من سوء توزيع الجريان. تستند هذه الطريقة على سحب نسبة محددة من المائع من النهاية المغلقة للانبوب المتفرع وذلك لتقليل الضغط المرتفع في هذه المنطقة. يتكون مقطع الاختبار المستخدم في البحث من انبوب رئيسي بقطر (152.4 ملم) وخمسة انابيب فرعية بقطر (76.2 ملم)، المسافة بين الانابيب الفرعية كانت (300 ملم). أنجزت التجارب في البداية على مقطع الاختبار بالتصميم التقليدي (النهاية مغلقة) بعد ذلك يتم السماح لكميات مختلفة من الماء من المرور من النهاية المغلقة من خلال صمام تحكم مثبت في نهاية الانبوب. استخدمت ثلاثة قيم مختلفة لكمية التدفق الداخل خلال التجارب وهي (625، 790، 950) لتر/ثانية. بينت النتائج ان عملية سحب

جزء من الماء من النهاية المغلقة للانبوب المتفرع يساهم الى حد كبير في تحسين توزيع الجريان، حيث انه عند نسبة اعادة تدوير مقدارها (15%) قلت قيم معامل الانحراف من 0.48 الى 0.13، وهذا يحسن من توزيع الجريان بمقدار 75%.

1. INTROUDUCTION

Multiple-outlet pipes, often referred to as manifolds, are used in many engineering applications such as infiltration systems, (**Burt et al., 1992**), heat exchanger (**Ranganayakulu et al., 1997**), gas pipe burners (**Mishra et al., 2013**), fuel cells (**Kang et al., 2009**), and ocean outfalls (**Kang et al., 2002**).The flow rate distribution through the lateral pipes depends on the pressure difference across, and, the shape of the header or manifold. Two main challenges of the multiple-outlet pipes are first, to obtain a even flow distribution through lateral pipes, and second, to reduce the pressure loss along the lenght of the manifold (**Hsien and Hin, 2008**, **Tong et al., 2007**). There are two types of multiple-outlet pipes. One of these categories is dividing multiple-outlet pipes, wherein there is a single inlet and multiple exits The other category is combininng multiple-outlet pipes, where there are multiple inlets and a single exit. Combining-flow multiple-outlet pipes are discussed in (**Graber, 2004, 2007**), The present paper addresses dividing-flow multiple-outlet pipes.

A major study has been investigated by (**Acrivos et al., 1959**) for pipe spargers. they found that the flow distribution depends on frictional pressure drop due to the miner and majer losses, and pressure recovery due to the reduction in velocity in the flow direction. In addition, the results showed that the high cross section area of distribution manifold give uniform flow distribution. **Kim et al., 1995**, numerically investigated the effect of outlet header shapes on the flow distribution with the same inlet velocity for three different header geometries (i.e., rectangular, triangular, and trapezoidal) with the Z-type flow direction. Their results indicated that the triangular shape provided the best distribution regardless the inlet flow rate. **Zhe and zhong, 2003**, and **Zhang et al.,2004** conducted the experimental studies as well as CFD simulation studies to understand the effect of manifold configuration in plate heat exchangers. **Tong et al., 2009**, investigated the influence of the cross sectional area of the header. They concluded that the simplest way to obtain outflow uniformity is to enlarge the header to increase the cross sectional area or reduce the flow area ratio.

Hassan et al., 2008, studied numerically the effect of the area ratio (the ratio between sum of areas of all outlets to the area of the main pipe) (AR) on the flow distribution through manifold with five lateral pipes. The simulation results showed that the area ratio has a highly impact on flow distribution through the lateral pipes.

Hassan et al., 2012, performed numerically model to predict the flow distribution in a square cross section header with five branch channels. Three geometrical parameters were considered to investigate their effect on flow distrbution. The geometrical parameters include the distance among laterals, the length of the laterals, and the laterals size. Results showed that increasing the length of the laterals and reducing lateral size give uniform flow profile at lateral outlet.

Fu et al., 1994, studied experimentally and numerically the flow distribution in distribution manifold of square cross-section. **Wang and Yu, 1989**, studied experimentally the flow distribution in inlet and outlet flow for solar collectors. The results show that the header systems can be categorized as pressure regain type and pressure decrease type according to the static pressure distribution along the multiple-outlet pipes. **Kenji and Hidesato, 2005**, presents an experimental study to determine energy loss coefficients for smooth, sharp-edged tees of circular cross-section with large area ratio. By using equations developed from the continuity, energy, and momentum principles they expressed the loss coefficients with correspond correction factors needed in the equations. The comparison of the proposed equations with the experimental results obtained by authors showed that the proposed equations with the correction factors gives good agreement with the experimental results for the area ratio greater than 8.

The literature survey indicates that a flow uniformity are gaining importance in many engineering applications. Also, it was found that impossible achieve this goal for conventional header has area ratio greater than unity (area ratio, AR the ratio between sum of areas of all outlets to the area of the main pipe). **Wissam, 2005**, studied numerically and experimentally several methodologies to improve the flow uniformity in distribution manifold. One of these methodologies were study the effect of drawing ratio (flow out from closed end of manifold) on the flow distribution at the manifold diameter of 101.6 mm (4 in). The results showed that the flow drawing from the end of manifold reduced the flow maldistribution through lateral pipes. The objective of the present study is to investigate the effect of drawing ratio on the flow distribution at **large header diameter** 152.6 mm (6 in), different drawing ratio, and different entrance velocities.

2. EXPERIMENTAL SETUP

The test rig of this study is shown in **Fig. 1**. The rig was built at a selected site in Department of Machinacl Engineering, University of Technology, Baghdad. The test rig, shown in Figure consists of the follwing parts: the main supply pipe, test section, shalow tank to collection water, flow meter, manometer and a centrifugal pump to recycle water to main supply pipe. In order to make a successful and accurate experimental study using the proposed approach, two test sections are made; the first one is made according to conventional design with large area ratio. It is simply shaped with uniform cross section header. The second is made according to the proposed approach. It connected with a globe valve to investigate the effect downstream outflow on uniformity of flow distribution. These test sections consist of a manifold with five-lateral pipe orizontal header and five parallel channels. The header is made of acrylic material to ensure the good visibility of developed flow. It has 1500 mm long and 152.4mm (6 in) diameter.

The inlet of each test section is connected to a 3500 mm length pipe made of clear polyvinyl chloride (PVC) at same diameter of test section. The long pipe provides a fully developed flow. The first test section is dead end where it is closed by a PVC plug. the end of another test section is connected to globel valve. Each branch has 76.2-mm diameter. The branches are regularly 300-mm spaced along the header. The diagrames in **Fig.2**. show the general configuration of the test sections used.

3. FLOW LOOP AND MEASURING DEVICES

The experimental loop is shown in **Fig.3**. Water is the test fluid. The water flow rate from each lateral pipe is collected in a shallow tank, with dimentioin 1500-mm x 1500-mm x 400-mm, then discharged continuously through pipe with diameter of 152.4 mm (6 in) to recycle water by centrifugal pump to main supply tank. The water flow rate is measured by five glass containers with a capacity of 50 liter for each container. The containers are placed on a movable support, which allows it to move freely at the same time of carrying out of experiments. The containers and support are shown in **Fig.4**. Nine pressure tapes are located along the length of the test section. These pressure tapes are used to measure the pressure head in inlet of manifold and at different points along the length of the distribution manifold. The inlet water to the test section is controlled by a globle valve and is measured by a target flo.wmeter.

4. EXPERIMENTAL CONDITIONS

The first tests are carried out with the reference geometry (a multiple-outlet pipes with dead end) to test the effect of the inlet flow rate on the flow distrbution. Inlet flow rates ranges are 625–950 l/min. Three different of drawing ratio are investigated to study its impact on the flow uniformity. All tests are performed at a room temperature and at a atmosphere pressure.

5. MATHEMATICAL MODEL

Fig. 5 shows The control volume in an dividing manifold. The theoretical flow model for present work is based on the same mathematical style as that in the previous work (**Wang, 2008, Wang, 2011).** The mass and momentum balances can be written as follows:

Mass Conservation:

$$\rho AW = \rho A(W + \frac{dW}{dZ}\Delta Z) + \rho A_L U_L \quad (1)$$

$$U_L = -\frac{AL}{A_l n}\frac{dW}{dZ} \quad (2)$$

where A and A_l are the cross-sectional areas of the header and the lateral pipe, respectively, W_l the axial velocity in header pipe, U_l the velocity in lateral pipe, Z axial coordinate, L length of the header, and *n* number of lateral pipes. Setting $\Delta X = L/n$

.

Momentum Conservation:

$$PA + \rho AW^2 - \tau_W \pi D\Delta Z = \left(P + \frac{dP}{dZ}\Delta Z\right)A + \left(W + \frac{dW}{dZ}\Delta Z\right)^2 + \rho A_l U_l W_l \quad (3)$$

Where P is pressure in the manifold, D diameter of header pipe, τ_w is given by Darcy–Weisbach formula, $\tau_w = f\rho W^2/8$, and $W_l = \beta W$. After inserting τ_w and W_l into Eq. (3) and neglecting the higher orders of ΔX, Eq. (3) can be rearranged as follows:

$$\frac{1}{\rho}\frac{dP}{dZ} + \frac{f}{2D}W^2 + (2-\beta)W\frac{dW}{dZ} = 0 \quad (4)$$

The flow in the lateral pipes can be described by Bernoulli's equation with a consideration of flow turning loss. Hence, the velocity in a lateral pipe, U_l, is correlated to the pressure difference between the manifold and the ambient as follows:

$$P - P_c = \rho\left(1 + C_f + f_l\frac{L_l}{d_l}\right)\frac{U_l^2}{2} = \rho\zeta\frac{U_l^2}{2} \quad (5)$$

where C_f is turning loss coefficient from the manifold into the lateral pipes, H is length of the lateral pipe, d_l is diameter of lateral pipe, f_l is coefficient of the friction for the lateral pipe. Inserting Eq. (2) into Eq. (5), gives:

$$P - P_c = \frac{1}{2}\rho\zeta\left(\frac{AL}{A_l n}\right)^2\left(\frac{dW}{dZ}\right)^2 \qquad (6)$$

Eqs. (4) and (6) can be reduced to dimensionless form using the following dimensionless groups.

$$p = \frac{P}{\rho W_o^2}, \qquad p = \frac{P_l}{\rho W_o^2}, \qquad w = \frac{W}{W_o}, \qquad u_l = \frac{U_l}{\rho W_o}, \qquad z = \frac{Z}{L}, \qquad (7)$$

$$\frac{dp}{dx} + \frac{fL}{2D}w^2 + (2-\beta)w\frac{dw}{dz} = 0 \qquad (8)$$

$$p - p_c = \frac{1}{2}\left(\zeta\frac{A}{A_l n}\right)^2\left(\frac{dw}{dz}\right)^2 \qquad (9)$$

where W_0 is the inlet velocity of the manifold. Inserting Eq. (9) into Eq. (8) and after rearranging, one obtains an ordinary differential equation for the velocity in the distributon manifold:

$$\frac{dw}{dz}\frac{d^2w}{dz^2} + \frac{2-\beta}{\zeta}\left(\frac{A_l n}{A}\right)^2 w\frac{dw}{dz} + \frac{fL}{2D\zeta}\left(\frac{A_l n}{A}\right)^2 w^2 = 0 \qquad (10)$$

5.1 Analytical Solution

We define two constants**:**

$$Q = \frac{2-\beta}{3\zeta}\left(\frac{A_l n}{A}\right)^2 \qquad (11)$$

$$R = \frac{fL}{4D_h\zeta}\left(\frac{A_l n}{A}\right)^2 \qquad (12)$$

Thus, Eq. (10) is reduced as follows:

$$\frac{dw}{dz}\frac{d^2w}{dz^2} + 3Qw\frac{dw}{dz} - 2Rw^2 = 0 \qquad (13)$$

The general solutions of the governing equation (13) for flow distribution in manifold is similar to that done by **Wang, 2008, 2011**. To solve Equation (13), we assume that the function, $w = e^{rz}$w, is a solution of Equation (13) and substitute it and its derivatives into Eq. (13), we obtain the characteristic equation of Equation (13).

$$r^3 + 3Qr - 2R \qquad (14)$$

The solutions of Equation (13) depends on the sign of $Q^3 + R^2$, which have three cases. The solutions of case ($Q^3 + R^2 > 0$) is listed here.

$$r = \left[R + \sqrt{Q^3 + R^2}\right]^{1/3} + \left[R - \sqrt{Q^3 + R^2}\right]^{1/3} \quad ; \quad \mathrm{r}_1 = -\frac{1}{2}B + \frac{1}{2}i\sqrt{3}J \quad ; \quad \mathrm{r}_2 = -\frac{1}{2}B - \frac{1}{2}i\sqrt{3}J$$

$$Where\, B = \left[R + \sqrt{Q^3 + R^2}\right]^{1/3} + \left[R - \sqrt{Q^3 + R^2}\right]^{1/3}$$

Thus, the general solution of Eq. (13) and boundary conditions can be written as follows:

$$w = e^{-Bz/2}\left[C_1 \cos\left(\sqrt{3Jz/2}\right) + C_2 \sin\left(\sqrt{3Jz/2}\right)\right] \tag{15}$$

$w = 0, \quad at \quad z = 1$
$\mathrm{w} = 1, \quad \mathrm{at} \quad \mathrm{z} = 0$

The equation of axial velocity in the manifold can be written as follows:

$$w = e^{-Bz/2}\left[\frac{\sin\left(\sqrt{3J(1-z)/2}\right)}{\sin\left(\sqrt{3J/2}\right)}\right] \tag{16}$$

The equation of velocity of lateral can be written as follows:

$$u_l = \left(\frac{A}{2nA_l}\right) e^{-Bz/2}\left[\frac{B\sin(\sqrt{3J}(1-z)/2) + \sqrt{3J}\cos(\sqrt{3J}(1-z)/2)}{\sin(\sqrt{3J}/2)}\right] \tag{17}$$

Flow distribution through lateral pipe:

$$v_\mathrm{i} = \left(\frac{\mathrm{nA_l}}{\mathrm{A}}\right)\mathrm{u_l} = \frac{1}{2}e^{-Bz/2}\left[\frac{B\sin(\sqrt{3J}(1-z)/2) + \sqrt{3J}\cos(\sqrt{3J}(1-z)/2)}{\sin(\sqrt{3J}/2)}\right] \tag{18}$$

5. RESULTS AND DISCUSSION

According to **Hassan et al., 2008** and **Wissam, 2015** the flow distribution along multi-outlet pipe is depended largely on the area ratio. They found that, when the area ratio increases to larger than unity, the flow distribution along multi-outlet pipe is far from uinform. On the contrary, when the area ratio decreases, the distribution of flow improves dramatically. Therefore, the present results are expected for area ratio greater than unity. These results will be a reference to investigate the effect of proposed approach on the flow and pressure distribution.

The results of the flow rate for each outlet at three different inlet flow rates (625, 790, 950) l/min. are given in **Fig.6**. As expected, the water flow in the outlets tends to increase, starting with the first outlet which is badly fed to the last one which is so highly fed (more than twice the mean water flow rate). In contrast, the pressure distribution along the length of manifold also be uneven.

There is a clear flow maldistribution which can be explained as follows: there are two factors control the pressure variations in multi-outlet header: friction and momentum. These two factors work in opposite directions to each other. The friction effect lowers the pressure along the header in opposing the momentum effect. In tradetional header, the momentum cannot balance the friction effect, resulting in a non-uniform flow distribution. When the multi-outlet pipe is dead end, water is recirculating at the closed end. This causes unstable flow and pressure increase, resulting in an increase in flow rate through branch No.5. This is in agreement with the findings in reference, **Pertorius, 1997**.This is in agreement with the results of reference, **Pertorius, 1997**.

The behavior of flow distribution is consistent with the pressure distributions that have been displayed in **Fig.7**. This figure shows that the pressure increases with increasing of downstream distances. Since the pressure difference drives the per-outlet water flow rate, so it is necessary to increase the flow rate with downstream distance.

The difficulty in obtaining uniform distribution is due to pressure build-up at the header end. To reduce the pressure, a portion of the flow is re-circulated to supply tank were carried out. **Figs. 8, 9**, and **10** present the results of flow rate at drawing ratios of 5%, 10%, and 15% respectively. From these figures, it can be seen that the ratio of withdrawal water from the closed end of manifold helps to a great extent to improve the distribution of the flow regardless of inlet flow rate (in the range used in the experiment that is from 625 l/min. to 950 l/min.). When the drawing ratio is 0%, it means that there is no flow from the end of the manifold. In this case, a part of the kinetic energy is converted to a rise in pressure at that region.Thus, the water flow through the outlets is increasing towards dead end of the header. When the drawing ratio is certain percentage, the pressure at the dead end will decrease and hence the water flow from the last outlet is also decreases. When the drawing ratio increses from 5% to 15%, the pressure along the manifold was become nearly uniform which gives a better flow distribution through the outlets.

Fig.11 shows the percentage of flow rate fraction for each outlet takes from the total flow at different drawing ratio. Comparing these results with those of traditional header (closed end), a clear improvement can be seen in flow distribution. For example, when the traditional header is used, the discharge from last outlet is about 29.5% of the total flow rate while for the header with 15% drawing ratio, the percentage is reduced from 29.5% to 22.5%. In other words, the flow discharge from first outlet is 64% less than that from last outlet but when the header with 15% drawing ratio is used, this percentage is reduced from 64% to 20%.

The percentage of absolute mean deviation from average flow rate is shown in **Fig.12**. From this figure, the values of standard deviation (STD) are 0.48, 0.439, 0.311, and 0.241 at Drawing ratio of 0%, 5%, 10%, and 15%, respectively. The lowest value of (Φ) was of the header with 15% drawing ratio that corresponding to 0.025. It is clear that water withdrawal in certain proportions from the high pressure region (in which the kinetic energy is converted to a rise in pressure) would help reduce pressure in this region, thus resulting in improved flow distribution.

A comparison between the present results and the result of **Wissam, 2015** shows (see Table 1) that the selection of drawing ratio depends largely on the header diameter. On the other hand, the total inlet flow rate does not affect the flow distribution. When the drawing ratio of 10%, the value of stander deviation is (0.377). Also, when using the same ratio but with header diameter of (6 in), the value of deviation coefficient is reduces from 0.377 to 0.311.

Experimental tests for flow distribution from manifold have been conducted, which made it possible to validate the analytical procedures. **Fig. 13** shows comparison between the computed and experimental flow rate per-outlet. It can be clearly seen from the figures that the different of flow rate between computed and experimental value is acceptable.

5. CONCLUSION

Two test sections representing different header structures were used in this study. The first test section is uniform header, the second header with drawingratio. In both test sections, the diameter of the main pipe was 152.4 mm and of the lateral pipe 76.2 mm. the method of withdrawal water from the dead end of manifold is a very successful approach to improve flow uniformity. where, the flow distribution is improved by 75% which means the stander devation is reduced from 0.48 to 0.241.Three different values of inlet flow rate of (625, 790,950) l/min had been used in the experiments. From the results, it is found that change in the total flow rate has a slight effect on flow uniformity. Therefore, it can be safely said that the inlet flow rate has no effect on flow distribution.

ACKNOWLEDGEMENTS

The authors would like to thank the Mechanical Engineering depertment, University of technology for its assistance.

REFFERENCE

- Acrivos, A., Babcock, B.D., and Pigford, R.L., 1959. Flow distribution in manifolds. Chem. Eng. Sci. vol. 10, pp. 112–124.
- Alawee, W. H., 2015, Solution Methodologies for the Fluid Flow Distribution Manifold Problem, Ph.D Thesis, Department of Mechanical Engineering, University of Technology, Iraq.
- Burt, C. M., Walker, R. E., Styles, S. W., 1992, Infiltration System Evaluation Manual. Irrigation Training And Research Center,. California polytechnic state, Univcity San Luis Obispo, CA.
- Bleninger, T., Lipari, G., and Jirka, G., 2002, Design And Optimization Program For Internal Diffuser, 2nd Int. Conf. on Marine Waste Water Discharges, MWWD 2002.
- FU H., Watkins, A. P., and Yianneskis M., 1994, The Effects Of Flow Split Ratio And Flow Rate In Manifolds,. Int. J. Numerical Methods in Fluids, vol.18, no.9, pp. 871-886.

- Graber, S. D., 2004, Concepts of spatially varied flow.” Proc., HTFED, 2004 ASME Heat Transfer/Fluids Engineering Summer Conf., ASME, New York.
- Graber, S. D., 2007, Full-flowing collection conduits with nonuniform inflow.” Journal. Environment Engineering, vol. 133, no. 6, pp. 575–580.
- Hassan, J. M., Mohamed, T. A., Mohammad, W. S., and Alawee,W. H., 2014, Experimental and Numerical Study on the Improvement of Uniformity Flow for Three-Lateral Dividing Manifold, World Research & Innovation Convention on Engineering & Technology, Putrajaya, Malaysia, 25-26 November 2014.
- Hsien-Ter Chou and Hin-Chi Lei, 2008, Outflow Uniformity along a Continuous Manifold, Journal of Hydraulic Engineering,ASCE / SEPTEMBER 2008 , pp. 1383-1388.
- Hassan, J. M.,208, Flow Distribution in Manifolds, Journal of Engineering and Development, vol. 12, no.4, pp. 159-177.
- Hassan, J. M., 2012, Study of Three Dimensional Fluid Flow in Manifold-Laterals System, Eng. & Tech. Journal, vol.30, no. 7,pp. 1132-1148.
- Kang, S., Min, K., Mueller, F., and Brouwer, J., 2009, Configuration effects of air, fuel, and coolant inlets on the performance of a proton exchange membrane fuel cell for automotive applications, International Journal of Hydrogen Energy, vol.34, no.16, pp. 6749–6764.
- Kim, S., Choi, E., and Cho, Y.I., 1995, The effect of header shapes on the flow distribution in a manifold for electronic packaging applications, International Communicationsin Heat and Mass Transfer, vol. 22, pp. 329-341.
- Kenji, O., Hidesato, I., 2005, Energy Losses at Tees with Large Area Ratios, Transactions of the ASME, Journal of Fluids Engineering, Vol. 127, pp. 110-116.
- Mishra, N. K., Muthukumar, P., and Mishra, S. C., 2013, Performance Tests on Medium-Scale Porous Radiant Burners for LPG Cooking Applications, International Journal of Emerging Technology and Advanced Engineering Vol. 3, Special Issue 3, pp. 126-130.
- Pertorius W.A., Dividing- flow Manifold Calculations with a Spreadsheet, water science, 23 (2) (1997) 147-150.
- Ranganayakulu, Ch., Seetharamu, K. N., and Sreevatsan, K.V., 1997, The Effects of Inlet Fluid FlowNonuniformity on Thermal Performance and Pressure Drops in Crossflow Plate-fin Compact Heat Exchangers, Int. J. Heat Mass Transfer, vol. 40, no. 1, pp. 27–38.
- Tong, J.C.K., Sparrow, E.M., Abraham, J.P., 2007, Attainment of flowrate uniformity in the channels that link a distribution manifold to a collection manifold, Journal Fluids Engineering, vol. 129, pp.1186–1192.
- Tong, J.C., Sparrow, E.M., and Abraham, J.P.,2009, Geometric strategies for attainment of identical outflows through all of the exit ports of a distribution manifold in a manifold system, Appl. Therm. Eng., vol. 29, pp. 3552–3560.
- Zhe Z., Yan-zhong, L., 2003, CFD simulation on inlet configuration of plate-fin heat exchangers, Cryogenics, vol. 43, no. 12, pp. 673-678.

- Zhe, Z., Yan-zhong, L., and Qing, X., 2004, Experimental research on the effects of distributor configuration in plate-fin heat exchangers, Heat Transfer-Asian Research, vol. 33, no.6, pp. 402.
- Wang, X. A. and P. Yu, Isothermal flow distribution in header systems, International Journal of Solar Energy, 7(1989)159-169
- Wang J., Pressure drop and flow distribution in parallel-channel configurations of fuel cells: U-type arrangement, International journal of hydrogen energy, 33(2008) 6339 – 6350.
- Wang, J., Theory of flow distribution in manifolds, Chem. Eng. J., 168 (2011)1331–1345.

7. NOMENCLATURE

C_f = coefficients of turning losses.
D= diameter of manifold, m.
d_l = diameter of the lateral pipe, m.
f =friction factor
A, A_l = cross-sectional area of manifold and lateral pipe, m^2.
H= length of lateral pipe, m.
L= length of manifold, m.
n = numbers of lateral pipes.
Pa = ambient pressure
p_a = dimensionless ambient pressure
P = pressure in manifold
P = dimensionless pressure.
Q = coefficient in Eq. (13), defined by Eq. (11)
R = coefficient in Eq. (13), defined by Eq. (11)
r, r_1, r_2 = roots of characteristic equation.
W = velocity in manifold (m/s)
w =dimensionless velocity in manifold.
U_l = velocity of lateral pipe, m/s.
u_l = dimensionless velocity of lateral pipe.
vc =dimensionless volume flow rate in lateral pipes.
β = average velocity ratio in manifold (W_l/W)
ρ = fluid density (kg/m_3)
τ_w = wall shear stress (N/m_2)
ζ = average total head loss coefficient for port flow

Table 1. A comparison of the results obtained in the present study with those of Ref., Alawee,2015.

Researcher	Drawing ratio, %	Percentage of flow rate fraction for each outlet takes from the total flow					
		Outlet 1	**Outlet 2**	**Outlet 3**	**Outlet 4**	**Outlet 5**	**STD**
Wissam, 2015	8	11%	15%	12%	22%	22%	**0.371**
Header diameter=101.6 mm (4")	10	11.9	16.6	23.1	23.6	24.8	**0.354**
The present work	10	13.3	16.6	22.0	23.8	24.1	**0.311**
Header daimeter=152.6 mm (6")	15	14.6	18.5	21.0	21.4	21.9	**0.241**

Figure 1. Plate of the experimental rig for five-lateral manifold.

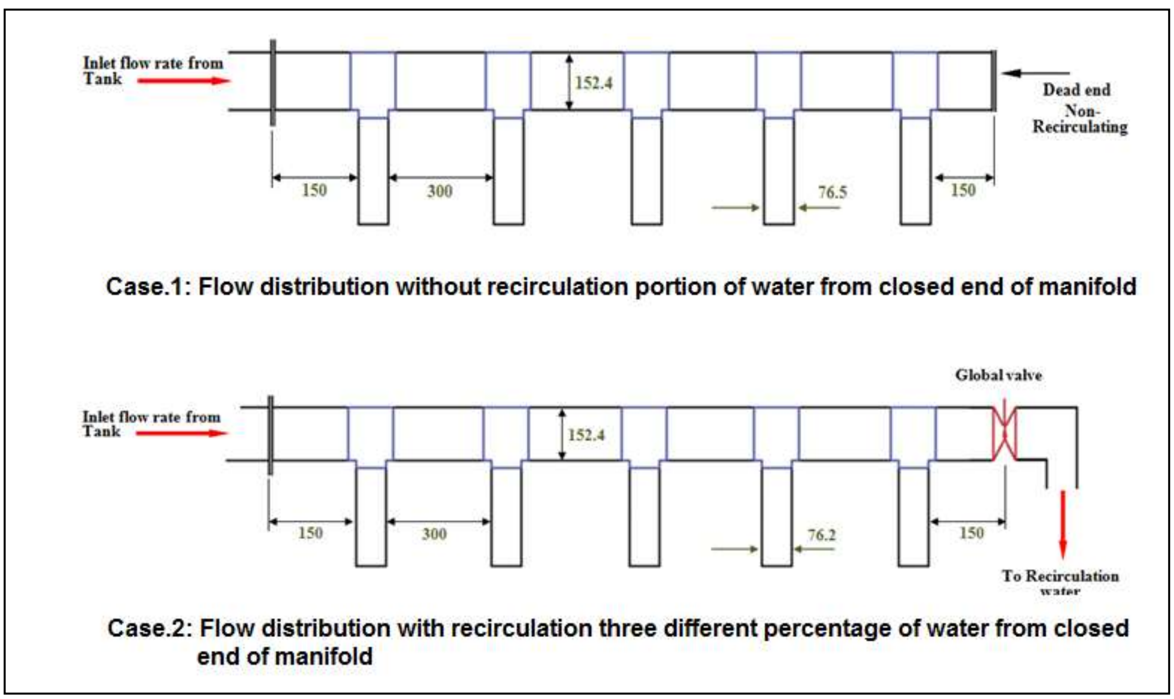

Figure 2. Multi-outlets pipe with/without recirculation ratio .

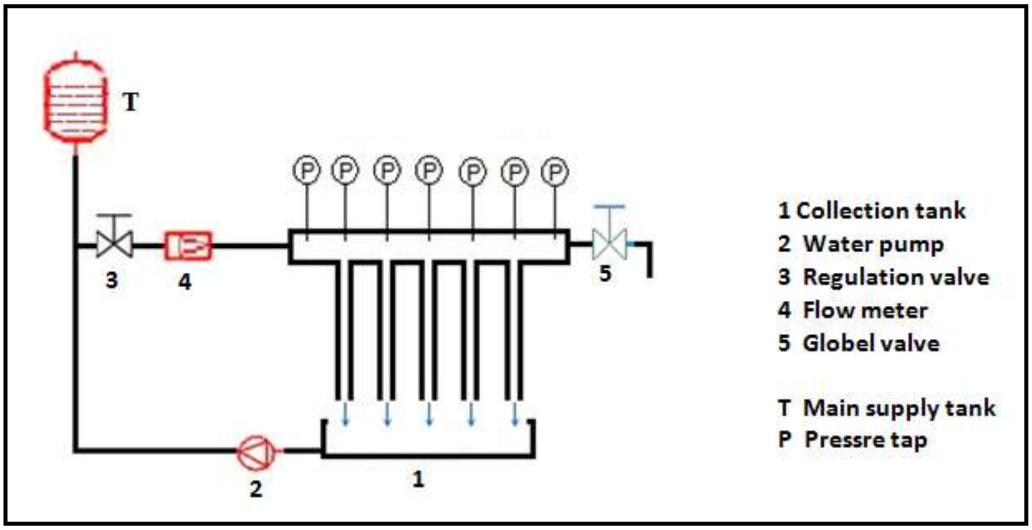

Figure 3: Schematic diagram of flow loop.

Figure 4: Containers to measure water from outlets

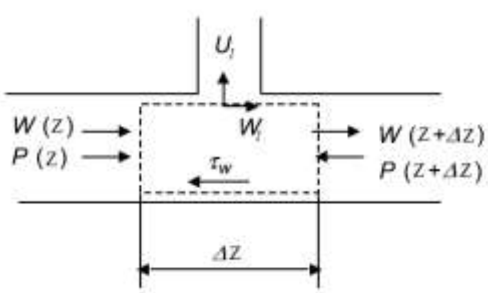

Figure 5: Control volume for the distrbution manifold.

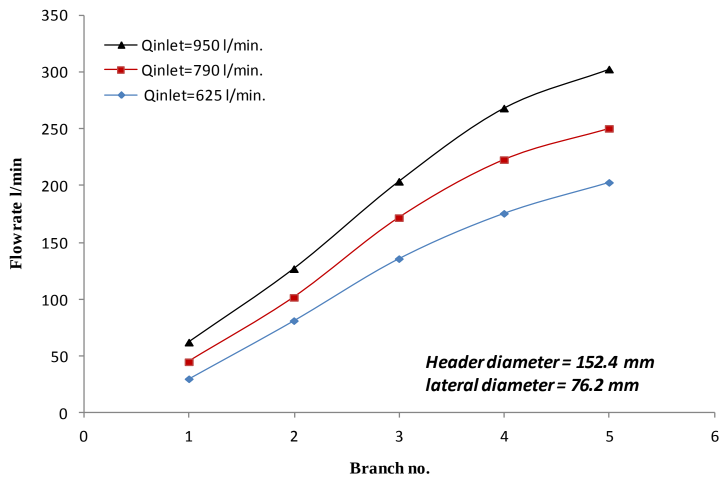

Figure 6: Flow distribution plot at three value of inlet flow water .

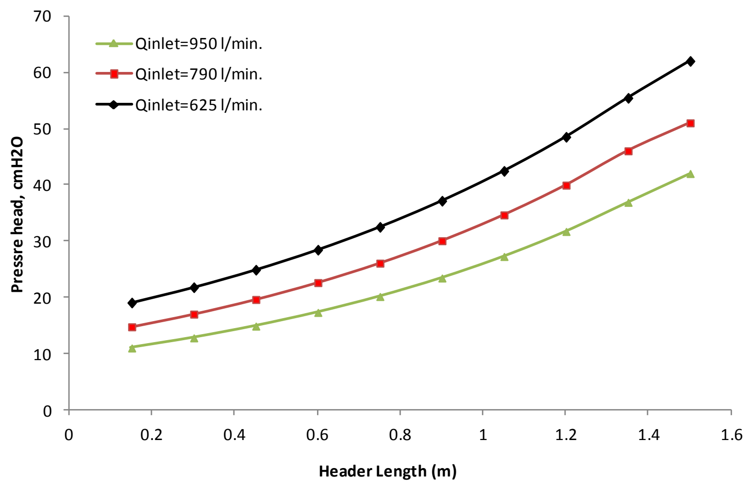

Figure 7: Variations of pressure head along the manifold .

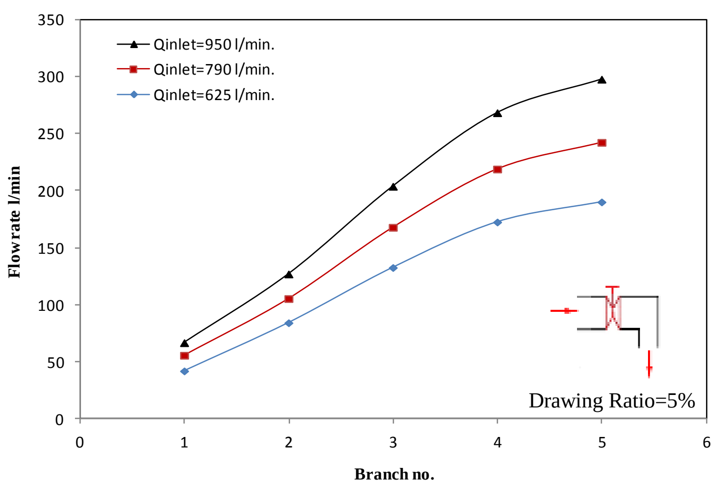

Figure 8: Flow distribution plot of manifold with 5% drawing ratio at three value of inlet flow water .

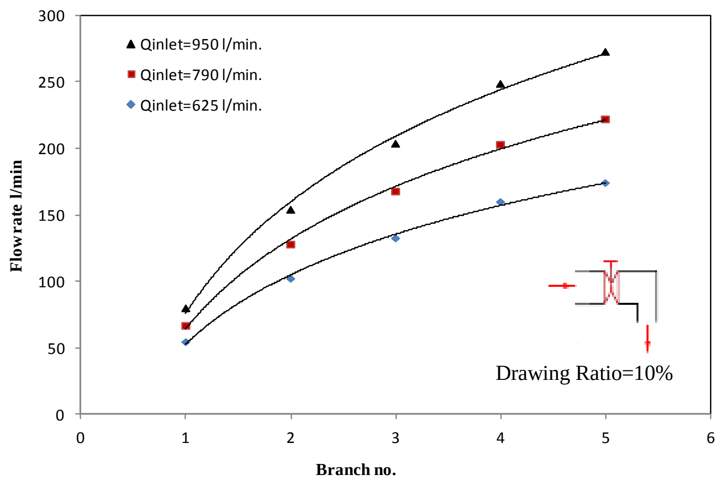

Figure 9: Flow distribution plot of manifold with 10% drawing ratio at three value of inlet flow water .

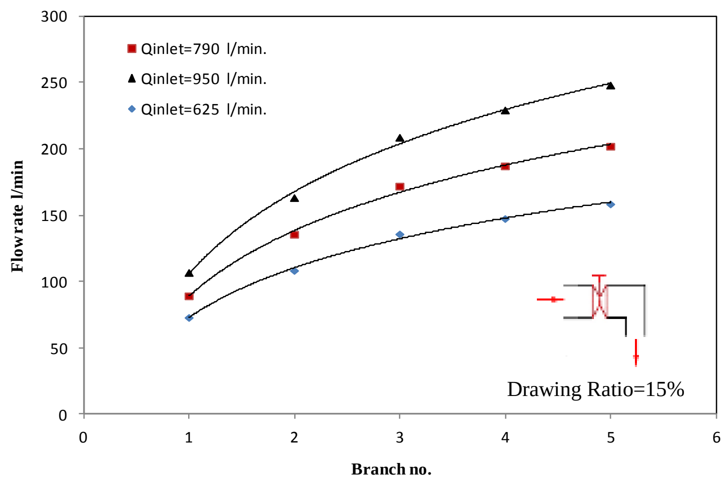

Figure 10: Flow distribution plot of manifold with 15% drawing ratio at three value of inlet flow water.

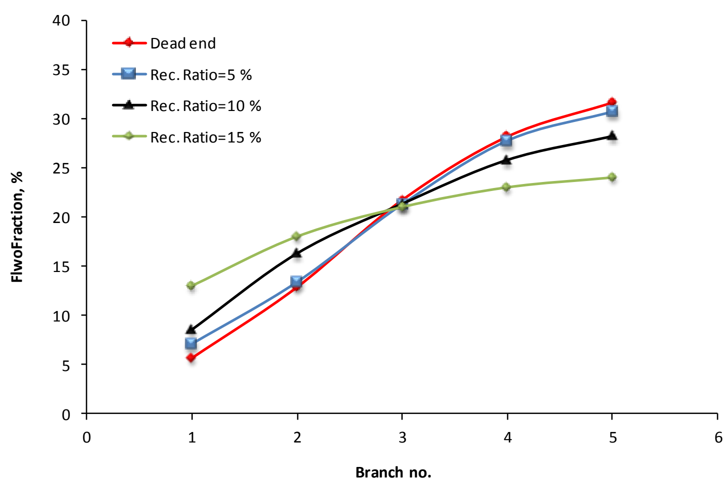

Figure 11: Flow rate fraction at three value of drawing ratio.

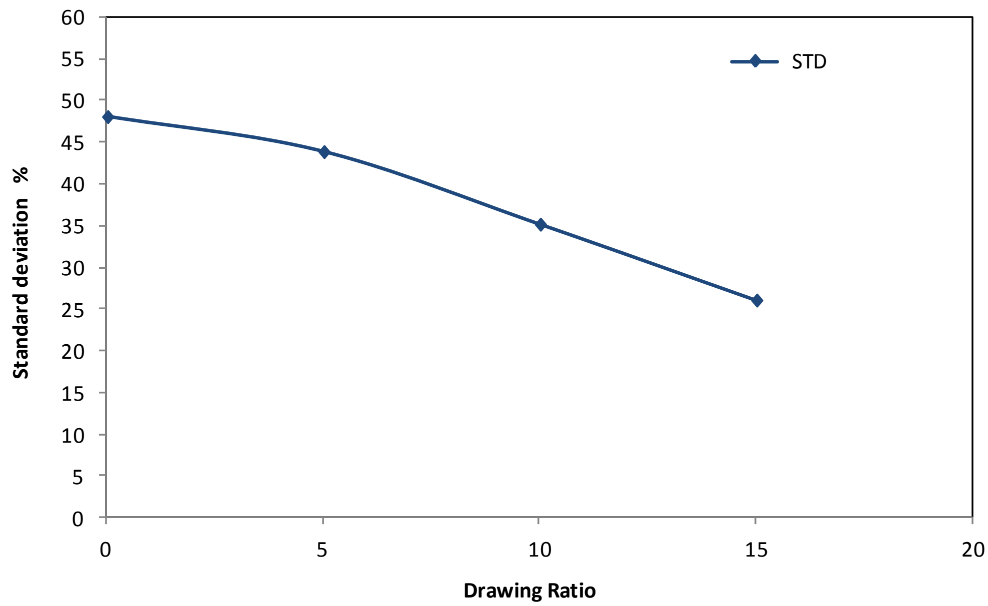

Figure 12: Percentage of absolute mean deviation from average for three drawing ratio

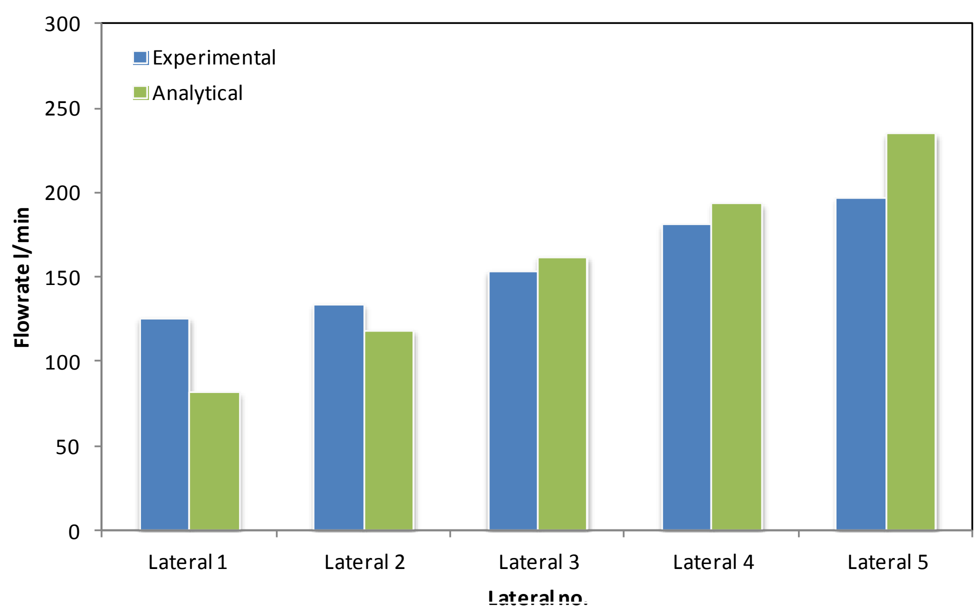

Figure 13: flow distribution per lateral pipe for manifold

Cost of Optimum Design of Trunk Mains Network Using Geographical Information System and Support Programs

Asst. Prof. Abdul Kareem Esmat Zainal
Department of Civil Engineering
College of Engineering
Baghdad University
Email: kareem_esmat@yahoo.com

Asst. Lect. Layla kais Abbas
Department of Surveying Engineering
College of Engineering
Baghdad University
Email: Layla_a2008@yahoo.com

ABSTRACT

Sewer network is one of the important utilities in modern cities which discharge the sewage from all facilities. The increase of population numbers consequently leads to the increase in water consumption; hence waste water generation. Sewer networks work is very expensive and need to be designed accurately. Thus construction effective sewer network system with minimum cost is very necessary to handle waste water generation.

In this study trunk mains networks design was applied which connect the pump stations together by underground pipes for too long distances. They usually have large diameters with varying depths which consequently need excavations and gathering from pump stations and transport the sewage to final waste water treatment plant. This situation urges to decrease the cost to minimum with efficient design of its performance. The aim of this research is minimizing the cost of all sewer components of trunk mains which are lengths, diameters, and volume of excavation with maintaining its performance.

In this research, the utilization of GIS (Geographical Information System) software and VBA (Visual Basic for Application) which is integrated with GIS was used to implement the MST (Minimum Spanning Tree) algorithm to create a visual basic computer program that was used to find the minimum total lengths of the trunk mains in a sewer network.

This method was applied on selected areas in Al-Mansour municipality where there is an existing sewer system containing trunk mains and pump stations. Total lengths of the existing trunk mains are calculated and later, the proposed method was implemented to find the minimum total lengths, with a difference in total lengths of (12601 m).

The new network used to design a proposed sewer system using the computer program SewerGemsV8i, which can be integrated with GIS. New pipes diameters and slopes were calculated by supplying the necessary information that is needed by the computer program.

New sewer system was designed which gave more reliable and economical aspects than the existing one. These results clearly show that when comparing the costs.

Key words: GIS, optimum design, trunk mains, pump stations, minimum cost.

كلفة التصميم الامثل لشبكة انابيب المجاري بإستخدام نظم المعلومات الجغرافية والبرامجيات الساندة

م.م. ليلى قيس عباس
قسم هندسة المساحة
كلية الهندسة / جامعة بغداد

أ.م.عبد الكريم عصمت زينل
قسم الهندسة المدنية
كلية الهندسة / جامعة بغداد

الخلاصـــــــــــــــــــــة

تعد شبكات المجاري من اهم البنى التحتية للبلد والتي تقوم بخدمة عموم الناس بتصريف مياه المجاري من المنازل والمصانع وكافة الانشطة الحيوية، ونظر لزيادة عدد السكان وبالتالي زيادة استهلاك الماء مؤديا الى زيادة تصريف مياه المجاري.فان انشاء شبكات المجاري عمل مكلف جدا ويحتاج الى الدقة في التصميم، فأعداد تصاميم لشبكات المجاري وملحقاتها ذات كفاءة اعلى في العمل وذات كلف اقل في الانشاء ضروري لمعالجة تصريف مياه المجاري.

في هذه الدراسة تم اخذ تصميم شبكات الانابيب الناقلة التي تربط محطات الضخ مع بعضها بانابيب طويلة ممتدة تحت سطح الأرض وباقطار كبيرة عادة واعماق مختلفة وتقوم بجمع مياه المجاري من كافة المحطات ونقلها الى محطة المعالج الاخيرة، وبهذه الحالة كان من الاوجب تصميم تلك الانابيب بأقل كلفة مع ضمان كفاءة العمل.الهدف من هذه الدراسه هو حساب الكلفة الاقل لكل عناصر شبكة الانابيب الناقلة التي تتضمن الاطوال، الأقطار، أعماق الحفر، أعداد محطات الضخ، الموقع الأفضل للمحطات الذي يؤثر على كلفة هذه الانابيب واداؤها.

اعتمد في هذا البحث على استخدام برنامج نظام المعلومات الجغرافية وبرنامج الفيجوال بيسك المدمج مع نظام المعلومات الجغرافية بما يسمى (GIS-VBA) والذي استخدم لتنفيذ خوارزمية شبكة ذات اقل امتداد (Minimum Spanning Tree) وتكوين برنامج يقوم بايجاد اقل مجموع اطوال لشبكة الانابيب الناقلة.

تم اخذ بعض المناطق ضمن وحدة بلدية المنصور كمنطقة للدراسة ولتطبيق البرنامج وتم تحديد مواقع محطات الضخ التي تخدم تلك المنطقة ورسم شبكة تمثل كل الشوارع التي ممكن ان يقترح فيها انشاء انابيب ناقلة وتنفيذ البرنامج لحساب اقصر مجموع اطوال لتلك الشوارع التي تربط بين مواقع محطات الضخ ، حيث لوحظ الفرق بالاطوال بين الانابيب المنفذة والانابيب المقترحة باستخدام البرنامج هو (12601متر).

ثم اعتماد تلك الشبكة المقترحة واستخدامها في احدى برامج تصميم شبكات المجاري المدمج مع برنامج GIS وهو برنامج SewerGemsV8i لغرض حساب اقل اقطار ممكنة للانابيب الناقلة وحساب اقل ميل ممكن لهذه الانابيب وبالتالي الحصول على اقل كميات للحفريات ولوحظ ايضا الفرق بين اقطار الانابيب المقترحة والميول الخاصة بها.

واستنتج أن تنفيذ الطرق المقترحة اعطى مساهمة بإيجابية كبيرة في تصميم وتحليل أنظمة الصرف الصحي الموجودة أو الجديدة.

الكلمات الرئيسية : نظم المعلومات الجغرافية، التصميم الأمثل, الانابيب الناقلة،محطات الضخ، اقل كلفة.

1. INTRODUCTION

Sewerage pipeline networks is one of the essential infrastructures of the modern cities and it is very important in serving all people in their houses, factories, hospitals, schools and other vital utility activities by getting rid of unwanted waste water and water environment prevention.

In recent years, the population has increased significantly, commercial and industrial activities have also grown dramatically. This has led to an increase in water consumption and consequentially increases in quantity of wastewater, so there is need to construct a new sewer networks in areas that suffered from decrease of discharge of waste water.

Design of sewer system includes layout of sewer network, finding lengths, diameters, depths of all pipes, in addition to finding the best locations of other sewer system components such as outfall, manholes, pump stations, etc.

Efficiency and good performance are required in the design of sewer network hence it is not an easy work, in addition it is expensive work; hence need to minimizing and decreasing of construction and operation costs to the minimum.

1.2 GIS Applications in Sewer Networks

GIS are powerful and cost effective tools for deigning intelligent maps for water, wastewater, and storm water systems. Effective waste and storm water management requires linking of specialized computer models to the GIS. Also, integration of engineering, environmental, and socioeconomic objectives into waste and storm water management could be included.Most of the physical, social and economic problems associated with waste and storm water are attributable to unwise land use, insufficient attention to land drainage in urban planning, and ineffective updating of existing waste and storm water control systems, **Rusko et al., 2010**.

Typical applications of GIS for waste and storm water systems include: (1) Watershed storm water management, (2) Floodplain mapping and flood hazard management, (3) Hydrologic and hydraulic modeling of combined and storm sewer systems, including estimating surface elevation and slope from digital elevation model data (DEM), (4) Documenting field work, (5) Planning, assessment of the feasibility and impact of system expansion, (6) Estimating storm water runoff from the physical characteristics of the watershed, e.g. land use, soil, surface imperviousness and slope **Shamsi, 2002 and Paul Longley, 1999**.

Various spatial data layers can be combined and manipulated in a GIS to address planning, operation, and management issues. For example, water and sewer line information can be combined with population statistics and ground elevation data to assess the adequacy of water and sewer utilities, **Shamsi, 2005**.

2. THE OBJECTIVE OF THE RESEARCH

Trunk mains extents for long distances under the ground, these trunk mains usually have large pipe diameters, and since they connect many pump stations, they are embedded deeply under the ground surface for their protection. The design of these trunk mains will be very expensive and need to be reduced with maintaining accuracy and efficiency in its performance. So the aim of this research is to find the optimum design of trunk mains network which implement the highest efficiency and minimum cost. This aim achieved by minimizing the cost of the sewer system components that includes:

i. Length of trunk mains, ii. Trunk mains diameter, and iii. Volume of excavation.

3. METHODOLOGY OF THE WORK

This research developed a methodology in the trunk mains design method that depend on graph theory algorithm to find the minimum total lengths of trunk mains which is Minimum Spanning Tree (MST); it was programmed in Visual Basic for Applications (VBA**)** which is integrated with GIS, this algorithm was implemented on some selected areas in Baghdad city to give minimum total pipe lengths.

Bentley SewerGEMs V8i program is one of computer program that could be integrated with GIS to compute the appropriate pipe diameters and slopes that affect the trunk mains pipes depths.

4. MINIMUM SPANNING TREE ALGORITHM

Using graph algorithm MST is very powerful in providing the tree that connects all nodes of a Graph (which are represented by pump stations in this research) with minimum length of edges (which are represented by the pipe lines connecting the pump stations), the root of the tree is the disposal location of the waste water. It is necessary to use this algorithm and obtain a tree shaped network because there will be only one root for this tree which is the location of waste water disposal and the other branches of the tree represent the links between pump stations. A minimum spanning tree is so named because it is constructed from the minimum of number of edges (lines) necessary to cover every node and it is in tree form because the resulting graph is acyclic (i.e. with no cycles). The minimum spanning tree depends entirely on the starting node. **Michael Mcmillan, 2005**.

From the researchers have studied the MST algorithm and its applications is **Jason Eisner, 1997** who explained that the classic "easy" optimization problem is to find the minimum spanning tree (MST) of a connected, undirected graph. Good polynomial-time algorithms have been known since 1930. This work reviews those methods, building up strategies step by step so as to expose the insights behind the algorithms. Implementation details are clarified, and some generalizations are given. And **Paola Flocchini et al., 2007** deduced that in many network applications the computation takes place on the minimum-cost spanning tree (MST) of the network G; unfortunately, a single link or node failure disconnects the tree.

5. SEWER SYSTEM DESIGN AND ANALYSIS USING GIS

5.1 Case Study

A sample districts in the west of Baghdad/Iraq city located in the municipality of Al-Mansour was taken as a case study for implementation the MST to obtain the minimum cost of trunk mains pipes construction and using SewerGEMs to complete the sanitary design. **Fig. 1** shows the satellite image that shows the sample districts was taken as a case study in municipality of Al-Mansour with the number of districts.

5.2 The Data Sources

In this research, the required data were gathered from different source, such as shapefile forms, satellite images, maps, and numerical tables from various resources, which are:

- ✓ Shape file includes all main streets in municipality of Al-Mansour from department of GIS in Mayoralty of Baghdad (MOB) projected by Universal Transfer Mercator (UTM) and the spheroid is world geodetic system 84 (WGS84), Zone 38 N.
- ✓ Shape file includes the locations of all pump stations in municipality of Al-Mansour from department of GIS in Baghdad Sewage Directorate (BSD) in (MOB) projected by Universal Transfer Mercator (UTM) and the spheroid is WGS84, Zone 38 N.
- ✓ Information about diameters and path of existing trunk mains which connect pump stations together in municipality of Al-Mansour was obtained from BSD.
- ✓ Information about each pump station, such as discharge, depths of wet-well was also obtained from BSD.
- ✓ Satellite image of Bagdad city with resolution of 60 cm was obtained from Quick Bird satellite.

Fig. 2 shows a satellite image of the study area in Al-Mansour municipality, and also shows the locations of pump stations (yellow rectangles) and the main streets (red lines), where each pump station is shown with a label of its name. **Fig. 3** shows the satellite image that shows existing sewer network of trunk mains in the municipality of Al-Mansour.

5.3 Existing Sewer Network

For the analysis of already existing network, collecting some necessary data needed to this study such as:

1. Ground elevation of Pump stations.
2. Waste water inflow to each pump station.
3. Path of the existing trunk mains, and
4. Trunk mains diameters.

5.4 Obtaining Ground Elevations

Source of the elevations that is depended in this research is from Baghdad Sewage Directorate (BSD). These elevations were produced by the Japanese Nippon Koie company, and were obtained in a shape file form. **Fig. 4** shows the satellite image that show point's network of the case study. Any point in these data has ground elevation in addition to Cartesian coordinates (X and Y).These points can be converted to terrain surface using ArcMap10 by interpolation these points by IDW method to product Digital Elevation Model (DEM). **Fig. 5** shows the satellite image that shows Digital Elevation Model (DEM) of the districts in municipality of Al-Mansour.

5.5 Waste Water Flow

Waste water flow information was obtained from Baghdad Sewage Directorates (BSD). Each pump station inflow is shown in **Table 1** in cubic meter per day (m3/day). This table also shows elevations of the pump stations.

5.6 Lengths of the Existing Trunk Mains

Fig. 3 showed the existing trunk mains that are in service, where the total lengths of the trunk mains have a sum of (44895.95 m) which was calculated using ArcGIS computer program. The depth of these trunk mains ranged generally from 3 m at the start of the pump station and ends at 8 m reaching the next pump station where the waste water level is raised using pumps to 3 m again. Trunk mains pipes lengths, diameters, and start depths and end depths are shown in **table 2**;additionally **table 2** shows the calculations of the soil excavations in cubic meters (m3) and the cost of the excavations. These calculations are necessary to obtain the approximate costs that will be used later for comparison with the new proposed method.

5.7 Pipes Diameters

Pipes diameters are an important factor that affects the cost of the sewer system. The pipes diameters contribute in the cost in two ways; first, the cost increases with the increase of the pipe diameter, and second, the pipe diameter affects the width of the excavations, consequently affecting the excavations cost.

5.8 Pipes Material

The cost also depends on the type of the material used for the pipes in trunk mains. There are five types of materials usually used for sewer trunk mains, and these types are as following:

- Ductile Iron Cement Lined (DICL),
- Unplasticised, Modified and Oriented Polyvinyl Chloride (PVC),
- Glass Reinforced Plastic (GRP),
- Steel Cement lined (SCL) (special applications only),and
- Polyethylene (PE) (Less than 100 mm internal diameter only).

The material of these pipes material are used in the districts under study is assumed the UPVC, the cost per unit length and the approximate total cost of the UPVC pipes for each used diameter is shown in **table 3**.The calculations which are shown in **table 2** give the approximate value of the total volume of the excavations in addition to an approximate cost for the excavations.Adding the cost of the pump stations to this cost gives us the total sewer system cost for the districts under the case study. This cost can be easily obtained approximately by multiplying the cost of one pump station by the total number of pump stations as follows:

Total cost of pump stations = No. of pump stations × Cost average of a pump station

Total cost = 23 × 3,000,000,000 = 69, 000,000,000 I.D.

The total cost of a sewer network is calculated and shown in **table 4.**

5.9 Design of the Proposed Network

Minimizing the total cost can be obtained by minimizing the three items which are: Length of trunk mains, Trunk mains diameter, and Volume of excavation. The design procedure can be implemented via the following steps.

5.9.1Obtaining the minimum pipe lengths

Obtaining the minimum trunk mains length can be achieved by implementing Minimum Spanning Tree (MST) algorithm. To implement the new proposed algorithm for network design, it is required to draw a complete streets network graph that connect almost every point which represents a pump stations to all other neighboring points (or other pump stations) in the districts as shown in **Fig. 6**.

These complete streets network represent all main streets in the districts which are connected to pump stations and represents a candidate path for trunk mains. The total length of the complete streets network was (94091.48 m).

Based on Visual Basic for Application (VBA) which integrated in GIS program a new scripting was designed to find the minimum total lengths of the streets by implementing the MST algorithm. This code execution can be done by pressing the command button added to the toolbar of the ArcGIS program as shown in **Fig. 7**, denoted by the small red circle.

When pressing the command button, a series of commands will be executed that asks for the required data to implement the algorithm and obtain the required solution, which are the streets with minimum total lengths.

As soon as the file is stored, the minimum streets network will be shown in the ArcGIS display area. **Fig. 8** shows the minimum spanning streets lengths that connect all pump stations together and provide the minimum required path for the waste water disposal. The total length of the streets network is (32294.10 m). **Table 5** shows the new total length of streets network.

A simple comparison between the two networks in **Fig. 3**and **Fig. 8** shows the difference in total lengths of (44895.95 – 32294.10 = 12601.51 m) which saves more than twelve kilometers of pipe lengths and excavation efforts which has a great economical effect on the total cost of the sewer system.

5.9.2 Design of sewer system

In the previous sections, the design and layout of the sewer pipes was obtained. The inflow of the waste water was already obtained as shown in **table 1**.The sanitary design will be carried out including the design of the pipe diameters, slopes, and required depths.

The computer program SewerGEMs V8i was used for this purpose as it can integrate with ArcGIS program and provide the sewer design environment in the ArcGIS environment, which means it can read the shape file of the new proposed street network and use it for the sewer system design.

The layout of the conduits is shown in **Fig. 9** which also shows that the pump stations, the pump station usually contain a) Wet-well, b) Pump or pumps battery, and c) Ductile iron pipes to uplift the waste water under pressure to a higher level and let it flow again under gravity till it reach the next pump station or the treatment plant. A larger scale of some sample pump stations is shown in **Fig. 10**, where the wet-well, the pump, and the pressure pipes combinations are drawn. A detailed schematic drawing of one pump station is shown in **Fig. 11**.

5.9.3 Computer program components

The next step is to prepare the appropriate data required for modifying the properties of the components of the sewer system, which includes:

1) Pump stations data: Elevations of pump and inflow quantities are already mentioned in **Table 4**. Depth of its will be initially 2 m. These values will be considered in the design of the new sewer network.
2) Conduits data: Conduits data can be represents the gravity pipes are represented as follows:
    a. Lengths: already found from minimum streets network.
    b. Type: UPVC pipes will be considered as it is typically used for the construction of trunk mains.
    c. Diameters: The initial pipe diameters used is 200 mm which is the smallest diameter; this diameter size will change automatically by the computer program as needed in the design procedure.
    d. Inlet and outlet elevations: the inlet elevation is taken from the manhole attached to the starting side of the pipe while the outlet elevation is taken from the wet-well that is at the end of the pipe.
3) Outfall data: (End point of sewer system e.g. treatment plant). The last point that was considered as the outfall is the al-Kadisiya pump station, because of the limitation of the area under study (actually, the Al-Kadisiya pump station convey waste water to other station).
4) Outfall data The last point that was considered as the outfall is the al-Kadisiya pump station, because of the limitation of the area under study (actually, the Al-Kadisiya pump station convey waste water to other station
5) Pressure Pipe: Pressure pipes are the link between the wet-well and the pump from one side and the link between the pump and the manhole from the other side, as the waste water flows from the wet-well through the pump to the next manhole. All pressure pipes were given a length of 300 mm (as recommended by the instructions of the sewer GEMs program manual), ductile iron material, and a diameter of 150 mm was taken as an initial value

5.9.4 Sewer GEMs program run

The computer program has two calculation alternatives, the first, is the design alternative, and the second is the analysis alternative.

The design alternative is the first choice where the computer program performs the design procedure regarding all constrains that were already supplied to the calculation options including the slope constrains (0.001 – 0.1), cover constrains (0.7m – 10m), and velocity constrains (0.61 m/sec – 4 m/sec) (as recommended by the instructions of the computer program manual).

The design was done for steady state condition neglecting the variation of the amount of waste water during the day (24 hrs.), only peak values were taken into consideration in the design procedure.

The results obtained from the design procedure affect the pipes diameters, slopes of pipes, and cover constrains. Minor adjustments were made at the analysis phase of the program including pipe invert level to maintain slopes within constrains.

Results of computer program run is shown in **table 6** which also includes the necessary calculations for the amount of excavations and its cost, while **table 7** shows the calculations of pipe costs considering the reduced lengths of pipes and its diameter which reflects the reduced cost. After the result was taken it can be compute the total cost of proposed sewer network as shown in **table 8** and the **table 9** that shows the comparison between the costs and the reduction obtained using the proposed network.

6. DISCUSSION& CONCLUSION

A. MST provides a successful solution for obtaining the minimum total lengths of trunk mains pipes, those pipes usually are large in diameters, they run for long distances and may go deep into the ground, consequently, they may cost a lot according to these factors, so any reduction in these costs may reduce the overall cost of the system.

B. MST algorithm can be very useful in estimating the paths for trunk mains (or any large pipes may be used in sewer systems) as any reduction may be obtained is reflected directly on the total cost of the sewer system.

C. After obtaining the MST, the integrated computer program (SewerGems) with the GIS program, can facilitate the sewer system design or analysis. This computer program takes the required information directly from the ArcGIS map. The trunk mains pipes lengths and pump stations locations are obtained through "Model Builder" command in the SewerGEMs menu.

D. Other hydraulic design operations are carried out by the computer program after all the complimentary information is supplied (e.g. hydraulic constrains, velocities, minimum and maximum cover, slopes, etc.).

E. The computer program (SewerGEMs) can work either in design mode or analysis mode. It depends on the required operation by the user. Usually a design process is carried out first then any required adjustments may be carried out then an analysis process is then worked out to see the effect of these adjustments. This operation may be repeated till the required design (or analysis) constrains are fulfilled.

F. For estimating the locations of new pump stations, the AHP process can be very handy. Any factors that may be considered as effective factors can be calculated among other factors to find the most candidate locations.

G. The resulting map from the AHP calculations can be very helpful for human judgment especially that these results are obtained in a map form for the area under consideration which facilitate recognition any environmental factors that many affect the human judgment in choosing the required locations for pump stations.

REFRENCES

- Bentley SewerGEMS V8i/ *User's Guide*, Bentley SewerCAD V8i/ *User's Guide*, XM Edition.
- City of San Diego, Public Utilities Department, 2013, *Sewer Design Guide*.
- Drainage Services Department, Government of the Hong Kong, 2013, *Sewerage Manual*,Second Edition.
- Drainage Services Department, Government of the Hong Kong, May 2013, *Key Planning Issues and Gravity Collection System*, Third Edition.
- Drešković Nusreta and Samir Đugb, 2012, *Applying The Inverse Distance Weighting And Kriging Methods Of The Spatial Interpolation On The Mapping The Annual Precipitation In Bosnia And Herzegovina*, *International Environmental Modeling and Software Society (iEMSs)*.
- Jason Eisner 2007,*State Of The Art Algorithm For Minimum Spanning Trees",* University of Pennsylvania.
- Longley, Paul, 1999, *GIS – Management Issues and Applications*. Volume 2, Publisher: John Wiley.
- Mcmillan, Michael, 2005, "*Data Structures And Algorithms Using Visual Basic.Net*", Cambridge University Press.
- Miroslav Rusko, Roman Chovanec and Dana Rošková, 2010, *An Overview Of Geographic Information System And Its Role And Applicability In Environmental Monitoring And Process Modeling*, Faculty Of Materials Science And Technology In Trnava Slovak, University Of Technology In Bratislava, no.29.
- Mcmillan, Michael, 2005, *Data Structures And Algorithms Using Visual Basic.Net*, Cambridge University Press.
- Paola Flocchini, T. Mesa Enriquez, Linda Pagli, Giuseppe Prencipe, and Nicola Santoro *"Distributed Computation of All Node Replacements of a Minimum Spanning Tree"*. ERO-PAR Parallel Processing, Rennes
- SewerCAD v5.5 for Windows/*User's Guide*, Second Printing
- Shamsi, U.M., 2005, *GIS Applications for Water, Wastewater, and Stormwater Systems*, CRC Press, ISBN 0-8493-2097-6.
- Shamsi, U.M., 2002, *GIS Tools for Water, Wastewater, and Stormwater Systems,* ASCE Press, ISBN 0-7844-0573-5.
- Thomas H. Cormen, Charles E. Leiserson, Ronald L. Rivest, Clifford Stein ,2009, *Introduction to Algorithms* , the MIT Press, Massachusetts Institute of Technology, third edition.

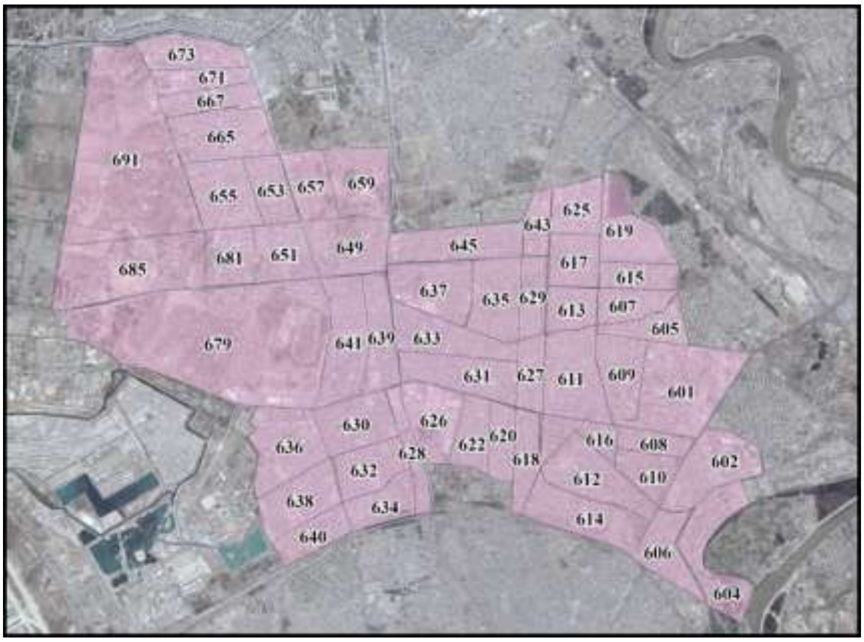

Figure1. Satellite image shows the sample districts as a case study in municipality of Al-Mansour, (source: MOB).

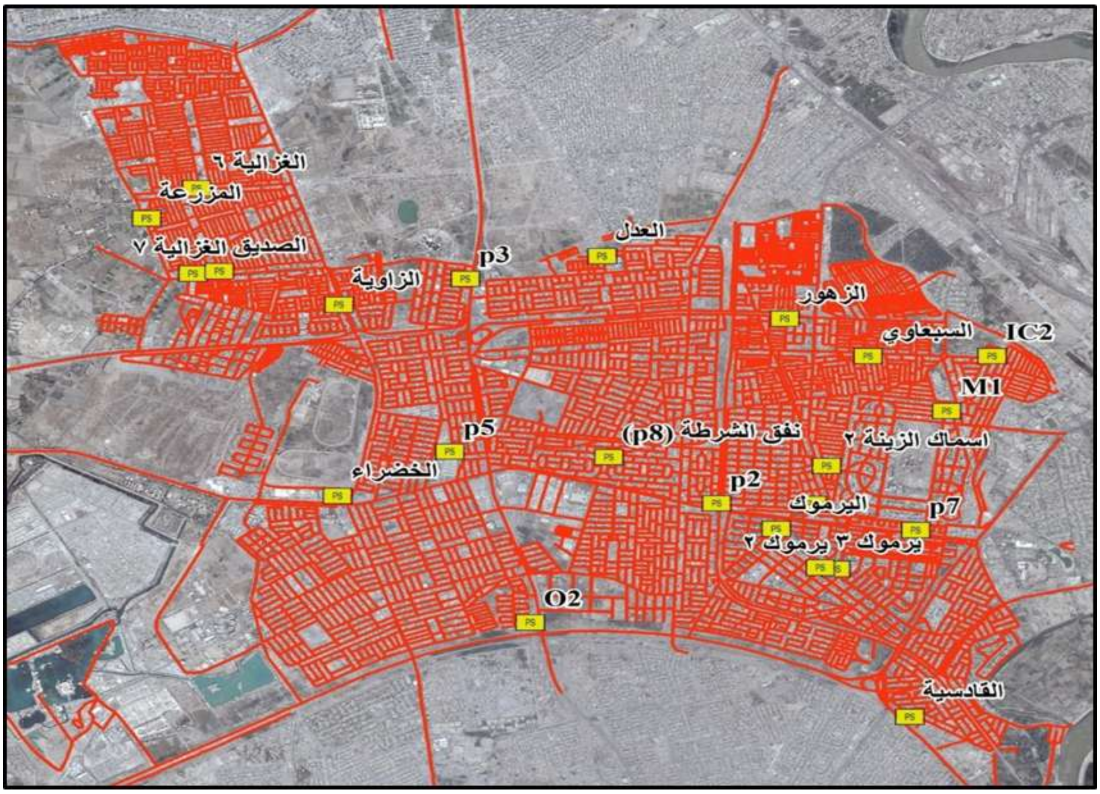

Figure 2. Satellite image shows pump stations and main streets in municipality of Al-Mansour, (source: MOB&BSD).

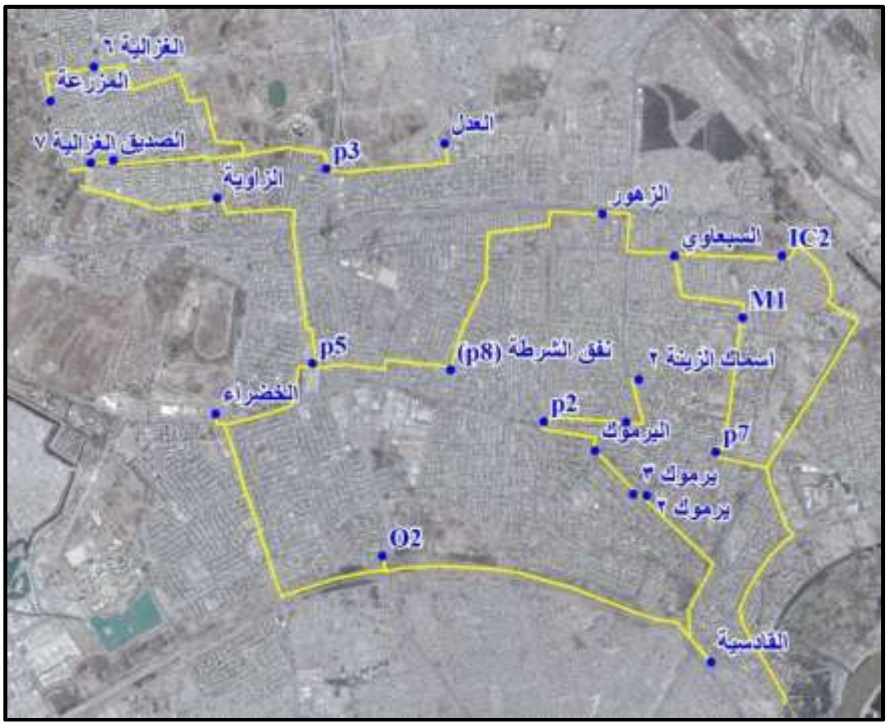

Figure3. Satellite image shows the existing sewer network of trunk mains in municipality of Al-Mansour, (source: DSD).

Figure 4. Satellite image shows the point's network of the districts in municipality of Al-Mansour, (source: DSD).

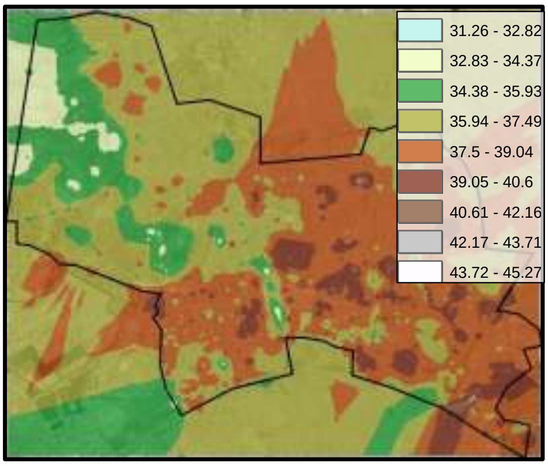

Figure 5. Satellite image shows Digital Elevation Model (DEM) for case study.

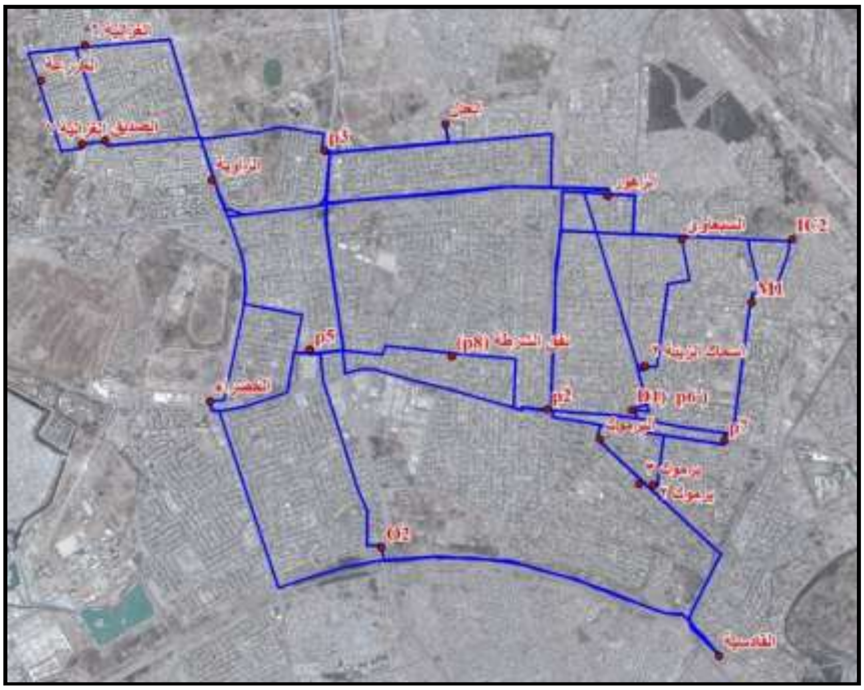

Figure 6. Complete streets network.

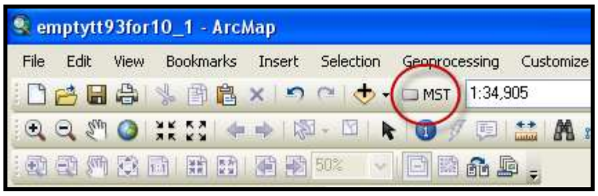

Figure 7. Command botton in the tool bar.

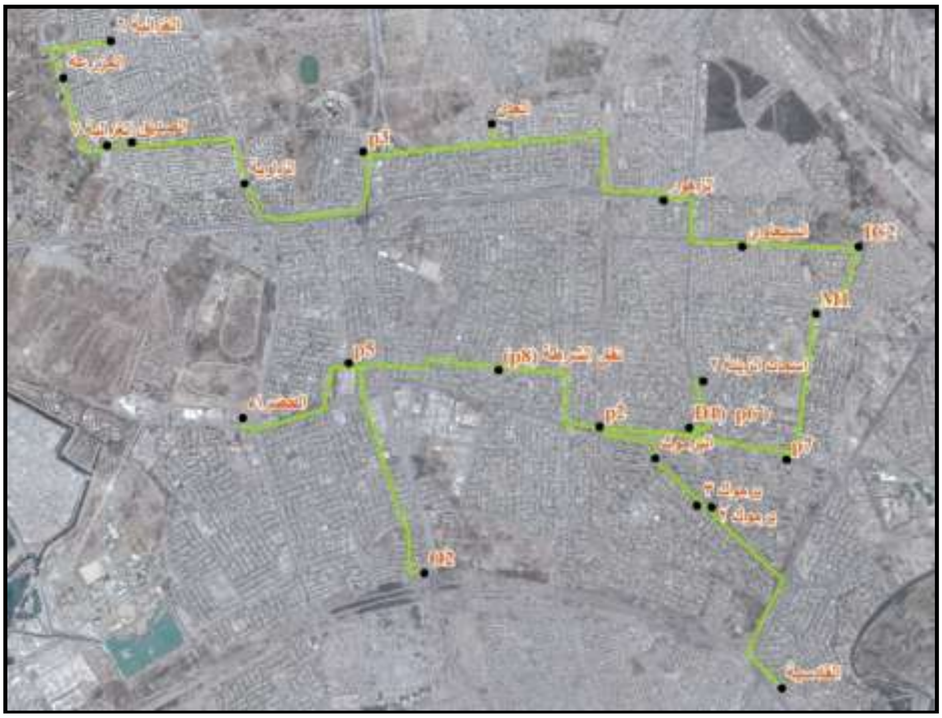

Figures 8. The minimum spanning streets network.

Figure 9. Project components after modification.

Figure 10. Larger scale of sample section showing wet-well, pump, and pressure pipes.

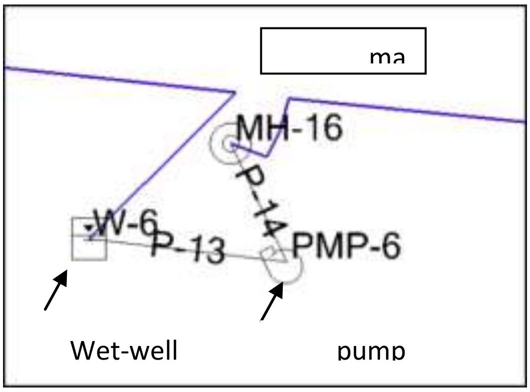

Figure 11. Schematic drawing showing wet-well, pump, and pressure pipes.

Table 1. Pump Stations names, Elevations, and Flow.

No	Name	Elevation (m)	Flow (m^3/day)
1	الغزالية 6	39.0	2000
2	المزرعة	36.0	800
3	الغزالية 7	37.5	1200
4	الصديق	37.0	800
5	الزاوية	36.0	1800
6	p3	38.0	1800
7	العدل	38.5	1000
8	الزهور	37.0	1400
9	السبعاوي	37.8	500
10	M1	38.8	400
11	IC2	37.0	1100
12	اسماك الزينة 2	36.0	600
13	p7	38.5	600
14	اليرموك 2	36.4	600
15	اليرموك 3	37.0	600
16	اليرموك	38.0	600
17	p2	38.0	800
18	نفق الشرطة (p8)	38.5	2100
19	p5	35.0	1600
20	الخضراء	40.0	600
21	O2	38.5	4400
22	D1 (p6)	37.7	2200
23	القادسية	37.0	Outlet

Table 2. Existing Trunk mains connecting Pump Stations.

No	From sta.	To sta.	Length (m)	Start depth (m)	end depth (m)	Area (m^2)	D. (m)	Vol. m^3
1	المزرعة	الغزالية6	924.95	1.5	5.0	3006.09	0.50	1503.04
2	الغزالية 6	P3	3953.76	2.0	6.0	15815.00	1.00	15815.04
3	الغزالية 7	الصديق	272.58	1.5	4.0	749.59	0.50	374.80
4	الصديق	Intersect	1598.66	1.5	6.0	5994.98	0.50	2997.49
5	الزاوية	P5	2958.93	2.0	6.5	12575.50	1.00	12575.45
6	O2	القادسية	4383.84	2.0	7.0	19727.30	1.00	19727.28
7	العدل	P3	1680.82	1.5	7.0	7143.49	1.00	7143.49
8	يرموك3	يرموك2	222.96	1.0	4.0	557.40	1.00	557.40
9	M1	P7	1715.00	1.5	6.5	6860.00	1.00	6860.00
10	اسماك الزينة	P6	839.44	1.5	4.5	2518.32	0.50	1259.16
11	P6	P2	1049.94	2.0	6.5	4462.25	1.00	4462.25
12	السبعاوي	IC2	1344.82	1.5	5.5	4706.87	1.00	4706.87
13	الزهور	السبعاوي	1405.76	1.5	6.0	5271.60	0.50	2635.80
14	P2	يرموك	889.00	1.5	5.0	2889.25	1.00	2889.25
15	يرموك	يرموك3	735.28	2.0	6.5	3124.94	0.75	2343.71
16	الزهور	P8	3265.19	2.0	7.0	14693.40	1.00	14693.35
17	الخضراء	P5	1727.79	2.0	7	7775.06	1.00	7775.06
18	السبعاوي	M1	1808.23	1.5	6	6780.86	1.30	8815.12
19	P7	Intersect	3906.17	2.0	7	17577.80	1.00	17577.77
20	يرموك2	القادسية	2511.46	2.0	6	10045.80	1.00	10045.84
21	IC2	Intersect	3622.53	2.0	7	16301.40	1.00	16301.39
22	P3	Intersect	1014.43	2.0	7	4564.94	1.00	4564.94
23	P5	P2	3173.72	1.5	6	11901.50	1.00	11901.45
24	P8	Intersect	306.18	2.0	7	1377.81	1.00	1377.81
Sum			44895.90			186421.00		178903.73

Unit cost (I.D.)	**500,000**
Total cost of excavation (I.D.)	**89,451,866,250**

Table 3. UPVC Pipes Cost.

No.	Dia. (m)	Total Length (m)	Price per unit length (I.D.)	Cost (I.D.)
1	0.50	5041	80,000	403,280,000
2	0.75	735	230,000	169,050,000
3	1.00	37726	400,000	15,090,000,000
4	1.30	1808	600,000	1,084,800,000
			Total Cost	**16,747,530,000**

Table 4. Total Cost of existing sewer network.

Item	Cost in I.D.
Excavations Cost	89,451,866,250
Pipes Cost	16,747,530,000
Pump Stations Cost	69,000,000,000
Total Cost	**175,199,396,250**

Table 5. Minimum Streets lengths.

No	From sta.	To sta.	Length (m)	No	From sta.	To sta.	Length (m)
1	19	20	272.58	12	8	12	2715.78
2	20	10	1685.27	13	22	21	1344.70
3	11	23	1063.62	14	23	19	1173.03
4	17	10	2223.12	15	1	17	1711.96
5	6	5	1793.10	16	16	14	1731.50
6	5	4	1193.12	17	15	4	832.86
7	8	9	216.19	18	1	18	2790.74
8	2	8	745.501	19	7	3	1701.25
9	4	14	1302.44	20	22	16	1016.30
10	5	2	900.05	21	7	13	2678.52
11	7	6	1812.05	22	18	21	1390.45
				Total length			**32294.10**

Table 6. Result of Program Run.

No	Pipe Label	From sta.	To sta.	Length (m)	Invert Elv. start (m)	Invert Elv. stop (m)	Start depth (m)	end depth (m)	Slope	Area (m^2)	Dia. (mm)	Vol. m^3
1	swr-7	MH-2	MH-1	216.20	35.45	34.74	0.95	2.26	0.0033	347.00	254.00	88.14
2	swr-1	MH-3	W-16	272.60	36.34	35.84	1.16	1.16	0.0018	316.22	457.20	144.57
3	swr-17	MH-5	W-7	832.90	35.05	32.31	0.95	5.39	0.0033	2640.29	254.00	670.64
4	swr-3	MH-7	W-1	1063.60	37.92	34.92	1.08	1.08	0.0028	1148.69	304.80	350.12
5	swr-8	MH-9	MH-1	745.50	36.23	34.74	1.77	2.26	0.0020	1502.19	914.40	1373.60
6	swr-10	MH-10	W-19	900.00	36.23	35.33	1.77	2.67	0.0010	1998.00	914.40	1826.97
7	swr-20	MH-11	W-9	1016.30	35.39	34.37	1.61	4.43	0.0010	3069.23	762.00	2338.75
8	swr-14	MH-8	W-17	1173.00	34.84	33.49	1.16	4.01	0.0012	3032.21	457.20	1386.32
9	swr-6	MH-6	W-4	1193.10	36.09	34.89	1.61	3.11	0.0010	2815.72	914.40	2574.69
10	swr-22	MH-13	W-11	1390.40	35.54	34.15	1.46	3.65	0.0010	3552.47	762.00	2706.99
11	swr-9	MH-15	W-7	1302.40	36.89	32.31	1.61	5.39	0.0035	4558.40	762.00	3473.50
12	swr-5	MH-16	W-4	1793.10	37.04	34.89	1.46	3.11	0.0012	4097.23	609.60	2497.67
13	swr-13	MH-14	W-10	1344.70	36.34	34.99	1.46	2.01	0.0010	2333.05	762.00	1777.79
14	swr-19	MH-18	MH-17	1701.20	39.10	33.61	0.90	1.39	0.0032	1947.87	203.20	395.81
15	swr-2	MH-4	W-15	1685.30	35.69	34.01	1.31	1.99	0.0010	2780.75	533.40	1483.25
16	swr-4	MH-19	W-14	2223.10	34.69	32.47	1.31	5.53	0.0010	7603.00	609.60	4634.79
17	swr-15	MH-20	W-13	1712.00	36.54	34.83	1.46	3.67	0.0010	4391.28	609.60	2676.93
18	swr-16	MH-12	W-8	1731.50	37.19	35.45	1.61	3.05	0.0010	4034.40	762.00	3074.21
19	swr-11	MH-17	W-6	1812.00	33.61	31.80	1.39	6.70	0.0010	7329.54	609.60	4468.09
20	swr-18	MH-21	W-12	2790.70	37.04	34.25	1.46	2.75	0.0010	5874.42	762.00	4476.31
21	swr-12	MH-1	O-1	2715.80	34.74	32.02	2.26	4.98	0.0010	9831.20	1,066.80	10487.92
22	swr-21	MH-23	W-5	2678.50	37.27	33.77	1.23	1.23	0.0013	3294.56	457.20	1506.27
sum				**32293.90**								**54413.32**
										Unit Cost		**500,000**
										Total Cost		**27,206,656,801**

Table 7. UPVC pipes cost.

No	Dia. (mm)	Total Length	unit price	Cost
1	203.20	1,701.20	50,000	85,060,000
2	254.00	1,049.00	60,000	62,940,000
3	304.80	1,063.60	70,000	74,452,000
4	457.20	4,124.10	80,000	329,928,000
5	533.40	1,685.30	120,000	202,236,000
6	609.60	7,540.20	180,000	1,357,236,000
7	762.00	9,576.10	230,000	2,202,480,000
8	914.40	2,838.70	400,000	1,135,480,000
9	1066.80	2,715.80	500,000	1,357,900,000
	Total Length	**32,294.00**	**Total Cost**	**6,807,735,000**

Table 8. Overall Total cost of proposed sewer network.

Item	Cost
Excavations Cost	19,510,900,000
Pipes Cost	6,807,735,000
Pump Stations Cost	69,000,000,000
Total Cost	**95,318,635,000**

Table 9. Cost comparison between existing network costs and proposed network costs.

Item	Existing Network	Proposed Network	Reduction in Cost
Excavations Cost	89,451,866,250	19,510,900,000	**69,941,366,250**
Pipes Cost	16,747,530,000	6,807,735,000	**9,939,795,000**
Pump Stations Cost	69,000,000,000	69,000,000,000	**0**
Total Cost	**175,199,396,250**	**95,318,235,000**	**79,880,761,250**